

DISSERTATION

NITRIC OXIDE GENERATION FROM S-NITROSOTHIOLS VIA INTERACTIVITY WITH  
POLYMER-SUPPORTED METAL-ORGANIC FRAMEWORKS

Submitted by

Megan J. Neufeld

Department of Chemistry

In partial fulfillment of the requirements

For the Degree of Doctor of Philosophy

Colorado State University

Fort Collins, Colorado

Spring 2018

Doctoral Committee:

Advisor: Melissa Reynolds

Eugene Chen

Richard Finke

Matthew Kipper

A. R. Ravishankara

Copyright by Megan J. Neufeld 2018

All Rights Reserved

## ABSTRACT

### NITRIC OXIDE GENERATION FROM *S*-NITROSOTHIOLS VIA INTERACTIVITY WITH POLYMER-SUPPORTED METAL–ORGANIC FRAMEWORKS

Catheters, extracorporeal systems, stents, and artificial heart valves are all common blood-contacting medical devices. Due to the differences in the chemical and physical properties of the polymeric materials used to construct medical devices and biological tissues in the cardiovascular system, complications such as thrombus formation arise from the resulting incompatibilities. Introduction of foreign materials that lack critical biological cues can result in disruption of the delicate balance maintained within the circulatory system. This disruption of homeostasis initiates a complex cascade of events such as platelet adhesion and protein deposition that ultimately result in thrombus formation. As such, the propensity of blood to clot upon contact with a foreign surface represents a challenge unique to devices intended for vascular applications. The current clinical use of devices such as vascular catheters includes the administration of anticoagulants, however their associated complications such as internal hemorrhaging renders this practice undesirable as a long-lasting solution. A general limitation of existing devices made from synthetic polymers is their inability to integrate with their environment through biological cues (natural regulators). Materials that lack this behavior are often described as passive towards their environment. In comparison, active materials that can simulate natural molecules used to maintain biological responses may result in enhanced integration of medical devices. In the natural, healthy endothelium, the prevention of thrombus formation occurs through the release of anticoagulants and platelet inhibitors such as gaseous nitric oxide (NO). While the use of NO for medicinal

purposes began indirectly in the late 1800s, the significance of its endogenous production was not known until the 1970s. In particular, NO is a key factor in the prevention of thrombus formation. While its remedial potential has led to its use as an exogenous therapeutic agent, its high reactivity limits its applicability as a localized therapeutic. This limitation is addressed by mimicking the natural endothelium and using small molecules in the bloodstream known as *S*-nitrosothiols (RSNOs) to produce NO directly from this physiological source. Biological RSNOs are theorized to aid in the stabilization and transport of NO and undergo an NO-forming decomposition in the presence of heat, light, and certain metals such as copper. Prior strategies have evaluated exploiting the physiological supply of RSNOs through the incorporation of copper complexes into polymeric materials. While these copper-based materials demonstrate the production of NO from RSNO decomposition, limitations arise due to the gradual loss of the catalytic material and toxicity from copper leaching. In order for this type of approach to be feasible, the active metal species must remain immobilized within the structural framework.

Metal–organic frameworks (MOFs) are a class of crystalline materials that consist of organic ligands coordinated to metal centers. Certain copper-based MOFs have demonstrated the ability to enhance the generation of NO from RSNOs without the gradual loss of the active species. Through integration of certain copper-based MOFs with medically relevant polymers, materials can be prepared that promote the localized generation of NO at their surfaces. However, the feasibility of utilizing copper-based MOFs for such applications depends on effective incorporation within a supporting polymeric matrix *and* the retention of useful activity thereafter. As such, it is necessary to assess different MOF/polymer composites for their ability to promote NO generation from RSNOs prior to use in medical applications. This dissertation investigates the incorporation of two distinct copper-based MOFs into a selection of medically-relevant polymeric materials including

cotton, poly(vinyl chloride), chitosan, and poly(vinyl alcohol). These MOF/polymer materials were subsequently tested for their ability to promote NO generation from RSNOs in an effort to assess the impact of incorporation within a polymer matrix. Overall, this work demonstrates the potential for blood-contacting MOF-containing materials in biomedical settings by identifying ideal characteristics that MOF/polymer composites should exhibit for optimization and translation to a clinical setting.

## ACKNOWLEDGEMENTS

Individual contributions and funding sources:

Chapter 2: In part, NOA measurements were obtained by J. L. Harding. ICP-AES analysis was performed by the Soil, Water and Plant Testing Laboratory at Colorado State University. All other work carried out by Megan J. Neufeld. This work was funded by Colorado State University, the National Science Foundation Division of Biomaterials (DMR1352201), and the National Institutes of Health (1R21EB016838-021).

Chapter 3:SNAP synthesis was performed by Alec Lutzke. Cytotoxicity studies performed by Brenton R. Ware. ICP-AES analysis was performed by the Soil, Water and Plant Testing Laboratory at Colorado State University. All other work carried out by Megan J. Neufeld. This work was funded by the National Science Foundation (CAREER Grant CBET-1351909), Colorado State University, National Science Foundation Division of Biomaterials (Grant DMR-1352201), and the National Institutes of Health (Grant 1R21EB016838021).

Chapter 4:GSNO synthesis and chitosan film preparation performed by Alec Lutzke. Alec Lutzke also assisted in preparation of the manuscript. Mass spectrometry analysis performed by Jesus B. Tapia. ICP-AES analysis was performed by Jim Self and Debbie Weddle at the CSU Soil, Water and Plant Testing Lab. Joseph Staver for donating blood for stability testing. All other work carried out by Megan J. Neufeld. Funding was provided by Colorado State University, the National Science Foundation Division of Biomaterials (Grant DMR1352201), and the National Institutes of Health (Grant 1R21EB016838-021).

Chapter 5:GSNO synthesis and film preparation were performed by Alec Lutzke. Alec Lutzke also assisted in preparation of the manuscript. William M. Jones performed TGA and DSC

experiments and is the primary author in the portions of the membrane characterization sections which discuss those two results. Jim Self performed ICP-AES analysis at the CSU Soil, Water and Plant Testing Lab. All other work was carried out by Megan J. Neufeld. Funding was provided by the National Science Foundation Division of Biomaterials (DMR-1352201), the National Institutes of Health (1R21EB016838-021), and Colorado State University.

## TABLE OF CONTENTS

|   |    |
|---|----|
| ABSTRACT.....   | ii |
| ACKNOWLEDGEMENTS .....  | v  |
| CHAPTER 1: INTRODUCTION.....  | 1  |
| 1.1 Blood-contacting devices: adverse interactions at the biointerface and a unique solution.....                               | 1  |
| 1.2 Preventing thrombogenicity.....   | 4  |
| 1.2.1 Platelet adhesion, activation, and aggregation on a material surface .....  | 6  |
| 1.2.2 The blood coagulation cascade .....   | 7  |
| 1.3 Nitric oxide .....  | 9  |
| 1.3.1 The biological activity of nitric oxide.....  | 11 |
| 1.3.2 Therapeutic applications of nitric oxide .....  | 15 |
| 1.4 <i>S</i> -nitrosothiols and their therapeutic potential .....   | 16 |
| 1.4.1 The biological role of <i>S</i> -nitrosothiols .....  | 18 |
| 1.4.2 Basal blood <i>S</i> -nitrosothiol concentration: an ongoing debate.....  | 20 |
| 1.4.3 Chemical and physical properties of <i>S</i> -nitrosothiols .....   | 21 |
| 1.4.4 <i>S</i> -Nitrosothiol decomposition: influence of copper ions .....  | 24 |
| 1.5 Catalytic methods of generating nitric oxide from <i>S</i> -nitrosothiols for medical applications .....                    | 27 |
| 1.6 Metal–organic frameworks .....  | 30 |
| 1.6.1 Metal–organic frameworks for delivery of exogenous nitric oxide.....  | 32 |
| 1.6.2 Metal–organic frameworks for nitric oxide generation .....  | 35 |
| 1.7 Dissertation overview .....   | 40 |
| REFERENCES .....  | 43 |
| CHAPTER 2: IMMOBILIZATION OF COPPER(II) BENZENE-1,3,5-TRICARBOXYLATE ONTO COTTON FABRIC AS A NITRIC OXIDE RELEASE CATALYST..... | 63 |
| 2.1 Introduction.....   | 63 |
| 2.2 Experimental section.....   | 66 |
| 2.2.1 Materials .....   | 66 |
| 2.2.2 Carboxymethylation of cotton fabric .....   | 66 |
| 2.2.3 Surface deposition of copper(II) benzene-1,3,5-tricarboxylate .....   | 66 |
| 2.2.4 Characterization techniques .....   | 67 |
| 2.2.5 Determination of weight percent copper (II)-benzene-1,3,5-tricarboxylate.....   | 67 |
| 2.2.6 Evaluation of structural robustness and durability.....   | 68 |
| 2.2.7 Chemiluminescence analysis of nitric oxide.....   | 68 |
| 2.2.8 Preparation of <i>S</i> -nitrosocysteamine .....  | 68 |
| 2.2.9 Measurement of nitric oxide generation catalyzed by copper (II) benzene-1,3,5-tricarboxylate cotton swatches.....         | 69 |
| 2.3 Results and discussion .....  | 70 |
| 2.3.1 Carboxymethylation of cotton .....  | 70 |

|  |    |
|--|----|
| 2.3.2 Growth and immobilization of copper (II) benzene-1,3,5-tricarboxylate on cotton.....   | 70 |
| 2.3.3 Monitoring the growth and formation of copper(II) benzene-1,3,5-tricarboxylate over successive deposition cycles.....              | 73 |
| 2.3.4 Morphology and surface coverage of copper(II) benzene-1,3,5-tricarboxylate cotton materials.....                                   | 75 |
| 2.3.5 Reactivity of copper(II) benzene-1,3,5-tricarboxylate materials towards <i>S</i> -nitrosocysteamine for nitric oxide release ..... | 78 |
| 2.3.6 Evaluation of catalytic lifetime and integrity.....  | 81 |
| 2.4 Conclusions.....   | 84 |
| REFERENCES .....   | 85 |

CHAPTER 3: WATER-STABLE COPPER(II) BENZENE-1,3,5-TRIS(1*H*-1,2,3-TRIAZOL-5-YL)/POLYMER COMPOSITES COMPATIBLE WITH HUMAN HEPATOCYTES .....

|   |     |
|---|-----|
| 3.1 Introduction.....   | 90  |
| 3.2 Experimental details.....   | 94  |
| 3.2.1 Materials .....   | 94  |
| 3.2.2 Characterization techniques .....   | 94  |
| 3.2.3 Copper(II) benzene-1,3,5-tris(1 <i>H</i> -1,2,3-triazoy-5-yl) synthesis.....  | 95  |
| 3.2.4 Preparation of copper(II) benzene-1,3,5-tris(1 <i>H</i> -1,2,3-triazoy-5-yl)/polymer films .....  | 95  |
| 3.2.5 Copper leaching analysis .....  | 96  |
| 3.2.6 Chemiluminescence-based analysis of nitric oxide .....  | 96  |
| 3.2.7 Preparation of <i>S</i> -nitroso- <i>N</i> -acetylpenicillamine.....  | 96  |
| 3.2.8 Measurement of nitric oxide generation .....  | 97  |
| 3.2.9 Cell studies.....   | 97  |
| 3.2.10 Liver functionality assays .....   | 98  |
| 3.2.11 Copper(II) benzene-1,3,5-tris(1 <i>H</i> -1,2,3-triazoy-5-yl)/polymer films toxicity assays on fibroblasts and micropatterned co-cultures..... | 98  |
| 3.3 Results and discussion .....  | 99  |
| 3.3.1 Synthesis and characterization.....   | 99  |
| 3.3.2 Nitric oxide release analysis .....   | 101 |
| 3.3.3 Cytocompatibility towards fibroblasts and primary human hepatocytes....   | 105 |
| 3.3.4 Copper leaching from copper(II) benzene-1,3,5-tris(1 <i>H</i> -1,2,3-triazoy-5-yl)/polymer composites.....                                      | 110 |
| 3.4 Conclusions.....  | 111 |
| REFERENCES .....  | 114 |

CHAPTER 4: CHITOSAN/COPPER(II) BENZENE-1,3,5-TRIS(1*H*-1,2,3-TRIAZOL-5-YL) HYBRID MATERIALS PROMOTE NITRIC OXIDE RELEASE FROM *S*-NITROSGLUTATHIONE IN AQUEOUS SOLUTION .....

|   |     |
|---|-----|
| 4.1 Introduction.....   | 122 |
| 4.2 Methods.....  | 127 |
| 4.2.1 Materials .....   | 127 |
| 4.2.2 Characterization methods.....   | 127 |
| 4.2.3 Preparation of copper(II) benzene-1,3,5-tris(1 <i>H</i> -1,2,3-triazoy-5-yl)..... | 128 |

|   |     |
|---|-----|
| 4.2.4 Preparation of chitosan membranes .....   | 128 |
| 4.2.5 Synthesis of <i>S</i> -nitrosoglutathione .....   | 129 |
| 4.2.6 Membrane swelling properties .....  | 129 |
| 4.2.7 Measurement of nitric oxide formation .....   | 129 |
| 4.2.8 Mass spectrometry analysis .....  | 130 |
| 4.3 Results and discussion .....  | 131 |
| 4.3.1 Synthesis and characterization of copper(II) benzene-1,3,5-tris(1 <i>H</i> -1,2,3-triazoy-5-yl) and chitosan/ copper(II) benzene-1,3,5-tris(1 <i>H</i> -1,2,3-triazoy-5-yl) composite materials ..... | 131 |
| 4.3.2 Evaluation of enhanced nitric oxide generation from <i>S</i> -nitrosoglutathione with chitosan/ copper(II) benzene-1,3,5-tris(1 <i>H</i> -1,2,3-triazoy-5-yl) membrane .....                          | 138 |
| 4.3.3 Impact of copper(II) benzene-1,3,5-tris(1 <i>H</i> -1,2,3-triazoy-5-yl) immobilization on enhancement of nitric oxide generation .....  | 141 |
| 4.3.4 Evaluation of structural integrity and copper leaching .....  | 142 |
| 4.3.5 Determination of reaction products .....  | 144 |
| 4.4 Conclusions .....   | 147 |
| REFERENCES .....  | 149 |

|  |     |
|--|-----|
| <b>CHAPTER 5: NITRIC OXIDE GENERATION FROM ENDOGENOUS SUBSTRATES USING COPPER(II) BENZENE-1,3,5-TRIS(1<i>H</i>-1,2,3-TRIAZOL-5-YL): INCLUSION WITH POLY (VINYL ALCOHOL) MEMBRANES TO INVESTIGATE REACTIVITY AND THERAPEUTIC POTENTIAL.....</b> |     |
| 5.1 Introductions .....  | 155 |
| 5.2 Materials and methods .....  | 159 |
| 5.2.1 Materials .....  | 159 |
| 5.2.2 Synthesis of copper(II) benzene-1,3,5-tris(1 <i>H</i> -1,2,3-triazoy-5-yl).....  | 160 |
| 5.2.3 Synthesis of cross-linked copper(II) benzene-1,3,5-tris(1 <i>H</i> -1,2,3-triazoy-5-yl)/poly(vinyl alcohol) membranes.....   | 160 |
| 5.2.4 Synthesis of tecoflex SG-80A polyurethane films.....   | 161 |
| 5.2.5 Synthesis of <i>S</i> -nitrosoglutathione .....  | 161 |
| 5.2.6 General Characterization .....   | 162 |
| 5.2.7 Thermogravimetric analysis.....  | 162 |
| 5.2.8 Differential scanning calorimetry .....  | 162 |
| 5.2.9 Water uptake studies .....   | 163 |
| 5.2.10 Nitric oxide release measurements .....   | 163 |
| 5.2.11 Statistical analysis.....   | 164 |
| 5.3 Synthesis and characterization of copper(II) benzene-1,3,5-tris(1 <i>H</i> -1,2,3-triazoy-5-yl)/poly(vinyl alcohol) membranes.....   | 164 |
| 5.3.1 Membrane preparation .....   | 165 |
| 5.3.2 Membrane characterization.....   | 168 |
| 5.4 Nitric oxide generation from <i>S</i> -nitrosoglutathione .....  | 174 |
| 5.4.1 Performance at physiological pH and temperature.....   | 176 |
| 5.4.2 Effect of varying copper(II) benzene-1,3,5-tris(1 <i>H</i> -1,2,3-triazoy-5-yl) concentration.....   | 184 |
| 5.4.3 Effect of polymer water permeability .....   | 185 |
| 5.4.4 Effect of lower temperature .....  | 187 |

|  |     |
|--|-----|
| 5.4.5 Effect of varying pH conditions.....                         | 188 |
| 5.4.6 Effect of thiol blocking with <i>N</i> -ethylmaleimide ..... | 194 |
| 5.5 Summary and conclusions .....                                  | 196 |
| REFERENCES .....   | 200 |
| <br>   |     |
| CHAPTER 6: CONCLUDING REMARKS AND FUTURE DIRECTIONS .....          | 209 |
| 6.1 Project Summary.....   | 209 |
| 6.2 Device fabrication.....  | 213 |
| 6.3 Assessment of blood compatibility.....                         | 217 |
| 6.4 Final thoughts.....  | 221 |
| REFERENCES .....   | 223 |

CHAPTER 1  
INTRODUCTION

**1.1 Blood-Contacting Devices: Adverse Interactions at the Biointerface and a Unique**

**Solution**

A medical device can be broadly defined as an instrument, implant, or apparatus used in humans for therapeutic, diagnostic or cosmetic applications. Medical devices are an inextricable element of modern healthcare and come in the form of syringes, sutures, and prostheses, as well as complicated instruments such as heart-lung or dialysis machines. Blood-contacting devices represent a specific niche, with millions used annually worldwide. These devices include catheters, guidewires, pacemakers, heart valves, stents, and extracorporeal systems. In clinical practice, these devices come into direct contact with circulating blood, but are distinctly unlike the biological tissues that make up the cardiovascular system in both their physical and chemical properties. Because blood is composed of a complex mixture of cells and proteins that exist in a delicate homeostasis with the environment of the circulatory system, these physical and chemical differences create challenges that are unique to instruments intended to interface with the vasculature. Consequently, a chief concern is the propensity of blood to clot upon contact with a foreign surface, which confounded pre-modern efforts to perform life-saving blood transfusions. Because of this, the earliest successes and failures in vascular access often avoided the use of devices altogether.

The concept of medical vascular access originates in the Middle Ages, as illustrated by the apocryphal tale surrounding the death of Pope Innocent VIII in 1429.<sup>1,2</sup> Following a stroke, the Pope fell into a coma and certain sources assert that the attending physician attempted a blood

transfusion by directly joining the veins from three young boys. Unfortunately, both the Pope and his ill-fated donors died.<sup>1,2</sup> While the veracity of this particular account is uncertain, the principle of linking the veins of a donor directly to those of the recipient was not abandoned. A surgical technique developed by Alexis Carr in 1902 involving direct suturing of the blood vessels became the predominant technique for blood transfer.<sup>3</sup> In general, these methods are difficult, invasive, time-consuming, and lack a reliable method for gauging blood transfer. This remained the predominant method until the development of instrumentation meant to channel or interact with blood. Although the common use of blood-contacting medical devices is a relatively recent development, their recorded history began much earlier.

At the University of Oxford in the seventeenth century, Christopher Wren developed the first working infusion device by using quills and a pig's bladder to administer a solution of beer, opium, antimony, and wine directly into a dog's veins.<sup>1,2,4</sup> One of the first documented reports of a blood-contacting device for blood transfer was in the seminal work performed by Richard Lower in 1665. In this account, Lower performed an animal to animal blood transfusion using silver tubes and animal arteries for the cannulation and transfer of blood.<sup>4</sup> Shortly thereafter, Lower and others went on to conduct blood transfusions from animals to humans. However, less than favorable outcomes led to the banning of blood transfusions across Europe, hindering their evolution for over a century.<sup>1</sup> In 1818, the topic was revisited when surgeon James Blundell performed the first human to human blood transfusion using a syringe to extract the blood from the donor and transfer it to the recipient.<sup>1,2,4</sup> While innovative, these earlier efforts to transfuse blood were constrained to the materials available at the time, which were primarily glass, metals, or animal products such as quills. Additionally, the rapid and inevitable propensity of blood to clot limited the quantity that could be safely administered.

The onset of World War I prompted the advancement of new strategies for transfusing blood. The first practical method of overcoming clotting came with the development of the Kimpton-Brown transfusion apparatus in 1913.<sup>1,5</sup> This device consisted of a glass tube coated in paraffin wax, which delayed the onset of blood clotting when used properly. The mid-twentieth century highlights the era of disposable medical devices spurred by the plastic revolution. In the years following World War II, the manufacturing of polymers such as poly(vinyl chloride) (PVC), Teflon, and polyurethanes revolutionized the healthcare industry.<sup>1</sup> Today, catheters can be used for days to years, that allow direct injection of medications into the bloodstream to optimize efficiency. However, the use of anticoagulants remains standard practice when utilizing many of these blood-contacting devices.<sup>6</sup>

Taken together, development of medical devices has influence on all aspects of healthcare. For many of these blood-material interactions, the absence of natural regulators is still a major factor in the onset of device-related complications. A central limitation of traditional synthetic materials is that they lack the ability to integrate with the biological system through molecular signals to regulate immune responses. This results in biomaterials having a *passive* or unresponsive role in regards to their surrounding environment and can lead to complications such as infection, improper healing, excessive tissue growth, and *thrombosis*.<sup>7-10</sup> The degree to which a material in contact with blood produces adverse side effects such as thrombus, is typically defined as thrombogenicity. One method of addressing these concerns entails the development of materials that generate certain endogenous therapeutic molecules used to maintain homeostasis or regulate immune responses biologically.<sup>7,8</sup> Such materials can be considered *active* with respect to the biological environment, and may integrate more completely with tissues through the production of natural biochemical signaling agents. For instance, in mammalian biology, a naturally occurring

radical species known as nitric oxide (NO) demonstrates substantial therapeutic potential towards these adverse outcomes.<sup>11</sup> In the bloodstream, it has been theorized that NO is stored and transported by small molecules called *S*-nitrosothiols (RSNOs).<sup>12</sup> These RSNOs display enhanced rates of decomposition in the presence of copper ions, resulting in the formation of the corresponding disulfide and NO.<sup>13</sup> Thus, significant research has explored capitalizing on these endogenous sources by integrating copper-based species (copper nanoparticles, copper complexes) into medically relevant polymers for localized generation of NO from RSNOs.<sup>14</sup> However, upon interaction with the RSNOs, the copper species leach into the surrounding environment, rendering them unsuitable for many medical applications. Alternatively, crystalline substances known as metal–organic frameworks (MOFs) are an attractive approach due to the immobilization of the active metal species (copper) within the framework. In an effort to circumvent the limitations associated with copper complexes, research by Harding *et al.* identified two copper-based MOFs capable of promoting NO release from several RSNOs for integration into medical polymers.<sup>15,16</sup> This research explores the unique approach of combining MOFs with medical polymers to create materials capable of generating a localized supply of NO at the blood-material interface.

## **1.2 Preventing thrombogenicity**

The exposure of blood to medical devices will initiate a complex cascade of events that ultimately result in thrombus formation (**Figure 1.1**).<sup>17,18</sup> The adverse clinical manifestations of thrombus formation are numerous and can include thrombotic occlusion in grafts, obstruction of stents, embolic complications, and may necessitate the life-long use of anticoagulants.<sup>6,19</sup> Thrombus associated complications are among the most prevalent challenges in patient care.<sup>20</sup> For example, in a systematic review of reports on extracorporeal life support (ECLS) from 1994-2015, the overall survival to discharge ranged from 50-79%.<sup>21</sup> Of these reports, bleeding-related death

accounted for up to 38%. Another report assessed all adult patients who had ECLS from 2010-2013. Of the 132 patients admitted for ECLS, 56.1% had a serious bleeding-related event with 13.6% being thrombosis related.<sup>22</sup> While blood-contacting devices are essential to modern patient care, the clinical concerns arising from incompatibility with blood illustrate a lingering problem. To date, hospitals administer anticoagulants such as intravenous heparin for the management of thrombus formation in procedures involving blood-contacting devices.<sup>23</sup> While anticoagulants can provide symptomatic relief, their associated complications make them undesirable as a permanent solution. As an example, the use of heparin can lead to low platelet count (thrombocytopenia) and

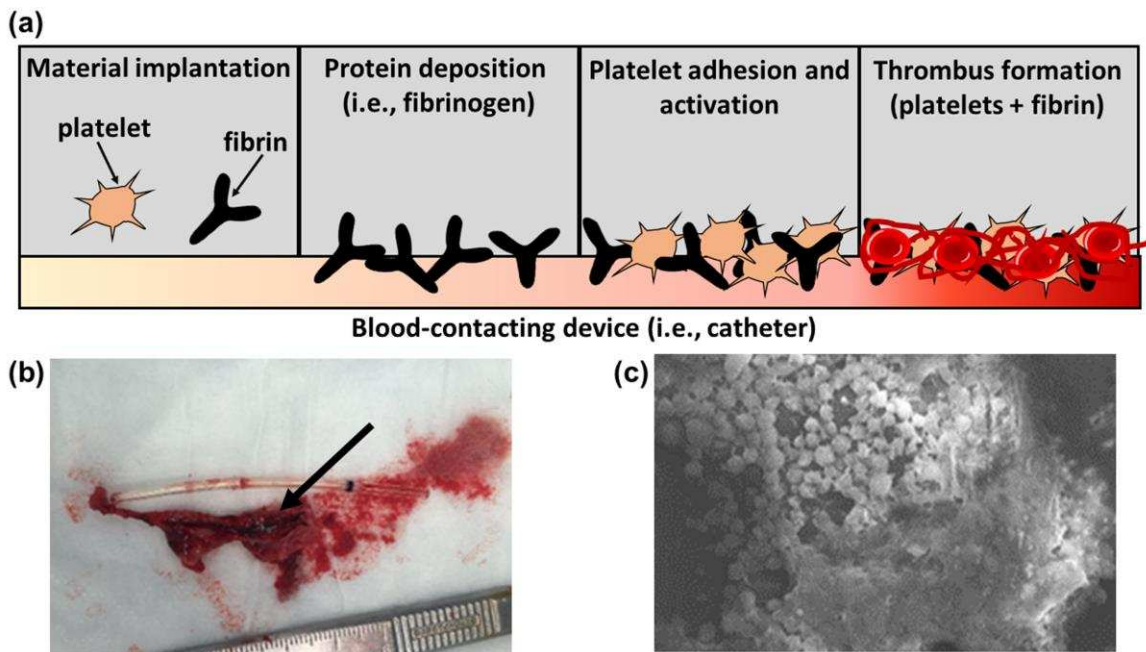


**Figure 1.1** (a) Generalized representation of events leading to clot (thrombus) formation including protein adsorption as well as platelet adhesion and activation. (b) Thrombus formation on the outside of an implanted catheter and indicated by the arrow. (c) Scanning electron microscope imaging of platelet adhesion on a material surface.

produce internal hemorrhaging that requires platelet transfusions to maintain patient vitality.<sup>22-25</sup>

Alternatively, a *localized* approach that prevents clotting on synthetic surfaces without systemic effects is ideal for future iterations of blood-contacting devices. In order to identify strategies and

develop rational designs for materials with enhanced blood compatibility, it is essential to understand why these outcomes occur when materials are in contact with blood and why they do not occur in healthy vasculature.

In the early 1800s, Freund and Haycraft independently discovered that a surface coated with paraffin wax lengthens blood coagulation time compared to glass.<sup>26-28</sup> During experimentation with blood, they discovered that blood failed to clot upon removal and placement in a tube coated with paraffin wax, or when directly added to a solution of paraffin oil.<sup>26-28</sup> However, if the blood came into contact with a surface that lacked the oily coating, it resulted in the induction of coagulation. While our understanding of blood's behavior upon contact with a material has significantly advanced since Freund and Haycraft's initial observations, it marks the foundation of our understanding of the clinical manifestations of blood-material incompatibility. These rudimentary observations of blood-material incompatibility by Freund and Haycraft were caused by the same factors which result in blood-device incompatibilities dealt with in current clinical practice. The typical sequence of events that result in thrombus formation upon device implantation proceeds as follows: (1) protein adsorption, (2) platelet adhesion and activation, (3) coagulation cascade activation, and (4) thrombus formation.<sup>29</sup> Upon implantation of a blood-contacting biomaterial, two distinct pathways can act in parallel or separately to trigger clot formation.<sup>29-31</sup> These include platelet adhesion and activation, and activation of the coagulation cascade which together forms the overall thrombus.

### **1.2.1 Platelet adhesion, activation, and aggregation on a material surface**

Initially, plasma proteins such as albumin, fibrinogen, and von Willebrand factor (vWF) are deposited onto the surface of the biomaterial. This adsorption of proteins at the surface is considered a reversible process with the composition of the proteins changing over time.<sup>32,33</sup> The

second phase of the sequence begins when adsorbed proteins interact with platelets through GPIIb/IIIa and GPIb receptors to promote platelet adhesion and activation. Additional receptors that stimulate platelet activation include thromboxane A<sub>2</sub> (TXA<sub>2</sub>), thrombin, and platelet activating factor.<sup>31</sup> The interaction between the GP receptors and blood proteins induces activation through the release of phospholipase C, leading to an increase in platelet cytoplasmic Ca<sup>2+</sup> concentration. An increase in the cytoplasmic Ca<sup>2+</sup> concentration leads to secretions of the granular contents (dense, alpha, and lysosomal granules) and subsequent shape change of the platelet.<sup>29-31,34</sup> Platelet activation is characterized by a morphological change from discoidal (inactivated) to spherical with the appearance of appendages known as pseudopods, which promote platelet contact and adhesion.<sup>34</sup> Additionally, the secreted granules then release their contents (ADP, Ca<sup>2+</sup>, platelet factor, fibrinogen, vWF) which further activate and induce platelet aggregation.<sup>31</sup> The process of platelet aggregation involves the binding of platelets to fibrinogen. Several factors such as collagen and thrombin can induce platelet aggregation through release or stimulation of pathways to form ADP and TXA<sub>2</sub>, both major agonists in the aggregation pathway.

### **1.2.2 The blood coagulation cascade**

The second factor responsible for thrombus formation involves the blood coagulation cascade, which leads to the formation of a fibrin clot.<sup>29-31,35</sup> The coagulation cascade consists of a series of proenzyme activations where one activated factor then activates another inactive precursor factor. The final enzyme activated is thrombin, a potent initiator of platelet aggregation and catalyst for conversion of fibrinogen to fibrin, which forms a stabilized cross-linked clot. Initiation of the blood coagulation cascade occurs through either an intrinsic or an extrinsic pathway. Intrinsic pathway activation initiates through the conversion of Factor XII to Factor XIIa upon contacting a foreign surface.<sup>29-31,35,36</sup> Factor XIIa then activates Factor XI to Factor XIa,

which then activates Factor X to Factor Xa. Alternatively, extrinsic activation arises from tissue trauma resulting in the expression of Tissue Factor (TF), which causes activation of Factor VII to Factor VIIa. Factor VIIa then proceeds to cleave Factor X to Factor Xa in the presence of TF.<sup>29-31,35,36</sup> Both the intrinsic and extrinsic pathways converge into the common pathway upon formation of Factor Xa. Factor Xa then activates thrombin, which activates fibrin, resulting in fibrin clot formation.<sup>29-31,35,36</sup> Collectively, the thrombus formed on the material surface is composed of aggregated platelets and the fibrin clot, as shown in **Figure 1.2**.

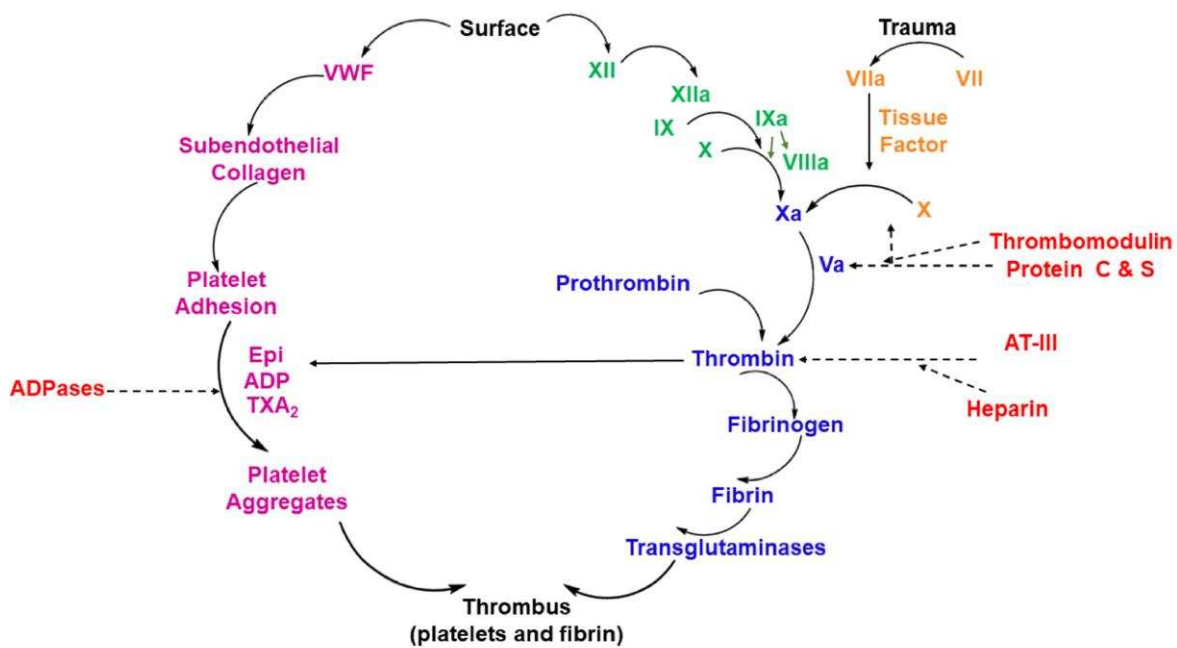


**Figure 1.2** Schematic illustration of the pathways involved in thrombus formation. Platelet adhesion and activation (pink), the coagulation cascade through the intrinsic (green) and extrinsic (orange) pathways which merge into the common pathway (blue). The resulting thrombi is a combination of activated platelets and fibrin.

Under normal conditions, the endothelium prevents thrombus formation and maintains homeostasis through a variety of factors.<sup>29-31</sup> These include anticoagulants such as thrombomodulin and glycosaminoglycans and platelet inhibitors such as prostacyclin, ADPase, matrix metalloproteinases, and the gaseous molecule NO.<sup>36</sup> Currently, the use of blood-contacting devices introduces a foreign surface into the bloodstream without the properties of the endothelium. However, the ability to use these platelet inhibitors at a material surface is an

attractive approach as their effect on platelets is not permanent and normal function will resume when no longer exposed to the inhibitor.<sup>36</sup> Of these different inhibitors, NO has been the most widely studied as an approach towards mimicking the biological functions of the endothelium. Rather than using passive materials such as a hydrophobic coating of paraffin wax, this approach permits improved blood compatibility through imitation of natural vascular tissue. As such, the next section will focus on the discovery of NO and its role in the cardiovascular system.

### **1.3 Nitric oxide**

The medicinal history of the small, diatomic radical NO began indirectly with Italian chemist Ascanio Sobrero and his discovery of nitroglycerin in 1846.<sup>37</sup> Sobrero achieved nitration of glycerol using a mixture of sulfuric and nitric acid and demonstrated the explosive nature of the new substance by detonating a small quantity during a lecture to the Accademia delle Scienze di Torino.<sup>1</sup> Notably, Sobrero was said to have tasted a small amount of the compound to which he remarked “great caution should be used for a very minute quantity put on the tongue produces a violent headache for several hours”.<sup>38</sup> In 1859, English chemist Frederick Guthrie noted that inhalation of amyl nitrite produced arterial throbbing in the neck and an increase in heart rate.<sup>39</sup> These observations led to interest in the medical potential of amyl nitrite, which was later determined to cause dilation of capillaries and lowered blood pressure. Later in the nineteenth century, physician T. Lauder Brunton first demonstrated the medical use of nitrites by providing relief for a patient suffering from angina.<sup>40,41</sup> Brunton believed that angina could be treated by inducing dilation of the blood vessels (vasodilation), a hypothesis which was confirmed when the patient’s symptoms were eased following administration of the compound by inhalation.<sup>40,41</sup> Following this innovative work, researchers focused on exploiting the physiological effects of organic nitrates. These efforts included the first use of nitroglycerin for angina relief by English

physician, Dr. William Murrell.<sup>42</sup> This eventually led to nitroglycerine becoming the preferred remedy for lowering arterial blood pressure.<sup>43</sup> While the nineteenth century witnessed the discovery of the vasodilatory properties of nitrites and their growing popularity for symptomatic relief of cardiovascular ailments, their biochemical mechanism of action would remain unexplained for decades.

In the 1970s, pharmacologist Ferid Murad and his colleagues were investigating the mechanism of action of various vasodilator molecules such as nitroglycerin and their impact on the enzyme guanylate cyclase (GC).<sup>44</sup> GC is an enzyme which synthesizes cyclic guanosine monophosphate (cGMP) from guanosine-5'-triphosphate (GTP), which is known to be a key regulator of the cardiovascular system. In their work, they discovered that nitrite-containing compounds stimulated GC, resulting in an increase in cGMP blood levels, which in turn induced vasodilation. Following their seminal report, Murad then observed that exposure of GC to NO also results in increased GC activity.<sup>45</sup> Based on these findings, Murad proposed that the vasodilatory effect of nitrite-containing compounds occurred through the formation of NO and subsequent activation of GC.<sup>44,45</sup> Independently, Robert Furchgott and colleagues were investigating the role of acetylcholine on vasodilation when they observed that blood vessel relaxation only occurred in the presence of endothelial cells.<sup>46</sup> Furchgott and his fellow researchers concluded that smooth muscle cells in the vasculature were unable to produce vasodilation in the absence of endothelial cells, suggesting the contribution of an unknown endothelium-derived relaxing factor (EDRF).<sup>47</sup> During the effort to identify this hypothesized EDRF, work headed by Louis Ignarro at the University of California revealed the identical properties between EDRF and NO in 1986.<sup>48,49</sup> Until these collective discoveries, it had not been previously considered that a chemically unstable, reactive radical gas such as NO could serve as an endogenous molecular signaling agent within

mammalian tissue. Taken together, this finding significantly advanced our understanding of the important role of NO in physiology. Consequently, Furchgott, Ignarro, and Murad received the 1998 Nobel Prize in Medicine and Physiology for their identification of NO as a signaling molecule in the cardiovascular system.

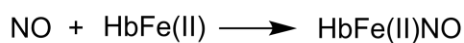
### **1.3.1 The biological activity of nitric oxide**

Today, the bioactivity of NO is well established and encompasses cardiovascular regulation, neurotransmission, promotion of wound healing, and antibacterial effects.<sup>50-52</sup> Collectively, three different isoforms of the NO synthase enzyme are responsible for NO production in mammalian biology.<sup>53</sup> These NO synthases are categorized as neuronal (NOS I or nNOS), inducible (NOS II or iNOS) and endothelial (NOS III or eNOS). NO production occurs through the NADPH-dependent conversion of the amino acid L-arginine to L-citrulline and NO in the presence of molecular oxygen.<sup>53</sup> Broadly speaking, eNOS and nNOS are Ca<sup>2+</sup>-dependent enzymes, whereas iNOS expression occurs through inflammatory agents such as cytokines.<sup>53</sup> NO generation can also occur in a NOS-independent manner in the nitrate-nitrite-nitric oxide pathway which involves the reduction of nitrate or nitrite to NO.<sup>54</sup> The nitrate-nitrite-nitric oxide pathway activity increases under low oxygen conditions (hypoxia) when the classical oxygen-dependent mechanism of NO synthesis is inhibited. During this process, bacteria, hemoglobin, myoglobin, and certain enzymes such as xanthine oxidase can reduce nitrate and nitrite to NO. Notably this pathway can be fueled by exogenous nitrate and nitrite sources in our diet that can produce therapeutic effects particularly for the treatment of cardiovascular disease.<sup>54-56</sup>

Due to the high reactivity of NO, microenvironmental conditions (erythrocytes or oxygen concentration) are factors in determining the biological response to NO exposure. Consequently, NO exhibits diverse chemical behavior with numerous biological effects. NO exhibits

dichotomous behavior in physiology, and biological effects of NO classified as either *direct* or *indirect*.<sup>57</sup> Biologically, NO reacts with metal centers or other radicals, the latter resulting in the production of reactive nitrogen species (RNS). Direct effects arise from chemical interactions between a receptor biomolecule and NO itself, such as the binding of NO to the Fe<sup>2+</sup> of the heme moiety to form a metal nitrosyl adduct (**Figure 1.3**).<sup>57,58</sup> Indirect effects involve the production of RNS such as peroxyxynitrite (ONOO<sup>-</sup>), nitrate (NO<sub>3</sub><sup>-</sup>), nitrite (NO<sub>2</sub><sup>-</sup>), dinitrogen trioxide (N<sub>2</sub>O<sub>3</sub>) and dinitrogen tetroxide (N<sub>2</sub>O<sub>4</sub>), which form through the reactions of NO with oxygen.<sup>57-59</sup> These RNS

**Direct**



**Indirect**



**Figure 1.3** Examples of direct and indirect in reactions of NO. The reactivity of NO allows the formation of RNS under physiological conditions which are highlighted red.

species proceed to target specific functions without the direct participation of NO. Vasodilation, platelet inhibition and aggregation, and various wound healing functions are typically attributed to direct effects of NO, while indirect effects are primarily responsible for antimicrobial activity.

In 1984, it was discovered by Ignarro *et al.* that NO activates the enzyme guanylate cyclase, which synthesizes cGMP from GTP.<sup>60</sup> Direct NO binding to the Fe<sup>2+</sup> species in the heme moiety of the enzyme induces a conformational change to the heme by pulling the Fe<sup>2+</sup> out of plane with respect to the planar porphyrin ring. This conformational shift causes stress between Fe<sup>2+</sup> and the distal histidine of the enzyme causing this bond to break. Detachment from the distal histidine

initiates enzyme activation of GC resulting in the conversion of the substrate GTP to cGMP.<sup>58,60</sup> The subsequent increase in cGMP levels triggers relaxation of the vascular smooth muscle cells, in addition to inhibiting platelet adhesion and activation to the surface of the cell walls that can lead to thrombosis.<sup>61</sup> NO is continuously produced by healthy endothelial cells at a basal level and in response to physiological stimuli. For example, previously Rubanyi *et al.* proposed an environmental trigger responsible for NO release from endothelial cells is the vascular flow rate of blood, and this hypothesis has been experimentally supported on numerous occasions.<sup>62-64</sup> Rubanyi originally demonstrated this concept by correlating increased blood flow rate and enhanced pulsatile flow with increased production of NO by the femoral artery endothelium in dogs.<sup>62</sup>

Nitric oxide prevents platelet adhesion and aggregation along the endothelium by increasing the intracellular concentration of cGMP. The presence of cGMP then decreases the intracellular concentration of  $\text{Ca}^{2+}$ , a key regulatory promoter of platelet activation.<sup>63-66</sup> Another route through which NO prevents platelet adhesion and activation is via inhibition of  $\text{TXA}_2$ , a signaling molecule produced by activated platelets with prothrombotic properties. Previous research has shown that cGMP can directly inhibit  $\text{TXA}_2$  activity, thus minimizing platelet adhesion and activation.<sup>65</sup> A report by Mendelsohn *et al.* observed that use of a NO donor material can inhibit fibrinogen binding to activated platelets in a dose-dependent manner. Fibrinogen inhibition was correlated with a corresponding increase in platelet cGMP levels.<sup>68</sup> This fibrinogen inhibition is potentially related in part to cGMP inhibition of PI3-K receptors, which activate the GP IIb-IIIa receptors on platelets that bind to fibrinogen. Ultimately, NO regulation of the cardiovascular system is largely through NO-induced formation of cGMP and its influence on a variety of receptors.

NO is also an important participant in the wound healing process where it is generated and secreted by inflammatory cells during wound healing, particularly in macrophages.<sup>51</sup> Prior to the identification of NO's role in wound healing, investigations by Albina *et al.* that evaluated arginine metabolism in wounds observed a corresponding increase in citrulline formation, a product of NO synthesis from L-arginine.<sup>69</sup> In 1990, it was demonstrated that administration of supplemental arginine enhanced wound healing in adults.<sup>70</sup> Shortly thereafter, a study by Smith *et al.* observed increased urinary nitrate levels in rats upon wound infliction, which they proposed was related to NO generation.<sup>71</sup> Bulgrin *et al.* then correlated dietary arginine deficiency with decreased nitrate output.<sup>72</sup> Bulgrin investigated nitrate outputs by feeding rats diets containing 0 or 3% L-arginine, then subjecting the rats to deliberate wound infliction. While nitrate levels initially increased, the endogenous arginine levels were not sufficient to maintain elevated nitrate levels in rats fed a 0% arginine diet and levels quickly returned to baseline. Comparatively, rats fed the 3% arginine diet were able to maintain elevated nitrate levels during the duration of wound healing.<sup>72</sup> The initial increase in nitrate levels following wound infliction and elevated nitrate levels in rats with a sufficient arginine supply supported the concept of increased NO production in wounds.<sup>71</sup> Shi *et al.* investigated the role of NO in wound healing by addition of supplemental L-arginine to the diet of diabetic Lewis rats. Their results showed that L-arginine supplementation enhanced wound healing and increased wound fluid nitrate/nitrite levels.<sup>73</sup> This outcome was also observed in the presence of NO supplied by a NO donor.<sup>74</sup> Furthermore, the impact of inhibiting iNOS expression during the wound healing process has also been investigated. Reicher *et al.* demonstrated that expression of iNOS is active within the first 72 hours of injury and suppressed as the wound ages.<sup>75</sup> Additionally, studies investigating the impact of iNOS inhibition detected a decrease in NO metabolites, collagen synthesis, wound breaking strength and contraction, and epithelialization.

Another study by Shi *et al.* demonstrated that supplemental arginine did not aid wound healing in iNOS knock out mice, suggesting that the metabolism of arginine through iNOS is essential in wound healing.<sup>76</sup> However, despite the lack of a comprehensive understanding of the role of NO in wound healing, it is clearly established to participate in the promotion and acceleration of the healing process.

### **1.3.2 Therapeutic applications of nitric oxide**

In light of the numerous biological effects of endogenous NO, the use of NO as a therapeutic agent is a logical progression. However, effective use of NO for medical applications must take into account that varying concentrations of NO have very different physiological impacts. As such, understanding the relationship between NO concentration and biological activity has been the target of substantial research efforts. At low concentrations (1-30 nM), NO exhibits regulation such as vasodilation and formation of new blood vessels (angiogenesis).<sup>77</sup> An increased NO concentration of approximately 100 nM results in protective effects towards cell apoptosis (anti-inflammatory and wound healing), whereas concentrations above 400 nM induce cellular apoptosis.<sup>77</sup> As NO is not cell specific, these high concentrations result in destructive cell damage towards all tissues. However, these higher concentrations prove beneficial for anticancer and antibacterial applications.<sup>70</sup> From a clinical perspective, the varied biological effects of NO illustrates the need for fine control over NO delivery when developing NO-based materials. The non-thrombogenic endothelium is seen to release NO with a surface flux of  $0.05\text{-}0.4 \times 10^{-10}$  mol NO cm<sup>-2</sup> min<sup>-1</sup>, thus materials for blood-contacting applications should fall within this target range.<sup>78</sup> Due to its reactivity, localized surface delivery of NO is desirable for antithrombotic applications without the systemic implications, such as hemorrhaging from use of anticoagulants. However, the applicability of therapeutic NO gas is limited by the overall reactivity of the

molecule. Several factors can influence the consumption of NO within the body, including the availability of oxygen and hemoglobin. In aqueous solution, the rate of NO consumption with oxygen and hemoglobin is proportional to the square of NO concentration and follows second order kinetics.<sup>79</sup> Thomas *et al.* reported the half-life of NO in extravascular tissue to fall within the range of 0.09 to > 2 s, depending on the concentration of oxygen present.<sup>80</sup> A study by Liu *et al.* calculated the half-life of NO to be  $1.8 \times 10^{-3}$  s in whole blood and correlated to the concentration of erythrocytes.<sup>81</sup> In blood, an additional route of NO consumption is through the reaction of NO with oxyhemoglobin or heme bound iron of the hemoproteins to yield iron(III)-peroxynitrite species.<sup>82</sup> As such, strategies that are employed to increase the life span of NO frequently involve the use of NO donors materials such as RSNOs.

#### 1.4 S-Nitrosothiols and their therapeutic potential

While NO is a short-lived biological messenger in a physiological environment, its effects can be harnessed using more stable NO precursors. RSNOs are NO-releasing compounds derived from thiols and are found to occur within the bloodstream.<sup>12</sup> Given the fleeting nature of NO in the presence of the reactive components of blood, RSNOs are theorized to function as intermediate species that serve to stabilize NO and transfer it from its site of origin. Since NO inhibits platelet activity in the healthy endothelium, strategies incorporating an exogenous supply of NO for blood

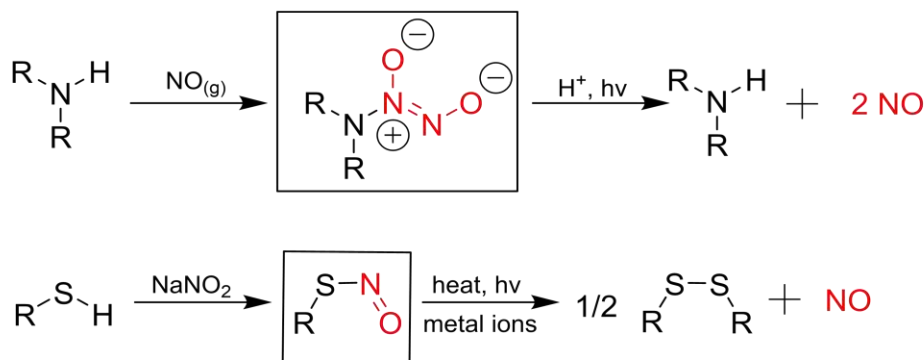


**Figure 1.4.** Generic structures for NONOates (top) and RSNOs (bottom).

contacting devices has been widely explored as a method for inhibiting thrombus formation.<sup>83-85</sup> These strategies aim to increase the lifespan of NO through the use of NO donors such as RSNOs or *N*-diazeniumdiolates (NONOates) (**Figure 1.4**). RSNOs occur in both natural and synthetic forms, and can be prepared through nitrosation of the sulfur atom of the thiol.<sup>83-85</sup> In contrast, NONOates are strictly synthetic molecules formed through nitrosation of secondary and primary amines. NONOates exhibit spontaneous decomposition that generates two molecules of NO per NONOate.<sup>83-85</sup> Comparatively, RSNOs decompose under certain conditions (heat, light, copper ions) to release one molecule of NO per RSNO. These synthesized NO donors have demonstrated their ability as potent antiplatelet agents and vasodilators and are therefore extremely promising for blood-contacting applications.<sup>84</sup>

In order to achieve targeted and controllable release, NO donors are often incorporated into a polymer scaffold. Two commonly used approaches include (a) covalently bound NO-releasing polymers and (b) direct blending of the NO donors through physical encapsulation in the polymer.<sup>83-85</sup> Towards this end, numerous reports exist where these NO donors are incorporated into PVC, hydrogels, polyurethanes, poly(ethylene glycol), silicone rubbers, polymethacrylates, sol-gel, polyethylene oxide, and silica particles, to name a few materials.<sup>83-85</sup> As an example, one of the first reports to incorporate NONOates into a blood-contacting polymer was by Smith *et al.* at the University of Akron in 1996.<sup>86</sup> Here, Smith coated vascular grafts with cross-linked poly(ethylenimine) containing covalently attached NONOates. To determine the effect of the NO-releasing polymer on platelet function, the vascular grafts were implanted in segments of artery-vein shunts in baboons. When compared to the control (poly(ethylenimine) coated vascular grafts) the NO-releasing grafts had substantially less platelet deposition after 1 hour.<sup>86</sup> The covalent attachment of RSNOs into polymers blends for blood-contacting surfaces has been investigated by

Seabra and coworkers at the State University of Campinas.<sup>87</sup> In this work, Seabra synthesized polynitrosated polyester/poly(methylmethacrylate) blends which released NO at a rate of  $1.8 \pm 0.1$  nmol g h<sup>-1</sup> for up to 24 h.<sup>87</sup> Platelet adhesion experiments showed that the use of polynitrosated polyester/poly(methylmethacrylate) blends resulted in complete inhibition of platelet deposition, demonstrating its potential as a blood-contacting surface. Despite the availability of alternative NO donor species such as NONOates, RSNOs exhibit significant advantages that include limited toxicity, and a diverse selection of environmental triggers. However, while the use of RSNOs as therapeutic NO donors has expanded rapidly, their formation *in vivo* remains disputed.

#### 1.4.1 The biological role of S-nitrosothiols

Plasma thiols are likely precursors for this role as well as nitrosating species and participate in the activation of nitrosovasodilators. In 1992, Stamler *et al.* were the first to demonstrate that the majority of S-nitroso adducts occur as S-nitrosoalbumin (SNO-albumin) through nitrosation of the lone cysteine residue.<sup>88</sup> The balance was proposed to consist of RSNOs derived from low molecular weight (LMW) thiols, such as S-nitrosoglutathione (GSNO) (**Figure 1.5**).<sup>88</sup> Scharfstein and colleagues later speculated that transnitrosation occurs *in vivo* between SNO-albumin and

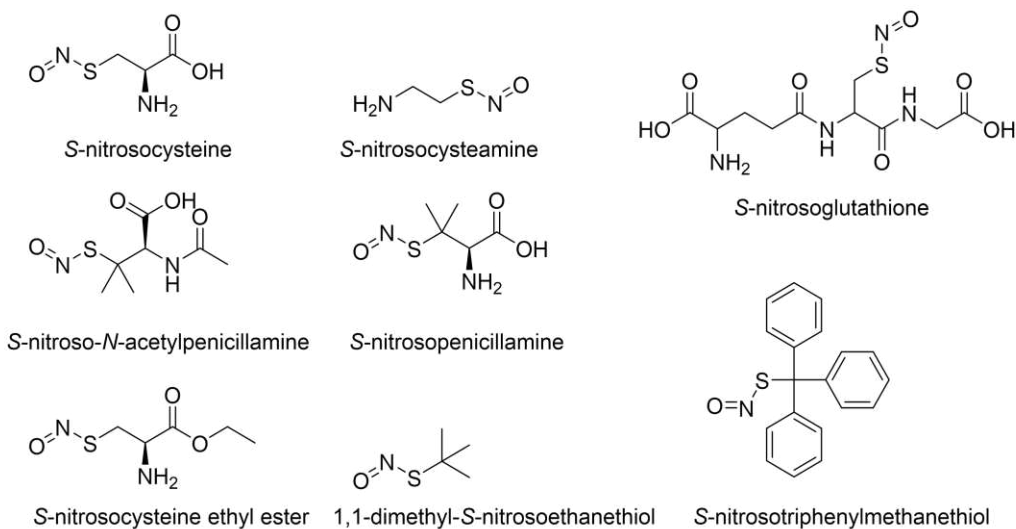


**Figure 1.5.** Examples of different RSNOs.

LMW thiols.<sup>89</sup> To study the role of low molecular weight (LMW) thiols in NO transfer, Scharfstein investigated the effects on rabbits of intravenous SNO-albumin administration on rabbits before and after transfusion with LMW thiols. Their results showed that dose-dependent low blood pressure (hypotension) became significantly accelerated in rabbits infused with LMW thiols prior to SNO-albumin administration.<sup>89</sup> Notably, the effects were mimicked by direct administration of the corresponding LMW RSNO. Based on this observation, Scharfstein proposed that SNO-albumin served as a reservoir of NO which could then be transferred to LMW thiols when necessary as a smaller, less diffusion limited species.<sup>89</sup> In 2000, Nedospasov *et al.* suggested an autocatalysis mechanism for albumin nitrosation.<sup>90</sup> In this publication, Nedospasov proposed that an accumulation of NO and O<sub>2</sub> within the hydrophobic compartments of the proteins catalyzed the formation of N<sub>2</sub>O<sub>3</sub> followed by electrophilic attack on the nucleophilic thiol groups of cysteine residues.<sup>90</sup> This mechanism was hypothesized to be dependent on the initial concentration of the reactants and the size and geometry of the hydrophobic portion of the protein. In 2002, Rafikova and coworkers claimed to demonstrate that saturation of albumin with NO accelerated the formation of LMW RSNOs both *in vivo* and *in vitro* by catalyzing the formation of RSNOs and extending the lifetime of the nitrosating species.<sup>91</sup> To test this hypothesis, they evaluated thiol nitrosation with and without the presence of albumin. Their results showed that the presence of NO saturated albumin enhanced RSNO formation when compared to their control (absence of albumin).<sup>91</sup> Additionally, by increasing the plasma thiol concentration, Rafikova observed newly formed RSNO at concentrations 2-fold higher than the preexisting RSNO. In rats, the direct administration of thiol was accompanied by up to a 4-fold increase in RSNO concentration and a corresponding decrease in arterial pressure. Overall, Rafikova concluded that the increased concentration of blood RSNOs following thiol administration was correlated with albumin-

catalyzed formation through the transfer of nitrosonium ( $\text{NO}^+$ ) to LMW thiols.<sup>91</sup> In 2003, Jourdeuil *et al.* proposed an additional mechanism involving thiyl radical formation by  $\text{NO}_2$  followed by subsequent reaction with  $\text{NO}$ .<sup>92</sup> Another route for nitrosation of LMW thiols is through the mechanism proposed for metalloproteins such as ferric heme catalyzed oxidation of  $\text{NO}$ . This resulting  $\text{NO}^+$  species proceeds to react with surrounding thiols.<sup>93</sup>

#### **1.4.2 Basal blood S-nitrosothiol concentration: an ongoing debate**

There is considerable discussion regarding the quantification of physiological RSNO concentrations, with reports ranging from  $\mu\text{M}$  to  $\text{nM}$ .<sup>94</sup> The feasibility of developing materials capable of generating therapeutically-relevant levels of  $\text{NO}$  from blood requires understanding of biological RSNO concentrations. In the initial 1992 report by Stamler, RSNOs were collectively quantified at a total blood plasma concentration of  $7 \mu\text{M}$  through a chemiluminescence-based detection method.<sup>88</sup> Of the reported concentration, 96% was due to nitroso-proteins with SNO-albumin accounting for 82% of the nitroso-proteins with no LMW RSNOs being identified. A 1998 report from Goldman *et al.* determined a blood plasma concentration of  $220 \text{ nM}$  using high-performance liquid chromatography with a Griess assay.<sup>94</sup> In 2000, using the same methodology, Jourdeuil and colleagues determined a plasma concentration of  $62 \text{ nM}$  with the majority in the form of SNO-albumin.<sup>95</sup> In parallel, reports by Marley (2000) and Rassaf *et al.* (2002) reported plasma concentrations of RSNOs ranging from  $15\text{-}40 \text{ nM}$  using a chemiluminescence detection method.<sup>96-98</sup> Furthermore, Tyurin *et al.* reported RSNO plasma concentrations of  $4.2 \mu\text{M}$  using spectrofluorophotometer techniques, whereas, Tsikas and colleagues used GC-MS to determine an SNO-albumin concentration of  $156 \text{ nM}$ .<sup>99,100</sup> As can be inferred from these examples, the physiological concentration of RSNOs remains a debated subject with accurate measurements remaining a developing field. Nevertheless, physiologically-available forms seem well

established, with SNO-albumin and GSNO occurring as the dominant species in the body with the reported range falling between the low nM (<100) and the low  $\mu\text{M}$  (<10).

### 1.4.3 Chemical and physical properties of S-nitrosothiols

Since Jones and Tasker's original synthesis of nitrite esters at the University of Cambridge in 1909, the understanding of RSNOs and their chemical reactivity continues to progress.<sup>101</sup> Interestingly, contradictory reports exist related to RSNO thermal stability in which they are alternately described as either extremely susceptible or resistant to thermolysis.<sup>102-105</sup> Based on bond dissociation energies between 20 and 32 kcal mol<sup>-1</sup>, the half-lives of RSNOs should be as long as years.<sup>102,104</sup> However, these calculated half-lives contradict experimental values ranging from minutes to hours. This led to the suggestion that thermally induced decomposition of the S-N bond is not the most significant contributor to RSNO decomposition under physiological conditions. The stability of RSNOs varies greatly with certain tertiary examples such as S-nitrosotriphenylmethanethiol and SNAP occurring as crystalline solids that can be isolated and stored for extended periods, while others exist only in the form of unstable solutions and decompose within minutes to hours of their synthesis.<sup>106</sup> The majority of unstable RSNOs are primary or secondary, with GSNO being the exception with it demonstrating excellent stability and is isolated as a solid. RSNO stability is hypothesized to be depend on both the strength of the S-N bond and the rate of S-S disulfide formation ( $2 \text{ RSNO} \rightarrow \text{RSSR} + 2 \text{ NO}$ ).<sup>107</sup> To investigate the stability of RSNOs, Bainbrigge *et al.* utilized differential scanning calorimetry (DSC) and thermogravimetric analysis (TGA) to evaluate the thermal stability of GSNO and SNAP. Notably, both RSNOs were found to exhibit NO-forming decomposition at 148 °C.<sup>17</sup> Based on these results, Bainbrigge suggested that the local chemical structure has little effect on the strength of the S-N bond. However, the combination of thiyl radicals formed from the decomposition of SNAP results

in a high energy, sterically hindered conformation compared to many primary RSNOs.<sup>107</sup> Therefore, it was proposed that thiyl radical dimerization was the rate determining process in solution due to the ability of the NO and thiyl radical to recombine with liberation of NO occurring only upon disulfide formation.

RSNOs are observed to be red (primary and secondary RSNOs) and green (tertiary RSNOs) in color and are commonly characterized by UV-Vis spectroscopy. Bond lengths obtained from crystal structures are approximately 0.18 nm and 0.12 nm corresponding to values expected for formal S-N single bond and N-O double bond.<sup>108,109</sup> However, RNSOs exhibit significant S-N double bond character and therefore occur in either *syn* or *anti* conformations (**Figure 1.6**). The preference for a specific orientation is driven by the degree of substitution on the R group. As such, primary and often secondary RSNOs exhibit *syn* orientations, whereas tertiary RSNOs will adopt an *anti* conformation. Interconversion between isomers does not readily occur and an appreciable barrier (11-12 kcal mol<sup>-1</sup>) to rotation has been calculated.<sup>110,111</sup> Additionally, theoretical

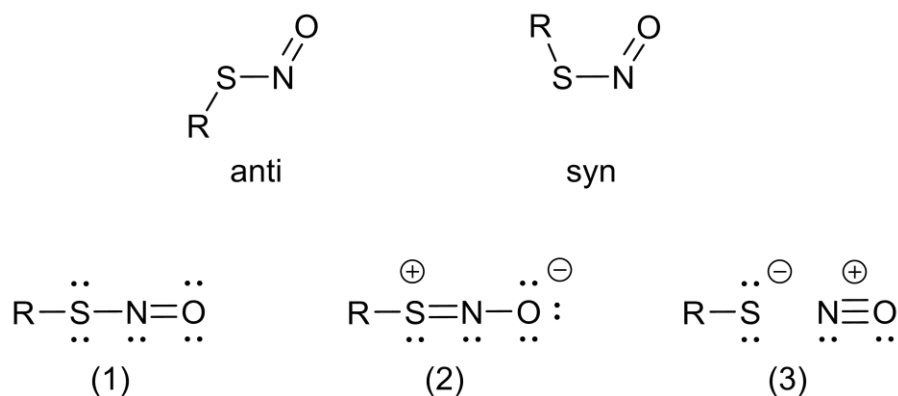
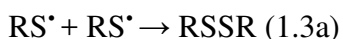


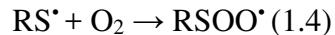
**Figure 1.6.** (a) Proposed conformations of RSNOs and (b) hypothesized resonance structures composed of (1) the conventional Lewis acid structure, (2) zwitterionic resonance structure, and (3) ion pair resonance structure.

calculations have suggested a degree of delocalization over the RSNO molecule.<sup>111</sup> Taken together, these findings strongly support the double bond character of the S-N bond. The bonding

of the RSNO functional group was further rationalized by Timerghazin *et al.* through a combination of three different resonance forms.<sup>112</sup> Density functional theory calculations and natural resonance theory calculations were used to generate the proposed resonance structures (**Figure 1.6**). In addition to the conventional Lewis structure, (1) a zwitterionic structure with a S-N double bond, (2) and an ion pair resonance (3) structure were proposed. The zwitterionic structure (2) was calculated to contribute to 15-25% of the overall structure and accounts for the observed *syn-anti* conformers of RSNOs, supporting the argument for delocalization of electrons around the S-N bond.<sup>112</sup> Additionally, the experimentally observed S-N bond length can be explained by the ion-pair resonance structure (3) contributing to elongation of the bond.

In comparison, factors influencing RSNO decomposition are fairly well understood, with RSNOs known to decompose through thermal and photochemical routes to yield the corresponding disulfide (RSSR) and NO (equation 1.1).<sup>13</sup> Under deoxygenated conditions, these reactions can occur through homolytic cleavage of the S-N bond (equation 1.2). Following this homolytic scission, disulfide formation is proposed to occur through the reaction of two thiyl radical species as suggested by Bainbrigge (equation 1.3a).<sup>107</sup> In an alternative mechanism, the thiyl radical is proposed to react with the more abundant RSNO molecules yielding the corresponding disulfide and generation of NO (equation 1.3b). The latter mechanism tends to be favored due to the relative abundance of the RSNO species compared to the thiyl radical.<sup>13</sup> In the presence of oxygen, the RSOO<sup>•</sup> radical is hypothesized to be generated first (equation 1.4) followed by the reaction with another RSNO molecule to yield NO and the corresponding disulfide (equation 1.5).





However, many results are erratic and generally inconsistent, leading to discrepancies in the literature with mechanistic pathways remaining unclear. As mentioned briefly, it has been observed that certain metal ions enhance RSNO decomposition in solution.

#### **1.4.4 S-Nitrosothiol decomposition: influence of copper ions**

In 1993, the Williams' group initially introduced this concept while investigating NO release from SNAP, where they observed that SNAP decomposition kinetics did not follow a simple rate law and displayed half-lives that varied every week with the same batch of SNAP.<sup>113</sup> Based on these observations, Williams evaluated the impact of adding the chelator ethylenediaminetetraacetic acid (EDTA) on SNAP decomposition. Upon EDTA addition, the rate of SNAP decomposition was dramatically reduced, suggesting potential metal ion contamination of the solution. Subsequent addition of  $\text{Cu}^{2+}$  ions to the solution resulted in the reintroduction of rapid SNAP decomposition. Taken together, these results formed the foundation of the hypothesis that  $\text{Cu}^{2+}$  had a catalytic effect on RSNO decomposition that accounted for their erratic results.<sup>113</sup> Following that work, Williams and colleagues evaluated the impact of different metal ions including  $\text{Zn}^{2+}$ ,  $\text{Ca}^{2+}$ ,  $\text{Mg}^{2+}$ ,  $\text{Ni}^{2+}$ ,  $\text{Co}^{2+}$ ,  $\text{Mn}^{2+}$ ,  $\text{Cr}^{3+}$ ,  $\text{Fe}^{3+}$ ,  $\text{Fe}^{2+}$ , and  $\text{Cu}^{2+}$  on the decomposition of multiple RSNOs decompositions.<sup>114</sup> These studies firmly established that  $\text{Cu}^{2+}$  and  $\text{Fe}^{2+}$  (to a lesser extent), could substantially increase the rate of RSNO decomposition. To test the effect of each metal ion, an appropriate salt was added in slight excess of EDTA into solution and measured RSNO decomposition. They then halted the reaction by the addition of excess EDTA to the solution. In these particular experiments, the most reactive substrates included S-

nitrosocysteamine (CysamNO), *S*-nitrosocysteine (CysNO), and *S*-nitrosopenicillamine (**Figure 1.6**).<sup>114</sup> In comparison, other structures such as 1,1-dimethyl-*S*-nitrosoethanethiol showed no activity. In general, many RSNOs showed rate constants and reactivity suggesting that the RSNO structure and its ability to interact with copper influenced catalytic efficacy. While no mechanistic details were proposed, Williams suggested the observed reactivity could be due to Cu<sup>2+</sup> binding with the RSNO through the nitroso group and the amine or carbonyl group to form a bidentate complex via a six-membered ring (**Figure 1.7**).<sup>114</sup>

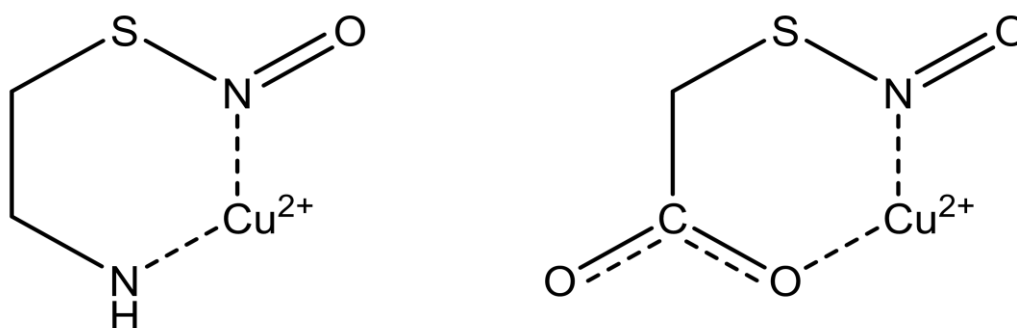
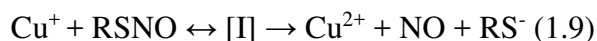
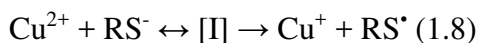


**Figure 1.7.** The proposed intermediate species for copper catalyzed decomposition of RSNOs. Copper can form a bidentate species through binding with the nitroso group and the corresponding functional group of the RSNO such as an amine or carbonyl group.

In a follow-up paper, Williams and colleagues examined the decomposition of SNAP in the presence of Cu<sup>2+</sup> ions with increasing concentrations of neocuproine, a molecule known for its ability to selectively bind Cu<sup>+</sup>.<sup>115</sup> As the neocuproine concentration was increased, decomposition of SNAP became progressively hindered until it was completely suppressed, suggesting that the formation of Cu<sup>+</sup> is a key component of copper-catalyzed RSNO decomposition. The formation of Cu<sup>+</sup> was suggested to occur from the reduction of Cu<sup>2+</sup> by adventitious thiolate arising from an impurity or hydrolysis of the RSNO (equation 1.7).<sup>115</sup> To examine this concept, NAP (the corresponding thiol), was added to the reaction in increasingly higher concentrations.



Initially, a linear correlation existed between the concentration of thiol and the increased rate of SNAP decomposition, until high concentrations of NAP resulted in a drop in the observed rate. They explained this pattern as complexation of the  $\text{Cu}^{2+}$  by NAP to form a copper carboxylate species and the accompanying decrease in the available concentration of catalyst. Thus, at lower NAP concentrations, reduction of  $\text{Cu}^{2+}$  to  $\text{Cu}^+$  is favored, while higher concentrations result in the sequestration of copper ions through complexation.<sup>115</sup> On this basis, Williams proposed a mechanism in which  $\text{Cu}^{2+}$  is reduced by  $\text{RS}^-$ , yielding  $\text{Cu}^+$  and  $\text{RS}^*$  (equation 1.8). This step is then followed by reaction between the  $\text{Cu}^+$  species and  $\text{RSNO}$  through an undetermined intermediate species [I] with the products being  $\text{Cu}^{2+}$ ,  $\text{NO}$ , and  $\text{RS}^-$  (equation 1.9). The regeneration of the  $\text{RS}^-$  allows for the continuous reduction of  $\text{Cu}^{2+}$  and the corresponding radical  $\text{RS}^*$  species results in disulfide formation (equation 1.10).<sup>115</sup>



Following this work, Williams *et al.* evaluated the influence of  $\text{Cu}^{2+}$  specifically on GSNO decomposition.<sup>116</sup> Similarly to SNAP, as the concentration of GSNO increased, the NO generation came to a halt. Williams hypothesized that the oxidized form of glutathione (GSSG) complexed with the  $\text{Cu}^{2+}$  in solution in a manner analogous to NAP, and the reaction was consequently suppressed at higher (mM) GSNO and increased at lower ( $\mu\text{M}$ ) concentrations.<sup>116</sup> In contrast to GSNO, evaluation of CysNO decomposition showed no great change in the rate of the reaction or the amount of NO recovered. This outcome was suggested to be correlated to the inability of  $\text{Cu}^{2+}$  to chelate with the disulfide species. Based on these findings, no correlation between RSNO structure and reactivity could be made for the observed rates of RSNOs when performed at mM

concentrations. Therefore, their previous reports, which invoked the requirement of a cyclic transition state, were rendered null.<sup>116</sup> Williams *et al.* then reported a follow-up to investigate the structure-reactivity impacts of four RSNOs: *S*-nitrosocysteine (SNC), *S*-nitrosocysteinylglycine (SNO-CysGly), *S*-nitrosoglutamylcysteine (SNO-GluCys), and GSNO at mM and  $\mu\text{M}$  concentrations.<sup>117</sup> These four were chosen due to the presence of glutamate residues in GSNO and SNO-GluCys, which could theoretically complex with the  $\text{Cu}^{2+}$  species upon disulfide formation. As predicted, they observed an increase in the reaction rate at  $\mu\text{M}$  concentrations for GSNO and SNO-GluCys that were suppressed at higher (mM) concentrations.<sup>117</sup> In contrast, rates for SNC and SNO-CysGly remained relatively unchanged regardless of the concentration. These findings supported the concept that with certain RSNOs the reaction rates will be dependent on the concentration of the corresponding disulfide present.<sup>117</sup>

The overall reactivity of RSNOs to metal ions is not solely limited to copper ions. Other reports have found that both mercury ( $\text{Hg}^{2+}$ ) and silver ( $\text{Ag}^+$ ) ions are able to substantially increase the rate of RSNO decomposition with marked differences observed between the different metal ions.<sup>118</sup> In the presence of  $\text{Hg}^{2+}$ , the major reaction product observed is nitrous acid ( $\text{HNO}_2$ ) which was not derived from NO. Additionally, the use of  $\text{Hg}^{2+}$  species was required in stoichiometric amounts compared to the catalytic quantities required for copper.<sup>118</sup> Overall, while the coordination of certain metal species to sulfur in the RSNO decreases the bond strength causing breakage and subsequent NO generation, the precise mechanism remains unclear.

### **1.5 Catalytic methods of generating nitric oxide from *S*-nitrosothiols for medical applications**

Understanding of the NO-forming properties of RSNOs, their biological relevance, and their susceptibility to accelerated decomposition in the presence of certain chemical species (e.g., copper ions, iron ions) has continued to expand over the years. As previously discussed, this has

led to their development as therapeutic materials intended for NO-forming decomposition through thermal or photolytic decomposition for the prevention of thrombus formation. However, the use of exogenous NO donors to produce NO-releasing medical implants for long-term applications is limited by a finite reservoir of the therapeutic agent. Once the donor species has been depleted through NO release, therapeutic effects from the action of NO are arrested. In the majority of cases, this depletion occurs within hours, days, or weeks. To transcend this limitation, alternative routes have proposed the generation of NO directly from these endogenous substrates. Materials that harness this concept have included polymer-immobilized organotellurium and selenium catalysts, as well as copper nanoparticles and complexes.<sup>14, 119-129</sup>

The majority of this research originates from the University of Michigan, where work by Meyerhoff has pioneered the catalytic generation of NO from RSNOs that occur naturally in blood. The use of catalysts developed from the Group 16 elements selenium and tellurium was inspired by a biomimetic approach that sought to reproduce the biological activity of glutathione peroxidase, a selenium-containing enzyme that generates NO from RSNOs through a catalytic reaction.<sup>130</sup> While selenide and telluride-based materials successfully generated NO from RSNOs such as GSNO and CysNO, the addition of thiol was necessary to maintain the catalytic cycle.<sup>119-122</sup> Other approaches have used copper species to induce the catalytic generation of NO from both RSNOs and nitrite.<sup>123-129,131</sup> However, many of these approaches proceed through the intentional generation and release of copper ions into solution.<sup>124-129</sup>

For example, research performed by Hwang *et al.* at the University of Michigan investigated the ability of Cu(II)-cyclen (cyclen= 1,4,7,10-tetraazacyclododecane) complexes to generate NO from both GSNO and CysNO following covalent attachment to cross-linked poly(2-hydroxyethyl methacrylate) (pHEMA).<sup>128</sup> NO release experiments demonstrated that immersion of Cu(II)-

cyclen/pHEMA films in solutions containing RSNOs could produce steady state NO surface fluxes in the realm of  $2.5 \times 10^{-10} \text{ mol cm}^{-2} \text{ min}^{-1}$ , a value that is within the range observed for NO release from healthy endothelial cells.<sup>128</sup> Copper leaching experiments showed that substantial copper leaching occurred (approximately 40%) after soaking the materials in phosphate buffer saline (PBS) with GSNO/GSH over 15 days. Subsequent evaluation of catalytic activity showed a resulting decrease in NO generation by 25-50%.<sup>11</sup> Another report by Hwang and colleagues investigated the catalytic properties of Cu(II)-cyclen complexes covalently attached to a hydrophilic polyurethane.<sup>129</sup> While this material generated an NO flux between  $1-3 \times 10^{-10} \text{ mol cm}^{-2} \text{ min}^{-1}$ , 25% of copper leaching within the first 24 h, with an additional 25% leaching within a week. In another report, Major *et al.* incorporated 1, 5, and 10 wt.% copper nanoparticles into a hydrophilic polyurethane to develop a material which mimicked the tubing of an extracorporeal circulation (ECC) device.<sup>124</sup> This approach was based on the slow corrosion of  $\text{Cu}^0$  to generate catalytically active  $\text{Cu}^{2+}$  ions. Addition of 1  $\mu\text{M}$  GSNO resulted in NO flux measurements of 5, 10 and  $12 \times 10^{-10} \text{ mol cm}^{-2} \text{ min}^{-1}$  with respect to the weight percentage of copper nanoparticles. Blood experiments performed using an ECC setup showed that the plasma copper concentration increased by a factor of 1-1.3 after 4 hours, suggesting a degree of leaching.<sup>124</sup> Meyerhoff and coworkers have also demonstrated the ability to electrochemically generate NO in the presence of nitrite through a  $\text{Cu}^+$ -mediated pathway. Generation of  $\text{Cu}^+$  proceeded either through the reduction of a  $\text{Cu}^{2+}$  or through the oxidation of  $\text{Cu}^0$  wire. The materials were able to generate NO in the range of  $0.5-3.5 \times 10^{-10} \text{ mol cm}^{-2} \text{ min}^{-1}$ , corresponding to physiologically produced levels.<sup>132-134</sup>

Two reports by Wonoputri and colleagues described the incorporation of a copper dibenzol [e,k]-2,3,8,9-tetraphenyl-1,4,7,10-tetraaza-cyclododeca-1,3,7,9-tetraene complex (CuDTTCT) into polymers for the catalytic generation of NO from nitrite.<sup>123,131</sup> In 2015, they incorporated

CuDTTCT species into PVC and produced NO from nitrite using ascorbic acids as the reducing agent. NO generation occurs through a copper-nitrite-ascorbic acid pathway in which ascorbic acid reduces the  $\text{Cu}^{2+}$  to  $\text{Cu}^+$  the  $\text{Cu}^+$  species then goes on to react with nitrite to produce NO, which gets oxidized back to  $\text{Cu}^{2+}$  during the process.<sup>123</sup> In 2016, they reported on an iron-based complex which was capable of facilitating the redox cycle for catalytic generation of NO from nitrite in the presence of the copper species.<sup>131</sup> This reaction occurred through the oxidation of iron(II) to iron(III) and the simultaneous reduction of  $\text{Cu}^{2+}$  to  $\text{Cu}^+$ . As in the previous system, the  $\text{Cu}^+$  species reacts with nitrite to generate NO, accompanied by regeneration of the  $\text{Cu}^{2+}$  species. In both reports, less than 1% of copper was leached after three days of incubation with nitrifying bacteria.<sup>131</sup> While these reports hold merit for medical applications, the ability to generate NO from nitrite becomes more relevant for antibacterial applications because nitrite is an established product of bacterial metabolism.<sup>123,131</sup>

While immobilized copper-based species generate NO from the decomposition of RSNOs, limitations arise with respect to long-term medical devices due to gradual loss of the catalytic materials and subsequent toxicity related to copper leaching. As such, research has progressed towards the development of a material in which the copper sites remain immobilized within the structural framework under physiological conditions, which is extremely desirable for medical applications. In particular, a promising alternative involves the use of metal–organic frameworks for NO generation.

## **1.6 Metal–organic frameworks**

Metal–organic frameworks (MOFs) are hybrid inorganic-organic crystalline materials prepared through the self-assembly of metal ions with organic ligands to form porous crystalline structures that exhibit one, two, or three-dimensional architectures. The most common synthetic

routes for MOF synthesis include hydrothermal, solvothermal, electrochemical, mechanochemical, and sonochemical techniques.<sup>135</sup> Factors such as solvents and structure-directing agents will have a strong influence on crystal formation and pore size.<sup>135</sup> The size and shape of MOF crystals can be manipulated through variation of the pH, metal ion, solvent, reaction concentrations, time, and temperature. MOF topology can be predicted by the atoms between the metal organic clusters and the linker that form defined geometric shapes referred to as secondary building units (SBUs).<sup>136</sup> The organic linkers can be mono-, di-, tri-, or tetravalent and function as bridging units between neighboring metal ions. The metal and organic linkers dictate the structure and are easily varied to control the chemical and physical properties of the MOFs. Due to many MOF architectures exhibiting a high degree of porosity and surface area, researchers have proposed their use in gas storage applications.<sup>137</sup> Uses of MOFs are not confined to gas storage; it has been demonstrated that MOFs show promise in sensing, catalysis, separations, magnetic, optical, electronics, and biomedical applications.<sup>138-140</sup> In particular, the value of MOFs in medical pursuits is well established in the literature, with applications ranging from antibacterial agents to drug delivery carriers and as a contrasting agent for biomedical imaging.<sup>141,142</sup> Due to the gas storage capabilities exhibited by certain MOFs, they were quickly recognized as potential carriers of therapeutic gases such as NO.<sup>143</sup> NO-releasing frameworks are obtained from direct coordination of gaseous NO to an open metal site to form metal-nitrosyl complexes or through incorporation of NO donor groups such as NONOates through post-synthetic modification (PSM).<sup>143,144</sup> While several reports have investigated PSM of MOFs, direct coordination of NO to open metal sites remains the most commonly utilized approach.<sup>145-147</sup> MOFs for delivery of NO is advantageous considering the observed dose-dependent nature of NO. By altering the MOF composition, researchers have tailored MOFs to deliver different quantities of NO.<sup>143,144</sup>

### 1.6.1 Metal–organic frameworks for delivery of exogenous nitric oxide

In particular, the Morris group at the University of St. Andrews has extensively studied the ability of MOFs to uptake and release NO through direct coordination to open metal sites. Xiao *et al.* evaluated the ability of copper(II) benzene 1, 3, 5-tricarboxylate (HKUST-1 or CuBTC) to adsorb NO. CuBTC demonstrated an NO adsorption capacity of  $3 \text{ mmol g}^{-1}$  at room temperature, a value significantly higher than the adsorption capacities of other porous materials such as zeolites ( $1\text{--}1.5 \text{ mmol g}^{-1}$ ).<sup>148</sup> Formation of a Cu-NO adduct was confirmed by IR spectroscopy through the appearance of a peak previously associated with NO stretching in Cu-NO zeolite complexes. Desorption of CuBTC occurred with significant hysteresis that was suggestive of irreversible NO adsorption to the open metal copper sites, with approximately  $2.21 \text{ mmol g}^{-1}$  remaining adsorbed to the MOF.<sup>148</sup> NO release from CuBTC under 11% relative humidity (RH) demonstrated a cumulative NO release of  $1 \text{ } \mu\text{mol g}^{-1}$  of CuBTC over 1 h, corresponding to only 0.03% of theoretical adsorbed NO. This lack of NO release implies strong interactions between copper and NO, likely due to the formation of Cu-NO adducts, rendering CuBTC a less than ideal candidate for NO release applications.<sup>148</sup>

In an effort to improve upon the NO release capabilities of CuBTC, McKinlay and coworkers evaluated two MOFs, based on cobalt and nickel, with 2, 5-dihydroxyterephthalic acid serving as the organic linking component (Co-CPO-27 and Ni-CPO-27).<sup>149</sup> Adsorption capacities of the materials were approximately  $6.0 \text{ mmol g}^{-1}$  (Co-MOF) and  $7.0 \text{ mmol g}^{-1}$  (Ni-MOF) at room temperature, with both MOFs exhibiting hysteresis upon desorption. NO release measurements showed that the MOFs released nearly 100% of the adsorbed NO over 15 h under 11% RH.<sup>149</sup> In this context, these NO uptake values correspond to a 400–700% increase in NO uptake compared to zeolite species and approximately 18–21% of the maximum theoretical storage capacity of NO

(based on the molecular weight of NO). While these MOFs demonstrate exceptional NO uptake and release the use of toxic Ni and Co produces biocompatibility concerns. The importance of coordinatively unsaturated metal nodes or open metal sites (OMS) in the NO storage capacity of MOFs is demonstrated by experiments performed using Al-MIL-53 and Cr-MIL-53.<sup>141</sup> Al-MIL-53 and Cr-MIL-53 are members of the MIL (MIL=Material Institut Lavoisier) family which is composed of different carboxylate-based MOFs. In this circumstance, the Al and Cr metal ions are coordinated with 1,4-benzenedicarboxylate with the extended framework lacking open metal sites. Correspondingly, gas sorption measurements revealed that these MOFs adsorb significantly smaller quantities of NO ( $1.0 \text{ mmol g}^{-1}$ ) compared to CuBTC, Co-CPO-27, and Ni-CPO-27. Indeed, desorption measurements show little to no hysteresis suggesting that NO is simply physisorbed to the walls inside the pores.<sup>143</sup>

Due to the potential for biocompatibility concerns arising from the use of MOFs derived from Ni, Co, and Cu, researchers proceeded to evaluate an iron carboxylate-based MOF in an attempt to circumvent toxicity concerns. McKinlay and colleagues assessed the iron(III) dicarboxylate MOFs with MIL architecture derived from either fumaric (MIL-88A) or terephthalic (MIL-88B) acid. Gas sorption measurements showed that the MOFs adsorbed 2.5 (MIL-88A) and 1.6 (MIL-88B)  $\text{mmol g}^{-1}$  of NO at room temperature.<sup>150</sup> IR spectroscopy suggested that some fraction of NO was chemisorbed to Fe(III) or Fe(II), however NO was only adsorbed to a total of 1.6% (MIL-88-A) and 7% (MIL-88-B) of available sites based on their predicted number. Because these values only accounted for 2.4 and 13% of total NO adsorption, the authors suggested that the majority of NO was bound through physisorption.<sup>150</sup> At 11% RH, NO release corresponded to 5% and 0% of adsorbed NO and continued to occur at low concentrations (10 ppb) for up to 24 h. McKinlay *et al.* hypothesized that the decreased NO adsorption compared to the CPO-27 and

CuBTC MOFs was correlated with the flexibility of these particular structures. This flexibility could result in narrowed pores following removal of solvent molecules, limiting the accessibility of the metal sites to NO.<sup>150</sup> From this notion, Eubank *et al.* investigated three MOFs with rigid frameworks and increased pore sizes.<sup>151</sup> These MOFs were derived from inorganic trinuclear clusters (Fe, Cr) and tricarboxylate ([Fe, Cr] MIL-100) or tetracarboxylate ligands (Fe-MIL-127). NO adsorption studies for the MIL-100 MOFs demonstrated adsorption capacities of 2.7 (Fe) and 3.2 (Cr) mmol g<sup>-1</sup>, corresponding to 75-88% of their theoretical uptake based on available metal sites. Interestingly, Fe-MIL-127 adsorbed 1.2 mmol g<sup>-1</sup> NO, corresponding to only 44% of theoretical uptake. This decrease in adsorption was proposed to correlate with the retention of water molecules within the pores upon activation.<sup>151</sup> NO release experiments at 11% RH yielded values of 0.6 (Cr-MIL-100), 0.35 (Fe-MIL-100,) and 0.2 (Fe-MIL-127) mmol g<sup>-1</sup> of NO which corresponded to the release of 26, 15, and 27% of available NO. Additionally, the majority of NO release took place within the first hour, with small quantities (>10 ppb) released for up to 40 h.<sup>151</sup>

While the Fe-based MOFs are beneficial for improving biocompatibility, they uptake and release significantly smaller quantities of NO compared to the CPO MOFs, rendering it a compromise between high NO adsorption capacity and biocompatibility. In an effort to obtain both high NO adsorption and biocompatibility, Bloch *et al.* reported on the formation of a new Fe-MOF that adopted the CPO-27 structure and used a non-toxic metal. The Fe-MOF architecture consists of coordinately unsaturated Fe(II) sites and 2,5-dihydroxyterephthalic acid as the linker (Fe<sub>2</sub>(dobdc)).<sup>152</sup> Due to the high density of accessible metal sites and the enhanced biocompatibility of iron, Fe<sub>2</sub>(dobdc) was investigated for NO storage and release by Bloch and colleagues.<sup>153</sup> NO adsorption measurements demonstrated that Fe<sub>2</sub>(dobdc) adsorbed approximately 6.21 mmol g<sup>-1</sup> NO, similar to the quantities observed for other CPO-27 MOFs.

However, NO release measurements at 11% RH, showed that Fe<sub>2</sub>(dobdc) had released only 64% of NO over 10 days.<sup>153</sup> While additional MOF systems composed of Ca (BioMIL-3), Co (Co-vitamin B<sub>3</sub>), and Ni (Ni-vitamin B<sub>3</sub>) have been investigated for NO adsorption and release, CPO based architectures have the highest NO sorption capacities reported to date (**Table 1.1**).<sup>154,155</sup>

**Table 1.1** Table of NO adsorption, release, and percent release reported in the literature for different MOF complexes.

| MOF                       | NO adsorbed (mmol g <sup>-1</sup> ) | NO released under RH (mmol g <sup>-1</sup> ) | % NO release |
|---------------------------|-------------------------------------|--|--------------|
| CuBTC                     | 3.0                                 | 0.001  | 0.03         |
| Co-CPO-27                 | 6.7                                 | 6.7  | 100          |
| Ni-CPO-27                 | 7.0                                 | 7.0  | 100          |
| Fe-MIL-88-A               | 2.5                                 | 0.12   | 7.5          |
| Fe-MIL-88-B               | 1.6                                 | 0.0  | 0.0          |
| Cr-MIL-100                | 3.2                                 | 0.6  | 18           |
| Fe-MIL-100                | 2.7                                 | 0.35   | 13           |
| Fe-MIL-127                | 1.2                                 | 0.2  | 17           |
| Fe <sub>2</sub> (dobdc)   | 6.2                                 | 4.0  | 65           |
| BioMIL-3                  | 0.8                                 | 0.005  | 0.6          |
| Ni-vitamin B <sub>3</sub> | 3.3                                 | 2.6  | 79           |
| Co-vitamin B <sub>3</sub> | 4.5                                 | 2.0  | 44           |

### 1.6.2 Metal–organic frameworks for nitric oxide generation

More recently, an alternative method of achieving NO release using MOFs has been derived from the known ability of copper ions to decompose RSNOs. As previously mentioned, one limitation of utilizing copper complexes for NO generation involves the large degree of copper leaching that occurs over the duration of use. In MOFs, the immobilization of the metals within the extended framework can result in their enhanced stability over other copper complexes, making them an attractive approach for NO generation.

With the seminal work in 1994 by Fujita *et al.* which first demonstrated catalysis using a MOF, interest was triggered in the rational design and development of MOFs for catalytic applications has continued.<sup>156</sup> To date, there are several main approaches for creating catalytically

active MOFs.<sup>157,158</sup> First, catalytically-active MOFs can be created using the structurally embedded metal nodes within the SBUs of the extended framework. In this approach, catalysis relies on the existence of open metal sites that arise from structural defects or topographical prevention of complete saturation. In the second approach, catalytic metals are included within porphyrins that also function as organic linkers that bind to catalytically-inactive metal nodes to form the frameworks itself. Thirdly, the organic linker may also contain a functional group which is either directly catalytically active or becomes active following PSM.<sup>158</sup> This functional group is considered terminal and does not connect to other portions of the MOF. Lastly, MOFs can encapsulate the catalytically active species, (either a molecule or metal nanoparticles) within the pore structure. The use of MOFs with unsaturated metal sites remains the most widely explored route for catalysis. Based on this logic, two copper-based MOFs have been investigated for their activity in the presence of certain NO donors. These include the copper-carboxylate based MOF, CuBTC and the copper triazoleate-based MOF, CuBTTri.<sup>15,16</sup>

Chui and coworkers reported the initial synthesis of CuBTC from solutions of copper(II) ions in the presence of trimesic acid (1, 3, 5-benzenetricarboxylic acid).<sup>159</sup> CuBTC forms face-centered cubic crystals composed of dimeric copper(II) ions at the vertices and four trimesate ligands, which form a paddle-wheel-type configuration (**Figure 1.8**). These units make up the SBU of CuBTC, which together with additional SBUs form the overall extended framework.<sup>159</sup> The local environment around the copper centers consists of dimeric copper tetracarboxylate units through coordination with the carboxylate oxygens of trimesic acid. The environment around the copper sites is considered pseudo-octahedral with the presence of labile water ligands or solvent ligands which can be removed upon desolvation. CuBTC has remained the subject of ongoing study and has been proposed for numerous applications. In particular, Harding *et al.* evaluated the

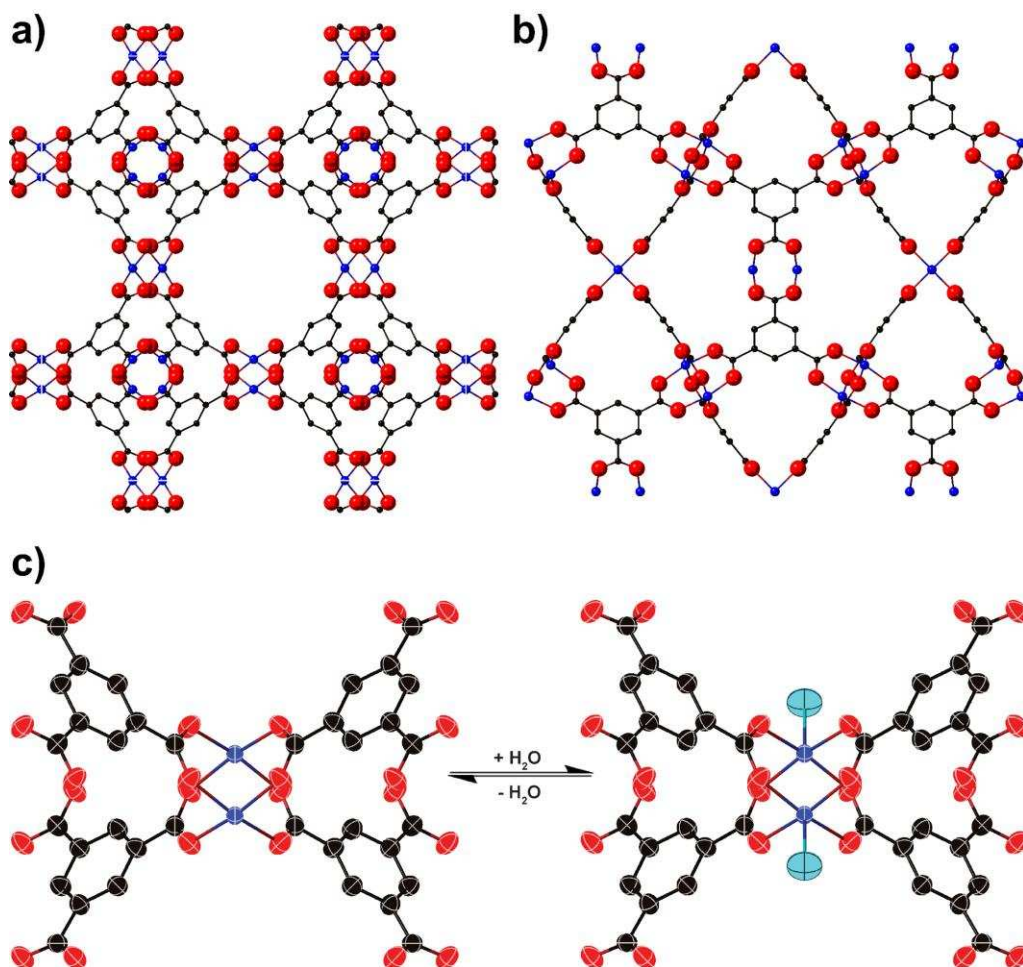


**Figure 1.8.** Structure of CuBTC (a) as viewed along the a-axis (b) viewed along the [110] plane (c) local environment around the copper centers which forms the SBUs. Image on the left illustrates the copper centers upon dehydration with two possible binding sites. Image on the right illustrates the hydrated version. Carbon atoms are represented in black, oxygen in red and copper in blue. Hydrogen atoms have been omitted for clarity.

ability of CuBTC to generate NO from the NO donor, *S*-nitrosocysteine (CysNO). Experiments performed in reagent alcohol in the presence of CysNO and cysteine (CysH), showed that CuBTC recovered nearly 100% of theoretical NO upon the addition of 2, 10, and 15-fold excesses of CysNO relative to theoretical copper sites in CuBTC.<sup>15</sup> To ensure that the catalytic activity did not result from the presence of nonframework copper complexes, the MOF particles and the reaction solution were characterized further via powder x-ray diffraction and inductively coupled plasma atomic emission spectroscopy (ICP-AES). Use of pXRD following the experiment confirmed

retention of crystallinity after exposure to the experimental conditions, while analysis of the reaction solution via ICP-AES determines whether copper ions are leaching into solution. In this report, analysis of CuBTC and surrounding solution supported retention of the original structure, implying the catalytic activity was not produced from copper ions.<sup>15</sup>

In 2009, Demessence *et al.* synthesized the robust, cubic sodalite-type metal-organic framework  $H_3[Cu_4Cl]_3(BTtri)_8(H_2O)_{12} \cdot 72H_2O$  (BTtri = 1,3,5-tris (1*H*-1,2,3-triazol-5-yl)benzene) that featured open Cu(II) coordination sites (**Figure 1.9**).<sup>28</sup> This MOF is described as isotopic to a previously reported copper tetrazole based MOF,  $H[Cu(CH_3OH)_6]_3[(Cu_4Cl)_3(BTT)_8(H_2O)_{12}] \cdot 3.5HCl \cdot 36CH_3OH$  (BTT=1,3,5-tris(tetrazol-5-yl)benzene).<sup>160</sup> The CuBTtri framework consists of square planar chloride-centered  $[Cu_4Cl]^{7+}$  units that coordinated through the nitrogen atoms of the triazole rings on the BTtri<sup>3-</sup> ligands (**Figure 1.9**). Each individual  $[Cu_4Cl]^{7+}$  is coordinated to eight individual BTtri<sup>3-</sup> ligands, and each BTtri<sup>3-</sup> ligand interacts with three different  $[Cu_4Cl]^{7+}$  units.<sup>160</sup> The fundamental building unit of CuBTtri consists of six  $[Cu_4Cl]^{7+}$  and eight BTtri<sup>3-</sup> units which form a truncated octahedral structure. Sharing of each square face between adjacent neighbors provides the overall cubic structure. Additionally, the copper centers in the framework exhibit octahedral coordination with one labile site typically occupied by solvent molecules. The most advantageous property of CuBTtri is its enhanced water stability compared to CuBTC. Notably, CuBTtri tolerates immersion in boiling water for 3 days without appreciable loss of structure (as characterized by pXRD).<sup>160</sup> These findings led to the initial studies by Harding and colleagues that assessed the promotion of NO from *S*-nitrosocysteamine by both CuBTtri itself and a CuBTtri/polymer blend. The presence of CuBTtri resulted in enhanced NO generation when compared to the baseline decomposition of the RSNO. The inclusion of CuBTtri into a polymer gave an 8-fold reduction

in the rate of NO generation, demonstrating that incorporation into a polymeric material can impact NO generation due to diffusion limitation of the RSNO.<sup>16</sup>

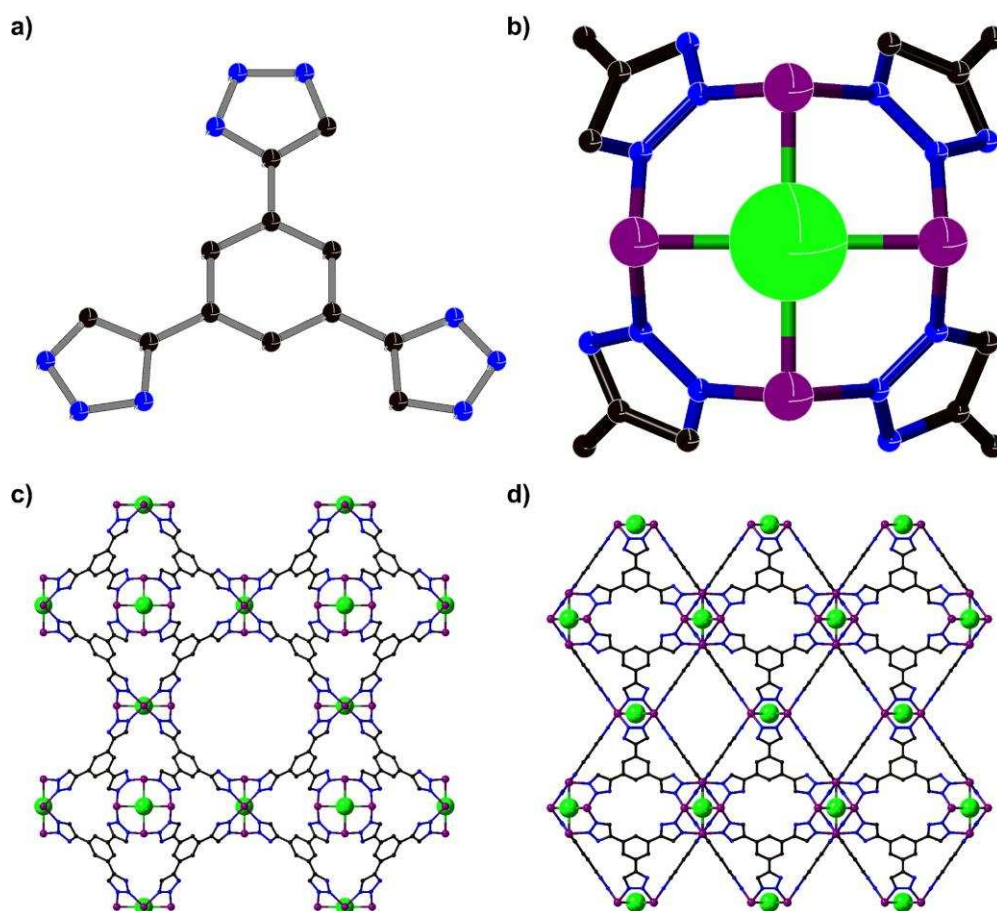


**Figure 1.9** Components of the CuBTTri MOF (a) structure of the BTTri ligand that binds with six different copper species (b) SBU with square planar geometry (c) viewed along the a-axis (d) view along the [110] plane.

While extremely promising, the use of MOFs as functional materials relies on the incorporation of particles into a secondary support system. Towards this end, MOFs are fabricated into thin films or membranes through two generalized approaches: the direct blending of the MOF within the polymer matrix and (b) chemical attachment of MOFs to a substrate via *in situ* growth. Direct incorporation of MOF particles into commercially available polymeric materials allows the potential to maintain properties of the parent material while adding the desired properties of the MOF.

## 1.7 Dissertation overview

This dissertation focuses on the fabrication and characterization of novel MOF-polymer composite materials and evaluation of their ability to generate NO from several different RSNOs (CysamNO, SNAP, and GSNO), which has never been previously demonstrated in the available literature (**Figure 1.10**). The initial reports by Harding *et al.* established that certain copper-based MOFs have the ability to accelerate NO generation from RSNOs, a concept never before demonstrated. However, these developed systems display certain limitations (non-aqueous conditions, non-physiological RSNOs) which will ultimately hinder their practical consideration in blood-contacting applications. This work expands on these initial reports through exploration of the factors which influence NO generation from these MOF-based systems. As such, this dissertation focuses on the identifying and optimizing key parameters necessary in these MOF-based systems for their practical implementation for potential clinical use.

As previously described, the use of MOFs for therapeutic enhancement of NO generation relies on their successful incorporation into a secondary support. To achieve this goal, two different approaches to the development of MOF/polymer composite materials have been explored: (1) *in situ* growth of MOF crystals directly on the surface of a polymeric substrate, and (2) blending of previously synthesized MOF particles into polymer matrices. The use of copper-based MOFs in the development of blood-contacting materials ideally requires their NO-forming function to occur within a certain set of parameters. In general, in order for these materials to be feasible for translation into clinical use, the MOF must maintain its structure and function upon incorporation into the polymeric material and under physiologically relevant conditions (pH 7.4, 37° C) with minimal to no leaching of copper or the organic ligand. Additionally, interactivity with the endogenous RSNOs should result in the generation of NO at physiologically relevant

concentrations (within the flux ranges associated with the endothelium  $0.05\text{-}0.4 \times 10^{-10}$  mol NO  $\text{cm}^{-2} \text{min}^{-1}$ ).

The polymers examined by this work are frequently used for medical applications and include cotton fabric (primarily cellulose), PVC, chitosan ( $\beta$ -(1,4)-linked glucosamine and *N*-acetyl-D-glucosamine units) and poly(vinyl alcohol) (PVA). In the medical industry, cotton fabric is found in the form of gauzes and swatches used as medical dressings. The primary constituent of cotton is cellulose, a polysaccharide composed of linear chains of  $\beta$  1 $\rightarrow$ 4 D-glucose units. Functionalization of the hydroxyl units through carboxymethylation provides a carboxylate anchoring point for copper ions similar to CuBTC. Chapter 2 demonstrates CuBTC growth on carboxylate-functionalized cotton substrate via a layer-by-layer synthetic approach. The ability of this material to generate NO from *S*-nitrosocysteamine was evaluated using nitric oxide analyzers (NOAs) a chemiluminescence-based detection technique. While this work provides insight into the development of supported MOF catalyst systems, the instability of CuBTC in an aqueous environment renders it unsuitable for many biological applications. Because the MOF is required to not degrade physically in aqueous conditions, the remaining chapters focus on the incorporation of CuBTTri into several different polymeric materials. PVC is a polymer which is commonly used in the fabrication of medical devices, including the tubing used for blood flow in extracorporeal circulation. Chapter 3 describes the incorporation of CuBTTri into PVC and assessment of NO generation from SNAP, a non-physiological NO donor. In addition, the CuBTTri/PVA materials were evaluated for cytotoxicity with respect to 3T3 murine fibroblast and primary human hepatocytes. Prior to the development of CuBTTri, the preparation of materials that combine copper-based MOFs with polymers they are typically processed from aqueous solution was limited due to the instability of MOFs such as CuBTC in an aqueous environment. Chapter 4 focuses on

the fabrication of chitosan/CuBTTri membranes and their ability to generate NO from GSNO, the sole LMW RSNO that has been unambiguously identified in blood. Chitosan is a naturally derived polysaccharide produced through the deacetylation of chitin used medically for its hemostatic and wound healing properties. Notably, the wound healing properties of chitosan overlap with those of NO, suggesting the potential for synergistic effects as a therapeutic. Chapter 5 focuses on the development of CuBTTri/PVA membranes to further study NO generation from GSNO. PVA is a hydrophilic linear polymer derived from poly(vinyl acetate) that is widely used in blood contact applications as a non-toxic material. Notably, the lack of certain functional groups allows the material to act a secondary support without exerting a chemical impact on the system. Taken together, these chapters report on the linear progression of investigating the reactivity and therapeutic potential of MOF-based materials for biomedical applications.

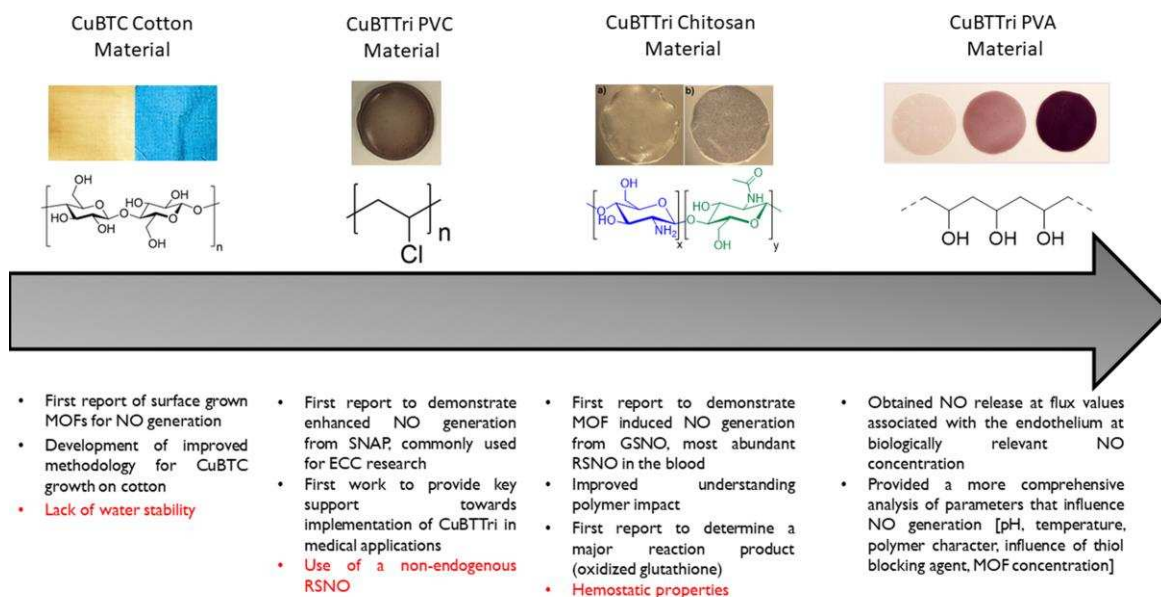


**Figure 1.10** Dissertation timeline showing the overall projects and the objectives that were achieved.

## REFERENCES

1. Rivera, A.M.; Strauss, K. W.; van Zundert, A.; Mortier, E. The History of Peripheral Intravenous Catheters: How Little Plastic tubes Revolutionized Medicine. *Acta Anaesth. Belg.* **2005**, *56*, 271-282.
2. Barsoum, N.; Kleeman, C. Now and Then, the History of Parenteral Fluid Administration. *Am. J. Nephrol.* **2002**, *22*, 284-289.
3. Konner, K. History of Vascular Access for Haemodialysis. *Nephrol., Dial., Transplant.* **2005**, *20*, 2629-2635.
4. Chandler, J. G.; Chin, T. L.; Wohlaer, M. V. Direct Blood Transfusions. *J. Vasc. Surg.* **2012**, *56*, 1173-2277.
5. Kimpton, A. R.; Brown, J. H. A New and Simple Method of Transfusion. *J. Am. Med. Assoc.* **1913**, *61*, 117-118.
6. Zerati, A. E.; Wolosker, N.; de Luccia, N.; Puech-Leao, P. Totally Implantable Venous Catheters: History, Implantation Technique and Complications. *J. Vasc. Bras.* **2017**, *16*, 128-139.
7. Anderson, J. M. Biological Responses to Materials. *Annu. Rev. Mater. Res.* **2001**, *31*, 81-110.
8. Harding, J. L.; Reynolds, M. M. Combating Medical Device Fouling. *Trends Biotechnol.* **2014**, *32*, 140-146.
9. Jaffer, I. H.; Fredenburg, J. C.; Hirsh, J.; Weitz, J. I. Medical Device-Induced Thrombosis: What Causes it and How Can We Prevent It? *J. Thromb. Haemostasis* **2015**, *13*, S72-S81.

10. Jung, F.; Braune, S. Thrombogenicity and Hemocompatibility of Biomaterials. *Biointerphases* **2016**, *11*, doi: 10.1116/1.4938557.
11. Moncada, S.; Higgs, E. A. The Discovery of Nitric Oxide and Its Role in Vascular Biology. *Br. J. Pharmacol.* **2006**, *147*, S193-S201.
12. Giustarini, D.; Milzani, A.; Colombo, R.; Dalle-Donne, I.; Rossi, R. Nitric Oxide and S-nitrosothiols in Human Blood. *Clinica Chimica Acta* **2003**, *330*, 85-98.
13. Williams, D. L. H. The Chemistry of S-Nitrosothiols. *Acc. Chem. Res.* **1999**, *32*, 869-876.
14. Wo, Y.; Brisbois, E. J.; Bartlett, R. H.; Meyerhoff, M. E. Recent Advances in Thromboresistant and Antimicrobial Polymers for Biomedical Applications: Just Say Yes to Nitric Oxide. *Biomater. Sci.* **2016**, *4*, 1161-1183.
15. Harding, J. L.; Reynolds, M. M. Metal Organic Frameworks as Nitric Oxide Catalysts. *J. Am. Chem. Soc.* **2012**, *134*, 3330-3333.
16. Harding, J. L.; Metz, J. M.; Reynolds, M. M. A Tunable, Stable, and Bioactive MOF Catalyst for Generating a Localized Therapeutic from Endogenous Sources. *Adv. Funct. Mater.* **2014**, *24*, 7503-7509.
17. Vroman, L. When Blood Is Touched. *Materials* **2009**, *2*, 1547-1557.
18. Gorbet, M. B.; Sefton, M. V. Biomaterial-Associated Thrombosis: Roles of Coagulation Factors, Complement, Platelets and Leukocytes. *Biomaterials* **2004**, *25*, 5681-5703.
19. Ratner, B. D. The Blood Compatibility Catastrophe. *J. Biomed. Mater. Res.* **1993**, *27*, 283-287.
20. Ratner, B. D. The Catastrophe Revisited: Blood Compatibility in the 21<sup>st</sup> Century. *Biomaterials* **2007**, *28*, 5144-5147.

21. Kareem, B.; Raghu, S.; Edward, K. Extracorporeal Life Support in Trauma: Worth the Risks: A Systematic Review of Published Series. *J. Trauma Acute Care Surg.* **2017**, *82*, 400-406.
22. Mazzeffi, M.; Greenwood, J.; Tanaka, K.; Menaker, J.; Rector, R.; Herr, D.; Kon, Z.; Lee, J.; Griffith, B.; Rajagopal, K.; Pham, S. Bleeding, Transfusion, and Mortality on Extracorporeal Life Support: ECLS Working Group on Thrombosis and Hemostasis. *Ann. Thorac. Surg.* **2016**, *101*, 682-689.
23. Laster, J.; Silver, D. Heparin-Coated Catheters and Heparin-Induced Thrombocytopenia. *J. Vasc. Surg.* **1988**, *7*, 667-672.
24. Pamboukian, S. V.; Ignaszewski, A. P.; Ross, H. J. Management Strategies for Heparin-Induced Thrombocytopenia in Heart-Transplanted Candidates: Case Report and Review of the Literature. *J. Heart Lung Transplant.* **2000**, *19*, 810-814.
25. Cohen, R. A.; Castellano, M.; Garcia, C. A. Heparin Induced Thrombocytopenia: Case Presentation and Review. *J. Clin. Med. Res.* **2012**, *4*, 68-72.
26. Tait, J.; Gunn, J. D. The Blood of *Astacus Fluviatilis*: A Study in Crustacean Blood, with Special Reference to Coagulation and Phagocytosis. *Exp. Physiol.* **1918**, *12*, 35-80.
27. Haycraft, J. B.; Carlier, E. W. A New Method for Preserving the Blood in a Fluid State Outside the Body. *Proc. R. Soc. Edinburgh* 1889, *15*, 130-131.
28. Haycraft, J. B. An Account of Some Experiments which show that Fibrin-Ferment is Absent from Circulating Blood. *J. Anat. Physiol.* **1888**, *22*, 172-190.
29. Furie, B.; Furie, B. C. Mechanisms of Thrombus Formation. *N. Engl. J. Med.* **2008**, *359*, 938-949.

30. Colman, R. W. Mechanisms of Thrombus Formation and Dissolution. *Cardiovasc. Pathol.* **1993**, *2*, 23S-31S.
31. Reviakine, I.; Jung, F.; Braune, S.; Brash, J. L.; Latour, R.; Gorbet, M.; van Oeveren, W. Stirred, Shaken, or Stagnant: What goes on at the Blood-Biomaterial Interface. *Blood Rev.* **2017**, *31*, 11-21.
32. Xu, L-C.; Bauer, J. W.; Siedlecki, C. A. Proteins, Platelets, and Blood Coagulation at Biomaterial Interfaces. *Colloids Surf., B* **2014**, *124*, 49-68.
33. Rao, G. H. R.; Chandy, T. Role of Platelets in Blood-Biomaterial Interactions. *Bull. Mater. Sci.* **1999**, *22*, 633-639.
34. Kalathottukaren, M. T.; Kizhakkedathu, J. N. Mechanisms of Blood Coagulation in Response to Biomaterials: Extrinsic Factors. Hemocompatibility of Biomaterials for Clinical Applications 2018, 29-49.
35. Annich, G. M.; Zaulan, O.; Neufeld, M.; Wagner, D.; Reynolds, M. M. Thromboprophylaxis in Extracorporeal Circuits: Current Pharmacological Strategies and Future Directions. *Am. J. Cardiovasc. Drugs* 2017,
36. Reynolds, M. M.; Annich, G. M. The Artificial Endothelium. *Organogenesis* **2011**, *7*, 42-49.
37. Marsh, N.; Marsh, A. A Short History of Nitroglycerine and Nitric Oxide in Pharmacology and Physiology. *Clin. Exp. Pharmacol. Physiol.* **2000**, *27*, 313-319.
38. Hughes R, Dake J. A Cyclopeda of Drug Pathogenesy. Boerike and Tafel, New York. 1888
39. Guthrie F. Contributions to the Knowledge of the Amyl Group. 1. Nitryl of Amyl and its Derivatives. *J. Chem. Soc.* **1859**, *11*, 245–252.

40. Brunton, T. L. On The Action of Nitrite of Amyl on the Circulation. *J. Anat. Physiol.* **1871**, 5, 92-101.
41. Brunton, T. L. On the Use of Nitrite of Amyl in Angina Pectoris. *The Lancet* **1867**, 90, 97-98.
42. Murrell, W. Nitro-glycerine as a Remedy for Angina Pectoris. *The Lancet* **1879**, 113, 80-81, 113-115, 225-227.
43. Editorial: Timidity in the use of Nitrite of Amyl. *Boston Med. Surg. J.* **1881**, 105, 597-598.
44. Katsuki, S.; Arnold, W.; Mittal, C.; Murad, F.; Stimulation of Guanylate Cyclase by Sodium Nitroprusside, Nitroglycerin and Nitric Oxide in Various Tissue Preparations and Comparison to the Effects of Sodium Azide and Hydroxylamine. *J. Cycl. Nucl. Prot. Phosphoryl. Res.* **1977**, 3, 23–25.
45. Arnold, W. P.; Mittal, C. K.; Katsuki, S.; Murad, F. Nitric Oxide Activates Guanylate Cyclase and Increases Guanosine 3',5,-Cyclic Monophosphate Levels in Various Tissue Preparations. *Proc. Natl. Acad. Sci. U. S. A.* **1977**, 74, 3203-3207.
46. Furchgott, R. F.; Zawadzki, J. V. The Obligatory Role of Endothelial Cells in the Relaxation of Arterial Smooth Muscle by Acetylcholine. *Nature* **1980**, 288, 373-376.
47. Cherry, P. D.; Furchgott, R. F.; Zawadzki, J. V. Role of Endothelial Cells in Relaxation of Isolated Arteries by Bradykinin. *Proc. Natl. Acad. Sci. U. S. A.* **1982**, 72, 20106-20110.
48. Ignarro, L. J.; Byrns, R. E.; Buga, G. M.; Wood, K. S.; Endothelium-derived Relaxing Factor from Pulmonary Artery and Vein Possesses Pharmacologic and Chemical Properties Identical to those of Nitric Oxide Radical. *Circ. Res.* **1987**, 61, 866-879.

49. Ignarro, L. J.; Buga, G. M.; Wood, K. S.; Byrns, R. E.; Chaudhuri, G. Endothelium-derived Relaxing Factor Produced and Released From Artery and Vein is Nitric Oxide. *Proc. Natl. Acad. Sci. U. S. A.* **1987**, *84*, 9265-9569.
50. Jaffrey, S. R.; Snyder, S. H. Nitric Oxide: A Neural Messenger. *Annu. Rev. Cell Dev. Biol.* **1995**, *11*, 417-440.
51. Witte, M. B.; Barbul, A. Role of Nitric Oxide in Wound Repair. *The American Journal of Surgery.* **2002**, *183*, 406-412.
52. Fang, F. C. Mechanisms of Nitric Oxide-related Antimicrobial Activity. *J. Clin. Invest.* **1997**, *99*, 2818-2825.
53. Andrew, P. J.; Mayer, B. Enzymatic Function of Nitric Oxide Synthases. *Cardiovasc. Res.* **1999**, *43*, 521-531.
54. Weitzberg, E. W.; Hezel, M.; Lundberg, J. O. Nitrate-Nitrite-Nitric Oxide Pathway. *Anesthesiology* **2010**, *113*, 1460-1475.
55. Lundberg, J. O.; Weitzberg, E.; Gladwin, M. T. The Nitrate-Nitrite-Nitric Oxide Pathway in Physiology and Therapeutics. *Nature* **2008**, *7*, 156-167.
56. Lundberg, J. O.; Weitzberg, E. NO Generation from Inorganic Nitrate and Nitrite: Role in Physiology, Nutrition and Therapeutics. *Arch. Pharm. Res.* **2009**, *32*, 1119-1126.
57. Bianco, C. L.; Toscano, J. P.; Fukuto, J. M. An Integrated View of the Chemical Biology of NO, CO, H<sub>2</sub>S and O<sub>2</sub>. In *Nitric Oxide: Biology and Pathobiology*, 3<sup>rd</sup> ed; Ignarro, L. J.; Freeman, B., Ed.; Elsevier: London, 2017; p 9-21.
58. Toledo, J. C. Jr.; Augusto, O. Connecting the Chemical and Biological Properties of Nitric Oxide. *Chem. Res. Toxicol.* **2012**, *25*, 975-989.

59. Goldstein, S.; Czapski, G. Kinetics of Nitric Oxide Autoxidation in Aqueous Solution in the Absence and Presence of Various Reductants. The Nature of the Oxidizing Intermediates. *J. Am. Chem. Soc.* **1995**, *117*, 12078-12084.
60. Ignarro, L. J.; Ballot, B.; Wood, K. S. Regulation of Soluble Guanylate Cyclase Activity by Porphyrins and Metalloporphyrins. *J. Biol. Chem.* **1984**, *259*, 6201-6207.
61. Ignarro, L. J. Haem-Dependent Activation of Guanylate Cyclase and Cyclic GMP Formation by Endogenous Nitric Oxide: A Unique Transduction Mechanism for Transcellular Signaling. *Pharmacol. Toxicol.* **1990**, *67*, 1-7.
62. Rubanyi, G. M.; Romero, J. C.; Vanhoutte, P. M. Flow-induced Release of Endothelium-Derived Relaxing Factor. *Am. J. Physiol.* **1986**, *250*, H1145-H1149.
63. de Wit, C.; Schäfer, C.; von Bismarck, P.; Bolz, S-S.; Pohl, U. Elevation of Plasma Viscosity Induces Sustained NO-Mediated Dilation in the Hamster Cremaster Microcirculation In Vivo. *Am. J. Physiol. Heart Circ. Physiol.* **1997**, *434*, 354-361.
64. Pohl, U.; Herlan, K.; Huang, A.; Bassenge, E. EDRF-mediated Shear-Induced Dilation Opposes Myogenic Vasoconstriction in Small Rabbit Arteries. *Am. J. Physiol. Heart Circ. Physiol.* **1991**, *261*, H2016-H2023.
65. Wang, G-R.; Zhu, Y.; Halushka, P. V.; Lincoln, T. M.; Mendelsohn, M. E. Mechanism of Platelet Inhibition by Nitric Oxide: In Vivo Phosphorylation of Thromboxane Receptor by Cyclic GMP-dependent Protein Kinase. *Proc. Natl. Acad. Sci. U. S. A.* **1998**, *95*, 4888-4893.
66. Ignarro, L. J.; Biological Actions and Properties of Endothelium-Derived Nitric Oxide Formed and Released From Artery and Vein. *Circ. Res.* **1989**, *65*, 1-21.

67. Gkaliagkousi, E.; Ritter, J.; Ferro, A. Platelet-Derived Nitric Oxide Signaling and Regulation. *Circ. Res.* **2007**, *101*, 654-662.
68. Mendelsohn, M. E.; O'Neil, S.; George, D.; Loscalzo, J. Inhibition of Fibrinogen Binding to Human Platelets by S-Nitroso-N-acetylcysteine. *J. Biol. Chem.* **1990**, *265*, 19028-19034.
69. Albina, J. E.; Mills, D. C.; Barbul, A.; Thirkill, C. E.; Henry, W. L. Jr; Mastrofrancesco, B.; Caldwell, M. D. Arginine Metabolism in Wounds. *Am. J. Physiol.* **1988**, *254*, E459-E467.
70. Barbul, A. Arginine Enhances Wound Healing and Lymphocyte Immune Responses in Humans. *Surgery* **1990**, *108*, 331-336.
71. Smith, D. J.; Dunphy, M. J.; Strag, L. N.; Marletta, M. A. The Influence of Wound Healing on Urinary Nitrate Levels in Rats. *Wounds* **1991**, *3*, 50-58.
72. Bulgrin, J. P.; Shabani, M.; Smith, D. Arginine-Free Diet Suppresses Nitric Oxide Production in Wounds. *J. Nut. Biochem.* **1993**, *4*, 588-593.
73. Shi, H. P.; Most, D.; Efron, D. T.; Witte, M. B.; Barbul, A. Supplemental L-arginine Enhances Wound Healing in Diabetic Rats. *Wound Repair Regen.* **2003**, *11*, 198-203.
74. Shabani, M.; Pulfer, S. K.; Bulgrin, J. P.; Smith, D. J. Enhancement of Wound Repair with a Topically Applied Nitric Oxide-Releasing Polymer. *Wound Repair Regen.* **1996**, *4*, 353-362.
75. Reicher, J. S.; Meszaros, A. J.; Louis, C. A.; Henry, W. L. Jr.; Mastrofrancesco, B.; Martin, B-A.; Albina, J. E. Molecular and Metabolic Evidence for the Restricted Expression of Inducible Nitric Oxide Synthase in Healing Wounds. *Am. J. Pathol.* **1999**, *154*, 1097-1104.

76. Shi, H. P.; Efron, D. T.; Most, D.; Tantry, U. S.; Barbul, A. Supplemental dietary arginine enhances wound healing in normal but not inducible nitric oxide synthase knockout mice. *Surgery* **2000**, *128*, 374–378.
77. Coneski, P. N.; Schoenfisch, M. H. Nitric Oxide Release: Part III. Measurement and Reporting. *Chem. Soc. Rev.* **2012**, *41*, 3753-3758.
78. Vaughn, M. W.; Kuo, L.; Liao, J. C. Estimation of Nitric Oxide Production and Reaction Rates in Tissue by use of a Mathematical Model. *Am. J. Physiol.* **1998**, *4*, H2163-2176.
79. Hakim, T. S.; Sugimori, K.; Camporesi, E. M.; Andersen, G. Half-life of Nitric Oxide in Aqueous Solutions with and without Haemoglobin. *Physiol. Meas.* **1996**, *17*, 267-277.
80. Thomas, D. D.; Liu, X.; Kantrow, S. P.; Lancaster, J. R. Jr. The Biological Lifetime of Nitric Oxide: Implications for the Perivascular Dynamics of NO and O<sub>2</sub>. *Proc. Natl. Acad. Sci. U. S. A.* **2001**, *98*, 355-360.
81. Liu, X.; Samouilov, A.; Lancaster, J. R. Jr.; Zweier, J. L. Nitric Oxide Uptake by Erythrocytes is Primarily Limited by Extracellular Diffusion Not Membrane Resistance. *J. Biol. Chem.* **2002**, *277*, 26194-26199.
82. Navati, M. S.; Chung, W.; Friedman, J. M. Trehalose-Based Glassy Matrices as an Effective Tool to Trap Short-Lived Intermediates in the Nitric Oxide Dioxygenation (NOD) Reaction of Hemoglobin. *J. Phys. Chem. B* **2016**, *120*, 4529-4539.
83. Jen, M. C.; Serrano, M. C.; van Lith, R.; Ameer, G. A. Polymer-Based Nitric Oxide Therapies: Recent Insights for Biomedical Applications. *Adv. Funct. Mater.* **2012**, *22*, 239-260.

84. Frost, M. C.; Reynolds, M. M.; Meyerhoff, M. E. Polymers Incorporating Nitric Oxide Releasing/Generating Substances for Improved Biocompatibility of Blood-Contacting Medical Devices. *Biomaterials* **2005**, *26*, 1685-1693.
85. Riccio, D. A.; Schoenfisch, M. H. Nitric Oxide Release Part I. Macromolecular Scaffolds. *Chem. Soc. Rev.* **2012**, *41*, 3731-3741.
86. Smith, D. J.; Chakravarthy, D.; Pulfer, S.; Simmons, M. L.; Hrabie, J. A.; Citro, M. L.; Saavedra, J. E.; Davies, K. M.; Hutsell, T. C.; Mooradian, D. L.; Hanson, S. R.; Keefer, L. K. Nitric Oxide-Releasing Polymers Containing the [N(O)NO]<sup>-</sup> Group. *J. Med. Chem.* **1996**, *39*, 1148-1156.
87. Seabra, A. B.; da Silva, R.; de Souza, G. F. P.; de Oliveria, M. G. Antithrombogenic Polynitrosated Polyester/Poly(methylmethacrylate) Blend for the Coating of Blood-Contacting Surfaces. *Artif. Organs* **2008**, *32*, 262-267.
88. Stamler, J. S.; Jaraki, O.; Osborne, J.; Simon, D. I.; Keaney, J.; Vita, J.; Singel, D.; Valeri, C. R.; Loscalzo, J. Nitric Oxide Circulates in Mammalian Plasma Primarily as an S-Nitroso Adduct of Serum Albumin. *Proc. Natl. Acad. Sci. U. S. A.* **1992**, *89*, 7674-7677.
89. Scharfstein, J. S.; Keaney, J. F. Jr.; Slivka, A.; Welch, G. N.; Vita, J. A.; Stamler, J. S. In Vivo Transfer of Nitric Oxide between a Plasma Protein-bound Reservoir and Low Molecular Weight Thiols. *J. Clin. Invest.* **1994**, *94*, 1432-1439.
90. Nedospasov, A.; Rafikov, R.; Beda, N.; Nudler, E. An Autocatalytic Mechanism of Protein Nitrosylation. *PNAS* **2000**, *97*, 13543-13548.

91. Rafikova, O.; Rafikov, R.; Nudler, E. Catalysis of S-nitrosothiols Formation by Serum Albumin: The Mechanism and Implication of Vascular Control. *PNAS* **2002**, *99*, 5913-5918.
92. Jourde'heuil, D.; Jourde'heuil, F. L.; Feelisch, M. Oxidation and Nitrosation of Thiols at Low Micromolar Exposure to Nitric Oxide. *J. Biol. Chem.* **2003**, *278*, 15720-15726.
93. Martinez-Ruiz, A.; Araujo, I. M.; Izquierdo-Alvarez, A.; Hernansanz-Agustin, P.; Lamas, S.; Serrador, J. M. Specificity in S-Nitrosylation: A Short-Range Mechanism for NO Signaling? *Antioxid. Redox Signaling* **2013**, *19*, 1220-1235.
94. Goldman, R. K.; Vlessis, A. A.; Trunkey, D. D. Nitrosothiol Quantification in Human Plasma. *Anal. Biochem.* **1998**, *259*, 98-103.
95. Jourde'heuil, D. Hallen, K.; Feelisch, M.; Grisham, M. B. Dynamic State of S-Nitrosothiols in Human Plasma and Whole Blood. *Free Radic. Biol. Med.* **2000**, *28*, 409-417.
96. Marley, R.; Feelisch, M.; Holt, S.; Moore, K. A Chemiluminescence-based Assay for S-Nitrosoalbumin and other Plasma S-Nitrosothiols. *Free Radic. Res.* **2000**, *32*, 1-9.
97. Rassaf, T.; Preik, M.; Kleinbongard, P.; Lauer, T.; Heiss, C.; Strauer, B. E.; Feelisch, M.; Kelm, M. Evidence for In Vivo Transport of Bioactive Nitric Oxide in Human Plasma. *J. Clin. Invest.* **2002**, *109*, 1241-1248.
98. Rassaf, T.; Kleinbongard, P.; Preik, M.; Dejam, A.; Gharini, P.; Lauer, T.; Erckenbrecht, J.; Duschin, A.; Schulz, R.; Heusch, G.; Feelisch, M.; Kelm, M. Plasma Nitrosothiols Contribute to the Systemic Vasodilator Effects of Intravenously Applied NO: Experimental and Clinical Study on the Fate of NO in Human Blood. *Circ. Res.* **2002**, *91*, 470-477.

99. Tyurin, V. A.; Liu, S. X. Tyurina, Y. Y.; Sussman, N. B.; Hubel, C. A.; Roberts, J. M.; Taylor, R. N.; Kagan, V. E. Elevated Levels of S-Nitrosoalbumin in Preeclampsia Plasma. *Circ. Res.* **2001**, *88*, 1210-1215.
100. Tsikas, D.; Sandmann, J.; Frolich, J. C. Measurement of S-Nitrosoalbumin by Gas Chromatography-Mass Spectrometry: III. Quantitative Determination in Human Plasma After Specific Conversion of the S-Nitroso Group to Nitrite by Cysteine and Cu<sup>2+</sup> via Intermediate Formation of S-Nitrosocysteine and Nitric Oxide. *J. Chromatogr. B, Biomed. Sci. Appl.* **2002**, *772*, 335-346.
101. Tasker, H. S.; Jones, H. O. Action of Mercaptans on Acid Chlorides. I. Oxalychloride; The Mono-and Dithioxalates. *J. Chem. Soc.* **1909**, *95*, 1904-1909.
102. Stamler, J. S.; Toone, E. J. The Decomposition of Thionitrites. *Curr. Opin. Chem. Biol.* **2002**, *6*, 779-785.
103. Grossi, L.; Montevecchi, P. C. A Kinetic Study of S-Nitrosothiol Decomposition. *Chem. Eur. J.* **2002**, *8*, 380-387.
104. Lü, J-M.; Wittbrodt, J. M.; Wang, K.; Wen, Z.; Schlegel, H. B.; Wang, P. G.; Cheng, J-P. NO Affinities of S-Nitrosothiols: A Direct Experimental and Computational Investigation of RS-NO Bond Dissociation Energies. *J. Am. Chem. Soc.* **2001**, *123*, 2903-2904.
105. Bartberger, M. D.; Mannion, J. D.; Powell, S. C.; Stamler, J. S.; Houk, K. N.; Toone, E. J. S-N Dissociation Energies of S-Nitrosothiols: On the Origins of Nitrosothiol Decomposition Rates. *J. Am. Chem. Soc.* **2001**, *123*, 8868-8869.
106. Zhang, C.; Biggs, T. D.; Devarie-Baez, N. O.; Shuang, S.; Dong, C.; Xian, M. S-Nitrosothiols: Chemistry and Reactions. *Chem. Commun.* **2017**, *53*, 11266.

107. Bainbrigge, N.; Butler, A. R.; Gorbitz, C. H. The Thermal Stability of S-nitrosothiols: Experimental Studies and Ab Initio Calculations on Model Compounds. *J. Chem. Soc., Perkin Trans 2* **1997**, 0, 351-354.
108. Yin, J.; Khan, M. A.; Lee, J.; Richter-Addo, G. B. The Solid-State Molecular Structure of the S-Nitroso Derivative of L-cysteine Ethyl Ester Hydrochloride. *Nitric Oxide*. **2005**, 12, 261-266.
109. Carnahan, G. E.; Lenhart, P. G.; Ravichandran, R. S-Nitroso-N-acetyl-DL-penicillamine. *Acta Cryst.* **1978**, B34, 2645-2648.
110. Bartberger, M. D.; Houk, K. N.; Powell, S. C.; Mannion, J. D.; Lo, K. Y.; Stamler, J. S.; Toone, E. J. Theory, Spectroscopy, and Crystallographic Analysis of S-Nitrosothiols: Conformational Distribution Dictates Spectroscopic Behavior. *J. Am. Chem. Soc.* **2000**, 122, 5889-5890.
111. Arulsamy, N.; Bohle, D. S.; Butt, J. A.; Irvine, G. J.; Jordan, P. A.; Sagan, E. Interrelationships between Conformational Dynamics and the Redox Chemistry of S-Nitrosothiols. *J. Am. Chem. Soc.* **1999**, 121, 7115-7123.
112. Timerghazin, Q. K.; Peslherbe, G. H.; English, A. M. Resonance Description of S-Nitrosothiols: Insights into Reactivity. *Org. Lett.* **2007**, 9, 3049-3052.
113. McAninly, J.; Williams, D. L. H.; Askew, S. C.; Butler, A. R.; Russell, C. Metal Ion Catalysis in Nitrosothiol (RSNO) Decomposition. *J. Chem. Soc., Chem. Commun.* **1993**, 23, 1758-1759.
114. Askew, S. C.; Barnett, D. J.; McAninly, J.; Williams, D. L. H. Catalysis by Cu<sup>2+</sup> of Nitric Oxide Release from S-Nitrosothiols (RSNO). *J. Chem. Soc. Perkin Trans 2* **1995**, 741-745.

115. Dicks, A. P.; Swift, H. R.; Williams, D. L. H.; Butler, A. R.; Ai-Sa'doni, H. H.; Cox, B. G. Identification of  $\text{Cu}^+$  as the Effective Reagent in Nitric Oxide Formation of S-Nitrosothiols (RSNO). *J. Chem. Soc., Perkin Trans. 2* **1996**, *4*, 481-487.
116. Noble, D. R.; Swift, H. R.; Williams, D. L. H. Nitric Oxide Release from S-Nitrosoglutathione (GSNO). *Chem. Commun.*, **1999**, *22*, 2317-2318.
117. Noble, D. R.; Williams, D. L. H. Structure-Reactivity Studies of the  $\text{Cu}^{2+}$ -Catalyzed Decomposition of Four S-Nitrosothiols Based Around the S-Nitrosocysteine/S-Nitrosoglutathione Structures. *Nitric Oxide: Biology and Chemistry* **2000**, *4*, 392-398.
118. Swift, H. R.; Williams, D. L. H. Decomposition of S-Nitrosothiols by Mercury (II) and Silver Salts. *J. Chem. Soc., Perkin Trans. 2* **1997**, *10*, 1933-1935.
119. Cha, W.; Meyerhoff, M. E. Catalytic Generation of Nitric Oxide from S-Nitrosothiols Using Immobilized Organoselenium Species. *Biomaterials* **2007**, *28*, 19-27.
120. Hwang, S.; Meyerhoff, M. E. Organoditelluride-mediated Catalytic S-Nitrosothiol Decomposition. *J. Mater. Chem.* **2007**, *17*, 1462-1465.
121. Cai, W.; Wu, J.; Xi, C.; Ashe, A. J. 3rd; Meyerhoff, M. E. Carboxyl-Ebselen-Based Layer-by-Layer Films as Potential Antithrombotic and Antimicrobial Coatings. *Biomaterials* **2011**, *32*, 7774-7784.
122. Yang, J.; Welby, J. L.; Meyerhoff, M. E. Generic Nitric Oxide (NO) Generating Surface by Immobilizing Organoselenium Species via Layer-by-Layer Assembly. *Langmuir*, **2008**, *24*, 10265-10272.
123. Wonoputri, V.; Gunawan, C.; Liu, S.; Barraud, N.; Yee, L. H.; Lim, M.; Amal, L. Copper Complex in Poly(vinyl chloride) as a Nitric Oxide-Generating Catalyst for the Control of Nitrifying Bacterial Biofilms. *ACS Appl. Mater. Interfaces* **2015**, *7*, 22148-22156.

124. Major, T. C.; Brant, D. O.; Burney, C. P.; Amoako, K. A.; Annich, G. M.; Meyerhoff, M. E.; Handa, H.; Bartlett, R. H. The Hemocompatibility of a Nitric Oxide Generating Polymer that Catalyzes S-Nitrosothiol Decomposition in an Extracorporeal Circulation Model. *Biomaterials* **2011**, *32*, 5957–5969.
125. Oh, B. K.; Meyerhoff, M. E. Spontaneous Catalytic Generation of Nitric Oxide from S-Nitrosothiols at the Surface of Polymer Films Doped with Lipophilic Copper(II) Complex. *J. Am. Chem. Soc.* **2003**, *125*, 9552–9553.
126. Puiu, S. C.; Zhou, Z.; White, C. C.; Neubauer, L. J. Zhang, Z.; Lange, L. E.; Mansfield, J. A.; Meyerhoff, M. E.; Reynolds, M. M. Metal Ion-Mediated Nitric Oxide Generation From Polyurethanes via Covalently Linked Copper (II)-Cyclen Moieties. *J. Biomed. Mater. Res., Part B* **2009**, *91*, 203-212.
127. Oh, B. K.; Meyerhoff, M. E. Catalytic Generation of Nitric Oxide from Nitrate at the Interface of Polymeric Films Doped with Lipophilic Cu(II)-complex: A Potential Route to the Preparation of Thromboresistant Coatings. *Biomaterials* **2004**, *25*, 283-293.
128. Hwang, S.; Cha, W.; Meyerhoff, M. E. Polymethacrylates with a Covalently Linked Cu(II)-Cyclen Complex for the In Situ Generation of Nitric Oxide from Nitrosothiols in Blood. *Angew. Chem. Int. Ed.* **2006**, *45*, 2745-2748.
129. Hwang, S.; Meyerhoff, M. E. Polyurethane with Tethered Copper (II)-Cyclen Complex: Preparation, Characterization and Catalytic Generation of Nitric Oxide from S-Nitrosothiols. *Biomaterials* **2008**, *29*, 2443-2452.
130. Hou, Y.; Gou, Z.; Li, J.; Wang, P. G. Seleno Compounds and Glutathione Peroxidase Catalyzed Decomposition of S-Nitrosothiols. *Biochem. Biophys. Res. Commun.* **1996**, *228*, 88-93.

131. Wonoputri, V.; Gunawan, C.; Liu, S.; Barraud, N.; Yee, L. H.; Lim, M.; Amal, R. Iron Complex Facilitated Copper Redox Cycling for Nitric Oxide Generation as Nontoxic Nitrifying Biofilm Inhibitor. *ACS Appl. Mater. Interfaces* **2016**, *8*, 30502-30510.
132. Ren, H.; Wu, J.; Xi, C.; Lehnert, N.; Major, T.; Bartlett, R. H.; Meyerhoff, M. E. Electrochemically Modulated Nitric Oxide (NO) Releasing Biomedical Devices via Copper (II)-Tri(2-pyridylmethyl)amine Mediated Reduction of Nitrite. *ACS Appl. Mater. Interfaces* **2014**, *6*, 3779-3783.
133. Hofler, L.; Koley, D.; Wu, J.; Xi, C.; Meyerhoff, M. E. Electromodulated Release of Nitric Oxide Through Polymer Material from Reservoir of Inorganic Nitrite Salt. *RSC Adv.* **2012**, *2*, 6765-6767.
134. Ren, H.; Coletta, A.; Koley, D.; Wu, J.; Xi, C.; Major, T. C.; Bartlett, R. H.; Meyerhoff, M. E. Thromboresistant/anti-biofilm Catheters Via Electrochemically Modulated Nitric Oxide Release. *Bioelectrochemistry* **2015**, *104*, 10-16.
135. Stock, N.; Biswas, S. Synthesis of Metal-Organic Frameworks (MOFs): Routes to Various MOF Topologies, Morphologies, and Composites. *Chem. Rev.* **2012**, *112*, 933-969.
136. Tranchemontagne, D. J.; Mendoza-Cortes, J. L.; O'Keeffe, M.; Yaghi, O. M. Secondary Building Units, Nets and Bonding in the Chemistry of Metal-Organic Frameworks. *Chem. Soc. Rev.* **2009**, *38*, 1257-1283.
137. Li, J-R.; Kuppler, R. J.; Zhou, H-C. Selective Gas Adsorption and Separation in Metal-Organic Frameworks. *Chem. Soc. Rev.* **2009**, *38*, 1477-1504.
138. Furukawa, H.; Cordova, K. E.; O'Keeffe, M.; Yaghi, O. M. The Chemistry and Applications of Metal-Organic Frameworks. *Science* **2013**, *341*, 1230444.

139. Suh, M. P.; Park, H. J.; Prasad, T. K.; Lim, D-W. Hydrogen Storage in Metal-Organic Frameworks. *Chem. Rev.* **2012**, *112*, 782-835.
140. Yoon, M.; Srirambalaji, R.; Kim, K. Homochiral Metal-Organic Frameworks for Asymmetric Heterogeneous Catalysis. *Chem. Rev.* **2012**, *112*, 1196-1231.
141. Keskin, S.; Kizilel, S. Biomedical Applications of Metal Organic Frameworks. *Ind. Eng. Chem. Res.* **2011**, *50*, 1799-1812.
142. Huxford, R. C.; Rocca, J. D.; Lin, W. Metal-Organic Frameworks as Potential Drug Carriers. *Curr. Opin. Chem. Bio.* **2010**, *14*, 262-268.
143. Hinks, N. J.; McKinlay, A. C.; Xiao, B.; Wheatley, P. S.; Morris, R. E. Metal Organic Frameworks as NO Delivery Materials for Biological Applications. *Microporous and Mesoporous Mater.* **2009**, *129*, 330-334.
144. Gregg, S. T.; Yuan, Q.; Morris, R. E.; Xiao, B. Functionalised Solids Delivering Bioactive Nitric Oxide Gas for Therapeutic Applications. *Mater. Today Commun.* **2017**, *12*, 95-105.
145. Ingelson, M. J.; Heck, R.; Gould, J. A.; Rosseinsky, M. J. Nitric Oxide Chemisorption in a Postsynthetically Modified Metal-Organic Framework. *Inorg. Chem.* **2009**, *48*, 9986-9988.
146. Lowe, A.; Chittajallu, P.; Gong, Q.; Li, J.; Balkus, K. J. Jr. Storage and Delivery of Nitric Oxide via Diazeniumdiolated Metal Organic Framework. *Microporous and Mesoporous Mater.* **2013**, *181*, 17-22.
147. Peikart, K.; McCormick, L. J.; Cattaneo, D.; Duncan, M. J.; Hoffman, F.; Khan, A. H.; Bertmer, M.; Morris, R. E.; Froba, M. Tuning the Nitric Oxide Release Behavior of

- Amino Functionalized HKUST-1. *Microporous and Mesoporous Mater.* **2015**, *216*, 118-126.
148. Xiao, B.; Wheatley, P. S.; Zhao, X.; Fletcher, A. J.; Fox, S.; Rossi, A. G.; Megson, I. L.; Bordiga, S.; Regli, L.; Thomas, K. M.; Morris, R. E. High-Capacity Hydrogen and Nitric Oxide Adsorption and Storage in a Metal-Organic Framework. *J. Am. Chem. Soc.* **2007**, *129*, 1203-1209.
149. McKinlay, A. C.; Xiao, B.; Wragg, D. S.; Wheatley, P. S.; Megson, I. L.; Morris, R. E. Exceptional Behavior over the Whole Adsorption-Storage-Delivery Cycle for NO in Porous Metal Organic Frameworks. *J. Am. Chem. Soc.* **2008**, *130*, 10440-10444.
150. McKinlay, A. C.; Eubank, J. F.; Wuttke, S.; Xiao, B.; Wheatley, P. S.; Bazin, P.; Lavalley, J.-L.; Daturi, M.; Vomont, A.; Weireld, G. De.; Horcajada, P.; Serre, C.; Morris, R. E. Nitric Oxide Adsorption and Delivery in Flexible MIL-88(Fe) Metal-Organic Frameworks. *Chem. Mater.* **2013**, *25*, 1592-1599.
151. Eubank, J. F.; Wheatley, P. S.; Lebars, G.; McKinlay, A. C.; Leclerc, H.; Horcajada, P.; Daturi, M.; Vimont, A.; Morris, R. E.; Serre, C. Porous, Rigid Metal (III)-Carboxylate Metal-Organic Frameworks for the Delivery of Nitric Oxide. *APL Materials* **2014**, *2*, 124112.
152. Bloch, E. D.; Murray, L. J.; Quenn, W. L.; Chavan, S.; Maximoff, S. N.; Bigi, J. P.; Krishna, R.; Peterson, V. K.; Grandjean, F.; Long, G. J.; Smit, B.; Bordiga, S.; Brown, C. M.; Long, J. R. Selective Binding of O<sub>2</sub> over N<sub>2</sub> in a Redox-Active Metal-Organic Framework with Open Iron(II) Coordination Sites. *J. Am. Chem. Soc.* **2011**, *133*, 14814-14822.

153. Bloch, E. D.; Queen, W. L.; Chavan, S.; Wheatley, P. S.; Zadrozny, J. M.; Morris, R.; Brown, C. M.; Lamberti, C.; Bordiga, S.; Long, J. R. Gradual Release of Strongly Bound Nitric Oxide from  $\text{Fe}_2(\text{NO})_2(\text{dobdc})$ . *J. Am. Chem. Soc.* **2015**, *137*, 3466-3469.
154. Miller, S. R.; Alvarez, E.; Fradcourt, L.; Devic, T.; Wuttke, S.; Wheatley, P. S.; Steunou, N.; Bonhomme, C.; Gervais, C.; Lautncin, D.; Morris, R. E.; Vimont, A.; Daturi, M.; Horcajada, P.; Serre, C. A Rare Example of a Porous Ca-MOF for the Controlled Release of Biologically Active NO. *Chem. Commun.* **2013**, *49*, 7773-7775.
155. Pinto, R. V.; Antunes, F.; Pires, J.; Graca, V.; Brandao, P.; Pinto, M. Vitamin B<sub>3</sub> Metal-Organic Frameworks as Potential Delivery Vehicles for Therapeutic Nitric Oxide. *Acta Biomaterialia* **2017**, *51*, 66-74.
156. Fujita, M.; Kwon, Y. J.; Washizu, S.; Ogura, K. Preparation, Clathration Ability, and Catalysis of a Two-Dimensional Square Network Material Composed of Cadmium(II) and 4,4'-Bipyridine. *J. Am. Chem. Soc.* **1994**, *116*, 1151-1152.
157. Gascon, J.; Corma, A.; Kapteijn, F.; Llabres Xamena, F. X. Metal Organic Framework Catalysis: Quo vadis? *ACS Catal.* **2014**, *4*, 361-378.
158. Rogge, S. M. J.; Bavykina, A.; Hajek, J.; Garcia, H.; Olivos-Suarez, A. I.; Sepulveda-Escribano, A.; Vimont, A.; Clet, G.; Bazin, P.; Kapteijn, F.; Daturi, M.; Ramos-Fernandez, E. V.; Llabres i Xamena, F. X.; Speybroeck, V. V.; Gascon, J. Metal-organic and Covalent Organic Frameworks as Single-Site Catalysts. *Chem. Soc. Rev.* **2017**, *46*, 3134-3184.
159. Chui, S. S.-Y.; Lo, S. M.-F.; Charmant, J. P. H.; Orpen, A. G.; Williams, I. D. A Chemically Functionalizable Nanoporous Material  $[\text{Cu}_3(\text{TMA})_2(\text{H}_2\text{O})_3]_n$ . *Science* **1999**, *283*, 1148-1150.

160. Demessence, A.; D'Alessandro, D. M.; Foo, M. L.; Long, J. R. Strong CO<sub>2</sub> Binding in a Water-Stable, Triazolate-Bridged Metal-Organic Framework Functionalized with Ethylenediamine. *J. Am. Chem. Soc.* **2009**, *131*, 8784-8786.

CHAPTER 2  
IMMOBILIZATION OF COPPER(II) BENZENE-1,3,5-TRICARBOXYLATE ONTO  
COTTON FABRIC AS A NITRIC OXIDE RELEASE  
CATALYST<sup>1</sup>

## 2.1 Introduction

The biological activity of nitric oxide (NO) includes antiplatelet activation, anti-inflammatory, and antibacterial properties, making NO-releasing materials an important class of therapeutic systems. Because of the short physiological half-life of NO (0.09 to >2 s) due to scavenging, this radical species is an ideal candidate for localized therapeutics.<sup>1-6</sup> To date, many researchers have explored the incorporation of NO donor species such as *S*-nitrosothiols (RSNOs) and *N*-diazeniumdiolates directly into polymeric materials to produce drug-eluting systems.<sup>7,8</sup> A potential shortcoming of this approach is the limited overall lifetime of NO release due to finite reservoirs of the drug that can be incorporated into the polymer.<sup>9-13</sup> Often, efforts to increase the incorporation of NO donors to achieve higher loading capacities result in changes to the mechanical properties of polymers rendering them unsuitable for clinical applications.<sup>10</sup> Metal-organic frameworks (MOFs) and nanoparticles have been used to achieve some of the highest NO loading capacities reported to date, yet this level of NO storage remains insufficient for long-term use.<sup>14,15</sup> An approach that would eliminate limitations resulting from finite NO reservoirs and allow local therapeutic action at the surface of a material is an attractive possibility for improving long-

---

<sup>1</sup> This chapter was reproduced in part with permission from:

Neufeld, M. J.; Harding, J. L.; Reynolds, M. M. Immobilization of Metal-Organic Framework Copper(II) Benzene-1,3,5-Tricarboxylate (CuBTC) onto Cotton Fabric as a Nitric Oxide Release Catalyst. *ACS Appl. Mater. Interfaces* **2015**, *7*, 26742-26750. Copyright 2015 American Chemical Society.  
<http://pubs.acs.org/doi/full/10.1021/acsami.5b08773>

term activity. Thus, the development of materials that do not rely solely on storage of the therapeutic agents within the polymeric matrix and permit generation of therapeutic agents at the material surface overcomes a significant challenge in NO storage and release applications. Previously, Harding et al reported on the ability of copper-based MOFs such as copper(II) benzene-1,3,5-tricarboxylate (CuBTC) to function as heterogeneous NO catalysts when reacted with endogenous RSNO substrates.<sup>16,17</sup> RSNOs are available in the blood at concentrations ranging from 10 to 100  $\mu\text{M}$  and decompose to liberate NO via thermal, pH-mediated, and copper ion-catalyzed pathways.<sup>18-22</sup> The translation of NO-generating MOFs for use in medical devices requires immobilization with a polymeric phase to formulate a composite material. Dispersion of MOF particles throughout the polymeric matrix is a frequently encountered and readily accessible approach.<sup>23,24</sup> However, polymeric encapsulation of the MOFs increases the likelihood of reduced efficacy, because accessibility to the active copper sites is limited by the diffusibility of the RSNO substrates. An alternative approach is to immobilize MOFs on the surface of polymeric substrates, which may improve accessibility to the active sites. Surface immobilization would be useful for preparing filtration membranes, sensor coatings, and extracorporeal devices.<sup>25-28</sup> In particular, the use of a copper-based MOF immobilized on a polymer surface would promote NO release from RSNOs at the biological interface. This has the potential to result in higher surface NO concentrations over time, an outcome that would be beneficial for long-term clinical applications.

The utilization of surface treatments is highly advantageous as it allows for control over the growth of the MOF catalysts. Surface immobilization has been well-studied with preparative techniques including direct and seeded growth, dip-coating, gel synthesis, electrochemical routes, as well as hydrothermal or step-by-step epitaxial growth methods using microwave assistance or membrane diffusion to deposit MOFs onto the surface.<sup>29-35</sup> Although many approaches have been

established, the majority of research has focused on MOF growth from rigid substrates such as gold, silica, and alumina, yet this substrate rigidity limits the applicability of these materials.<sup>36-44</sup> More recently, MOF immobilization has been expanded to include polymeric materials such as polyacrylamide, polyHIPE, polyester, polystyrene, silk, and cotton.<sup>45-49</sup> Although these studies demonstrated that MOFs can be attached to polymeric surfaces, the functional utility of the surfaces for therapeutic applications remains limited. The utilization of cotton-based materials is an attractive option for functionalization due to the natural abundance of this cellulosic fiber. Many of these cotton-based materials are commonly used for development of biomedical materials. Previous reports have looked at modifying cotton fabrics with copper nanoparticles and CuBTC.<sup>50-54</sup> These reports focus on potential antibacterial effects resulting from the copper species acting as a biocide but have yet to utilize the functionalized material for the catalytic production of therapeutic molecules such as NO.

Herein, we demonstrate that immobilization of CuBTC on a cotton substrate produces a material capable of generating NO from the RSNO substrate *S*-nitrosocysteamine (CysamNO). The CuBTC-cotton material was fabricated from commercial cotton functionalized with pendant carboxyl groups for growth of the archetypal MOF CuBTC. This was achieved via alternating immersion in aqueous solutions containing copper(II) acetate and the benzene-1,3,5-tricarboxylic acid ligand precursor. The resulting CuBTC-cotton swatches were characterized by powder X-ray diffraction (pXRD), ATR-IR, and UV-vis spectroscopy. SEM imaging showed excellent surface coverage on individual cotton fibers and uniform crystal growth. Overall, we demonstrate the first report of in situ growth of CuBTC on cotton for catalytic NO generation from RSNOs. As a proof of concept, the work highlights not only further expansion of MOF polymer interfaces, but also demonstrates a meaningful alternative route for the development of supported catalytic systems.

## 2.2 Experimental section

### 2.2.1 Materials

Natural cotton fabric (TIC/400 standard woven cotton) was obtained from SDL Atlas (Rock Hill, SC, USA) and used as received. Copper(II) acetate (98%) and *tert*-butyl nitrite (90%) were purchased from Sigma-Aldrich (St. Louis, MO, USA). Benzene-1,3,5-tricarboxylic acid (BTC) (98%) was purchased from Acros Organics (Somerville, NJ, USA). Sodium chloroacetate (98%) was obtained from Alfa Aesar (Ward Hill, MA, USA). Cysteamine hydrochloride (99.3%) was purchased from Chem-Impex International (Wood Dale, IL, USA). *N,N*-Dimethylformamide (DMF), reagent alcohol, and sodium hydroxide were all purchased from Fisher Scientific (Lafayette, CO, USA). All reagents were used as received without any further purification.

### 2.2.2 Carboxymethylation of cotton fabric

In order to obtain an anchoring point for the deposition of CuBTC onto the cotton fabric, the material was carboxymethylated with sodium chloroacetate in the presence of sodium hydroxide. A 1 M solution of sodium chloroacetate was prepared in 15% w/v sodium hydroxide, and the cotton fabric was immersed in this solution and stirred for 1 h. The resulting carboxymethylated material was thoroughly rinsed with Millipore water ( $3 \times 10$  mL) to remove any non adhered material and allowed to air dry. ATR-IR:  $\nu_{\max}$  ( $\text{cm}^{-1}$ ) 3400 (cellulosic O-H stretches), 2897 (cellulosic C-H stretches), 1590 (C=O stretches), 1110-980 (cellulosic C-O stretches).

### 2.2.3 Surface deposition of copper (II) benzene-1,3,5-tricarboxylate

Copper(II) acetate (1.078 g) was dissolved in 15 mL of Millipore water ( $18.2 \Omega \cdot \text{cm}$ ). Benzene-1,3,5-tricarboxylic acid (0.631 g) was dissolved in 15 mL of equal parts DMF, ethanol, and Millipore water. Cotton samples were immersed in the copper(II) acetate solution for 5 min,

rinsed thoroughly with water, then immersed in the benzene-1,3,5-tricarboxylic acid ligand precursor solution for an additional 5 min. The material was then thoroughly rinsed with water, and the procedure was repeated for a total of eight complete cycles. Afterwards, the samples were sonicated to remove CuBTC, copper(II) acetate, and benzene-1,3,5-tricarboxylic acid that was not directly adhered to the surface. ATR-IR:  $\nu_{\max}$  ( $\text{cm}^{-1}$ ) 3400 (cellulosic O-H stretches), 1644 (CuBTC  $\text{COO}^-$  asymmetric), 1447 (CuBTC C-C stretches), 1343 (CuBTC  $\text{COO}^-$  symmetric stretching), 729 (CuBTC C-H out-of-plane bending).

#### **2.2.4 Characterization techniques**

Images were taken at magnification values of 150 $\times$ , 500 $\times$ , 2000 $\times$ , and 5000 $\times$ , using a JEOL JSM-6500F scanning electron microscope with an accelerating voltage of 20.0 kV and a working distance of 10.1 mm (JEOL USA Inc., MA, USA). All data was processed using Thermo NSS Release candidate 7 software. Powder X-ray diffraction (pXRD) measurements were carried out using a Scintag X2 diffractometer (Scintag Inc., CA, USA) with Cu  $K\alpha$  radiation ( $\lambda = 1.5406 \text{ \AA}$ ), and the resulting data was plotted as intensity vs. theta in Origin Pro. ATR-IR spectra were recorded in the range of 600-4000  $\text{cm}^{-1}$  on a Nicolet 6700 spectrometer (Thermo Electron Corporation, Madison, WI, USA). Absorption experiments were performed using a Nicolet Evolution 300i spectrometer (Thermo Electron Corporation). Surface robustness and durability of the material was evaluated with tensiometer measurements on an Instron 4442 (Instron Industrial Products, Grove City, PA, USA). A Varian (Agilent) SpectrAA 55B (Agilent Technologies, Santa Clara, CA, USA) was used for atomic absorption spectroscopy (AAS) studies.

#### **2.2.5 Determination of weight percent of copper (II) benzene-1,3,5-tricarboxylate**

AAS was used to determine the copper content of the CuBTC-cotton material. This value was subsequently used to calculate the average CuBTC content. This was achieved by suspending

samples of CuBTC-cotton ( $n = 7$ ) in 5 mL of  $3.5 \times 10^{-3}$  M aqueous hydrochloric acid. Samples were then sonicated until the CuBTC crystals had dissolved (30 min) and the fabric returned to its original appearance. The solution was then analyzed for copper content by AAS, and the overall CuBTC content (% w/w) was calculated using the determined copper concentration.

### **2.2.6 Evaluation of structural robustness and durability**

Tensiometer measurements were performed by extension measurements taken of the CuBTC-cotton samples ( $n = 3$ ) cut into dimensions of 28 x 5 mm. Instrumental gauge length was set to  $10 \pm 1$  mm at an extension rate of 2 mm/min. These experiments were repeated for a total of five extension cycles. The resulting material was then evaluated by SEM for any obvious changes to the structural robustness of the composite materials, such as the loss of material and changes to the overall morphology.

### **2.2.7 Chemiluminescence analysis of nitric oxide**

NO release of *S*-nitrosocysteamine (CysamNO) was recorded in real time using a Sievers nitric oxide analyzer (NOA 280i, GE Analytical, Boulder, CO, USA). The instrument was calibrated with nitrogen (zero gas) and 45 ppm NO/nitrogen prior to all experiments. Rates of NO release were determined for NO releasing decomposition of CysamNO samples ( $n = 3$ ) under ambient conditions, in the presence of unmodified cotton fabric as a control experiment. Catalytic NO generation from CysamNO ( $n = 3$ ) was determined by copper-mediated NO release in the presence of CuBTC-cotton fabric. Total NO release was measured for a total time length of 6 h. The resulting NO emission was recorded and used to calculate the total release of NO.

### **2.2.8 Preparation of *S*-nitrosocysteamine**

A stock solution of  $5.0 \times 10^{-2}$  M CysamNO was prepared *in situ* from 5 mg of cysteamine hydrochloride dissolved in 1 mL of Millipore water, followed by the addition of excess ( $1 \times 10^{-4}$

mol) *t*-butyl nitrite. The reaction solution was protected from light and placed in an ice bath at 0 °C. After the reaction proceeded for 15 min, the solution was placed under vacuum to assure complete removal of residual *t*-butyl nitrite. Complete removal of *t*-butyl nitrite was verified using UV-vis spectroscopy by following the disappearance of the characteristic six point absorbance features between 330 and 410 nm. The concentrations of the RSNO solutions were monitored by UV-vis spectroscopy by following the absorbance band at 545 nm ( $\epsilon = 14.5 \text{ M}^{-1} \text{ cm}^{-1}$ ), for CysamNO.

### **2.2.9 Measurement of nitric oxide generation catalyzed by copper (II) benzene-1,3,5-tricarboxylate-cotton swatches**

The catalytic activity of CuBTC-cotton swatches was investigated using CysamNO as the RSNO substrate, and the total amount of generated NO was determined by NOA. CuBTC-cotton swatches were used that contained 1 mg of deposited CuBTC ( $5 \times 10^{-6} \text{ mol Cu}^{2+}$ ). The swatches were immersed in 20 mL of deoxygenated reagent grade alcohol in custom analysis cells connected to the NOA. A gas flow of ultra-high purity nitrogen (200 mL/min flow rate) was maintained to sweep released NO into the NOA, and this release was measured at 1 s intervals. The analysis cell was protected from light at ambient temperature. Initial baseline measurements of CuBTC-cotton swatch in the ethanol were recorded. The reactive CysamNO substrate was injected directly into the reaction medium for a starting solution concentration of  $5 \times 10^{-4} \text{ M}$  ( $1 \times 10^{-5} \text{ mol RSNO}$ ). The reaction was determined to have reached completion once the NO measurement returned to baseline. Control experiments to determine the role of cotton were examined by immersing unmodified cotton into the RSNO ethanol reaction solution. All experiments were performed in triplicate and the average and standard deviation reported for the total NO recovered (mol).

## 2.3. Results and discussion

### 2.3.1 Carboxymethylation of cotton

To immobilize CuBTC on cotton fabric, the material was first functionalized with carboxylate linkers necessary for binding  $\text{Cu}^{2+}$  ions from solution. This was achieved by the base-catalyzed carboxymethylation of cotton fabric with sodium chloroacetate (**Figure 2.1**). Cotton fabric was submerged in the solution and allowed to react for 1 h. Carboxymethylation of the cotton was confirmed by comparison to the IR spectrum of unmodified cotton. The appearance of an absorption peak at  $1590\text{ cm}^{-1}$  for the carboxymethylated material indicates the presence of a C=O stretch corresponding to the incorporation of carboxylate functionalities, confirming the formation of the carboxymethylated cotton (CMC) substrate.

### 2.3.2 Growth and immobilization of copper (II) benzene-1,3,5-tricarboxylate on cotton

Surface immobilization of CuBTC on the CMC substrate was achieved by the alternating immersion of CMC for 5 min intervals in solutions of saturated copper(II) acetate and the BTC ligand, respectively at room temperature (**Figure 2.1**).

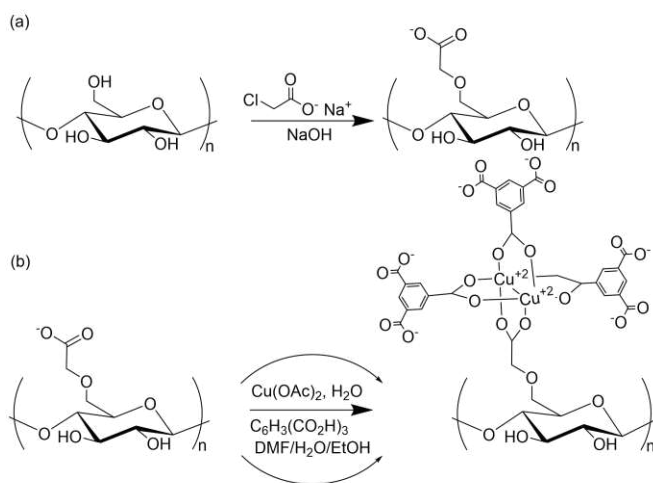


**Figure 2.1.** (a) Carboxymethylation of cotton fabric by submersion into an aqueous solution of sodium chloroacetate and sodium hydroxide (b) proposed mechanism of CuBTC formation and immobilization achieved through alternating submersion of cotton fabric into solutions of copper (II) acetate and 1,3,5-tricarboxylic acid. Reproduced by permission of the American Chemical Society.

The CMC substrate was immersed in the solutions for eight complete cycles. The resulting composite material was thoroughly washed to remove any nonadhered particles by rinsing with ethanol and sonicating until the wash solution was colorless. The resulting cotton fabric was transformed from white to deep blue, which underwent characteristic color changes associated with CuBTC upon dehydration from light to dark blue (Figure 2.2). The uniform dispersion of CuBTC particles on the surface of the cotton fibers was confirmed by the characteristic blue color of the material. These findings were confirmed by X-ray diffraction patterns of the CuBTC-cotton patterns of the CuBTC-cotton fabric corresponding to a superposition of the patterns observed for both crystalline CuBTC particles and cotton (**Figure 2.3**). The presence of the major diffraction peaks associated with CuBTC at 7.8, 9.5, 12, 13.5, 15, 17.8 and 19.3 degrees can be seen in the diffraction pattern of the CuBTC-cotton material. The additional broad diffraction peaks observed between 14-24 degrees are associated with amorphous cotton (**Figure 2.3**).



**Figure 2.2.** (a) Cotton fabric prior to CuBTC growth (b) CuBTC-cotton fabric following growth and cleaning (c) CuBTC-cotton fabric upon dehydration demonstrating the characteristic color change. Reproduced by permission of the American Chemical Society.

Additionally, the ATR-IR spectrum of CuBTC-cotton is consistent with the spectrum of free CuBTC particles where, upon CuBTC deposition, strong absorption bands were observed at 1644  $\text{cm}^{-1}$  ( $\text{COO}^-$ , asymmetric) and 1371  $\text{cm}^{-1}$  ( $\text{COO}^-$  symmetric) vibrations and 728  $\text{cm}^{-1}$  (C-H, out-of-plane bending) corresponding to BTC coordination with copper.<sup>46,55</sup> Taken together, the diffraction patterns and IR spectra clearly confirm the formation and immobilization of CuBTC

on the cotton fabric. Additional evidence of CuBTC growth and immobilization on cotton fabric was verified by diffuse reflectance UV-vis spectroscopy (**Figure 2.4**). Upon the synthesis of CuBTC on the cotton material, an absorbance feature at 704 nm appeared corresponding to the d to d transition band that is characteristic of copper(II) carboxylate complexes (**Figure 2.4**). These findings are consistent with previous reports of CuBTC growth on polymeric substrates.<sup>46,55,56</sup>

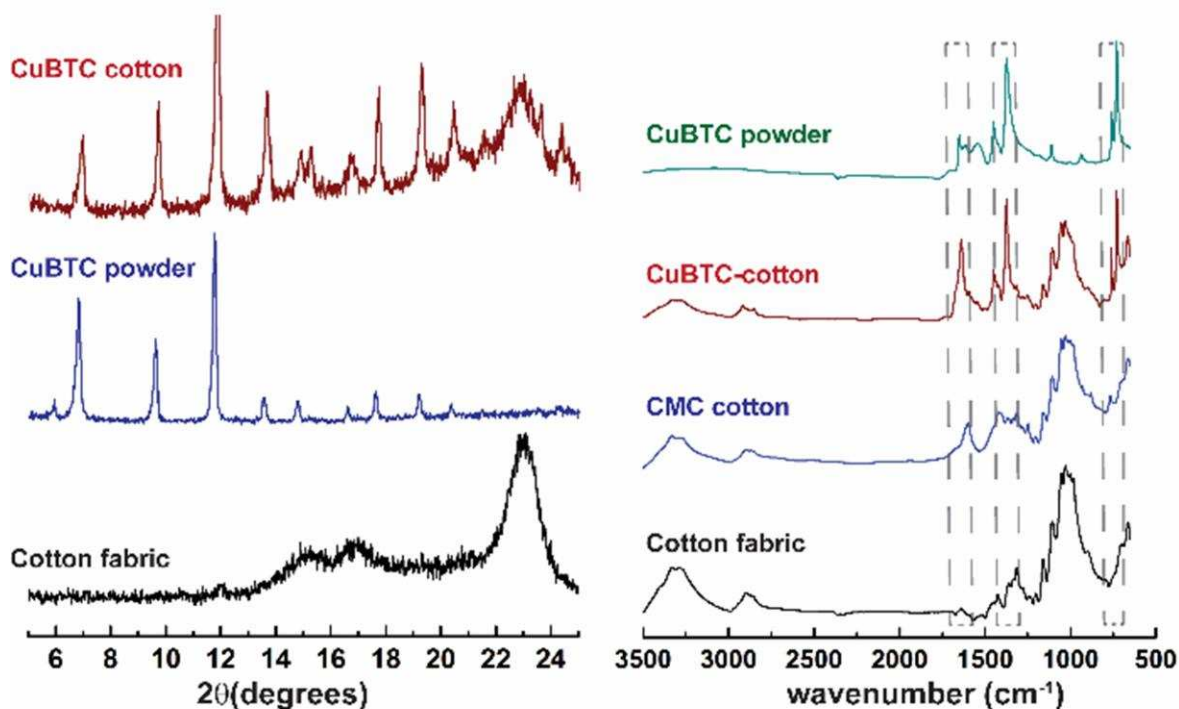


**Figure 2.3** pXRD diffraction patterns show intensity vs. 2 theta of CuBTC powder, CuBTC-cotton and unmodified cotton. ATR-IR spectra show absorbance vs. wavelength of CuBTC powder, CuBTC-cotton material where resonances seen at 1644  $\text{cm}^{-1}$  (C=O), 1371  $\text{cm}^{-1}$  (C-C) and 728  $\text{cm}^{-1}$  (C-H) correlate to CuBTC indicating that deposition was achieved, carboxymethylated cotton where resonances at 1590  $\text{cm}^{-1}$  (C=O) indicating functionalization of cotton and unmodified cotton. Reproduced by permission of the American Chemical Society.

Additionally, elemental analysis by AAS was utilized to determine the overall weight percentage of CuBTC on the composite material from the total copper concentration. The CuBTC content of the material was calculated by weight (to be  $18 \pm 2\%$ ). Collectively, the utilization of pXRD, ATR-IR, UV-vis and AAS techniques has provided indisputable evidence for successful surface immobilization of CuBTC onto the modified cotton fabric.

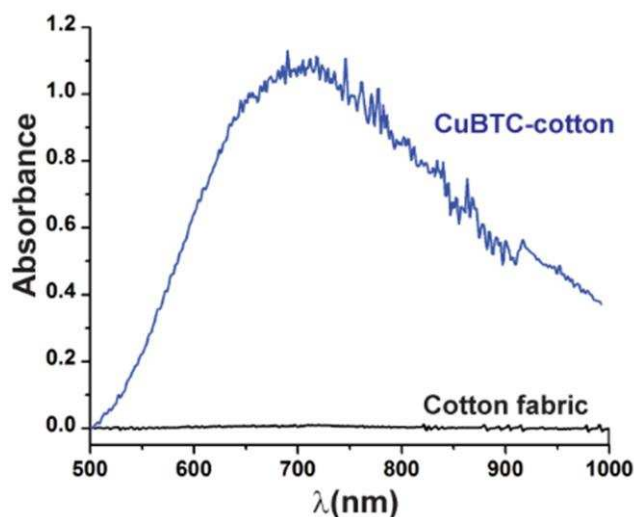


**Figure 2.4** Diffuse reflectance spectra comparing unmodified cotton fabric to blue CuBTC-cotton fabric. The increase of absorbance seen at 704 nm is consistent with the formation of the  $\text{Cu}^{2+}$  carboxylate species in CuBTC. Reproduced by permission of the American Chemical Society.

### 2.3.3 Monitoring the growth and formation of copper(II) benzene-1,3,5-tricarboxylate over successive deposition cycles

The growth and formation of CuBTC on cotton was monitored by diffuse reflectance UV-Vis, ATR-IR and pXRD for each successive cycle. UV-vis measurements were taken every other cycle and were monitored for observed changes in the absorption at 704 nm corresponding to the coordination between  $\text{Cu}^{2+}$  and carboxylate species. As seen in **Figure 2.5**, a continuous increase in the absorption band can be observed at 704 nm, suggesting new CuBTC deposition with each successive cycle. Additionally, IR measurements showed the formation and increase of peak intensities at  $1644\text{ cm}^{-1}$  ( $\text{COO}^-$ , asymmetric),  $1371\text{ cm}^{-1}$  ( $\text{COO}^-$  symmetric) vibrations and  $728\text{ cm}^{-1}$  (C-H, out-of-plane bending) after every additional iteration, corresponding to BTC coordination with copper. Crystal formation was further supported by monitoring the appearance of diffraction peaks at 6.8, 9.5 and 12 degrees, after every successive cycle. These peaks were chosen because they are well-defined CuBTC peaks with little interference from the broad diffraction peaks of the

cotton fabric. After consecutive cycles, the appearance of each diffraction peak became sharper with well-defined peaks observed after the completion of the sixth cycle (**Figure 2.6**). In summary, these results demonstrate continuous CuBTC growth and formation over successive deposition cycles.

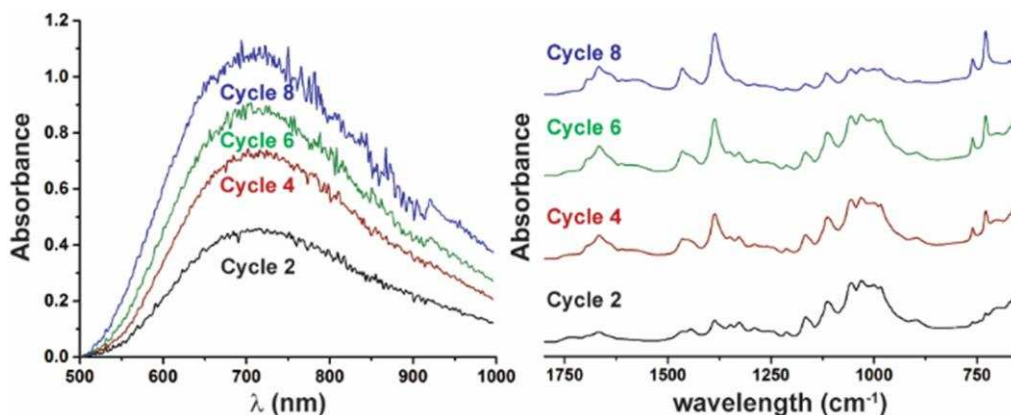


**Figure 2.5** Monitoring of CuBTC growth on cotton fabric (left) diffuse reflectance spectra of the CuBTC-cotton materials after two, four, six and eight cycles showing the increase in absorbance at 704 nm due to the formation of the Cu<sup>2+</sup> carboxylate species in CuBTC. (right) ATR-IR of the CuBTC cotton materials after two, four, six and eight cycles showing the increase in the peak intensities at 1644 cm<sup>-1</sup> (COO<sup>-</sup>, asymmetric), 1371 cm<sup>-1</sup> (COO<sup>-</sup> symmetric) and 728 cm<sup>-1</sup> (C-H, out-of-plane) due to the formation of CuBTC. Reproduced by permission of the American Chemical Society.

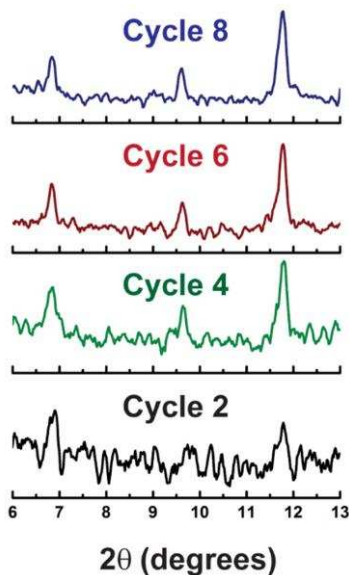


**Figure 2.6** pXRD data obtained during monitoring of CuBTC growth and formation on the cotton fabric. Reproduced by permission of the American Chemical Society.

### 2.3.4 Morphology and surface coverage of copper(II) benzene-1,3,5-tricarboxylate -cotton materials

SEM analysis provided evidence of crystal growth on the surface of the cotton fabric (**Figure 2.7**). Panels a-d in Figure 2.7 show significant changes to the cotton fabric in comparison to the unmodified cotton with uniform crystal growth being seen along the bulk of the material at various magnification intensities. Analysis of the swatches at 500× (**Figure 2.7c**) revealed dense surface coverage of particles with growth along the fibrous strands that comprise the bulk material. This

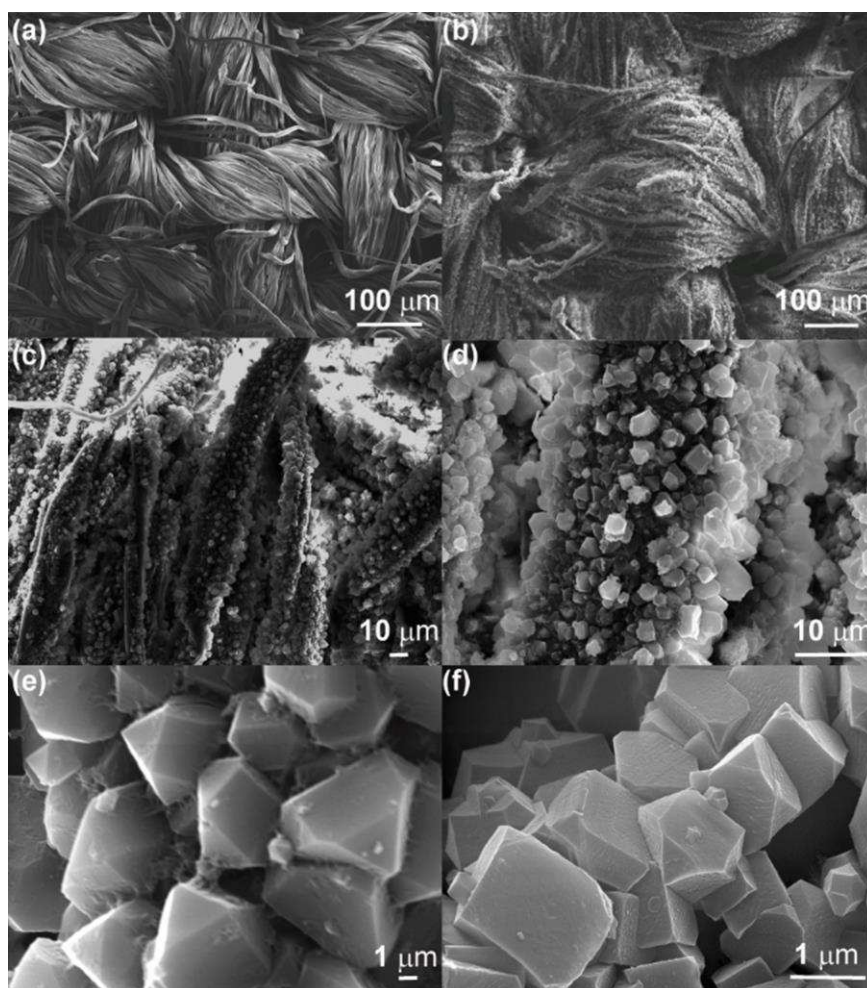


**Figure 2.7** SEM images of unmodified cotton fabric at (a) 100× and CuBTC-cotton fabric at (b) 150× (c) 500× (d) 2,000× (e) 5,000× and (f) 15,000× magnification. These images show excellent surface coverage of the cotton surface as well as the crystalline nature of the MOF in comparison to unmodified cotton. Reproduced by permission of the American Chemical Society.

image clearly shows the formation of well-defined crystal particles along the material surface with a broad range in size. Upon closer examination at 5000× and 15,000× (**Figure 2.7e, f**) each MOF crystal is independently formed and adhered to the substrate. The crystal faces of the MOFs are also clearly defined showing an overall uniform truncated cubic morphology, which is characteristic of CuBTC. The dispersion of the CuBTC particles across the cotton fabric was also

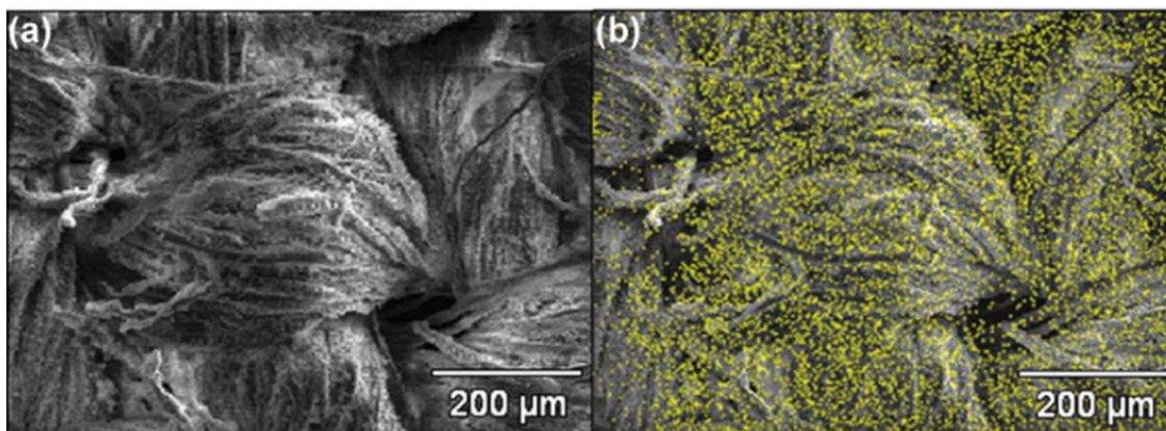


**Figure 2.8** (a) Representative SEM image of CuBTC-cotton material (b) Representative SEM image with EDX overlaid elemental map demonstrating copper distribution on the material as indicated in yellow demonstrating overall uniform distribution of Cu throughout the cotton fabric. Reproduced by permission of the American Chemical Society.

evaluated by SEM-EDX analysis using a copper probe. **Figure 2.8b** shows the EDX image with the copper content overlaid on the SEM image of the CuBTC-cotton material. From this experiment copper is uniformly dispersed over the entire surface area of the analyzed material.

Previous reports of CuBTC immobilization onto cotton show distinct regions of fibers that remain unmodified following the MOF growth process. Excitingly, in contrast, these materials show that the cotton fibers have been completely coated by CuBTC crystal growth. In a prior report, cotton fabric was immersed into a solution of copper(II) acetate for a 24 h time frame. Immediately thereafter, a solution of benzene-1,3,5-tricarboxylic acid was added to the initial solution and allowed to react.<sup>46</sup> Although this technique initially allowed for the fabric to coordinate with Cu<sup>2+</sup> ions, the direct addition of the ligand solution may allow for an increase in

competing CuBTC nucleation sites, ultimately resulting in a decrease in the observed CuBTC immobilization. Excitingly, in contrast, the repeated cycling and immersion in separated MOF precursor solutions limits the potential sites for CuBTC deposition, affording the observed increase in surface immobilization of CuBTC. This dramatic increase in CuBTC surface uniformity is most likely associated with variations in the synthetic procedure.

The integrity of the CuBTC particles adhered to the cotton fabric was evaluated by application of cyclic tensile force applied to the materials. In this study the sustained adhesion of CuBTC particles was investigated by applying a tensile force of 2N. The materials were relaxed and the tensile force was then applied again for a total of 5 cycles. Analysis of the materials by

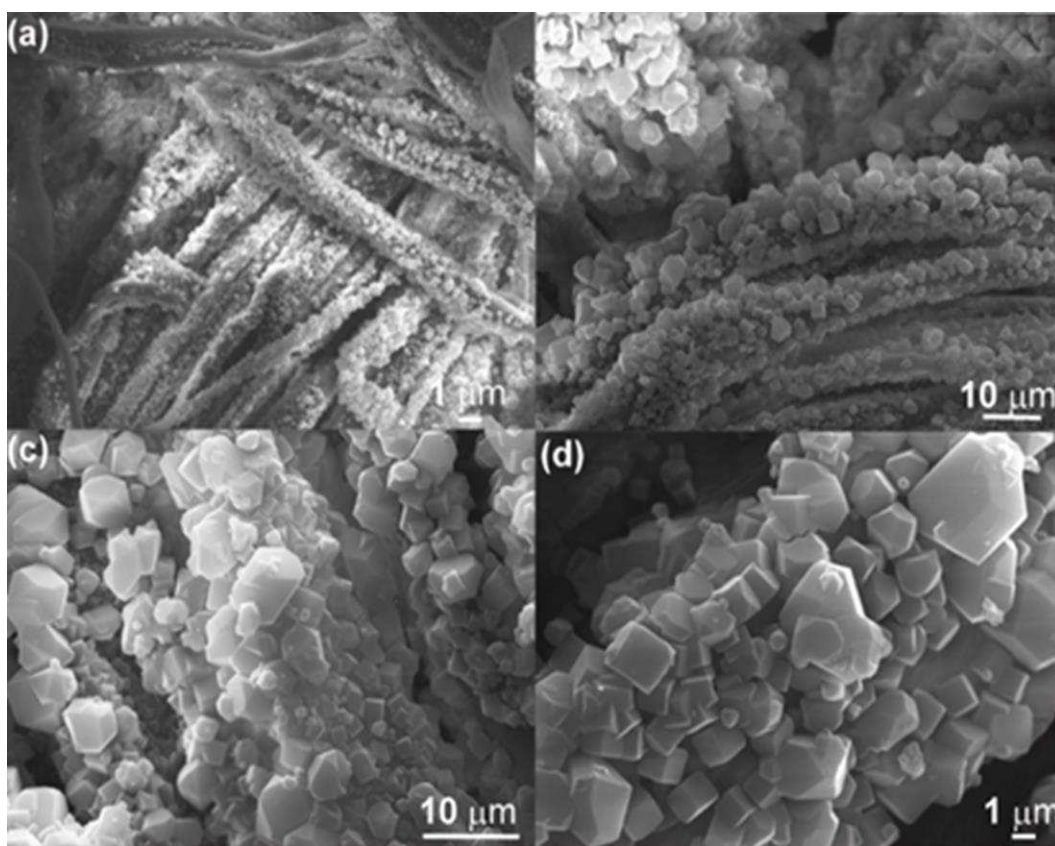


**Figure 2.9.** (a) SEM images of CuBTC-cotton fabric after testing for structural robustness at (a) 500× (b) 1,000× (c) 2,000× (d) 5,000×. Images clearly show no significant changes to the MOF content along the cotton fibers. Reproduced by permission of the American Chemical Society.

SEM found that the particles remained adhered to the substrate without incurring deformations of the crystalline phase after repeated stress was applied to the materials (**Figure 2.9**).

### **2.3.5 Reactivity of copper(II) benzene-1,3,5-tricarboxylate materials toward *S*-nitrosocysteamine for nitric oxide release**

CysamNO hydrochloride was chosen as the substrate for NO generation because it is similar in size to small molecule RSNOs responsible for storage and transport of NO in blood. In addition, CysamNO hydrochloride exhibits sufficient stability to permit reliable characterization of NO release properties as demonstrated previously in our group.<sup>16,17,57</sup> The ability of the functionalized cotton fabric to catalyze NO release from *S*-nitrosothiols, was investigated using a Sievers 280i Nitric Oxide Analyzer. This method is widely utilized for monitoring NO emission through the formation of excited state nitrogen dioxide by reaction between NO and ozone ( $\text{NO} + \text{O}_3 \rightarrow \text{NO}_2^* + \text{O}_2$ ). The excited state nitrogen dioxide subsequently relaxes through chemiluminescence, which can be used to quantify released NO. This specific technique permits highly selective detection of NO. Furthermore, for evaluating NO release as a therapeutic agent, chemiluminescent detection is vital toward measuring instantaneous NO release and total release over time. Although additional techniques including the Greiss assay and electrochemistry are available for NO detection, these methods can be subject to false positives from interfering species.<sup>58</sup> Additionally, the utilization of the Greiss assay relies solely on indirect measurement of NO through the formation of nitrite. Thus by using a chemiluminescence detection technique the decomposition of RSNO and subsequent release of NO was monitored directly. NO release was monitored by recording the concentration of NO released over time using CysamNO in the absence (**Figure 2.10**) and in the presence of CuBTC-cotton catalyst materials (**Figure 2.10**). The concentration of total added CysamNO was determined using the previously reported molar extinction coefficients.<sup>17, 57</sup> In

order to confirm that the observed increase in NO generation was a result of the presence of CuBTC, controls were performed with unmodified fabric and CysamNO. The total NO ( $\mu\text{mol}$ ) released over time is depicted in **Figure 2.11a** for CuBTC-cotton swatches vs. unmodified cotton. After a six h reaction period, CuBTC-cotton material released a total concentration of  $7.1 \pm 1.2 \mu\text{mol NO}$  (**Figure 2.11**). In comparison, the blank solutions released a total concentration of  $0.74 \pm 0.13 \mu\text{mol NO}$ , or 10% of the total NO release observed for the catalytic material, see equation 1. The overall rate of NO generation for CysamNO ( $n=3$ ) in the blank solution (**Figure 2.10**) was  $2.1 \pm 0.31 \text{ (nM s}^{-1}\text{)}$  relative to  $19 \pm 3.0 \text{ (nMs}^{-1}\text{)}$  in the presence of the catalytic material. In short, the CuBTC-cotton material results in a 7 to 9 fold enhancement of NO generation compared to that of the solution without any catalyst.

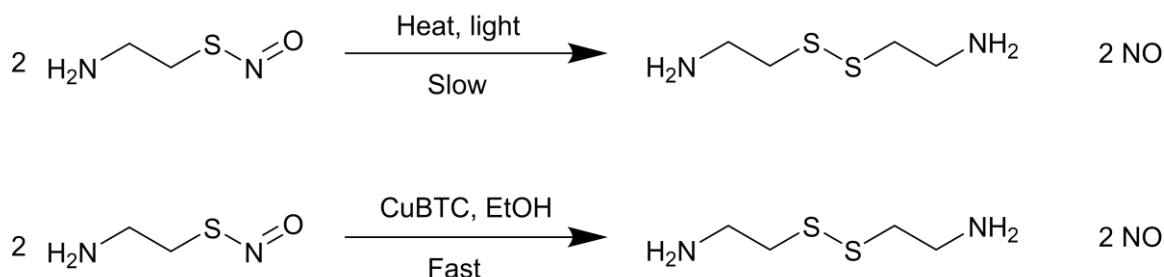


**Figure 2.10** (top) Equation of RSNO decomposition in the presence of heat or light, (control). (bottom) proposed reaction equation for RSNO in the presence of CuBTC. Reproduced by permission of the American Chemical Society.

To confirm that the observed catalytic activity was not due to  $\text{Cu}^{2+}$  chelated to the cotton swatches, we treated the cotton swatches in a copper (II) acetate solution used in the preparation of the CuBTC-cotton swatches. As shown in **Figure 2.11a**, with the copper-cotton swatch, the amount of NO generation was significantly reduced ( $4.3 \pm 0.27 \mu\text{mol}$ ). Upon removal following completion of the reaction, it was observed that the cotton swatches had returned to white. Furthermore analysis of the solution following reaction completion determined by ICP-AES for  $\text{Cu}^{2+}$  was found to range from 200 to 600 nM, whereas with CuBTC-cotton material there was only

trace amounts of  $\text{Cu}^{2+}$  in solution following the reaction, and the MOF particles remained affixed to the cotton substrate. These results indicate that  $\text{Cu}^{2+}$  particles not incorporated into the MOF are removed from the swatch upon reaction with CysamNO. As a result on the basis of the trace

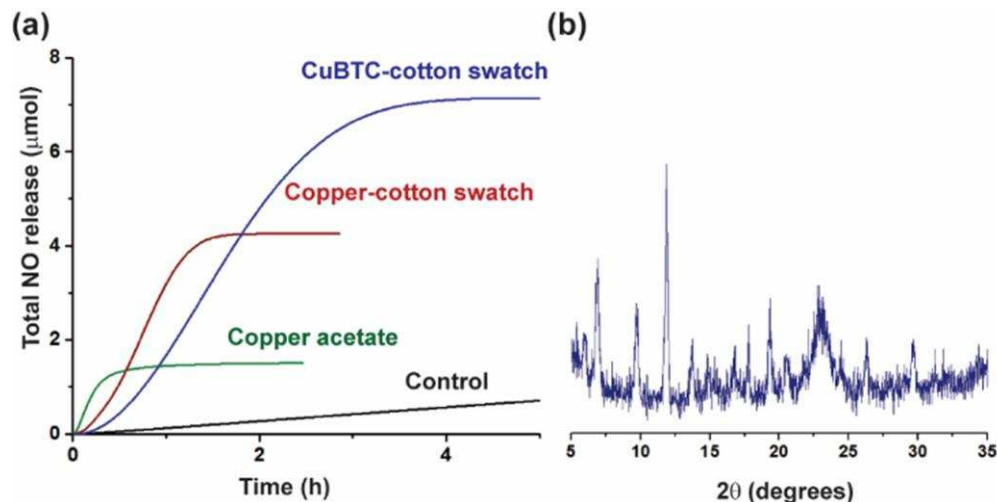


**Figure 2.11** (a) Total NO release ( $\mu\text{mol}$ ) over time for the CuBTC-cotton material (equation 2), copper-cotton material, copper acetate and for the control solutions consisting solely of the corresponding RSNO in solution over time. The CuBTC content of the material was calculated by weight (to be  $18 \pm 2\%$ ). All experiments were repeated in triplicate. (b) CysamNO pXRD data of the swatches after reaction demonstrating that the structural integrity of CuBTC remained intact. Reproduced by permission of the American Chemical Society.

amounts of  $\text{Cu}^{2+}$  in solution, we can conclude that the observed activity of the CuBTC-cotton material is attributed to MOF bound copper particles. A summary of these results can be seen in Table 2.1.

**Table 2.1** Summary of Total NO ( $\mu\text{mol}$ ) and NO Release Rates

| Experiment                            | Total NO ( $\mu\text{mol}$ ) | NO Release Rate ( $\text{nMs}^{-1}$ ) |
|---------------------------------------|------------------------------|---------------------------------------|
| CysamNO                               | $0.74 \pm 0.13$              | $2.1 \pm 0.31$                        |
| Copper acetate <sup>a</sup> + CysamNO | $1.5 \pm 0.53$               | $8.5 \pm 2.9$                         |
| Copper-cotton <sup>a</sup> + CysamNO  | $4.3 \pm 0.27$               | $21 \pm 1.3$                          |
| CuBTC-cotton <sup>a</sup> + CysamNO   | $7.1 \pm 1.2$                | $19.0 \pm 3.0$                        |

<sup>a</sup> Materials were all prepared based on the theoretical copper concentration of the CuBTC-cotton material.

Furthermore, the behavior of the supported catalyst was compared with the release rate of the unsupported catalyst in solution and direct blending. In comparison, the unsupported CuBTC catalyst as a control shows an NO release rate of  $21 \pm 0.86 \text{ nMs}^{-1}$ . Whereas, the cotton-supported

catalyst has a rate of  $19 \pm 3.0 \text{ nM s}^{-1}$  with CysamNO that is the same within experimental error.<sup>17</sup> For an unsupported CuBTC catalyst, the reaction was complete within 90 min. In comparison, the supported CuBTC-cotton catalyst reached reaction completion in roughly 4 h. This observed variation in reactivity may be attributable to the uniform dispersion of unsupported CuBTC throughout the CysamNO solution, whereas immobilization of CuBTC on cotton confines the catalyst to the surface of the cotton fibers. In previous reports where CuBTC was directly blended into a polyurethane matrix, a 90 min induction period was observed, followed by completion of the reaction within 1 h. However, by surface immobilization of the material, a shorter induction period was observed for the CuBTC-cotton materials.<sup>17</sup> These findings provide valuable insight into the potential impact that material processing and development methods can have on catalytic activity.

Lastly, when evaluating NO-generating materials for therapeutic uses, it is imperative for the biomedical community to be able to deliver the relevant NO dose for the intended therapy. As such, there exists a delicate balance regarding the physiological response of the body toward NO, with values in the nM range demonstrating beneficial outcomes (vasodilation, anti-inflammatory, wound-healing).<sup>58</sup> Thus, we see that these materials fall within the range of acceptable values for these therapeutic applications.

### **2.3.6 Evaluation of catalytic lifetime and integrity**

To probe the susceptibility of the catalyst toward degradation under the conditions used in the experiments, we tested the remaining solution was tested for the presence of unbound copper, and the catalytic material itself was evaluated for structural integrity. The possible degradation of the catalysts was monitored after the reaction occurred. ICP-AES was performed on the remaining solution to determine the concentration of any solvated copper and pXRD and UV-vis were

utilized for the catalytic material itself for structural integrity. The diffraction pattern of the reacted CuBTC-cotton material shows that all diffraction peaks corresponding to CuBTC remain present (**Figure 2.11b**). This can be compared to the diffraction pattern of the unreacted material (**Figure 2.3**). UV-Vis measurements following reaction completion provided additional evidence of the retention of structural integrity due to the absence of significant changes to the absorption band at 704 nm and the loss of the absorption band at 335 nm, which correlates to the absence of CysamNO in solution (**Figure 2.12**). Furthermore, analysis of solvated copper ions in the reaction solution using ICP-AES showed that any potential decomposition (>5 nM) of the CuBTC particles was not substantial enough to result in catalysis from the presence of copper. These findings, taken together with copper analysis, suggest that CuBTC retains structural integrity following the reaction with CysamNO.

The demonstrated stability of CuBTC adhered to cotton swatch after the catalytic generation of NO in an ethanol medium supports our claim for the preparation of an NO generating material. However from the perspective of use as a biomaterial stability in biological fluids is imperative. It is well known that upon immersion in an aqueous medium the structural integrity of the Cu-carboxylated paddlewheel is compromised due to displacement of the carboxylates with strongly coordinating water molecules.<sup>59</sup> Interestingly CuBTC is known to exist in a hydrated state (**Figure 2.2**). In consideration of the intended use of the material as an external use only biomaterial in wound healing applications the low moisture environment will limit the degradation of the material while still providing an adequate supply of body fluids to promote NO generation upon contact.

Although the mechanism of catalytic decomposition of RSNOs in the presence of copper ions has been well established, whether or not Cu-based MOFs will operate under the known mechanistic pathways remains an open question.<sup>22</sup> The previously reported mechanism for NO

release from RSNOs in the presence of  $\text{Cu}^{2+}$  ions is suggested to proceed through the formation of five and six membered cyclic intermediates, followed by the catalytic release of  $\text{NO}$ .<sup>22</sup> However, this mechanism seems less feasible due to the hindered environment around these coordinated copper sites. An alternative mechanistic pathway previously reported by the English group describes the use of Cu metal centers as Lewis acid sites for the decomposition of RSNOs resulting in the formation of  $\text{NO}$ .<sup>60</sup> This represents a plausible reaction pathway given the evidence supporting the Lewis acidity of the Cu metal center in CuBTC. Conversely, there have been several reports of the reversible formation of Cu(I/II)-thiolate species in the presence of RSNO.<sup>61</sup> The formation of such a species would suggest an equilibrium between the RSNO decomposition, Cu(I/II)-thiolate formation and resulting disulfide formation. In short, the precise mechanism for conversion of RSNO to  $\text{NO}$  with Cu-based MOFs is unknown at present and, hence, the focus of an ongoing, separate study.

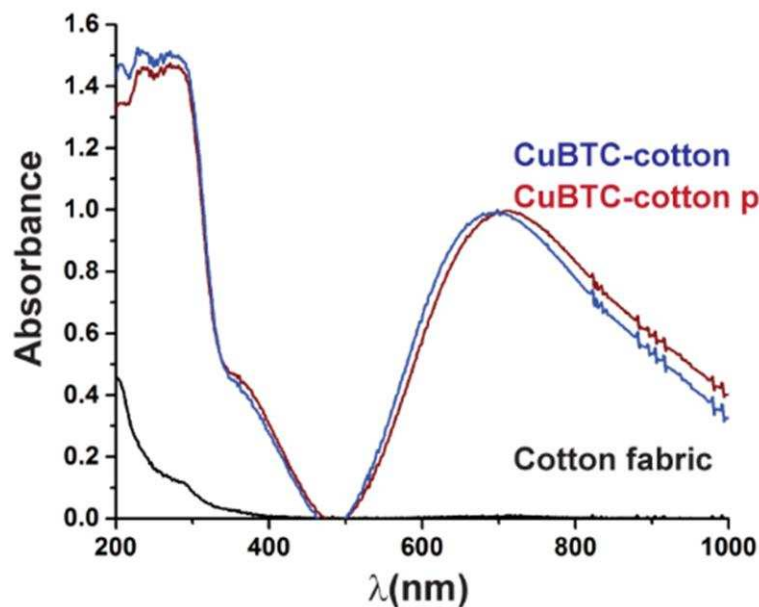


**Figure 2.12** Diffuse Reflectance UV-Vis data showing the spectrum obtained before and after the CuBTC-cotton material was evaluated for catalytic activity with CysamNO. It can be clearly seen that there is no significant decrease in absorbance suggesting the CuBTC species remains intact following reaction completion. Reproduced by permission of the American Chemical Society.

## 2.4. Conclusions

Overall, we have demonstrated the immobilization of Cu-based MOFs on cotton as an alternative approach to produce NO at a surface. The successful deposition of CuBTC crystals were validated by analysis techniques that included, pXRD, ATR-IR, UV-vis and SEM. Notably, excellent surface coverage with well-defined CuBTC crystals was evident on the cotton fibers. The crystals were found to remain intact after mechanical deformation of the material. Subsequent exploration of the material as a supported catalyst for the generation of NO from the NO-donor substrate, CysamNO were also reported. The CuBTC-cotton material demonstrated a reaction rate of  $19.0 \pm 3.0 \text{ nM s}^{-1}$  or a 7-9 fold enhanced generation of NO in comparison to controls. Thus, we have reported a novel material for utilizing Cu-based MOFs for localized NO release via CuBTC immobilization at the material interface without impeding catalytic function. The underdeveloped area of literature regarding multifunctional hard/soft interfaces for catalytic NO generation makes our application particularly impactful. Further development of such materials can allow for a better understanding as to the impact of materials processing on catalytic functionality. Excitingly, these systems have strong potential for clinical applications and further development is currently underway.

## REFERENCES

1. Zhu, H.; Ka, B.; Murad, F. Nitric Oxide Accelerates the Recovery from Burn Wounds. *World J. Surg.* **2007**, *31*, 624-631.
2. Wu, Y.; Zhou, Z.; Meyerhoff, M. E. In vitro Platelet Adhesion on Polymeric Surfaces with Varying Fluxes of Continuous Nitric Oxide Release. *J. Biomed. Mater. Res., Part A* **2007**, *81*, 956-963.
3. Gross, S. S.; Wolin, M. S. Nitric Oxide: Pathophysiological Mechanisms. *Annu. Rev. Physiol.* **1995**, *57*, 737-769.
4. Marletta, M. A. Nitric Oxide: Biosynthesis and Biological Significance. *Trends Biochem. Sci.* **1989**, *14*, 488-492.
5. Witte, M. B.; Barbul, A. Role of Nitric Oxide in Wound Repair. *Am. J. Surg.* **2002**, *183*, 406-412.
6. Bogdan, C. Nitric Oxide and the Immune Response *Nat. Immunol.* **2001**, *2*, 907-916.
7. Al-Sa'doni, H. H.; Ferro, A. S-Nitrosothiols as Nitric Oxide-Donors: Chemistry, Biology and Possible Future Therapeutic Applications. *Curr. Med. Chem.* **2004**, *11*, 2679-2690.
8. Reynolds, M. M.; Hrabie, J. A.; Oh, B. K.; Politis, J. K.; Citro, M. L.; Keefer, L. K.; Meyerhoff, M. E. Nitric Oxide Releasing Polyurethanes with Covalently Linked Diazeniumdiolated Secondary Amine. *Biomacromolecules* **2006**, *7*, 987-994.
9. Seabra, A. B.; Duran, N. Nitric Oxide-Releasing Vehicles for Biomedical Applications. *J. Mater. Chem.* **2010**, *20*, 1624-1637.

10. Jen, M. C.; Serrano, M. C.; van Lith, R.; Ameer, G. A. Polymer-Based Nitric Oxide Therapies: Recent Insights for Biomedical Applications. *Adv. Funct. Mater.* **2012**, *22*, 239-260.
11. McKinlay, A. C.; Morris, R. E.; Horcajada, P.; Ferey, G.; Gref, R.; Couvreur, P.; Serre, C. BioMOFs: Metal-Organic Frameworks for Biological and Medical Applications. *Angew. Chem., Int. Ed.* **2010**, *49*, 6260-6266.
12. Carpenter, A. W.; Schoenfish, M. H. Nitric Oxide Release: Part II. Therapeutic Applications. *Chem. Soc. Rev.* **2012**, *41*, 3742-3752.
13. McKinlay, A. C., Allan, P., Renouf, C. L., Duncan, M.J., Wheatley, P. S., Warrender, S.J., Dawson, D. M., Ashbrook, S. E. M., Gil, B., Marszalek, B., Duren, T., Williams, J. J., Charrier, C., Mercer, D. K., Teat, S. J., Morris, R. E. Multirate Delivery of Multiple Therapeutic Agents from Metal-Organic Frameworks. *APL Mater.* **2014**, *2*, 124108-124115.
14. Horcajada, P.; Chalati, T.; Serre, C.; Gillet, B.; Sebrie, C.; Baati, T.; Eubank, J. F.; Heurtaux, D.; Clayette, P.; Kreuz, C.; Chang, J.-S.; Hwang, Y. K.; Marsaud, V.; Bories, P.-N.; Cynober, L.; Gil, S.; Ferey, G.; Couvreur, P.; Gref, R. Porous Metal-Organic-Framework Nanoscale Carriers as a Potential Platform for Drug Delivery and Imaging. *Nat. Mater.* **2010**, *9*, 172-178.
15. Horcajada, P.; Gref, R.; Baati, T.; Allan, P. K.; Maurin, G.; Couvreur, P.; Ferey, G.; Morris, R. E.; Serre, C. Metal-Organic Frameworks in Biomedicine. *Chem. Rev.* **2012**, *112*, 1232-1268.
16. Harding, J. L.; Reynolds, M. M. Metal Organic Frameworks as Nitric Oxide Catalysts. *J. Am. Chem. Soc.* **2012**, *134*, 3330-3333.

17. Harding, J. L.; Reynolds, M. M. Composite Materials with Embedded Metal Organic Framework Catalysts for Nitric Oxide Release from Bioavailable S-Nitrosothiols. *J. Mater. Chem. B* **2014**, *2*, 2530-2536.
18. Davies KM, Wink DA, Saavedra JE, Keefer LK. Chemistry of the Diazeniumdiolates. 2. Kinetics and Mechanism of Dissociation to Nitric Oxide in Aqueous Solution. *J. Am. Chem. Soc.* **2001**, *123*, 5473-5481.
19. Singh, R. J.; Hogg, N.; Joseph, J.; Kalyanaraman, B. Mechanism of Nitric Oxide Release from S-Nitrosothiols. *J Biol Chem* **1996**, *271*, 18596-18603.
20. Zhang, Y.; Hogg, N. S-Nitrosothiols: Cellular Formation and Transport. *Free Radical Biol. Med.* **2005**, *38*, 831-838.
21. Giustarini, D.; Milzani, A.; Colombo, R.; Dalle-Donne, I.; Rossi, R. Nitric Oxide and S-nitrosothiols in Human Blood. *Clin. Chim. Acta.* **2003**, *330*, 85-98.
22. Dicks, A. P.; Swift, H. R.; Williams, D. L. H.; Butler, A. R.; AlSadoni, H. H.; Cox, B. G. Identification of Cu<sup>+</sup> as the Effective Reagent in Nitric Oxide Formation from S-Nitrosothiols (RSNO). *J. Chem. Soc., Perkin Trans. 2* **1996**, 481-487.
23. Bradshaw, D.; Garai, A.; Huo, J. Metal-Organic Framework Growth at Functional Interfaces: Thin Films and Composites for Diverse Applications. *Chem. Soc. Rev.* **2012**, *41*, 2344-2381.
24. Shekhah, O.; Liu, J.; Fischer, R. A.; Woll, C. MOF Thin Films: Existing and Future Applications. *Chem. Soc. Rev.* **2011**, *40*, 1081-1106.
25. Kreno, L. E.; Leong, K.; Farha, O. K.; Allendorf, M.; Van Duyne, R. P.; Hupp, J. T. Metal-Organic Framework Materials as Chemical Sensors. *Chem. Rev.* **2012**, *112*, 1105-1125.

26. Li, J.-R.; Sculley, J.; Zhou, H.-C. Metal-Organic Frameworks for Separations. *Chem. Rev.* **2012**, *112*, 869-932.
27. Yu, Y.; Ren, Y.; Shen, W.; Deng, H.; Gao, Z. Applications of Metal-Organic Frameworks as Stationary Phases in Chromatography. *TrAC, Trends Anal. Chem.* **2013**, *50*, 33-41.
28. Furukawa, H.; Cordova, K. E.; O'Keeffe, M.; Yaghi, O. M. The Chemistry and Applications of Metal-Organic Frameworks. *Science* **2013**, *341*, 974.
29. Hinterholzinger, F.; Scherb, C.; Ahnfeldt, T.; Stock, N.; Bein, T. Oriented Growth of the Functionalized Metal-Organic Framework CAU-1 on -OH- and -COOH-Terminated Self-Assembled Monolayers. *Phys. Chem. Chem. Phys.* **2010**, *12*, 4515-4520.
30. Liu, B.; Tu, M.; Zacher, D.; Fischer, R. A. Multi Variant Surface Mounted Metal-Organic Frameworks. *Adv. Funct. Mater.* **2013**, *23*, 3790-3798.
31. Zhaung, J. L.; Terfort, A.; Woll, C.. Formation of Oriented and Patterned Films of Metal-Organic Frameworks by Liquid Phase Epitaxy: A Review, *Coordination Chemistry Reviews* **2016**, *307*, 391-424.
32. Schoedel, A.; Scherb, C.; Bein, T. Oriented Nanoscale Films of Metal-Organic Frameworks by Room-Temperature Gel-Layer Synthesis. *Angew. Chem., Int. Ed. Engl.* **2010**, *49*, 7225-7228.
33. Zhuang, J. L.; Ar, D.; Yu, X. J.; Liu, J. X.; Terfort, A. Patterned Deposition of Metal-Organic Frameworks onto Plastic, Paper, and Textile Substrates by Inkjet Printing of a Precursor Solution. *Adv. Mater.* **2013**, *25*, 4631-4635.
34. Tsotsalas, M.; Liu, J. X.; Tettmann, B.; Grosjean, S.; Shahnas, A.; Wang, Z. B.; Azucena, C.; Addicoat, M.; Heine, T.; Lahann, J.; Overhage, J.; Brase, S.; Gliemann, H.; Woll, C.

Fabrication of Highly Uniform Gel Coatings by the Conversion of Surface-Anchored Metal-Organic Frameworks. *J. Am. Chem. Soc.* **2014**, *136*, 8-11.

35. Arslan, H. K.; Shekhah, O.; Wohlgemuth, J.; Franzreb, M.; Fischer, R. A.; Woll, C. High-Throughput Fabrication of Uniform and Homogenous MOF Coatings. *Adv. Funct. Mater.* **2011**, *21*, 4228-4231.

## CHAPTER 3

### WATER-STABLE COPPER(II) BENZENE-1,3,5-TRIS(1*H*-1,2,3-TRIAZOL-5-YL) POLYMER COMPOSITES<sup>2</sup>

#### 3.1 Introduction

Metal-organic frameworks (MOFs) are a versatile class of crystalline materials that consist of organic ligands coordinated to metal centers. Variation of both the organic linker and the incorporated metal has resulted in the development of a wide variety of structurally distinct MOFs that differ in their dimensionality, porosity, and physicochemical characteristics. Due to the diversity in possible MOF architectures and their unique properties, these self-assembled crystalline structures exhibit promise in the areas of gas storage, catalysis, chromatography, sensor applications, and drug delivery.<sup>1-8</sup> The implementation of MOFs in a variety of fields has continued to expand over the past decade. In particular, the use of MOFs as vehicles for the encapsulation and delivery or catalytic generation of small molecule therapeutics has been proposed and investigated for efficacy in such applications. As drug delivery vehicles, the ability of MOFs to encapsulate and release anticancer, antiviral, antiarrhythmic agents, and therapeutic gases such as nitric oxide (NO) has been previously established.<sup>8-19</sup> Certain copper-based MOFs such as copper benzene-1,3,5-tricarboxylate (CuBTC) are able to induce the formation of NO from the catalytic decomposition of *S*-nitrosothiols (RSNOs), which occur naturally in blood.<sup>20, 21</sup> When released from a material as a therapeutic agent, NO is capable of modulating interfacial responses to reduce

---

<sup>2</sup> This chapter was reproduced in part with permission from:

Neufeld, M. J.; Ware, B. R.; Lutzke, A. Khetani, S. R.; Reynolds, M. M. Water-Stable Metal–Organic Framework/Polymer Composites Compatible with Human Hepatocytes. *ACS Appl. Mater. Interfaces* **2016**, *8*, 19343-19352. Copyright 2016 American Chemical Society.  
<http://pubsdc3.acs.org/doi/full/10.1021/acsami.6b05948>

the likelihood of thrombus formation, among other beneficial functions. For this reason, copper-based MOFs have been incorporated within medical grade polymers to create potential blood-contacting biomaterials that produce NO in the presence of endogenous RSNOs. Such materials may be advantageous if used to reduce the risk of thrombus formation in extracorporeal circuits (ECCs) or similar blood-contacting devices. However, important toxicity concerns arise when considering such materials for biomedical applications. CuBTC and many other MOFs are not stable under aqueous, physiological conditions and readily decompose into their constituent organic ligands and metal ions. Consequently, there are concerns regarding the medical use of CuBTC and similar copper-based MOFs due to potential accumulation of toxic levels of copper resulting from decomposition. For this reason, investigation of copper leaching from biomaterials that incorporate copper-based MOFs is a necessary step toward validating their extended use in physiological environments.

To date, the investigation of MOF toxicity has been constrained to MOF particles and their toxic effects on a variety of cell lines. In one example, a magnesium-gallate MOF was assessed for the *in vitro* effects of its decomposition on human promyelocytic leukemia (HL-60), non-small lung cancer (NCI-H460), and murine leukemic monocyte (RAW-264-7) lines.<sup>27</sup> Similarly, *in vitro* toxicity of lanthanide-based MOFs was assessed using human colon adenocarcinoma (HT-29) and with acute lymphoblastic leukemia human cells.<sup>28</sup> Furthermore, a recent report evaluated 14 different MOFs consisting of iron, zinc, and zirconium carboxylates or imidazoles for their effects on fetal cervical carcinoma (HeLa) and murine macrophage cell lines (J774).<sup>29</sup> Another study examined a zinc-based MOF loaded with busulfan on mouse bone marrow fibroblasts (3T3), mouse breast tumor cell (4T1), human lung cancer cell (A549), and human liver cancer cell (HepG2) lines.<sup>30</sup> To the best of our knowledge, only four reports of *in vivo* experiments exist to

date, including two by Horcajada and colleagues that evaluated toxicity effects of a series of iron-carboxylate based MOFs.<sup>31,32</sup> Kundu and colleagues evaluated toxicity of a gadolinium-based MOF for anticancer drug delivery on murine models.<sup>33</sup> Another report from Ruyra and colleagues investigated the toxicity of nine different MOFs on zebrafish embryos.<sup>34</sup> In general, these studies have focused on evaluating toxicity on mutated cells as drug carriers as well as the short-term interaction of MOF particles with cells assessed through cell viability, metabolism, penetration, and excretion. However, there are few published data that investigate the incorporation of MOFs into biomedical grade polymers and the resulting cytocompatibility of such materials over an extended duration.

Longer-term use of MOFs as components of polymer-based biomaterials requires prolonged exposure to a physiological environment. Therefore, it is crucial that MOFs intended for such purposes are comprehensively evaluated to either ensure their degradation into nontoxic (or low-toxicity) components or confirmed to retain their structural integrity in a biological environment. In the case of copper-based MOFs used to produce NO from RSNO substrates, this goal is best achieved through both improved MOF stability under physiological conditions (reducing the likelihood of degradation) and appropriate toxicological assessment. While the carboxylate linkers present in CuBTC result in insufficient stability for long-term use, nitrogenous heterocycles are capable of forming exceptionally stable complexes with copper.<sup>35</sup>

One such MOF developed by Long et al. is  $H_3[(Cu_4Cl)_3-(BTri)_8]$  (CuBTTri), where the triazole 1,3,5-tris(1*H*-1,2,3-triazol-5-yl)benzene) ( $H_3BTri$ ) serves as the coordinating ligand (**Figure 3.1**).<sup>36</sup> CuBTTri exhibits high stability in organic solvents, boiling water, PBS, and importantly, whole blood.<sup>21</sup> Furthermore, CuBTTri is capable of enhancing the rate of NO release from RSNOs similarly to CuBTC.<sup>21</sup> As a result, CuBTTri is a promising candidate for potential

biomedical applications. We have tested a material formulation in which CuBTri was incorporated within a mixture of poly(vinyl chloride) (PVC) and dioctyl sebacate (DOS) plasticizer to mimic the proprietary composition of medical grade Tygon® used in ECCs. This formulation was used to prepare plasticized PVC films containing CuBTri, which were

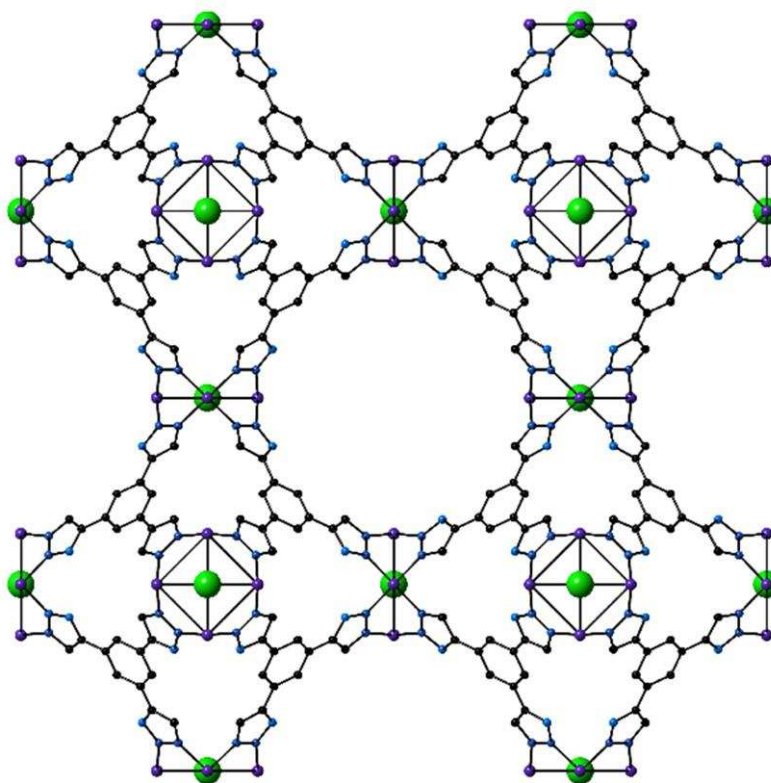


**Figure 3.1** A portion of the structure of the sodalite framework of CuBTri. Copper (purple), chlorine (green), carbon (black), and nitrogen (blue) atoms are depicted in the structure. Hydrogen atoms have been omitted for clarity. Reproduced by permission of the American Chemical Society.

subsequently characterized by PXRD, ATR-FTIR, and SEM-EDX analysis. Additionally, the composite CuBTri/polymer films were assessed for their ability to enhance NO generation from *S*-nitroso-*N*-acetyl-*D*-penicillamine (SNAP). The films were then monitored for copper leaching under physiological conditions over 4 weeks, and monitored for adverse effects *in vitro* on 3T3-J2 fibroblasts and primary human hepatocytes (PHHs) to assess both general cytotoxicity and hepatotoxicity of the composite material. This is the first report to explore the potential cellular

toxicity of a copper-based MOF/polymer formulation intended for blood-contacting medical applications.

## **3.2 Experimental details**

### **3.2.1 Materials**

All reagents and solvents were purchased from commercial vendors and used without further purification unless otherwise noted. 1,3,5-Tribromobenzene (98%), trimethylsilylacetylene (98%), trimethylsilyl azide (94%), diethylamine (99%), and dioctyl sebacate (95%) were purchased from Alfa Aesar (Ward Hill, MA, USA). Copper(I) iodide (99.5%) and PVC were purchased from Sigma-Aldrich (St. Louis, MO, USA). Copper(II) chloride dihydrate was purchased from EMD Chemicals (Gibbstown, NJ, USA). Bis(triphenylphosphine)palladium(II) dichloride (98%) was obtained from TCI America (Portland, OR, USA). Ultrahigh purity N<sub>2</sub> and O<sub>2</sub> gases were supplied by Airgas (Denver, CO, USA). Tissue culture polystyrene 24-well plates and phosphate buffered saline (PBS) were purchased from Corning Life Science (Tewksbury, MA, USA). The cryopreserved PHHs used in this study were from the HUM4055A donor (54 year old Caucasian female who died of stroke) purchased from Triangle Research Laboratories (Research Triangle Park, NC, USA). Murine embryonic 3T3-J2 fibroblasts were a gift from Howard Green (Harvard Medical School).<sup>37</sup> Components for the culture medium for each cell type were purchased from Corning Life Sciences and Sigma-Aldrich unless noted otherwise. NucBlue® and propidium iodide LIVE/DEAD stain was obtained from Life Technologies (Carlsbad, CA, USA).

### **3.2.2 Characterization techniques**

Images were taken at magnification values of 1000× and 2500×, using a JEOL JSM-6500F scanning electron microscope with an accelerating voltage of 20.0 kV and a working distance of 10.1 mm (JEOL USA Inc., Peabody, MA, USA). All data was processed using TEAM Software.

Powder X-ray diffraction measurements were carried out using a Scintag X2 diffractometer (Scintag Inc., Cupertino, CA, USA) with Cu K $\alpha$  radiation ( $\lambda = 1.5406 \text{ \AA}$ ), and the resulting data were plotted as intensity vs. theta in Origin Pro. ATR-FTIR spectra were recorded in the range of 600-4000  $\text{cm}^{-1}$  on a Nicolet 6700 spectrometer (Thermo Electron Corporation, Madison, WI, USA). Phase contrast and fluorescent images of cell cultures were acquired using the EVOS<sup>®</sup> FL Imaging System (Thermo Fisher Scientific, Carlsbad, CA, USA). Absorbance of samples was measured using the Synergy H1 multimode reader (BioTek, Winooski, VT, USA).

### **3.2.3 Copper(II) benzene -1,3,5-tris(1*H*-1,2,3-triazole-5-yl) synthesis**

H<sub>3</sub>BTTri was synthesized following a previously reported method.<sup>36</sup> To prepare the MOF, 225 mg H<sub>3</sub>BTTri was suspended in 40 mL of DMF and the solution was adjusted to pH 4 using dilute hydrochloric acid to dissolve the compound. In a separate vial, CuCl<sub>2</sub>·2H<sub>2</sub>O was dissolved in 10 mL of DMF and added to the triazole solution. The mixture was then heated at 100 °C for 3 days. During this period, a crystalline violet precipitate formed and was isolated by centrifugation and washed thoroughly with water. The powder was then suspended in water and heated at 100 °C for 24 h. The mixture was filtered, washed with water, and allowed to air dry for several days. The resulting fine light purple crystals were characterized by PXRD to confirm formation of the product (**Figure 3.2**).

### **3.2.4 Preparation of copper(II) benzene -1,3,5-tris(1*H*-1,2,3-triazole-5-yl)/polymer films**

Composite films were prepared from 150 mg/mL solutions of 3:1 high molecular weight PVC and DOS in 60 mL of THF. CuBTTri was ground by mortar and pestle until visually uniform, and, then suspended in a solution of PVC/DOS in THF at concentrations of either 0.1 or 0.5% w/v. In a typical procedure, the solution was agitated vigorously for 1 min followed by 10 min of sonication at room temperature. This resulted in the formation of a visually well-dispersed

solution. Immediately after sonication, the solution was slowly pipetted into a glass mold. The solution was then covered and allowed to cure. Upon complete curing ( $\geq 10$  h), the films were punched into 13 mm diameter disks.

### 3.2.5 Copper leaching analysis

The stability of the CuBTTri composite materials was evaluated by immersing composite films in 5 mL of PBS or cell culture medium and incubating at 37 °C with constant agitation. For the first week, the solution was removed and replaced with an equivalent volume of PBS or cell culture medium every 24 h. For the remaining 3 weeks, the solutions were removed and replaced with an equivalent volume every 7 days. The concentration of copper present in the samples was determined by ICP-OES analysis.

### 3.2.6 Chemiluminescence-based analysis of nitric oxide

NO release from SNAP was recorded in real time using a Sievers nitric oxide analyzer (NOA 280i, GE Analytical, Boulder, CO, USA). The instrument was calibrated with ultrahigh purity nitrogen (zero gas) and 45 ppm NO/balance nitrogen prior to all experiments. A gas flow of UHP nitrogen (200 mL/min) was maintained to sweep released NO into the NOA, and this release was measured at 1 s intervals.

### 3.2.7 Preparation of *S*-nitroso-*N*-acetylpenicillamine

1.00 g (5.2 mmol) of *N*-acetyl-*D*-penicillamine was suspended in 20 mL of 1 M hydrochloric acid, followed by the addition of 0.451 g (6.5 mmol) of sodium nitrite. The mixture was stirred rapidly at 0°C for 40 min, then filtered and washed thoroughly with 5 x 20 mL Millipore water, 20 mL acetone, and 20 mL diethyl ether. The resulting green powder was placed under vacuum (0.1 Torr) for 3 h to remove residual solvent. The overall yield of SNAP was 54%:  $\lambda_{\max}$  340 ( $\pi \rightarrow \pi^*$ ), 591 ( $n \rightarrow \pi^*$ ) nm.

### **3.2.8 Measurement of nitric oxide generation**

The ability of the CuBTri/polymer films to enhance the rate of NO generation from RSNOs was investigated using SNAP. CuBTri/polymer films were punched into 13 mm disks and immersed in 2 mL pH 7.4 PBS in custom analysis cells connected to the NOA and protected from light at ambient temperature. SNAP was injected directly into the PBS solution at an initial concentration of 2.0 mM (4.0  $\mu$ mol total RSNO). The resulting CuBTri-accelerated SNAP decomposition was allowed to proceed for a total of 24 h, and the formation of NO was measured during this period. Control experiments were performed in the absence of CuBTri/polymer films to establish the baseline level of NO release from SNAP. Total NO release was measured for a duration of 24 h. The resulting NO emission was recorded and used to calculate the total release of NO. All experiments were performed in triplicate, and the mean  $\pm$  standard deviation reported for total recovered NO (mol). Following each experiment, the PBS solution was analyzed for trace copper content by ICP-OES.

### **3.2.9 Cell studies**

The 3T3-J2 murine embryonic fibroblasts were passaged in T-150 tissue culture flasks for up to 12 times as previously described.<sup>38</sup> Cells were plated at 90,000 per well in a standard tissue culture treated 24-well plate with culture medium change every 2 days. Cryopreserved PHHs were purchased from Triangle Research Laboratories (Research Triangle Park, NC), a vendor permitted to sell products derived from human organs procured in the United States by federally designated Organ Procurement Organizations. All studies were conducted using the HUM4055A donor (see Materials). PHH vials were thawed at 37°C for 120 s and diluted with 25 mL of prewarmed hepatocyte seeding medium, the formulation of which was described previously.<sup>39</sup> The cell suspension was then spun at 500 rpm for 10 min, the supernatant was discarded, the cells were

resuspended in fresh hepatocyte seeding medium, counted, and plated. PHH viability was assessed using trypan blue exclusion (typically 80-95%). Liver-derived nonparenchymal cells were consistently found to be less than 1% of all the cells.

Micropatterned cocultures (MPCCs) were created as previously described.<sup>39</sup> Briefly, adsorbed collagen was lithographically patterned in each well of an industry standard 24-well plate to create 500  $\mu\text{m}$  diameter circular domains spaced 1200  $\mu\text{m}$  apart, center-to-center. PHHs selectively attached to the collagen domains leaving ~30,000 attached cells on ~90 collagen-coated islands within each well of a 24-well plate. 3T3-J2 murine embryonic fibroblasts were seeded 18 to 24 h later in each well to create MPCCs. Serum-supplemented culture medium, the formulation of which has been described previously, was replaced on cultures every other day (300  $\mu\text{L}$ /well).<sup>40</sup> Cellular morphology was observed using an EVOS-FL microscope (Thermo Fisher).

### **3.2.10 Liver functionality assays**

Urea concentration in supernatants was assayed using a colorimetric endpoint assay utilizing diacetyl monoxime with acid and heat (Stanbio Labs, Boerne, TX, USA). Albumin levels were measured using an enzyme-linked immunosorbent assay (MP Biomedicals, Irvine, CA, USA) with horseradish peroxidase detection and 3,3',5,5'-tetramethylbenzidine (TMB, Fitzgerald Industries, Concord, MA, USA) as the substrate.<sup>38</sup>

### **3.2.11 Copper(II) benzene -1,3,5-tris(1*H*-1,2,3-triazole-5-yl)/polymer films toxicity assays on fibroblasts and micropatterned co-cultures**

Fibroblast-only cultures were allowed 3 days to stabilize, while MPCCs were allowed ~2 weeks to stabilize prior to incubations with films. Throughout the duration of the studies, the media was changed on the cultures every other day. After the stabilization period, the CuBTTri/polymer films (0%, 0.1%, and 0.5%) were sterilized in 70% ethanol, rinsed in sterile ddH<sub>2</sub>O, and placed in

the culture medium with the cells. Albumin and urea secretions were assayed in the supernatants that were collected at each media change. The LIVE/DEAD staining (see Materials) on fibroblasts was carried out according to manufacturer instructions.

### 3.3 Results and discussion

#### 3.3.1 Synthesis and characterization

The CuBTTri ligand was synthesized according to a previously reported procedure.<sup>36</sup> In brief, 1,3,5-tris((trimethylsilyl)ethynyl)benzene was prepared from the Sonogashira coupling of 1,3,5-tribromobenzene and trimethylsilylacetylene in diethylamine. This intermediate was purified via column chromatography (silica gel) and subsequently deprotected by rapid stirring in a biphasic mixture of DCM, methanol, and aqueous sodium hydroxide. The resulting 1,3,5-triethynylbenzene was converted to 1,3,5-tris(1*H*-1,2,3-triazol-5-yl)benzene through the copper-catalyzed azide-alkyne reaction with trimethylsilyl azide in DMF/methanol. After isolation of the triazole ligand, the MOF was synthesized by reaction with CuCl<sub>2</sub>·2H<sub>2</sub>O for 3 days at 100 °C. After work-up, CuBTTri was obtained as a light purple powder.

Once synthesized, the MOF was characterized using PXRD (**Figure 3.2a**) and ATR-FTIR (**Figure 3.2b**). PXRD was found to match the previously reported diffraction pattern.<sup>21,36</sup> CuBTTri was then incorporated into a mixture of dissolved 3:1 PVC and DOS plasticizer in THF. The resulting MOF/composite material was then characterized using ATR-FTIR to confirm the incorporation of the MOF within the polymeric material. Figure 3.2 shows the ATR-FTIR spectrum obtained for CuBTTri powder, CuBTTri/polymer composite, and PVC:DOS control film. The IR spectrum of CuBTTri features characteristic peaks at 1614 (aromatic C=C), 830, and 770 cm<sup>-1</sup> (C-H out-of-plane bends). When incorporated within the polymer matrix, the absorptions from CuBTTri are predictably diminished, however all three diagnostic bands remain discernible.

Additional IR features appear at 1723 (C=O stretch), 1252, and 1174  $\text{cm}^{-1}$  (C-O stretches) from DOS. Furthermore, the PXRD pattern obtained for the MOF/polymer film retained the characteristic peaks of CuBTTri, suggesting that the MOF remained intact.

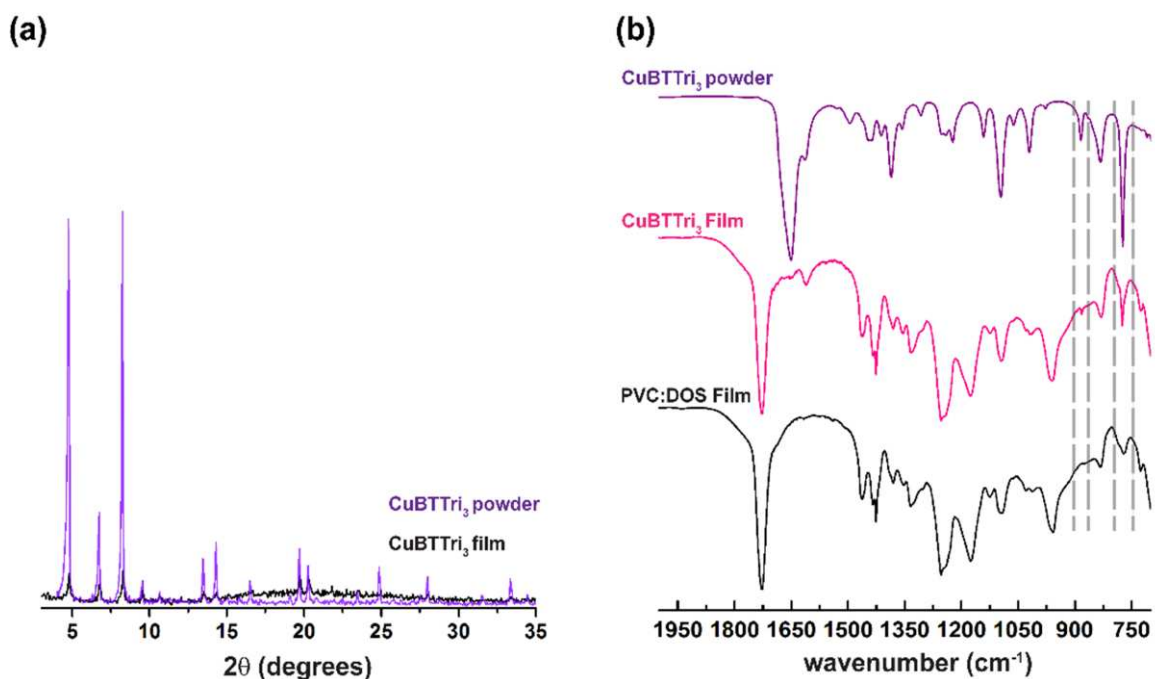


**Figure 3.2** (a) PXRD diffraction pattern of CuBTTri powder and CuBTTri/polymer films. Key diffraction peaks  $2\theta$ : 4.7, 6.7, 8.2, 9.5, 10.7, 13.5, 14.3, 16.5, 19.7, 20.3, 25, 28, and 33. (b) ATR-FTIR spectrum for CuBTTri powder and CuBTTri/polymer film and PVC:DOS polymer films. Key characteristic peaks are highlighted and can be observed at 1614 (aromatic C=C), 830, and 770  $\text{cm}^{-1}$  (C-H out-of-plane bends). Reproduced by permission of the American Chemical Society.

Examination of the CuBTTri/polymer film by SEM analysis provided additional evidence that CuBTTri was successfully incorporated into the polymeric material. As shown in Figure 3.3, the majority of the MOF particles are directly embedded within the polymeric matrix. The dispersion of the MOF particles within the polymeric material was evaluated by SEM-EDX analysis using a copper probe. Figure 3.3a-e shows SEM images for a control PVC:DOS film, 0.1% and 0.5% CuBTTri/polymer films with copper content (EDX) overlaid on the SEM image of the CuBTTri/polymer material in Figures 3.3c and e. From this experiment it can be observed

that the copper content is distributed over the entire area of the material and is concentrated in the areas containing the crystalline MOF.

### 3.3.2 Nitric oxide release analysis

NO has received significant attention due to its multiple biological functions, including anti-inflammatory, antibacterial, and antiplatelet activation properties.<sup>41,42</sup> NO also has an important role in the normal function of the endothelium, where it is known to exert protective antithrombotic effects.<sup>43</sup> The use of NO as an exogenous therapeutic agent has been well established, and NO

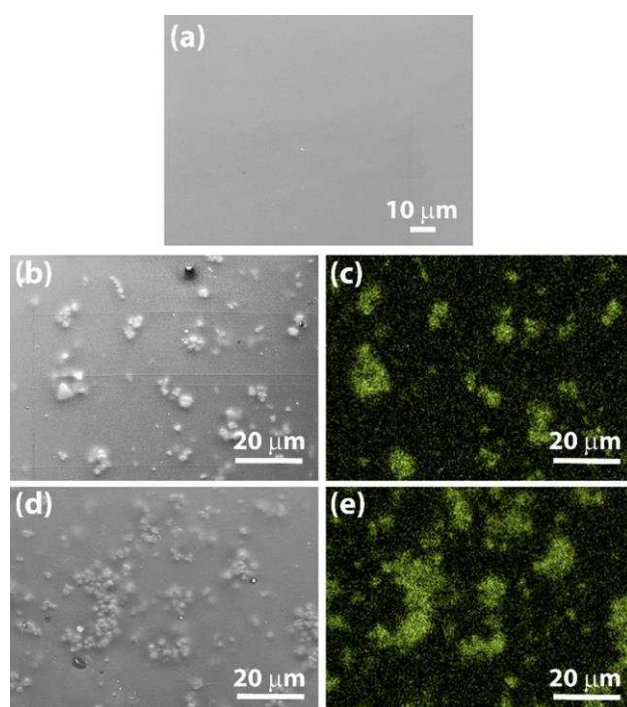


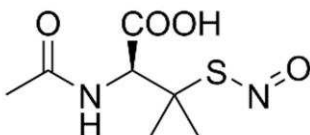
**Figure 3.3** (a) 1000× magnification for control film. (b) 1000× for 0.1% CuBTri/polymer film. (c) 1000× for 0.1% CuBTri/polymer film with EDX overlay for copper analysis containing copper in the films concentrated at the areas containing the crystalline materials. (d) 1000× for 0.5% CuBTri/polymer film. (e) 1000× 0.5% CuBTri/polymer film with EDX overlay for copper analysis on 0.5% CuBTri/polymer film with copper concentrated at the areas containing the crystalline materials. Reproduced by permission of the American Chemical Society.

release has been widely used as a method of improving the performance of blood-contacting materials by reducing the likelihood of thrombosis or by acting as an antimicrobial agent to lower the risk of infection. As previously stated, certain copper-based MOFs such as copper benzene-

1,3,5-tricarboxylate (CuBTC) are able to induce the NO-forming catalytic decomposition of RSNOs, which occur naturally in the blood.<sup>20, 44</sup> This method presents an opportunity for continuous NO generation using MOF particles to initiate the accelerated decomposition of endogenous RSNO.

The ability of water-stable CuBTTri/polymer films to increase the rate of NO release from SNAP was assessed using chemiluminescence-based detection of NO. Like the majority of reported RSNOs, SNAP (**Figure 3.4**) is unstable in aqueous solution and continuously decomposes to form NO. It has been previously observed that this baseline rate of NO release can be significantly accelerated in the presence of CuBTTri. Prior work by Williams and others has

(a)



S-Nitroso-N-acetyl-D-penicillamine

(b)

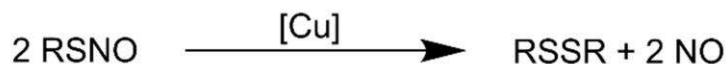


**Figure 3.4** (a) Structure of SNAP (b) proposed scheme of *S*-nitrosothiol (RSNO) decomposition in the presence of copper, resulting in the formation of NO and the corresponding disulfide (RSSR). Reproduced by permission of the American Chemical Society.

proposed that copper ions form five- and six-membered cyclic intermediates with RSNOs to catalytically initiate their NO-forming decomposition, according to the overall reaction depicted in Figure 3.4b.<sup>45-47</sup> This process is considered less feasible at hindered copper sites within the lattice of copper-containing MOFs, and alternative pathways involving Lewis acid-type catalysis or the formation of intermediate copper(I/II)-thiolates have been suggested.<sup>48,49</sup> However, the

mechanism by which copper-based MOFs initiate the accelerated decomposition of RSNOs remains under investigation. To demonstrate this acceleration in the case of CuBTTri/polymer films, the increased rate of NO release after exposure of SNAP to the MOF films was examined.

When SNAP (2 mM initial concentration) was exposed to films prepared from 0.5% (w/v) CuBTTri/polymer solution in 2 mL of pH 7.4 PBS at ambient temperature over 24 h, a noticeable increase in NO production was observed relative to the baseline release of SNAP in the absence of the films (**Figure 3.5**). In the presence the CuBTTri/polymer film, NO release was observed to increase over time, with NO generation reaching a steady level after approximately 10 h. This

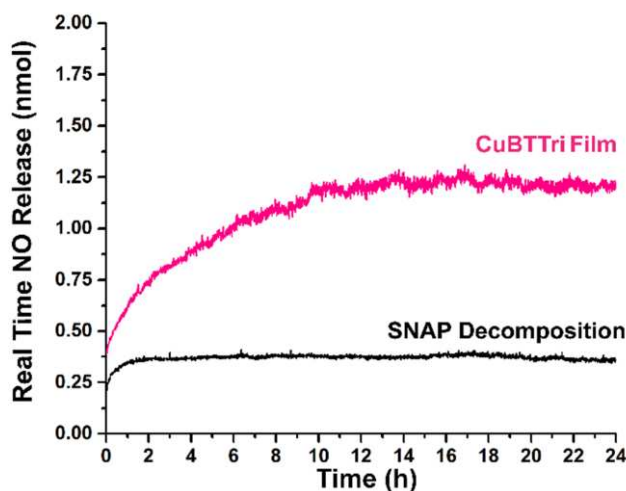


**Figure 3.5** Real time NO release over 24 h from SNAP decomposition (heat and light) in the absence of CuBTTri and SNAP in the presence of the CuBTTri/polymer films (PBS, pH 7.4, 22 °C). This figure depicts the enhanced generation of NO from the addition of the CuBTTri material with the generation reaching a steady level at approximately 10 h. Reproduced by permission of The American Chemical Society.

increase in NO production may arise from the diffusion of SNAP into the polymeric material prior to interaction with the MOF particles. The presence of the CuBTTri/polymer film was determined to result in an average total NO release of  $3.13 \pm 0.34 \mu\text{mol}$  over 24 h, corresponding to the release of  $70 \pm 7\%$  of theoretical NO. In comparison, SNAP decomposition in the absence of the CuBTTri/polymer material was found to result in an average total NO release of  $1.07 \pm 0.18 \mu\text{mol}$  ( $23 \pm 4\%$  of theoretical NO). It was observed that the CuBTTri/polymer films continued to

generate NO at a steady level at the 24 h time point. These findings show that the presence of the CuBTTri/polymer films results in a nearly 300% increase in NO generation over 24 h when compared to baseline SNAP decomposition.

Figure 3.6 depicts the real-time NO flux observed for the CuBTTri/polymer films, with the dashed line representing the average physiological NO flux for endothelial cells. The mean NO flux of the CuBTTri/polymer films was determined to be  $0.90 \pm 0.13 \text{ nmol cm}^{-2} \text{ min}^{-1}$  after reaching a steady level. This NO flux can be compared to that exhibited by the endothelium, which

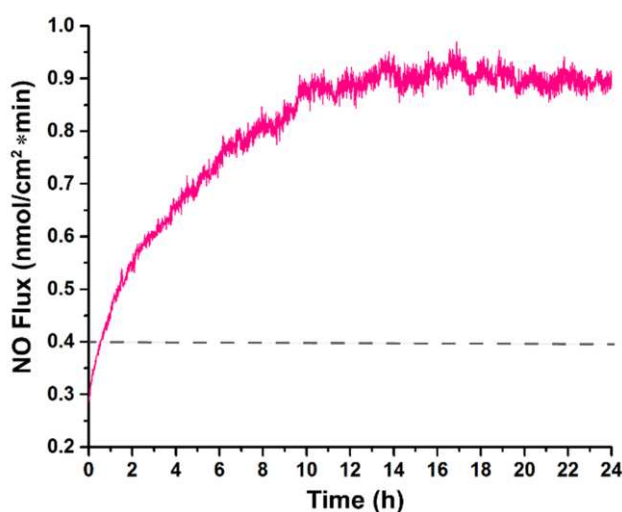


**Figure 3.6** Real time NO flux observed for CuBTTri/polymer films (PBS, pH 7.4, 22 °C). The dotted line represents the physiological NO flux that is seen in endothelial cells. The average NO flux of the films is  $0.90 \pm 0.13 \text{ nmol cm}^{-2} \text{ min}^{-1}$ . Reproduced by permission of the American Chemical Society.

has been reported to fall within the range of  $0.05 - 0.4 \text{ nmol cm}^{-2} \text{ min}^{-1}$ .<sup>50,51</sup> In addition, studies showing the impact of NO release on processes such as thrombus formation have reported an all-inclusive flux in the range of  $0.024 - 12 \text{ nmol cm}^{-2} \text{ min}^{-1}$  when antiplatelet and antithrombogenic effects are observed.<sup>52,53</sup> As such, the mean NO surface flux of a potentially antithrombotic material should fall within this range.<sup>54</sup> The CuBTTri/polymer films have demonstrated the capability to generate an NO flux within the range of previously reported values, suggesting that the material has the potential to produce therapeutically-relevant quantities of NO.

To ensure that the material remained intact and did not release large quantities of copper, PBS solutions were analyzed for trace copper content using ICP-OES following each NOA experiment. The results showed no statistical difference in copper concentration between experiments performed with ( $1.0 \pm 0.5 \mu\text{M}$ ) or without ( $1.6 \pm 1.5 \mu\text{M}$ ) CuBTTri/polymer films, suggesting that copper was not introduced through leaching from the materials. This contamination was attributable to the SNAP precursor *N*-acetyl-D-penicillamine, which was analyzed by ICP-OES and found to contain trace copper. Since a steady release from SNAP was achieved in the presence of trace copper, additional purification of *N*-acetyl-D-penicillamine was not performed. Additionally, PXRD was taken post-reaction with SNAP and showed the retention of the diffraction peaks corresponding with CuBTTri following NO generation (**Figure 3.7**). Thus, we concluded that CuBTTri is likely to remain intact under these experimental conditions and that the enhanced NO generation was not attributable to copper leaching from the MOF, since any potential contribution would be minor relative to the background level of copper originating from *N*-acetyl-D-penicillamine.

### **3.3.3 Cytocompatibility towards fibroblasts and primary human hepatocytes**

The liver is the organ principally involved in the uptake and metabolism of many pharmaceuticals.<sup>55</sup> In addition, the liver is the primary site for the storage and excretion of copper in the body.<sup>56</sup> Copper is important in key biological processes such as being a co-factor for several types of enzymes.<sup>57</sup> Excess copper in the body, beyond physiological requirements, is taken up by hepatocytes in the liver, where it can be either stored, bound to specific metal-binding proteins (i.e. metallothionein) or incorporated into several cuproenzymes. Hepatocytes can also excrete excess copper into the plasma or bile. However, if the storage and excretion capacities for copper are exceeded, unbound copper can generate hydroxyl radicals, that can lead to cytotoxicity. As a result,

evaluating effects of copper-based MOFs on liver cells *in vitro* constitutes an important step in better understanding any toxicological liabilities of MOFs resulting from copper accumulation.

Given the differences in liver pathways between animals and humans, the use of human-relevant liver models for evaluating material and drug effects has become necessary and is being encouraged by the US FDA and US EPA.<sup>58</sup> PHHs, the main parenchymal cell type of the liver, are

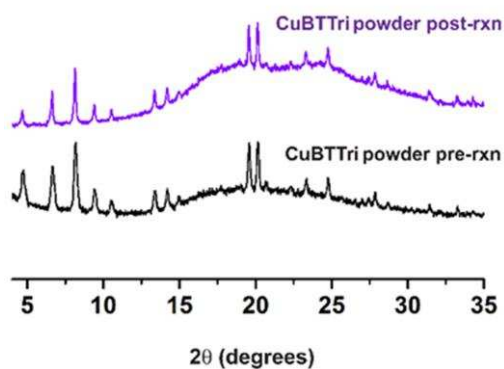


**Figure 3.7** pXRD diffraction patterns of CuBTTri/polymer films pre-reaction with SNAP and post-reaction resulting in NO generation. It can be seen that the diffraction peaks corresponding to CuBTTri remain intact following reaction with SNAP. Reproduced by permission of the American Chemical Society.

the ideal cell type to construct *in vitro* models of the human liver since these cells are relatively simple to use in medium-to-high throughput culture formats for screening applications.<sup>59</sup> However, PHHs rapidly (hours) lose phenotypic functions under culture formats that rely exclusively on extracellular matrix (ECM) manipulations (i.e. adsorbed collagen), which limits their utility for evaluating the chronic effects of materials and drugs.<sup>60</sup> Semiconductor-driven microfabrication tools can be used to control homotypic interactions between PHHs and stromal cells to prolong the functional lifetime *in vitro*. In particular, Khetani and Bhatia developed a MPCC platform in which PHHs are micropatterned onto collagen-coated domains of empirically optimized dimensions and subsequently surrounded by 3T3-J2 murine embryonic fibroblasts (**Figure 3.8**).<sup>38</sup> In this format, PHHs display high levels of major liver functions for 4-6 weeks *in vitro* and are more sensitive for detection of drug toxicities than when cultured in standard monolayers.<sup>60</sup> In this

study, we sought to measure the cellular toxicity of films incorporating the water-stable, copper-based MOF, CuBTri, in a tiered strategy starting with 3T3-J2 fibroblasts to assess cytotoxicity and then MPCCs to assess hepatotoxicity. Time-dependent effects of CuBTri/polymer films on the morphology and viability of the fibroblasts and morphology and liver-specific functions of the PHHs were evaluated.

Films were added to a 24-well plate containing cells with media changes every other day and morphology pictures obtained every 4 days. Cellular morphology of fibroblasts was monitored with an EVOS-FL microscope under phase contrast. Initial results of fibroblast studies after an

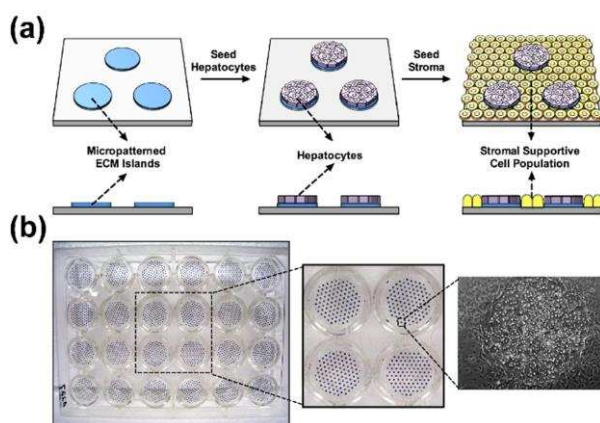


**Figure 3.8** MPCC of PHHs and stromal fibroblasts. (a) Collagen is micropatterned onto tissue culture polystyrene using soft lithographic techniques. PHHs selectively attach to the collagen domains. Once these cells have spread on the collagen, stromal cells (i.e. 3T3-J2 murine embryonic fibroblasts) are seeded the next day in the surrounding bare areas to create the MPCCs. Reproduced with permission from reference 61. Copyright 2015 Oxford University Press. (b) Left: 24-well plate in which hepatocytes are patterned in each well (500 microns diameter, 1200 microns center-to-center spacing) and stained with a purple formazan dye. Middle: Enlarged image of 4 wells from plate image on left. Right: Phase contrast image of single PHH island surrounded by 3T3-J2 fibroblasts. Reproduced with permission from reference 62. Copyright 2015 John Wiley and Sons. Reproduced by permission of the American Chemical Society.

approximately 3-week time frame (22 days) showed no significant aberrations in fibroblast morphology. Figure 3.9a-c shows phase contrast images obtained from the control, 0.1% CuBTri, and 0.5% CuBTri. Cell viability studies were performed by LIVE/DEAD staining assays using NucBlue® and propidium iodide. NucBlue stains all cells, whereas propidium iodide stains only

cells with a compromised cell membrane (i.e. dead cells). All cells were imaged using the EVOS-FL microscope using different fluorescent light cubes, specifically 357 nm excitation/447 nm emission for all cells (NucBlue) and 531 nm excitation/593 nm emission for dead cells (propidium iodide). The images of all cells and dead cells were superimposed to obtain the overall viability images (Fig. 8d-f). Fibroblast viability was found to be at least 98% across triplicate wells of the control, 0.1% CuBTTri, and 0.5% CuBTTri after the 22 day time frame, suggesting that no significant cytotoxicity was observed. Based on these initial findings, PHH studies were carried out as the next step in a tiered strategy of testing cytotoxicity followed by hepatotoxicity.

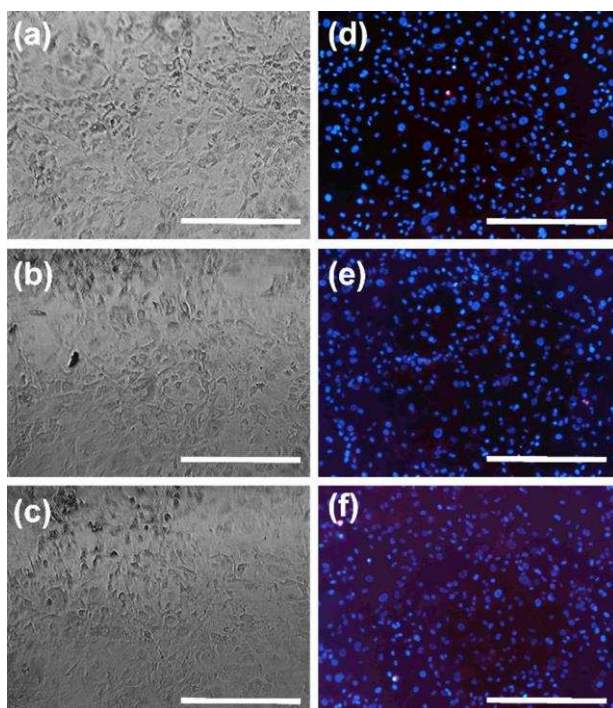


**Figure 3.9** (top) Representative phase contrast images of fibroblasts taken at 2 weeks: (a) control films, (b) 0.1% CuBTTri, and (c) 0.5% CuBTTri. Cell viability studies (staining with NucBlue for nuclei and propidium iodide for dead cells) conducted at 22 days: (d) control films, (e) 0.1% CuBTTri, and (f) 0.5% CuBTTri. Scale bars = 400  $\mu\text{m}$ . Reproduced by permission of the American Chemical Society.

PHHs stability was *qualitatively* assessed by evaluating morphology at the 16 day time frame and found that it was maintained relative to the control wells (**Figure 3.10**). The fibroblast morphology was also maintained in co-cultures as we observed in the aforementioned fibroblast-

only studies. For the 0.1% and 0.5% CuBTTri film conditions, the opacity of the films somewhat limited the quality of phase contrast images. Therefore, PHH stability was *quantitatively* assessed by monitoring liver-specific functions, in particular albumin (surrogate for liver protein synthesis) and urea (surrogate for liver nitrogen metabolism) secretions in the supernatants.

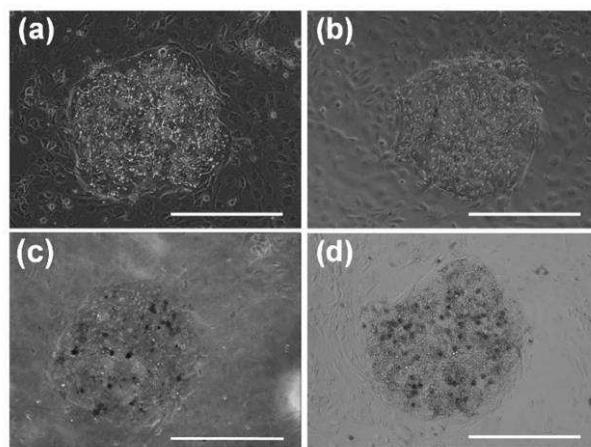


**Figure 3.10** Phase contrast images of MPCCs at 16 days (with PHH islands and surrounding fibroblasts): (a) no-film control, (b) control film, (c) 0.1% CuBTTri, and (d) 0.5% CuBTTri. Scale bars = 400  $\mu\text{m}$ . Reproduced by permission of the American Chemical

These markers have been shown to previously correlate with drug toxicity and are more sensitive than measurements of ATP.<sup>60,61</sup> The fibroblasts in MPCCs do not secrete albumin and urea per our experience (data not shown). The films placed on the cultures caused some down-regulation of albumin and urea levels over  $\sim 2$  weeks of incubations relative to no-film controls (**Figure 3.11**); however, these effects were not due to the copper incorporation when comparing the secretion levels in cultures containing 0% and 0.1% CuBTTri/polymer films. More importantly, albumin and urea were not down-regulated to 50% (or less) of controls, suggesting that the material with incorporated CuBTTri is not hepatotoxic based on previous studies using a set of drugs with available clinical information.<sup>60</sup> Interestingly, the 0.5% CuBTTri film placed on the cultures led to higher functions than the 0% and 0.1% CuBTTri/polymer films. The mechanism underlying this observation merits additional study in the future, but further shows that these films with copper-MOFs are not inherently toxic to PHHs.

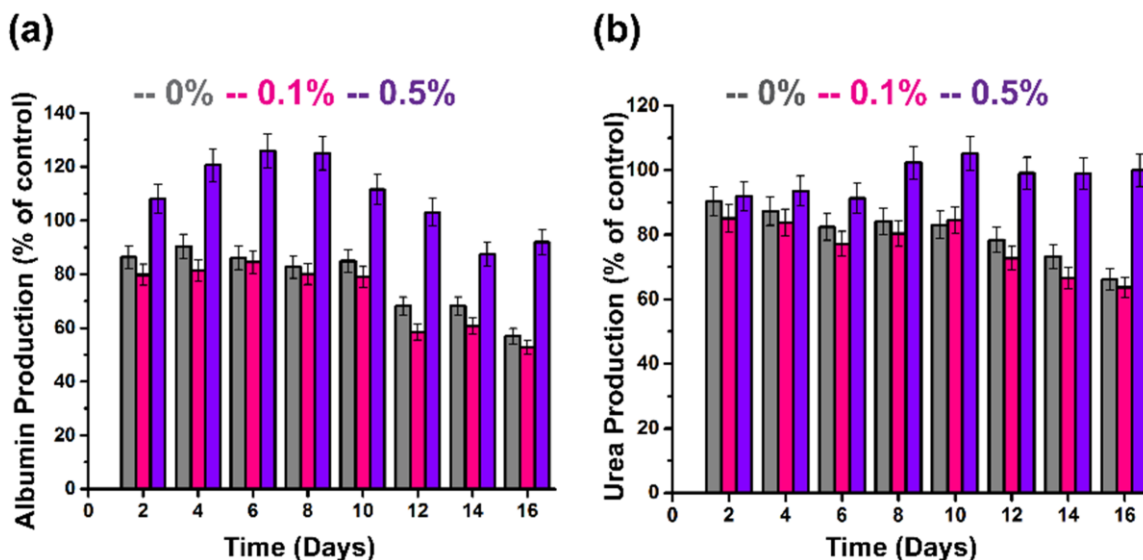


**Figure 3.11** (a) Albumin and (b) urea production for 0%, 0.1%, and 0.5% CuBTtri/polymer films. All data has been normalized to no-film controls and presented as days after the addition of CuBTtri/polymer films on day 12 of culture. Error bars represent standard deviation ( $n = 3$ ). Reproduced by permission of the American Chemical Society.

### 3.3.4 Copper leaching from copper(II) benzene -1,3,5-tris(1*H*-1,2,3-triazole-5-yl)/polymer composites

In order to address the possibility of toxicologically significant copper leaching, the CuBTtri/polymer films were assessed for their ability to tolerate a physiological environment. CuBTtri/polymer films were prepared in the exact same manner as the films used in the cell studies. Films were incubated at 37 °C and pH 7.4 in PBS or cell culture medium (Dulbecco's modified eagle's medium or DMEM) over the duration of a month. For the first week, all liquid was removed and replaced with an equivalent volume of the appropriate solution every 24 h. The combined solutions from the first week were tested for the presence of copper by ICP-OES. For the remaining 3 weeks, the solutions were replaced every week and similarly tested for the presence of copper. Cell media solutions were shown to have a cumulative total of  $0.84 \pm 0.21\%$  copper of the theoretical amount of copper present in the films (**Figure 3.12**). PBS solutions were determined to have a total of  $0.18 \pm 0.01\%$  of the total theoretical amount of copper present. While

these results indicate that small amounts of leachable copper are initially present in the materials, the rapid decline in rate of leaching suggests that this may be primarily attributable to the presence

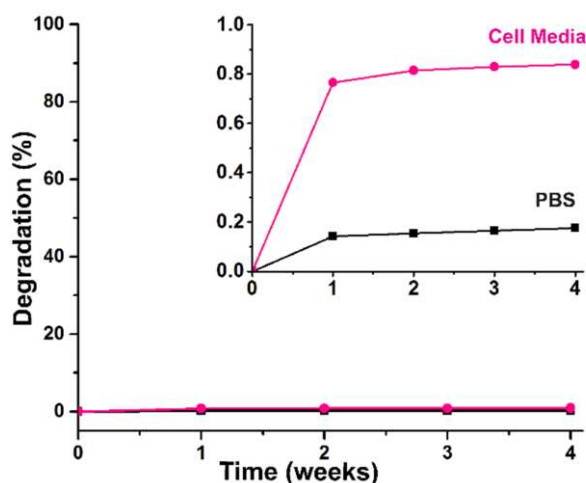


**Figure 3.12** Percent degradation of CuBTTri in cell media and PBS solutions (37 °C, pH 7.4) for 0.5% CuBTTri/polymer films for copper leaching. Percent degradation is based on the theoretical total amount of copper in the films. Films were agitated in 5 mL solutions in a water bath with the solutions being replaced every 24 h for the first week followed by removal every week for the remaining three. Cell media solutions were shown to have a total of  $0.84 \pm 0.21$  % copper of the theoretical amount of copper present in the films. PBS solutions were shown to have a total of  $0.18 \pm 0.01$  % of the total theoretical amount of copper present in the films. Inset shows 0-1% on the y-axis. Reproduced by permission of the American Chemical Society.

of residual trace copper rather than deterioration of the MOF. This outcome was anticipated since both the H<sub>3</sub>BTTri ligand and the water-stable CuBTTri are synthesized under conditions where copper salts are employed. Considering that copper is known to exist in the body at appreciable levels (68 μM) and the general cytocompatibility of the materials with both fibroblasts and PHHs, these findings suggest that the observed trace copper leaching does not produce a toxicological impact under the conditions used.<sup>57</sup>

### 3.4 Conclusion

Overall, cell compatibility studies performed suggest that MOF/polymer composite materials prepared from PVC/DOS and CuBTTri are compatible to stable cultures of both murine embryonic fibroblasts and PHHs. While PHHs constitute ~70% of the liver cell mass and are the

principal cell type involved in the uptake, storage and excretion of copper, it is conceivable that additional cell types of the liver (such as Kupffer macrophages, sinusoidal endothelial cells, stellate cells, and cholangiocytes) may also be susceptible to these materials. As culture methods for these specialized cell types become more standardized in the tissue engineering field, copper-based MOFs can be tested further *in vitro* for any toxic effect. Additionally, testing lead copper-MOF designs on microfluidic human-on-a-chips being designed by several groups may be useful to provide an assessment of interactions between different tissue types in either mitigating or exacerbating copper-MOF toxicity.<sup>63</sup> Ultimately, before copper-MOF materials can be tested in patients, FDA-required live animal studies will need to be carried out. The use of *in vitro* testing on different cell types as the first phase of a tiered toxicity screening strategy can greatly streamline the *in vivo* animal testing with respect to reduction in the number of animals used as well as which animal species (i.e. rat, mouse, dog, or monkey) constitutes a good model of any human liabilities for a given MOF design. The results presented here exemplify a strategy to test the toxicities of MOFs in a continuum of *in vitro* to *in vivo* models. Thus, we have successfully incorporated CuBTri into a medically-relevant polymer as validated through PXRD, ATR-FTIR, and SEM analysis techniques. The MOF-composite materials were investigated for stability and cytotoxicity. Additionally, as an application, the materials were explored as a material for enhanced generation of NO from an NO donor. The MOF-composite material was found to have an NO flux in the range of  $0.90 \pm 0.13 \text{ nmol cm}^{-2} \text{ min}^{-1}$  which correlates to physiologically relevant levels. Subsequent evaluation of material stability and copper leaching was performed under physiological conditions and found to result in a cumulative percentage of theoretical copper released of  $0.84 \pm 0.21\%$  in cell media and  $0.18 \pm 0.01\%$  in PBS. Evaluation of cytocompatibility showed that the MOF/composite materials are not inherently toxic to fibroblast or hepatocyte

culture as albumin and urea secretions were not down-regulated by 50% or more of the controls, nor was morphology of either cell type affected to any considerable degree over extended culture (16-22 days).

MOFs have been proposed for a range of biomedical applications including drug delivery systems, medical imaging, and small molecule applications. While these applications have been projected, the lack of investigation into the toxicological impacts of these next generation materials presents a major concern limiting further advancement toward clinical use including MOF-polymer composites for ECCs. In order for this to be achieved, steps need to be taken toward the development of methods that provide insight into the biological interactions of MOF-based materials. Overall, we have provided the first evidence of the cytocompatibility (i.e. lack of overt toxicity) of a copper-based MOF/polymer composite with both fibroblasts and PHHs. While further testing is ongoing to determine the full potential of using these materials in a therapeutic setting. The results shown herein demonstrate the exciting potential for MOF-based materials necessary to enable possible applications in biomedical settings.

## REFERENCES

1. Farrusseng, D.; Aguado, S.; Pinel, C. Metal-Organic Frameworks: Opportunities for Catalysis. *Angew. Chem., Int. Ed.* **2009**, *48*, 7502-7513.
2. Corma, A.; Garcia, H.; Llabres i. Xamena, F. X. Engineering Metal Organic Frameworks for Heterogeneous Catalysis. *Chem. Rev. (Washington, DC, U. S.)* **2010**, *110*, 4606-4655.
3. Jeazet, H. B. T.; Staudt, C.; Janiak, C. Metal-Organic Frameworks in Mixed-Matrix Membranes for Gas Separation. *Dalton Trans.* **2012**, *41*, 14003-14027.
4. Yu, Y.; Ren, Y.; Shen, W.; Deng, H.; Gao, Z. Applications of Metal-Organic Frameworks as Stationary Phases in Chromatography. *TrAC, Trends Anal. Chem.* **2013**, *50*, 33-41.
5. Li, J.-R.; Sculley, J.; Zhou, H.-C., Metal-Organic Frameworks For Separations. *Chem. Rev.* **2012**, *112*, 869-932.
6. Furukawa, H.; Cordova, K. E.; O'Keeffe, M.; Yaghi, O. M., The Chemistry and Applications of Metal-Organic Frameworks. *Science* **2013**, *341*, 974-986.
7. Horcajada, P.; Gref, R.; Baati, T.; Allan, P. K.; Maurin, G.; Couvreur, P.; Ferey, G.; Morris, R. E.; Serre, C. Metal-Organic Frameworks in Biomedicine. *Chem. Rev.* **2012**, *112*, 1232-1268.
8. Gimenez-Marques, M.; Hidalgo, T.; Serre, C.; Horcajada, P. Nanostructured Metal-Organic Frameworks and their Bio-Related Applications. *Coord. Chem. Rev.* **2016**, *307*, 342-360.
9. Keskin, S.; Kizilel, S. Biomedical Applications of Metal Organic Frameworks. *Ind. Eng. Chem. Res.* **2011**, *50*, 1799-1812.

10. McKinlay, A. C.; Morris, R. E.; Horcajada, P.; Ferey, G.; Gref, R.; Couvreur, P.; Serre, C. BioMOFs: Metal-Organic Frameworks for Biological and Medical Applications. *Angew. Chem., Int. Ed.* **2010**, *49*, 6260-6266.
11. Zheng, H.; Zhang, Y.; Liu, L.; Wan, W.; Guo, P.; Nystrom, A. M.; Zou, X. One-pot Synthesis of Metal-Organic Frameworks with Encapsulated Target Molecules and Their Applications for Controlled Drug Delivery. *J. Am. Chem. Soc.* **2016**, *138*, 962-968.
12. An, J.; Geib, S. J.; Rosi, N. L. Cation-Triggered Drug Release from a Porous Zinc-Adeninate Metal-Organic Framework. *J. Am. Chem. Soc.* **2009**, *131*, 8376-8377.
13. Ingleson, M. J.; Heck, R.; Gould, J. A.; Rosseinsky, M. J. Nitric Oxide Chemisorption in a Postsynthetically Modified Metal-Organic Framework. *Inorg. Chem.* **2009**, *48*, 9986-9988.
14. Taylor-Pashow, K. M. L.; Della Rocca, J.; Xie, Z.; Tran, S.; Lin, W. Postsynthetic Modifications of Iron-Carboxylate Nanoscale Metal-Organic Frameworks for Imaging and Drug Delivery. *J. Am. Chem. Soc.* **2009**, *131*, 14261-14263.
15. Ke, F.; Yuan, Y.-P.; Qiu, L.-G.; Shen, Y.-H.; Xie, A.-J.; Zhu, J.-F.; Tian, X.-Y.; Zhang, L.-D. Facile Fabrication of Magnetic Metal-Organic Framework Nanocomposites for Potential Targeted Drug Delivery. *J. Mater. Chem.* **2011**, *21*, 3843-3848.
16. Peikert, K.; McCormick, L. J.; Cattaneo, D.; Duncan, M. J.; Hoffmann, F.; Khan, A. H.; Bertmer, M.; Morris, R. E.; Froeba, M. Tuning the Nitric Oxide Release Behavior of Amino Functionalized HKUST-1. *Microporous and Mesoporous Mater.* **2015**, *216*, 118-126.
17. McKinlay, A. C.; Eubank, J. F.; Wuttke, S.; Xiao, B.; Wheadey, P. S.; Bazin, P.; Lavalley, J. C.; Daturi, M.; Vimont, A.; De Weireld, G.; Horcajada, P.; Serre, C.; Morris,

- R. E. Nitric Oxide Adsorption and Delivery in Flexible MIL-88(Fe) Metal-Organic Frameworks. *Chem. Mater.* **2013**, *25*, 1592-1599.
18. Nguyen, J. G.; Tanabe, K. K.; Cohen, S. M. Postsynthetic Diazeniumdiolate Formation and NO Release from MOFs. *Crystengcomm* **2010**, *12*, 2335-2338.
  19. Seabra, A. B.; Duran, N. Nitric Oxide-Releasing Vehicles for Biomedical Applications. *J. Mater. Chem.* **2010**, *20*, 1624-1637.
  20. Harding, J. L.; Reynolds, M. M. Metal Organic Frameworks as Nitric Oxide Catalysts. *J. Am. Chem. Soc.* **2012**, *134*, 3330-3333.
  21. Harding, J. L.; Metz, J. M.; Reynolds, M. M. A Tunable, Stable, and Bioactive MOF Catalyst for Generating a Localized Therapeutic from Endogenous Sources. *Adv. Funct. Mater.* **2014**, *24*, 7503-7509.
  22. Harding, J. L.; Reynolds, M. M. Composite Materials with Embedded Metal Organic Framework Catalysts for Nitric Oxide Release from Bioavailable S-Nitrosothiols. *J. Mater. Chem. B* **2014**, *2*, 2530-2536.
  23. Neufeld, M. J.; Harding, J. L.; Reynolds, M. M. Immobilization of Metal-Organic Framework Copper(II) Benzene-1,3,5-tricarboxylate (CuBTC) onto Cotton Fabric as a Nitric Oxide Release Catalyst. *ACS Appl. Mater. Interfaces* **2015**, *7*, 26742-26750.
  24. Bhunia, M. K.; Hughes, J. T.; Fetting, J. C.; Navrotsky, A. Thermochemistry of Paddle Wheel MOFs: Cu-HKUST-1 and Zn-HKUST-1. *Langmuir* **2013**, *29*, 8140-8145.
  25. ul Qadir, N.; Said, S. A. M.; Bahaidarah, H. M. Structural Stability of Metal Organic Frameworks in Aqueous Media - Controlling Factors and Methods to Improve Hydrostability and Hydrothermal Cyclic Stability. *Microporous and Mesoporous Mater.* **2015**, *201*, 61-90.

26. Gao, W.-Y.; Cai, R.; Pham, T.; Forrest, K. A.; Hogan, A.; Nugent, P.; Williams, K.; Wojtas, L.; Luebke, R.; Weselinsk, L. J.; Zaworotko, M. J.; Space, B.; Chen, Y.-S.; Eddaoudi, M.; Shi, X.; Ma, S. Remote Stabilization of Copper Paddlewheel Based Molecular Building Blocks in Metal-Organic Frameworks. *Chem. Mater.* **2015**, *27*, 2144-2151.
27. Cooper, L.; Hidalgo, T.; Gorman, M.; Lozano-Fernandez, T.; Simon-Vazquez, R.; Olivier, C.; Guillou, N.; Serre, C.; Martineau, C.; Taulelle, F.; Damasceno-Borges, D.; Maurin, G.; Gonzalez-Fernandez, A.; Horcajada, P.; Devic, T. A Biocompatible Porous Mg-Gallate Metal-Organic Framework as an Antioxidant Carrier. *Chem. Commun.* **2015**, *51*, 5848-5851.
28. Huxford, R. C.; deKrafft, K. E.; Boyle, W. S.; Liu, D.; Lin, W. Lipid-Coated Nanoscale Coordination Polymers for Targeted Delivery of Antifolates to Cancer Cells. *Chem. Sci.* **2012**, *3*, 198-204.
29. Tamames-Tabar, C.; Cunha, D.; Imbuluzqueta, E.; Ragon, F.; Serre, C.; Blanco-Prieto, M. J.; Horcajada, P. Cytotoxicity of Nanoscaled Metal-Organic Frameworks. *J. Mater. Chem. B.* **2014**, *2*, 262-271.
30. Ma, D.-Y.; Li, Z.; Xiao, J.-X.; Deng, R.; Lin, P.-F.; Chen, R.-Q.; Liang, Y.-Q.; Guo, H.-F.; Liu, B.; Liu, J.-Q., Hydrostable and Nitryl/Methyl-Functionalized Metal-Organic Framework for Drug Delivery and Highly Selective CO<sub>2</sub> Adsorption. *Inorg. Chem.* **2015**, *54*, 6719-6726.
31. Horcajada, P.; Chalati, T.; Serre, C.; Gillet, B.; Sebrie, C.; Baati, T.; Eubank, J. F.; Heurtaux, D.; Clayette, P.; Kreuz, C.; Chang, J.-S.; Hwang, Y. K.; Marsaud, V.; Bories, P.-N.; Cynober, L.; Gil, S.; Ferey, G.; Couvreur, P.; Gref, R. Porous Metal-Organic-

- Framework Nanoscale Carriers as a Potential Platform for Drug Delivery and Imaging. *Nat. Mater.* **2010**, *9*, 172-178.
32. Baati, T.; Njim, L.; Neffati, F.; Kerkeni, A.; Bouttemi, M.; Gref, R.; Najjar, M. F.; Zakhama, A.; Couvreur, P.; Serre, C.; Horcajada, P. In Depth Analysis of the In Vivo Toxicity of Nanoparticles of Porous Iron(III) Metal-Organic Frameworks. *Chem. Sci.* **2013**, *4*, 1597-1607.
33. Kundu, T.; Mitra, S.; Patra, P.; Goswami, A.; Diaz, D. D.; Banerjee, R., Mechanical Downsizing of a Gadolinium(III)-Based Metal-Organic Framework for Anticancer Drug Delivery. *Chem.-Eur. J.* **2014**, *20*, 10514-10518.
34. Ruyra, A.; Yazdi, A.; Espin, J.; Carne-Sanchez, A.; Roher, N.; Lorenzo, J.; Imaz, I.; Maspoch, D. Synthesis, Culture Medium Stability, and In Vitro and In Vivo Zebrafish Embryo Toxicity of Metal-Organic Framework Nanoparticles. *Chem.-Eur. J.* **2015**, *21*, 2508-2518.
35. Aromi, G.; Barrios, L. A.; Roubeau, O.; Gamez, P. Triazoles and Tetrazoles: Prime Ligands to Generate Remarkable Coordination Materials. *Coord. Chem. Rev.* **2011**, *255*, 485-546.
36. Demessence, A.; D'Alessandro, D. M.; Foo, M. L.; Long, J. R. Strong CO<sub>2</sub> Binding in a Water-Stable, Triazolate-Bridged Metal-Organic Framework Functionalized with Ethylenediamine. *J. Am. Chem. Soc.* **2009**, *131*, 8784-8786.
37. Rheinwald, J. G.; Green, H. Formation of a Keratinizing Epithelium in Culture by a Cloned Cell Line Derived From a Teratoma. *Cell* **1975**, *6*, 317-330.
38. Khetani, S. R.; Bhatia, S. N. Microscale Culture of Human Liver Cells for Drug Development. *Nat. Biotechnol.* **2008**, *26*, 120-126.

39. March, S.; Ramanan, V.; Trehan, K.; Ng, S.; Galstian, A.; Gural, N.; Scull, M. A.; Shlomai, A.; Mota, M. M.; Fleming, H. E.; Khetani, S. R.; Rice, C. M.; Bhatia, S. N. Micropatterned Coculture of Primary Human Hepatocytes and Supportive Cells for the Study of Hepatotropic Pathogens. *Nat. Protoc.* **2015**, *10*, 2027-2053.
40. Diane, R.; Donald, T. J.; Tom, C. S.; Timothy, T. S. Altered CYP2C9 Activity Following Modulation of CYP3A4 Levels in Human Hepatocytes: An Example of Protein-Protein Interactions. *Drug Metab. Dispos.* **2014**, *42*, 1940-1946.
41. Bogdan, C. Nitric Oxide and the Immune Response. *Nat. Immunol.* **2001**, *2*, 907-916.
42. Gross, S. S.; Wolin, M. S. Nitric-Oxide-Pathophysiological Mechanisms. *Annu. Rev. Physiol.* **1995**, *57*, 737-769.
43. Knowles, R. G.; Moncada, S. Nitric-Oxide Synthases in Mammals. *Biochem. J.* **1994**, *298*, 249-258.
44. Zhang, Y.; Hogg, N. S-Nitrosothiols: Cellular Formation and Transport. *Free Radical Biol. Med.* **2005**, *38*, 831-838.
45. Dicks, A. P.; Williams, D. L. Generation of Nitric Oxide from S-Nitrosothiols using Protein-Bound Cu<sup>2+</sup> Sources. *Chem. Biol.* **1996**, *3*, 655-659.
46. Dicks, A. P.; Swift, H. R.; Williams, D. L. H.; Butler, A. R.; AlSadoni, H. H.; Cox, B. G. Identification of Cu<sup>+</sup> as the Effective Reagent in Nitric Oxide Formation from S-Nitrosothiols (RSNO). *J. Chem. Soc., Perkin Trans. 2* **1996**, 481-487.
47. Singh, R. J.; Hogg, N.; Joseph, J.; Kalyanaraman, B. Mechanism of Nitric Oxide Release from S-Nitrosothiols. *J. Biol. Chem.* **1996**, *271*, 18596-603.
48. Baciu, C.; Cho, K. B.; Gauld, J. W. Influence of Cu<sup>+</sup> on the RS-NO Bond Dissociation Energy of S-Nitrosothiols. *J. Phys. Chem. B* **2005**, *109*, 1334-1336.

49. Zhang, S.; Celebi-Oelcuem, N.; Melzer, M. M.; Houk, K. N.; Warren, T. H., Copper(I) Nitrosyls from Reaction of Copper(II) Thiolates with *S*-Nitrosothiols: Mechanism of NO Release from RSNOs at Cu. *J. Am. Chem. Soc.* **2013**, *135*, 16746-16749.
50. Radomski, M. W.; Palmer, R. M. J.; Moncada, S. The Role of Nitric-Oxide and Cgmp in Platelet-Adhesion to Vascular Endothelium. *Biochem. Biophys. Res. Commun.* **1987**, *148*, 1482-1489.
51. Vaughn, M. W.; Kuo, L.; Liao, J. C. Estimation of Nitric Oxide Production and Reaction Rates in Tissue by use of a Mathematical Model. *Am. J. Physiol.: Heart Circ. Physiol.* **1998**, *274*, H2163-H2176.
52. Robbins, M. E.; Hopper, E. D.; Schoenfisch, M. H. Synthesis and Characterization of Nitric Oxide-Releasing Sol-Gel Microarrays. *Langmuir* **2004**, *20*, 10296-10302.
53. Fleser, P. S.; Nuthakki, V. K.; Malinzak, L. E.; Callahan, R. E.; Seymour, M. L.; Reynolds, M. M.; Merz, S. I.; Meyerhoff, M. E.; Bendick, P. J.; Zelenock, G. B.; Shanley, C. J. Nitric Oxide-Releasing Biopolymers Inhibit Thrombus Formation in a Sheep Model of Arteriovenous Bridge Grafts. *J. Vasc. Surg.* **2004**, *40*, 803-811.
54. Coneski, P. N.; Schoenfisch, M. H. Synthesis of Nitric Oxide-Releasing Polyurethanes with *S*-Nitrosothiol-Containing Hard and Soft Segments. *Polym. Chem.* **2011**, *2*, 906-913.
55. Chen, M.; Suzuki, A.; Borlak, J.; Andrade, R. J.; Lucena, M. I. Drug-Induced Liver Injury: Interactions between Drug Properties and Host Factors. *J. Hepatol.* **2015**, *63*, 503-514.
56. Roberts, E. A.; Sarkar, B. Liver as a Key Organ in the Supply, Storage, and Excretion of Copper. *Am. J. Clin. Nutr.* **2008**, *88*, 851S-854S.

57. Luza, S. C.; Speisky, H. C. Liver Copper Storage and Transport During Development: Implications for Cytotoxicity. *Am. J. Clin. Nutr.* **1996**, *63*, 812-820.
58. Khetani, S. R.; Berger, D. R.; Ballinger, K. R.; Davidson, M. D.; Lin, C.; Ware, B. R. Microengineered Liver Tissues for Drug Testing. *Jala* **2015**, *20*, 216-250.
59. Lin, C.; Ballinger, K. R.; Khetani, S. R. The Application of Engineered Liver Tissues for Novel Drug Discovery. *Expert Opin. Drug Discovery* **2015**, *10*, 519-540.
60. Khetani, S. R.; Kanchagar, C.; Ukairo, O.; Krzyzewski, S.; Moore, A.; Shi, J.; Aoyama, S.; Aleo, M.; Will, Y. Use of Micropatterned Cocultures to Detect Compounds That Cause Drug-Induced Liver Injury in Humans. *Toxicol. Sci.* **2013**, *132*, 107-117.
61. Ware, B. R.; Berger, D. R.; Khetani, S. R. Prediction of Drug-Induced Liver Injury in Micropatterned Co-Cultures Containing iPSC-Derived Human Hepatocytes. *Toxicol. Sci.* **2015**, *145*, 252-262.
62. Berger, D. R.; Ware, B. R.; Davidson, M. D.; Allsup, S. R.; Khetani, S. R. Enhancing the Functional Maturity of Induced Pluripotent Stem Cell-Derived Human Hepatocytes by Controlled Presentation of the Cell-Cell Interactions In Vitro. *Hepatology* **2015**, *61*, 1370-1381.
63. Huh, D.; Kim, H. J.; Fraser, J. P.; Shea, D. E.; Khan, M.; Bahinski, A.; Hamilton, G. A.; Ingber, D. E. Microfabrication of Human Organs-On-Chips. *Nat. Protoc.* **2013**, *8*, 2135-2157.

## CHAPTER 4

# CHITOSAN/COPPER(II) BENZENE-1,3,5-TRIS(1*H*-1,2,3-TRIAZOL-5-YL) HYBRID MATERIALS PROMOTE NITRIC OXIDE RELEASE FROM *S*-NITROSOGLUTATHIONE IN AQUEOUS SOLUTION<sup>3</sup>

### 4.1 Introduction

Metal-organic frameworks (MOFs) are crystalline structures consisting of organic linkers bound to metal centers, producing highly porous lattices that are frequently utilized in gas storage and heterogeneous catalysis, among other applications.<sup>1</sup> It has been previously reported by Harding *et al.* that copper-based MOFs may be capable of inducing the nitric oxide (NO)-forming decomposition of *S*-nitrosothiols (RSNOs), a class of NO-donating compounds that are unique in their biological occurrence.<sup>2</sup> NO itself is produced endogenously by a family of NO synthase enzymes, where it contributes to the immune response, neurotransmission, and regulation of vascular tone.<sup>3</sup> Biological NO production is essential to the wound-healing process, and exogenous NO supplementation has been shown to promote accelerated wound closure.<sup>4-6</sup> These properties have led to the exploitation of copper-based MOFs for their ability to induce the release of NO directly from RSNOs. Biological RSNOs are believed to function collectively as a physiological reservoir of NO, most commonly in the form of *S*-nitrosoglutathione (GSNO) and *S*-nitrosoalbumin, which exist in blood in the nM to  $\mu$ M range.<sup>7,8</sup> Biologically-relevant GSNO and other RSNO species have been established to produce NO through thermal decomposition or

---

<sup>3</sup> This chapter was reproduced in part with permission from:

Neufeld, M. J.; Lutzke, A.; Tapia, J. B.; Reynolds, M. M. Metal–Organic Framework/Chitosan Hybrid Materials Promote Nitric Oxide Release from *S*-nitrosoglutathione. *ACS. Appl. Mater. Interfaces* **2017**, *9*, 5139-5148. Copyright 2017 American Chemical Society.  
<http://pubs.acs.org/doi/full/10.1021/acsami.6b14937>

photolysis that leads to the formation of disulfide, according to the equation  $2\text{RSNO} \rightarrow 2\text{NO} + \text{RSSR}$ .<sup>9</sup> In addition to these reaction pathways, it has been shown that exposure to copper ions induces the catalytic, NO-forming decomposition of many RSNOs.<sup>10</sup> This phenomenon has led to the development of copper-based materials intended to produce a localized supply of NO through the controlled decomposition of bioavailable RSNOs, typically through inclusion of simple copper salts or complexes.<sup>11,12</sup>

The ability of copper-based MOFs to promote NO release from RSNOs is exemplified by the decomposition of *S*-nitrosocysteine and *S*-nitrosocysteamine by copper benzene-1,3,5-tricarboxylate (HKUST-1) under nonaqueous conditions.<sup>2,13</sup> It was later discovered that the triazolate-bridged framework (**Figure 4.1a**) derived from reaction of 1,3,5-tris(1*H*-1,2,3-triazol-5-yl)benzene (H<sub>3</sub>BTTri) with CuCl<sub>2</sub>·H<sub>2</sub>O in DMF (H<sub>3</sub>[(Cu<sub>4</sub>Cl)<sub>3</sub>-(BTTri)<sub>8</sub>], or CuBTTri) exhibits a similar ability to promote the decomposition of both *S*-nitrosocysteamine and *S*-nitroso-*N*-acetylpenicillamine (SNAP) under aqueous, physiological conditions and exhibits an exceptional degree of aqueous stability.<sup>14,15</sup> For this reason, CuBTTri represents a useful candidate for the development of MOF-based biomaterials that are intended to trigger NO release from RSNOs in a physiological environment. However, the feasibility of utilizing copper-based MOFs for this application depends on their effective incorporation within a supporting polymeric matrix, *and* the retention of useful activity thereafter. Consequently, the identification of polymers that allow the productive, NO-forming interaction between aqueous-phase RSNOs and CuBTTri is a prerequisite to biological implementation. Nevertheless, previous work has been confined to hydrophobic polymers that are unlikely to permit the rapid diffusion of polar (and potentially charged) RSNO substrates. For this reason, hydrophilic materials such as polysaccharides may represent a useful alternative.

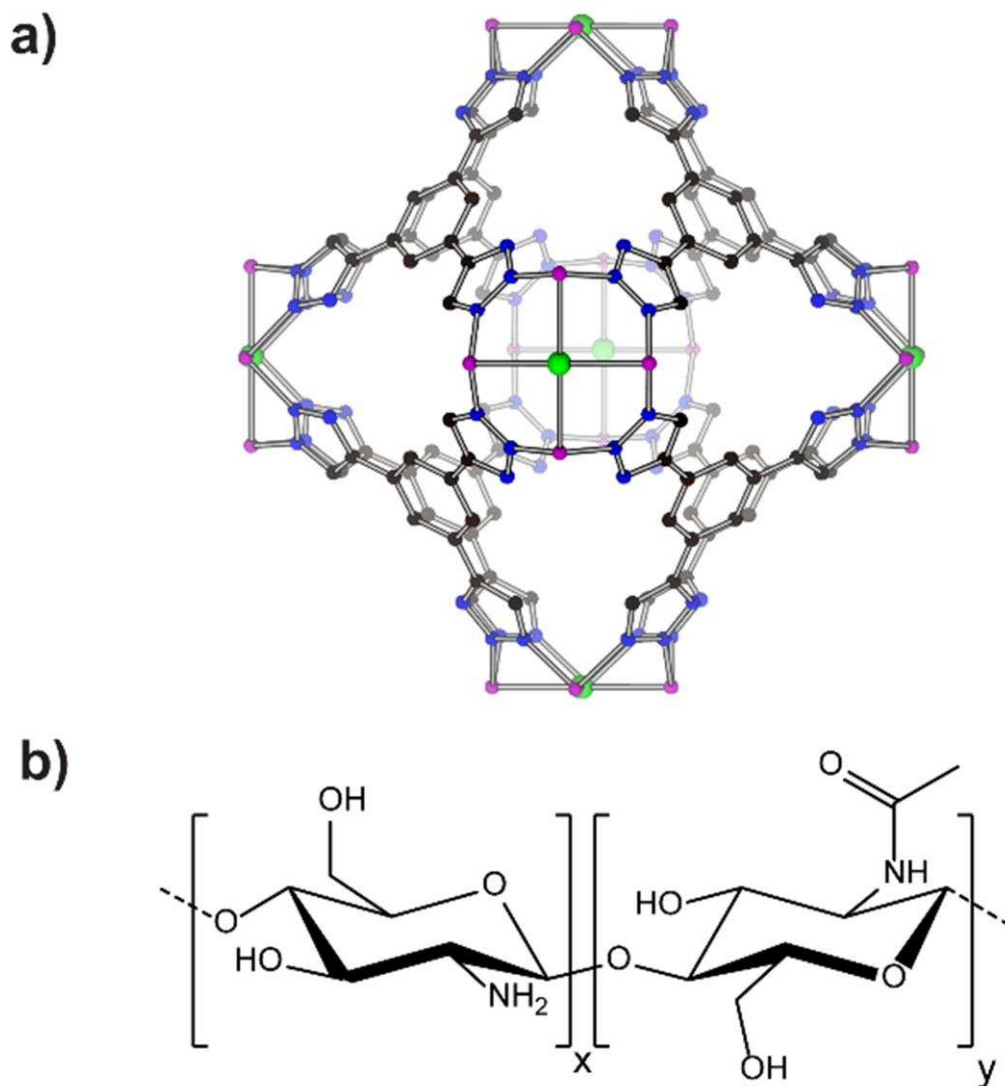


**Figure 4.1** (a) Fundamental building unit of CuBTtri. Copper (red), chlorine (green), carbon (black), and nitrogen (blue) atoms are depicted. Hydrogen atoms have been omitted for clarity. (b) Structure of the glucosamine (x) and *N*-acetyl glucosamine (y) units of chitosan. Reproduced by permission of the American Chemical Society.

Chitosan is a versatile, naturally-derived polysaccharide consisting of  $\beta$ -(1,4)-linked glucosamine and *N*-acetyl glucosamine units (**Figure 4.1b**). Because chitosan is biodegradable, typically regarded as nontoxic, and exhibits important therapeutic properties, it has been widely utilized for biomedical applications ranging from drug delivery to tissue engineering.<sup>16</sup> The conversion of chitosan to water-soluble polycationic salts or other easily-processed derivatives

permits the preparation of films, fibers, hydrogels, and other materials with useful characteristics.<sup>17</sup> As a biomaterial, chitosan has been reported to exhibit inherent bacteriostatic/antimicrobial properties, in addition to well-characterized hemostatic properties that have resulted in its commercial adoption for the treatment of hemorrhagic injuries.<sup>18</sup> Furthermore, numerous studies have shown that chitosan-based wound dressings can significantly accelerate the wound healing process.<sup>19,20</sup> Notably, both the wound-healing and antimicrobial properties of chitosan overlap significantly with those of NO, suggesting the possibility for combined action. Due to the potential for NO and chitosan to exhibit synergistic effects as a therapeutic, multiple publications have reported the development of NO-releasing materials based on chitosan. NO-releasing chitosan derivatives have been proposed as potential candidate polymers for the development of wound-healing dressings, while NO-releasing chitosan oligosaccharides have been utilized as solution-phase antibacterial agents.<sup>21-23</sup> These previous examples of NO-releasing chitosan derivatives have been universally prepared through the inclusion of unstable synthetic NO-donor species that release a finite quantity of NO through irreversible decomposition processes. In wound dressings, this may produce complications arising from both storage limitations and toxicity concerns.<sup>24</sup> For these reasons, an alternative method of producing localized NO release is desirable. In the case of potential blood-contacting materials, this goal may be achieved through the recruitment of natural RSNOs.<sup>25,26</sup>

Herein, the concept of promoting accelerated NO release from naturally-occurring GSNO using chitosan membranes containing water-stable CuBTri was investigated. This work represents the first inclusion of a water-stable MOF within chitosan, and expands the potential biological utility of CuBTri blends to nonsynthetic polymers. CuBTri was incorporated within a chitosan matrix and characterized by pXRD, ATR-FTIR, and SEM. The chitosan/CuBTri

membranes were subsequently exposed to GSNO at physiological temperature and pH, and chemiluminescence-based NO detection was utilized to confirm that the MOF retained its ability to accelerate the NO-forming decomposition of the RSNO substrate. Confinement of CuBTTri within the polysaccharide was not observed to significantly impact the enhanced NO generation observed when unbound CuBTTri particles were tested separately with GSNO. Additionally, mass spectrometry was used to qualitatively determine the major product of the MOF-promoted decomposition of GSNO as oxidized glutathione (GSSG). Although it is known that thermal or photolytic RSNO decomposition typically results in the formation of the corresponding disulfide ( $2\text{RSNO} \rightarrow 2\text{NO} + \text{RSSR}$ ), this is the first report to definitively identify the production of disulfide from an RSNO by CuBTTri.<sup>27</sup> These findings reveal that CuBTTri may be successfully immobilized within chitosan membranes without impairment of its ability to induce NO release from GSNO, providing further insight into the function of such MOF/polymer systems. The ability of CuBTTri to generate an enhanced level of NO release from GSNO complements the existing therapeutic uses of chitosan, particularly in the realm of future wound-healing applications. While previous reports have examined promotion of NO release from putatively endogenous *S*-nitrosocysteine, this structure primarily occurs in the form of *S*-nitrosated cysteine residues in biological macromolecules, which may limit the ability of a MOF to interact with the RSNO and induce NO release.<sup>26</sup> Similar efforts have been constrained to *S*-nitrosocysteamine and SNAP, which are not known to occur biologically. This work is the first to expand the substrate scope to include GSNO, a biologically available RSNO identified in human blood. Furthermore, the use of water-stable and potentially reusable CuBTTri and naturally-derived chitosan represents a new and potentially more environmentally-benign approach to achieving NO release from RSNOs compared to previous systems based on synthetic polymers.

## 4.2 Methods

### 4.2.1 Materials

1,3,5-Tribromobenzene (98%), trimethylsilylacetylene (98%), trimethylsilyl azide (94%), and diethylamine (99%) were purchased from Alfa Aesar (Ward Hill, MA, USA). Sodium nitrite (97%), phosphate buffered saline (PBS) tablets, and copper(II) chloride dihydrate were obtained from EMD Chemicals (Gibbstown, NJ, USA). Glutathione (98%) was purchased from AMRESCO (Solon, OH, USA). Low molecular weight chitosan (96% deacetylated) and copper (I) iodide (99.5%) were purchased from Sigma-Aldrich (St. Louis, MO, USA). Deionized water (18.2 M $\Omega$ ·cm) was obtained from a Millipore Direct-Q water purification system (EMD Millipore, Billerica, MA, USA). Ultrahigh purity nitrogen and oxygen gases were supplied by Airgas (Denver, CO, USA). Bis(triphenylphosphine)palladium(II) dichloride (98%) was purchased from TCI America (Portland, OR, USA). All materials were used as received without any further purification.

### 4.2.2 Characterization methods

Powder X-ray diffraction (pXRD) measurements and ATR-FTIR were used to examine the incorporation of CuBTTri within chitosan. All pXRD measurements were made using a Bruker D-8 Discover DaVinci X-ray diffractometer (Cu-K $\alpha$  X-ray source, line focus) (Bruker, Billerica, MA, USA). A 0.6 mm divergent slit was placed on the primary beam side and a high-resolution energy-dispersive LYNXEYE-XE-T detector on the diffracted beam side during the XRD studies. XRD measurements were performed with Soller slits on the primary and diffracted beam side (2.5° separation). The instrument alignment was tested using the NIST 1976b SRM. All measurements were performed from 4 – 50 $\Theta$  with a step count of 1.0. ATR-FTIR spectra were obtained in the range of 600 – 4000 cm<sup>-1</sup> on a Nicolet 6700 FTIR spectrometer equipped with a Smart iTR ATR

sampling module and ZnSe crystal plate (Thermo Electron Corporation, Madison, WI, USA). Images of chitosan/CuBTTri membranes were acquired using a JEOL JSM-6500F scanning electron microscope with an accelerating voltage of 10.0 kV and a working distance of 10.0 mm (JEOL USA Inc., MA, USA). All samples were placed under vacuum and coated with 20 nm of gold prior to runs. Images were taken at magnifications of 250×, 1000×, 2000×, and 3000×. All data were processed using TEAM Software. Thermogravimetric analysis (TGA) was performed under nitrogen on a TA Instruments Q500 thermogravimetric analyzer at a rate of 5 °C/min from 25 to 500 °C (New Castle, DE, USA), and data was processed using TA Instruments Universal Analysis 2000.

#### **4.2.3 Preparation of copper(II) benzene -1,3,5-tris(1*H*-1,2,3-triazole-5-yl)**

1,3,5-Tris(1*H*-1,2,3-triazol-5-yl)benzene (H<sub>3</sub>BTTri) was synthesized following the method reported by Demessence *et al.* and suspended (225 mg) in 10 mL of DMF.<sup>28</sup> This mixture was treated with 0.1 M hydrochloric acid to dissolve the triazole, and then copper(II) chloride dihydrate (383 mg) was added to the solution. After thorough agitation to ensure dissolution of all solids, the mixture was heated at 100 °C for 3 d to form CuBTTri-DMF as a dark violet precipitate. CuBTTri-DMF was isolated by centrifugation and washed with DMF and Millipore water, then heated in water at 80 °C for 3 d to produce CuBTTri-H<sub>2</sub>O as a light purple solid. This solid was isolated by centrifugation, dried, and subsequently characterized by ATR-FTIR and pXRD.

#### **4.2.4 Preparation of chitosan membranes.**

Chitosan (2.5 g) was dissolved in 100 mL of 1% acetic acid, and the resulting water-soluble chitosan acetate was isolated by lyophilization. To prepare chitosan membranes, chitosan acetate (180 mg) was dissolved in 6 mL of Millipore water, followed by the addition of CuBTTri-H<sub>2</sub>O (20 mg) to form a suspension. This mixture was allowed to air-dry within a PTFE mold and the

prepared film was treated twice with 100 mL of 250 mM pH 8.0 sodium phosphate buffer to produce a flexible hydrated sheet. This material was washed with  $5 \times 100$  mL of Millipore water, and subsequently punched into smaller 13 mm diameter membranes. Chitosan control membranes were prepared without CuBTri-H<sub>2</sub>O, following an otherwise identical procedure.

#### **4.2.5 Synthesis of S-nitrosoglutathione.**

GSNO was prepared using a protocol adapted from a previously reported synthesis.<sup>29</sup> 1.53 g of glutathione was suspended in 8 mL of water at 0 °C, followed by the addition of 2.5 mL of 2 M hydrochloric acid and 0.345 g of sodium nitrite. This mixture was stirred at 0 °C for 40 min, then the precipitated solid was isolated by filtration and washed with ice-cold water, acetone, and diethyl ether. The resulting light pink powder was placed under vacuum to remove residual solvent and stored at -20 °C in the absence of light. Following synthesis, ICP-AES analysis of an aqueous GSNO solution showed no copper detected. UV-vis:  $\lambda$  335 ( $\pi \rightarrow \pi^*$ ), 545 nm ( $n_N \rightarrow \pi^*$ ).

#### **4.2.6 Membrane swelling properties.**

Water swelling of chitosan and chitosan/CuBTri membranes was determined gravimetrically by obtaining their dry masses ( $W_d$ ), followed by immersion in Millipore water for 24 h. Samples were then withdrawn and reweighed ( $W_w$ ) after the removal of excess water. The following calculation was then applied to determine the overall water uptake and swelling ratio of each sample.<sup>30</sup>

$$\% \text{ Swelling} = \frac{W_w - W_d}{W_d} * 100\%$$

#### **4.2.7 Measurement of nitric oxide formation.**

NO release measurements were obtained using Sievers chemiluminescence-based nitric oxide analyzers (NOA 280i, GE Analytical, Boulder, CO, USA). Calibration was performed with ultrahigh purity nitrogen (0 ppm NO) and 45 ppm of NO/nitrogen. Prior to use, dry membranes

were immersed in Millipore water overnight to produce 13 mm diameter hydrated membranes. In each experiment, a single chitosan/CuBTTri ( $n \geq 3$ ) or chitosan control ( $n \geq 3$ ) membrane was suspended in 5 mL deoxygenated PBS (pH 7.4) in a custom analysis cell connected directly to an NO analyzer under a constant flow/purge of nitrogen gas and protected from exposure to light. Baseline was acquired for several minutes, then an aqueous GSNO solution was injected into the cell to produce an initial concentration of 20  $\mu\text{M}$ . After GSNO injection, each experiment was allowed to continue until NO detection returned to the baseline level. As an additional control, the NO release profile from the decomposition of GSNO in the absence of membranes was also obtained. In all cases, gas phase NO concentration (ppb/ppm) was used to determine total NO release (mol) using an instrument-specific calibration constant obtained from the reduction of sodium nitrite. Following each experiment, the membrane was removed and the buffer solution was analyzed for copper content using ICP-AES. To evaluate reuse of the chitosan/CuBTTri membranes, each previously tested membrane was re-suspended in Millipore water overnight and the previously described experimental procedure was repeated.

#### **4.2.8 Mass spectrometry analysis.**

The products formed following exposure of CuBTTri to GSNO were determined by suspension of approximately 20 mg of chitosan/CuBTTri membrane in a 1 mM solution of GSNO/Millipore water. The experiment was protected from light and maintained at 37 °C until disappearance of the characteristic red/pink color of GSNO. A control experiment was similarly conducted using chitosan membrane without CuBTTri (intended to reflect thermal decomposition of GSNO), while a second control experiment involved exposure of GSNO to 365 nm UV light using a 100 W Blak-Ray B-100AP UV lamp (UVP, Upland, CA, USA). The solutions were subsequently analyzed using an Agilent 6224 LC-MS (Agilent Technologies, Palo Alto, CA).

## 4.3 Results and discussion

### 4.3.1 Synthesis and characterization of copper(II) benzene -1,3,5-tris(1*H*-1,2,3-triazole-5-yl) and chitosan/ copper(II) benzene -1,3,5-tris(1*H*-1,2,3-triazole-5-yl) composite materials

Chitosan-based biomaterials have been shown to accelerate the wound healing process, resulting in significant overlap with the wound-healing properties of NO. Although previous reports have examined the inclusion of NO donor moieties within chitosan, this report is the first to evaluate an alternative approach involving the incorporation of CuBTTri, a copper-based MOF that has demonstrated the ability to promote release of NO from endogenous RSNOs. As previously described by Demessence et al., the cubic sodalite framework of CuBTTri consists of  $[\text{Cu}_4\text{Cl}]^{7+}$  square planar units bound to BTTri<sup>3-</sup> ligands. Within this structure, each triazolate ligand interacts with six distinct copper sites in  $[\text{Cu}_4\text{Cl}]^{7+}$  units. This fundamental building unit is depicted in Figure 4.1a. Interactions between the triazolate ligands and copper produce an increase in metal-ligand bond strength, conferring greater water stability in comparison to many copper carboxylate based structures.

To prepare chitosan/CuBTTri membranes, water-soluble chitosan acetate was dissolved in Millipore water and CuBTTri was blended into the mixture to produce membranes containing 10% w/w MOF (**Figure 4.2**). The polysaccharide was deprotonated and rendered insoluble by treatment with 250 mM pH 8 phosphate buffer, resulting in 13 mm diameter circular chitosan membranes containing  $295 \pm 8$  nmol of Cu  $\text{mg}^{-1}$  (11% w/w CuBTTri), as determined by dissolution and subsequent copper determination *via* ICP-AES. While aqueous sodium hydroxide is typically utilized to cure chitosan membranes, it was observed that treatment of CuBTTri with concentrated base had an adverse effect on the integrity of the MOF.<sup>31</sup> Similarly, immersion of chitosan acetate/CuBTTri membranes in 10% sodium hydroxide produces a visual color change (dark violet

to blue) and the loss of CuBTTri diffraction peaks when examined by pXRD. In order to ensure preservation of the MOF, comparatively mild pH 8 phosphate buffer was used as an alternative method of neutralizing the membranes. To isolate the effect of CuBTTri in subsequent analyses,

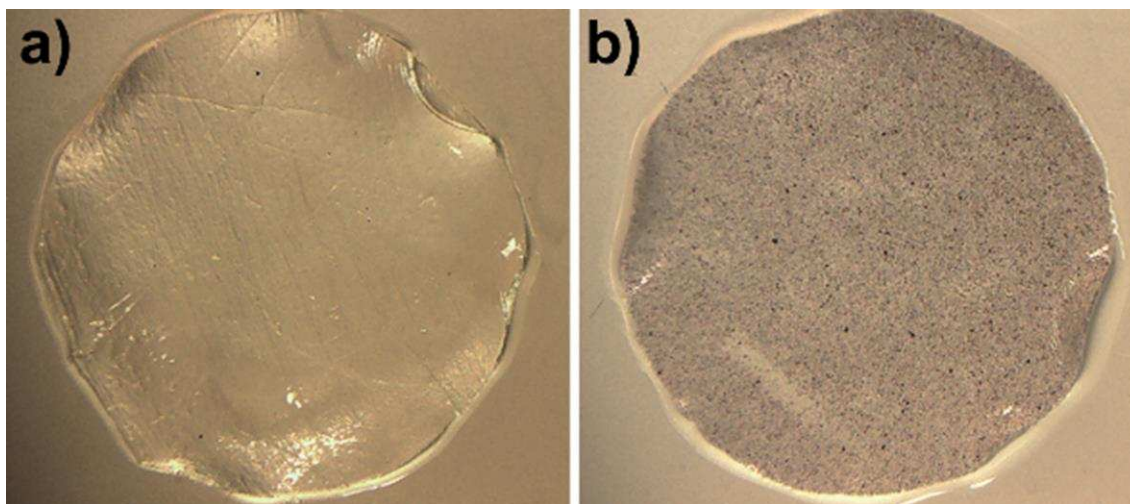


**Figure 4.2** Images of (a) chitosan membrane and (b) chitosan/CuBTTri membrane, depicting the dispersion of CuBTTri throughout the material. Images were taken after the materials had been hydrated by immersion in deionized water. Reproduced by permission of the American Chemical Society.

control membranes were prepared without addition of the MOF. Both chitosan/CuBTTri and chitosan control membranes were characterized by ATR-FTIR, pXRD, and SEM. IR absorptions characteristic of chitosan are present in the control membranes, including the broad hydroxyl O–H stretch feature occupying the region of  $3650\text{--}3000\text{ cm}^{-1}$  (**Figure 4.3**). This feature overlaps with the bands associated with the C2 primary amine, and both asymmetric and symmetric N–H stretching modes are identifiable at  $3355$  and  $3278\text{ cm}^{-1}$ . Additional diagnostic bands are observed at  $2849$  (C–H stretch),  $1636$  (amide I),  $1577$  (amide II),  $1056$ , and  $1025$  (C–O stretch). These typical features are accompanied by new absorptions at  $2917$  (acetate  $\text{CH}_3$ ),  $1542$  (acetate salt) and  $1258\text{ cm}^{-1}$  (phosphate), arising from preparation of the membrane. Incorporation of CuBTTri produces additional features characteristic of the MOF at  $1617$  (C=C stretch),  $830$ , and  $775\text{ cm}^{-1}$  (C–H out-of-plane bend). Furthermore, finished membranes exhibited the major pXRD diffraction

peaks associated with CuBTTri (**Figure 4.3b**). The pXRD spectrum in conjunction with ATR-IR data indicates that the MOF is indeed present and has retained crystallinity after incorporation into the chitosan membrane.

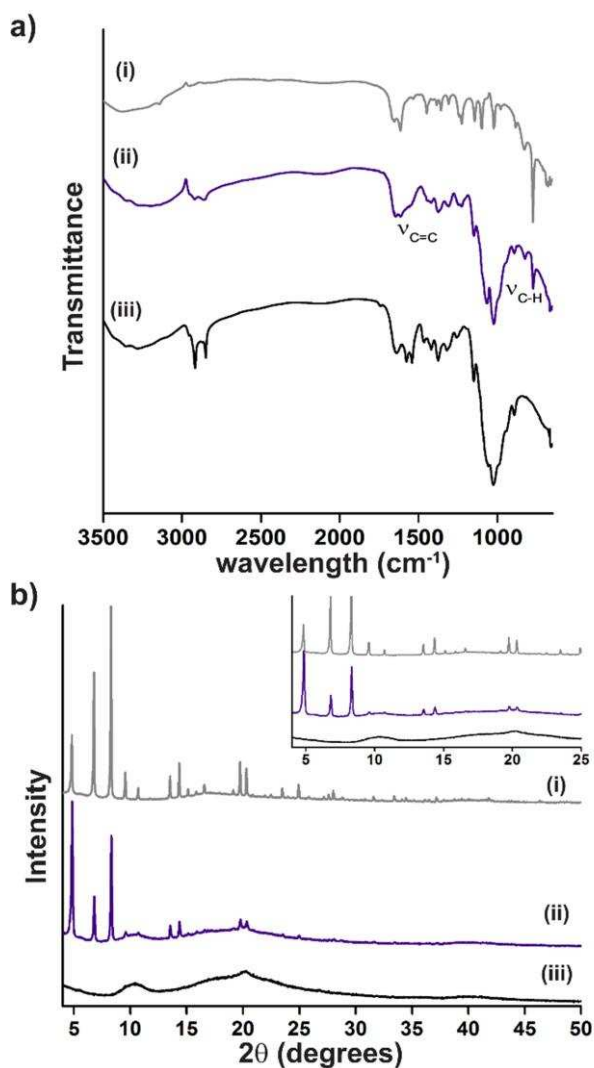


**Figure 4.3** (a) ATR-FTIR spectrum for (i) CuBTTri, (ii) chitosan/CuBTTri membrane, and (iii) chitosan. In (a), the weak C=C stretch and more prominent C-H out-of-plane bend from CuBTTri (i) are conserved in the spectrum of chitosan/CuBTTri (ii). (b) pXRD diffraction patterns of (i) CuBTTri, (ii) chitosan/CuBTTri membrane, and (iii) chitosan. Inset: 4-25 $\theta$ . Reproduced by permission of the American Chemical Society.

Imaging of the membranes by SEM showed clear incorporation of CuBTTri within the chitosan matrix (**Figure 4.4c – f**) with distinct crystals observed at the membrane surface. In Figure 4.4b, the distribution of CuBTTri at the surface of the membrane is shown. At greater

magnification, the octahedral morphology of CuBTTri was evident, and the crystals displayed an apparent trimodal particle size distribution with an overall range of 1 to 15  $\mu\text{m}$  (**Figure 4.4e, f**). The materials were further evaluated for overall copper distribution by SEM-EDX using a copper

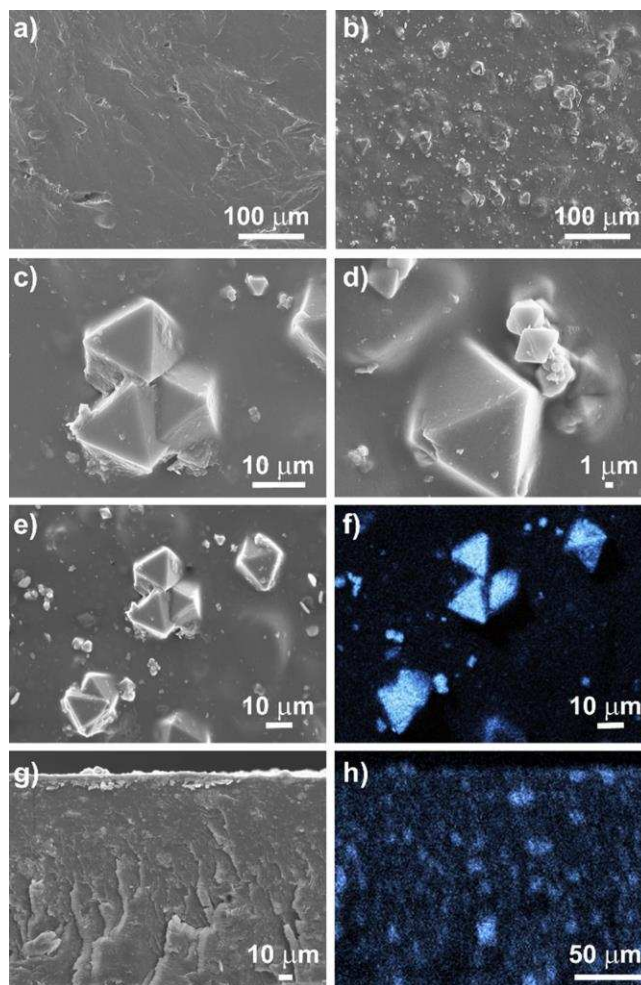


**Figure 4.4** (a) 250 $\times$  magnification of chitosan membrane, (b) 250 $\times$  (c) 2000 $\times$ , and (d) 3000 $\times$  of chitosan/CuBTTri membrane. (e) 1000 $\times$  magnification of chitosan/CuBTTri membrane and (f) 1000 $\times$  magnification with EDX copper analysis overlaid. (g) 500 $\times$  magnification of cross-sectional of chitosan/CuBTTri membrane (h) EDX copper analysis overlay of cross-section. Reproduced by permission of the American Chemical Society.

analysis probe. **Figure 4.4e** and **Figure 4f** depict the copper overlay on the SEM image of the chitosan/CuBTTri membrane. As can be observed, the overall distribution of copper is concentrated in regions that contain CuBTTri. Cross-sectional SEM images of non-hydrated chitosan/CuBTTri membrane indicated a thickness of 150  $\mu\text{m}$ . Additionally, SEM-EDS was

performed on the cross-section to assess CuBTTri particle distribution throughout the bulk of the membrane (**Figure 4.4 g, h**). This analysis showed copper distributed within the membrane, with greater concentration in regions of noticeable particle agglomeration (**Figure 4.5**). Taken together, these findings suggest dispersion of CuBTTri throughout the entire membrane, with certain areas of higher concentration indicative of CuBTTri agglomeration following incorporation within the polymer matrix.<sup>32</sup>

Additionally, the water swelling ratio of each material was determined gravimetrically after

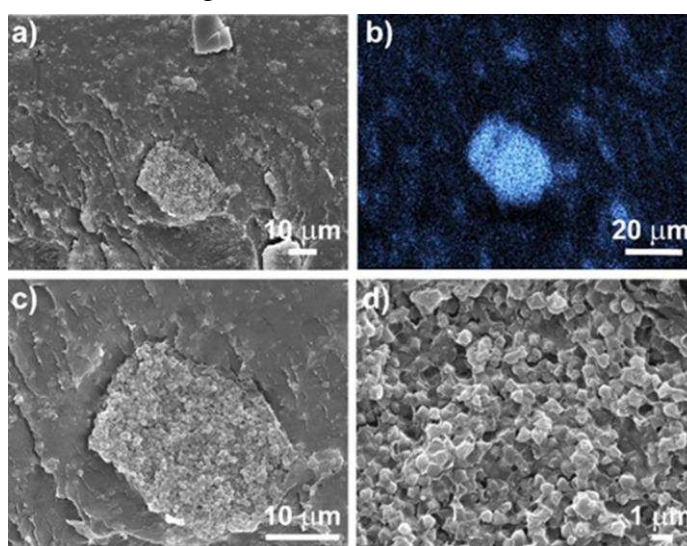


**Figure 4.5** Cross sectional SEM images of chitosan/CuBTTri (a) 1000× magnification (b) 1000× magnification with EDS overlay for copper distribution where it can be seen the copper is concentrated in areas with high concentrations of CuBTTri. (c) 2000× magnification (d) 7500× magnification. Reproduced by permission of the American Chemical Society.

24 h of immersion to assess if incorporation of CuBTTri into the chitosan membrane produced changes to the ability of the polymer to uptake water. Chitosan/CuBTTri membranes exhibited  $244 \pm 26\%$  swelling, while chitosan control membranes swelled by  $240 \pm 26\%$ . These results suggest that incorporation of CuBTTri does not have a significant impact on the ultimate water uptake of the chitosan materials. The stability of both the chitosan membrane and incorporated CuBTTri at pH 8 was established by characterization carried out subsequent to a preparatory step

performed in pH 8 phosphate buffer (**Figure 4.3b**). Behavior of the membrane under other pH conditions was assessed by immersing the materials in Millipore water and adjusting the pH with dilute hydrochloric acid or sodium hydroxide. The stability of the membrane when directly exposed to either 1 M hydrochloric acid or sodium hydroxide was also examined. Immersion in 1 M hydrochloric acid produced rapid decolorization and deterioration of the membrane, resulting

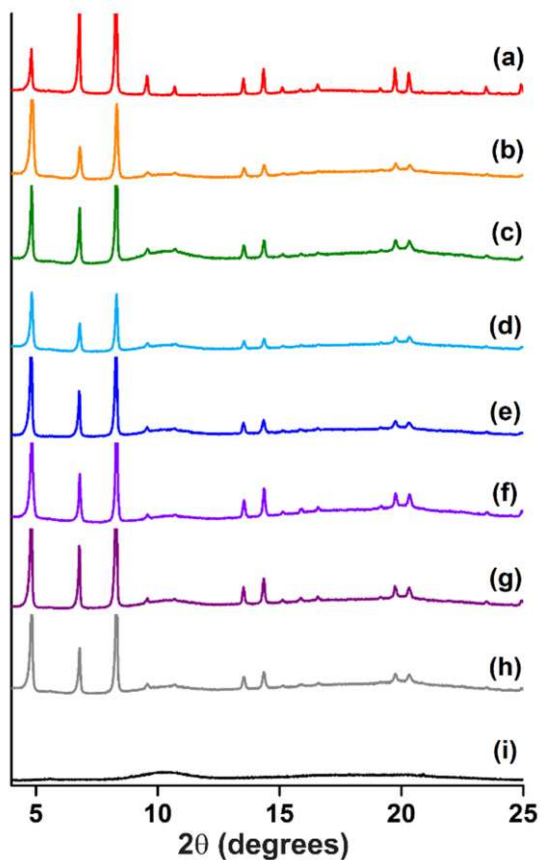


**Figure 4.6** pXRD diffraction patterns (a) CuBTTri powder (b) chitosan/CuBTTri membranes (c) after exposure to platelet-rich plasma (d) after exposure to whole blood (e) after exposure to pH 4 water (f) after exposure to pH 5 water (g) after exposure to pH 6 water (h) after exposure to pH 9 water (i) after exposure to 1M NaOH. Chitosan/CuBTTri membranes exposed to 1 M HCl resulted in complete dissolution of the material. Reproduced by permission of the American Chemical Society.

from both the dissolution of chitosan and digestion of the MOF. At pH 4-5, the membrane exhibited swelling and a change in appearance consistent with the early stages of dissolution. This outcome was anticipated from the known solubility of chitosan following protonation in hydrochloric acid. Despite the onset of polymer dissolution, pXRD of the membrane indicated that

CuBTTri remained intact under mildly acidic conditions (**Figure 4.6e, f**). At pH values of 6 and 9, the membrane retained a normal appearance and did not exhibit signs of swelling or deterioration. Subsequent pXRD characterization supported the survival of the MOF within this pH range, as well (**Figure 4.6g, h**). Immersion of the membrane in 1 M NaOH resulted in a pronounced color change from dark violet (imparted by CuBTTri) to blue and associated loss of the MOF diffraction pattern (**Figure 4.6i**). To examine the ability of the chitosan/CuBTTri membrane to tolerate biological media, samples of the material were immersed in both whole blood and platelet-rich plasma for two hours, followed by rinsing with water. The stability of the MOF was then evaluated by pXRD, which showed the retention of all major diffraction peaks

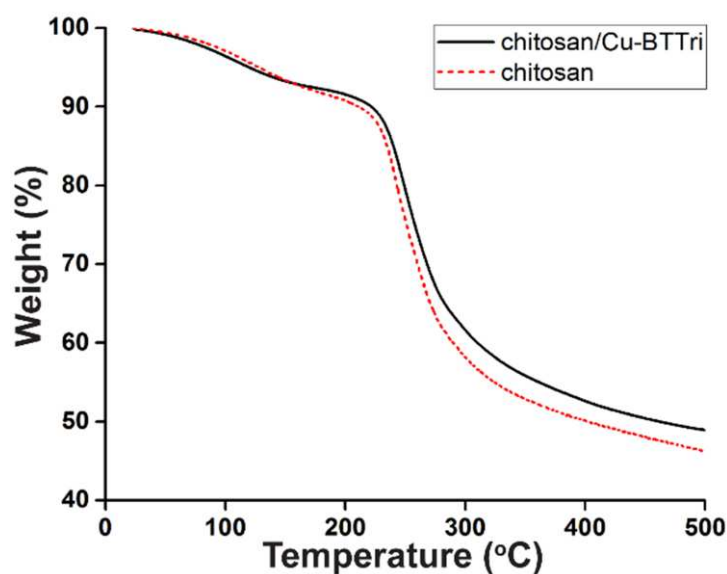


**Figure 4.7** Representative thermogravimetric analysis of chitosan and chitosan/CuBTTri membrane under nitrogen flow. Reproduced by permission of the American Chemical Society.

(**Figure 4.6c, d**). Analysis of chitosan/CuBTTri membrane by TGA yielded an onset decomposition temperature of  $232 \pm 0.12$  °C, a value that was consistent with the decomposition of chitosan alone (**Figure 4.7**). In general, CuBTTri membrane appeared to demonstrate appropriate chemical and thermal stability for potential use in biomedical applications, where extreme pH or temperature conditions are not anticipated.

### 4.3.2 Evaluation of enhanced nitric oxide generation from *S*-nitrosoglutathione with chitosan/ copper(II) benzene -1,3,5-tris(1*H*-1,2,3-triazole-5-yl) membrane

As previously noted, NO exhibits numerous beneficial properties, including the ability to accelerate healing when delivered to the site of an injury.<sup>4,6</sup> It was reasoned that the ability of CuBTTri to significantly enhance the rate of NO release from biologically-relevant RSNOs could potentially permit the conscription of these endogenous species as useful sources of NO. The retention of this function when incorporated within a chitosan membrane may allow for the future development of blood-contacting materials exhibiting both the desirable antimicrobial and wound-healing effects of chitosan, as well as the ability to generate enhanced levels of therapeutic NO

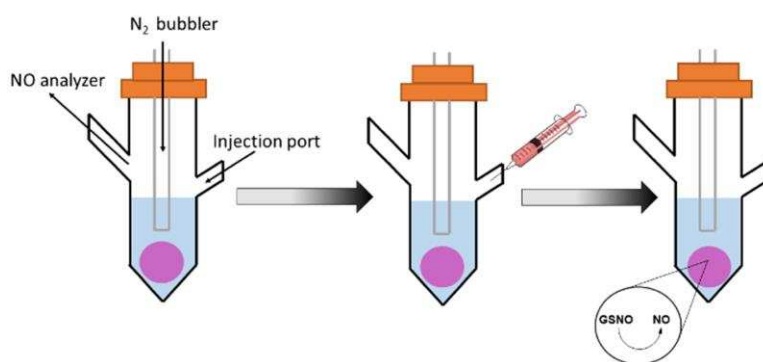


**Figure 4.8** Schematic illustrating the NO analyzer cell, where chitosan/CuBTTri membrane is suspended in pH 7.4 PBS at 37 °C, followed by injection of GSNO and subsequent chemiluminescence-based monitoring of NO formation. Reproduced by permission of the American Chemical Society.

from endogenous sources. To assess the ability of chitosan/CuBTTri membranes to generate NO from physiologically-relevant GSNO, membranes were swelled in Millipore water (18.2 MΩ·cm) and subsequently immersed in pH 7.4 10 mM phosphate buffered saline (PBS) at 37 °C inside custom gas-flow analysis cells connected to Sievers chemiluminescence-based NO analyzers (NOA 280i) (**Figure 4.8**). The effect of chitosan/CuBTTri membranes on NO formation from GSNO was evaluated through the addition of 100 nmol of GSNO to the analysis cell (sufficient to produce a 20 μM initial concentration), and the resulting gas-phase NO concentration (ppb) was

recorded under nitrogen atmosphere until reaching baseline levels ( $n \geq 3$ ) (**Figure 4.8**). Subsequently, a predetermined NO calibration constant (mol of NO ppb<sup>-1</sup> s<sup>-1</sup>) was used to determine the overall NO release (mol). Control experiments ( $n \geq 3$ ) were performed using GSNO alone, chitosan membranes without incorporated CuBTtri, and CuBTtri in free particulate form (equivalent to the mass incorporated within chitosan/CuBTtri membranes). In all cases, experiments were protected from light to avoid photolytic decomposition of GSNO. At the end of experiments involving chitosan/CuBTtri membranes, the reaction medium was exposed to light to test for the presence of residual, non-decomposed GSNO.

When GSNO was added to analysis cells containing chitosan/CuBTtri membranes, a noticeable increase in NO generation was observed in comparison to the behavior of GSNO alone (**Figure 4.9a**). In the presence of chitosan/CuBTtri membranes, NO generation was found to continuously increase over the duration of the experiment until depletion of the available GSNO after approximately 4 h (**Figure 4.9a**). In contrast, the decomposition and corresponding NO release of GSNO alone remained steady over the same interval, indicating the clear role of chitosan/CuBTtri membranes in promoting NO formation from the GSNO substrate. Chitosan/CuBTtri membranes induce a mean release of  $97 \pm 3$  nmol NO (mean  $\pm$  SD) over  $4.3 \pm 0.3$  h, resulting in 97% recovery of total theoretical NO (**Figure 4.9b, Table 4.1**). Comparatively, GSNO decomposition in the absence of chitosan/CuBTtri membranes resulted in the recovery of  $1.5 \pm 0.7$  nmol NO (1.5% of theoretical) over the same mean interval (**Figure 4.9b, Table 4.1**). In order to provide support that membrane-enhanced NO generation was primarily attributable to the inclusion of CuBTtri, chitosan membranes without incorporated MOF were assessed, and a moderate increase in GSNO decomposition ( $9.8 \pm 0.3$  nmol NO, 9.8% of theoretical) was observed (**Figure 4.9b, Table 4.1**). This elevation was constant and did not result in the distinctive NO

release profile produced by CuBTTri/membranes, and may be attributable to the presence of trace metal ions chelated by the chitosan matrix (*e.g.* Fe<sup>2+</sup>), which have been previously demonstrated to enhance NO generation.<sup>33,34</sup> Overall, it was observed that chitosan/CuBTTri membranes are capable of producing a 65-fold increase in NO generation over the thermal baseline decomposition of GSNO, with a significantly smaller 7-fold elevation seen for the chitosan control membranes.

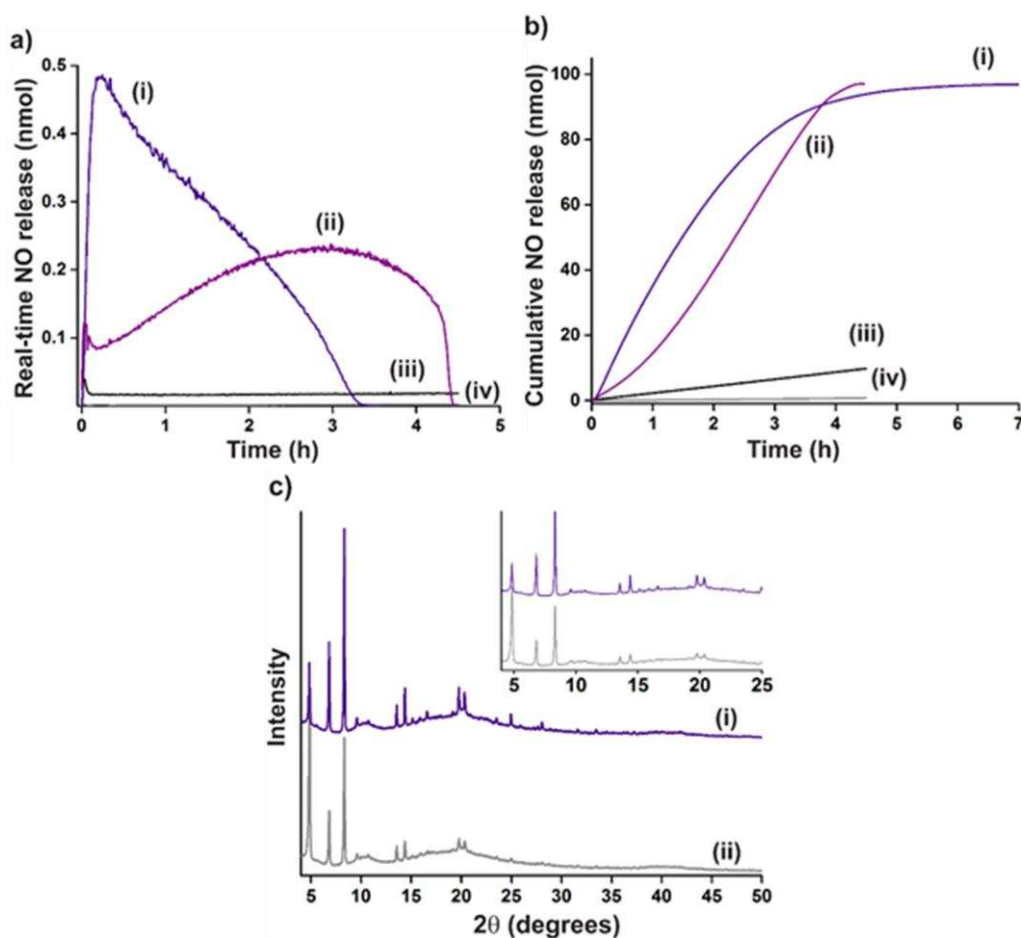


**Figure 4.9** (a) Representative real-time NO release from (i) CuBTTri + GSNO (ii) chitosan/CuBTTri membranes + GSNO (iii) chitosan + GSNO, and (iv) GSNO assessed under physiological conditions (PBS, pH 7.4, 37 °C). (b) Cumulative NO release from (i) CuBTTri + GSNO (ii) chitosan/CuBTTri membranes + GSNO (iii) chitosan + GSNO, and (iv) GSNO all under physiological conditions (PBS, pH 7.4, 37 °C). For (i) and (ii) data collection ended after the depletion of GSNO. (c) (i) pXRD diffraction pattern of chitosan/CuBTTri materials taken after NO analyzer experiment and (ii) prior to the NO analyzer runs, pXRD clearly shows the retention of all diffraction peaks. Inset 4-25 $\theta$ . Reproduced by permission of the American Chemical Society.

After the chitosan/CuBTTri membranes were demonstrated to successfully enhance NO generation from GSNO, they were reused to produce NO from subsequent additions of GSNO (up to 3 additional times). Following initial experiments, the membranes were removed from the reaction medium and suspended in Millipore water for 1 d. The NO generation experiment was then repeated as described previously (3 times), with a consistent quantitative NO recovery (**Table 4.2**). This result suggests that the chitosan/CuBTTri membranes possess the capability for reuse, potentially indicating the ability to continuously generate NO from endogenous GSNO. This property may reduce concerns related to the finite loading currently associated with many NO-releasing polymeric materials.

**Table 4.1** Total average NO release from GSNO. Data reported as the mean  $\pm$  SD ( $n > 3$ )

| Substrate               | Total NO Release (nmol) | Total Recovery (%) |
|-------------------------|-------------------------|--------------------|
| GSNO                    | 1.5 $\pm$ 0.7           | 1.5 $\pm$ 0.7      |
| Chitosan + GSNO         | 9.8 $\pm$ 0.3           | 9.8 $\pm$ 0.3      |
| Chitosan/CuBTTri + GSNO | 97 $\pm$ 3              | 97 $\pm$ 3         |
| CuBTTri + GSNO          | 97 $\pm$ 6              | 97 $\pm$ 6         |

**Table 4.2** Total average NO release for chitosan/CuBTTri membranes after reuse. Data reported as the mean  $\pm$  SD ( $n \geq 3$ ).

| Chitosan/CuBTTri membrane + GSNO | Total NO Release (nmol) |
|----------------------------------|-------------------------|
| Cycle 1                          | 97 $\pm$ 3              |
| Cycle 2                          | 107 $\pm$ 7             |
| Cycle 3                          | 98 $\pm$ 3              |

#### 4.3.3 Impact of copper(II) benzene -1,3,5-tris(1H-1,2,3-triazole-5-yl) immobilization on enhancement of nitric oxide generation

To evaluate the effect of CuBTTri immobilization within chitosan on the activity of the MOF, the ability of free CuBTTri particles to decompose GSNO was examined for comparison. CuBTTri particles were found to promote the release of 97  $\pm$  6 nmol NO (97% of theoretical) over 5.0  $\pm$  1.6 h, indicating the absence of a statistical difference between the performance of

chitosan/CuBTTri membranes and free CuBTTri particles (**Figure 4.9a and 4.9b, Table 4.1**). In contrast, it was previously shown that incorporation of CuBTTri within a biomedical grade polyurethane resulted in an 8-fold reduction in the activity of CuBTTri.<sup>14</sup> Additionally, CuBTTri particles incorporated into poly(vinyl chloride) (PVC) were shown to require 10 h to reach a steady rate of NO release in the presence of SNAP.<sup>15</sup> These observed differences in NO generation may be attributable to the restricted ability of GSNO to diffuse through hydrophobic polymer matrices, inhibiting interaction with incorporated CuBTTri.<sup>15,35</sup> This hypothesis is supported by the calculated swelling ratio of 244% for chitosan/CuBTTri membranes, indicating significant uptake of water, while PVC and polyurethane compositions exhibit weight increases from water uptake ranging from 0.02% to 20%.<sup>36-38</sup> Since hydrophilic chitosan membranes readily swell in the presence of water, this process may encourage uptake and diffusion of GSNO, permitting more rapid interaction with the MOF. It was also observed that CuBTTri particles showed wider variability in the overall time required to fully decompose GSNO, which ranged from 3 to 7 h. This variability may be due to random particle agglomeration resulting in decreased access to CuBTTri active sites, while immobilization of the MOF within the chitosan membrane limits this outcome. Because incorporation of CuBTTri within chitosan reduces variability in reaction time, it allows for increased control of NO generation from GSNO. For this reason, further understanding of these types of MOF/polymer composite systems may provide valuable insight into the tunability of such materials for future applications.

#### **4.3.4 Evaluation of structural integrity and copper leaching**

Following NO release experiments with GSNO, the chitosan/CuBTTri membranes were analyzed by pXRD to ensure that they remained structurally intact following NO generation. The observed pXRD pattern retained all major diffraction peaks corresponding to CuBTTri, supporting

that the MOF remains intact over the course of the experiment (**Figure 4.9c**). Furthermore, the buffer solutions remaining at the end of each experiment were subjected to copper content determination by ICP-AES after the removal of the chitosan/CuBTTri material. This analysis tests for the presence of copper that may have been released by deterioration of the MOF or detachment of fine MOF particles. Results indicated that  $1.5 \pm 1.1 \times 10^{-9}$  mol copper was present in solution following exposure to GSNO during NO release experiments, corresponding to  $0.10 \pm 0.07\%$  of theoretical (based on the mass of incorporated CuBTTri) and resulting in a mean copper concentration of approximately  $3 \times 10^{-7}$  M. This lack of significant copper leaching was particularly encouraging due to the fact that solution-phase glutathione (the parent thiol of GSNO) is an established copper chelator.<sup>39</sup>

GSNO decomposition experiments performed in the presence of copper(II) chloride at a concentration of  $3 \times 10^{-7}$  M did not result in a greater rate of NO production, as evaluated by chemiluminescence-based detection. This outcome reduces the likelihood that dissolved copper ions contribute to the acceleration of the NO-forming decomposition of GSNO, and is consistent with reports from Williams *et al.*, where higher copper concentrations of  $10^{-6}$  M were needed to initiate decomposition.<sup>9</sup> Over a total of three subsequent cycles (each performed in quadruplicate), a mean copper quantity of  $5.2 \pm 3.5 \times 10^{-9}$  mol copper was found in solution (corresponding to  $0.3 \pm 0.2\%$  of theoretical), with individual cycles varying from  $1.9 \pm 0.3 \times 10^{-9}$  to  $8.8 \pm 9.6 \times 10^{-9}$  mol. These values were not found to statistically differ from the amount of copper determined in the original experiment, and generally indicate that loss of copper from the membranes remains low. To contrast potential MOF-related copper leaching from chitosan/CuBTTri membranes with that from copper(II) ions directly chelated to chitosan, 13 mm chitosan membranes were exposed to copper(II) chloride to prepare additional control materials containing an average of 300 nmol of

Cu mg<sup>-1</sup>. These membranes were exposed to GSNO as described in previous experiments, and the buffer solution was subsequently tested for copper content. Notably, the NO-forming reaction completed within  $0.68 \pm 0.08$  h and resulted in the recovery of  $86 \pm 6$  of theoretical NO, indicating a significantly faster rate of GSNO decomposition. More importantly, ICP-AES was used to determine a solution-phase copper content equivalent to  $3.6 \pm 0.8\%$  of theoretical, indicating up to 36-fold greater leaching than in the case of chitosan/CuBTTri membranes.

Previous publications have described the incorporation of copper nanoparticles or copper complexes within polymers to produce materials capable of promoting NO release from RSNOs. These approaches often rely upon the deliberate generation of copper ions or use of labile complexes that readily release copper ions into solution.<sup>40,41</sup> In one significant report, Hwang et al. covalently attached copper(II)-cyclen complexes to biomedical polymers and evaluated these materials for their ability to induce NO-forming RSNO decomposition.<sup>42</sup> In this example, copper leaching as high as 25% was observed, which may limit applicability due to toxicity concerns. In comparison, the substantially lower copper leaching observed for chitosan/CuBTTri membrane suggests greater retention of copper attributable to the stability of the MOF. In the case of potential biological applications, this lower level of copper leaching may reduce concerns related to copper toxicity.<sup>43</sup>

#### **4.3.5 Determination of reaction products**

To complement data supporting the preservation of CuBTTri following NO release experiments with chitosan/CuBTTri membranes, an additional experiment was performed in which chitosan/CuBTTri membrane was exposed to a higher 1 mM concentration of GSNO in Millipore water at 37 °C. This solution was subsequently analyzed *via* mass spectrometry to screen for evidence of CuBTTri degradation, which was anticipated to regenerate the triazole ligand

H<sub>3</sub>BTtri. This compound was not detected in solution following the experiment, supporting the lack of MOF degradation. The thermal decomposition of GSNO in the presence of chitosan membrane (without incorporated CuBTtri) and the UV-initiated decomposition of GSNO in the absence of any polysaccharide were carried out for comparative purposes. In all cases, GSSG (C<sub>20</sub>H<sub>32</sub>N<sub>6</sub>O<sub>12</sub>S<sub>2</sub>) was identified as the major organic decomposition product of GSNO (**Figure 4.10**). In comparative experiments performed using chitosan membrane at 37 °C or GSNO alone in the presence of UV light, the formation of GSSG was anticipated by the equation  $2\text{RSNO} \rightarrow 2\text{NO} + \text{RSSR}$ , which describes the decomposition of RSNO to form the corresponding disulfide dimer.<sup>9</sup> In the case of chitosan/CuBTtri membranes, the identification of GSSG provides new evidence that the end products of the MOF-accelerated reaction are consistent with the decomposition under thermal or UV-mediated conditions. In general, the mass spectra resulting from analysis of GSNO decomposition solutions containing either chitosan/CuBTtri or chitosan membranes were consistent with one another, while the GSNO solution exposed to UV light (without the presence of any material) predictably did not exhibit the peaks associated with the polysaccharide (*e.g.* monomeric glucosamine or *N*-acetylglucosamine). In the case of thermal or UV-induced decomposition, NO-forming homolytic cleavage of the S-N bond is believed to be followed by the combination of thiyl radicals to form disulfide.<sup>9</sup> It has been observed that dissolved copper ions are capable of catalyzing NO release from RSNOs, with five- and six-membered copper chelates described as potential mechanistic intermediates.<sup>44</sup> Previous reports examining the use of copper-based MOFs for the generation of NO from RSNOs have suggested that the MOF behaves similarly to copper ions by reduction of the copper(II) sites to copper(I), producing both NO and disulfide (**Figure 4.10**).<sup>9,27,44</sup> However, it has not been previously verified that CuBTtri (or any MOF) forms products consistent with those generated in other known decomposition

pathways. In this study, it is shown that the formation of GSSG accompanies the accelerated NO release from GSNO in the presence of chitosan/CuBTTri membranes, indicating that the ultimate fate of GSNO remains the same when decomposed by the MOF. While the overall mechanism remains unknown, it has been argued that steric considerations prevent the formation of the ring intermediates often invoked in the case of dissolved copper ions. For certain systems, it has been proposed that MOF copper sites may act as Lewis acids that facilitate the formation of NO from RSNOs.<sup>45</sup> A computational study carried out by Li *et al.* suggests that free copper ions interact with an initial RSNO molecule in solution to form a Cu-S bond, accompanied by the release of NO. This process is repeated with a second RSNO molecule to form a CH<sub>3</sub>S-Cu-SCH<sub>3</sub><sup>+</sup> species,

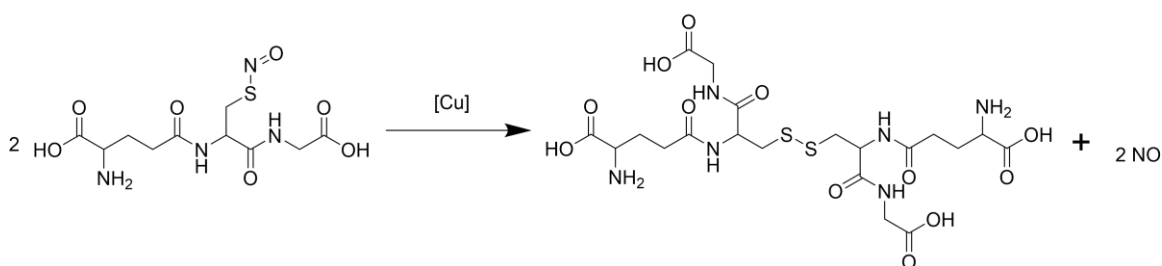


**Figure 4.10** Proposed overall reaction for GSNO in the presence of solution-phase copper ions, resulting in the subsequent formation of NO and oxidized glutathione. Reproduced by permission of the American Chemical Society.

which subsequently leads to disulfide formation and regeneration of the copper species. Comparison of this solution-phase scenario to the MOF Cu-BTC indicated that the approach of the initial RSNO molecule was nearly isoenergetic with free copper, but the addition of a subsequent RSNO molecule to the same copper site or adjacent copper sites displayed a higher energy barrier. This suggests that this particular reaction would only be plausible for a flexible MOF that could allow for distortion around the copper center to accommodate the additional RSNO molecule.<sup>46</sup> Regardless of actual mechanism, the identification of GSSG is a crucial step toward understanding the interaction of copper-based MOFs with RSNOs.

#### 4.4 Conclusions

These findings demonstrate the ability of chitosan/CuBTTri membranes to generate an enhanced level of NO release from GSNO, a compound that occurs naturally in blood as a hypothesized NO storage and transport agent. Preservation of CuBTTri following incorporation within chitosan was verified by pXRD and ATR-FTIR, and SEM revealed the clear distribution of octahedral CuBTTri crystals on the surface of the material. In the presence of 20  $\mu\text{M}$  (100 nmol total) GSNO at physiological temperature and pH, chitosan/CuBTTri membranes produced  $97 \pm 3$  nmol over  $4.3 \pm 0.3$  h, representing a 65-fold increase in NO generation relative to the baseline thermal decomposition of GSNO. Under otherwise identical conditions, CuBTTri powder (without immobilization in chitosan) produced  $97 \pm 6$  nmol NO over  $5.0 \pm 1.6$  h, indicating no significant difference in performance compared to chitosan/CuBTTri membranes. While CuBTTri has been previously shown to induce the accelerated decomposition of synthetic RSNOs such as *S*-nitrosocysteamine and SNAP, this is the first extension of that function to GSNO. Furthermore, inclusion of CuBTTri within chitosan membranes did not result in a significant impairment of function, contrasting with earlier polyurethane and PVC-based systems, where polymeric incorporation diminished the activity of the MOF. Following initial experiments, chitosan/CuBTTri membranes were capable of promoting accelerated NO release for at least three additional cycles. Characterization by pXRD and SEM subsequent to GSNO exposure supported the lack of extensive CuBTTri decomposition, and this outcome was corroborated by the low level of copper leaching as determined by ICP-AES. Moreover, mass spectrometry was used to identify GSSG as the major product of GSNO decomposition in the presence of chitosan/CuBTTri, substantiating the hypothesis that disulfides are formed from RSNOs by copper-based MOFs. Taken together, this work indicates that chitosan-based materials incorporating CuBTTri may be

capable of inducing NO formation from endogenous GSNO in the blood. Examining the assembly and properties of these and similar materials facilitates the use of MOFs for localized NO release, further expanding their potential applications.

## REFERENCES

1. Furukawa, H.; Cordova, K. E.; O’Keeffe, M.; Yaghi, O. M. The Chemistry and Applications of Metal-Organic Frameworks. *Science* **2013**, *341*, 974 – 986.
2. Harding, J. L.; Reynolds, M. M. Metal Organic Frameworks as Nitric Oxide Catalysts. *J. Am. Chem. Soc.* **2012**, *134*, 3330 – 3333.
3. Ignarro, L. J., Ed. Nitric Oxide: Biology and Pathobiology, 2<sup>nd</sup> ed; Elsevier: Amsterdam, 2010.
4. Witte, M. B.; Barbul, A. Role of Nitric Oxide in Wound Repair. *Am. J. Surg.* **2002**, *183*, 406 – 412.
5. Shabani, M.; Pulfer, S. K.; Bulgrin, J. P.; Smith, D. J. Enhancement of Wound Repair with a Topically Applied Nitric Oxide-Releasing Polymer. *Wound Repair Regen.* **1996**, *4*, 353 – 362.
6. Lowe, A.; Bills, J.; Verma, R.; Lavery, L.; Davis, K.; Balkus, K. J., Jr. Electrospun Nitric Oxide Releasing Bandage with Enhanced Wound Healing. *Acta Biomater.* **2015**, *13*, 121 – 130.
7. Stamler, J. S. S-Nitrosothiols in the Blood: Roles, Amounts, and Methods of Analysis. *Circ. Res.* **2004**, *94*, 414 – 417.
8. Giustarini, D.; Milzani, A.; Dalle-Donne, I.; Rossi, R. Detection of S-Nitrosothiols in Biological Fluids: A Comparison Among the Most Widely Applied Methodologies. *J. Chromatogr. B* **2007**, *851*, 124 – 139.
9. Williams, D. L. H. The Mechanism of Nitric Oxide Formation from S-Nitrosothiols (Thionitrites). *Chem. Commun.* **1996**, 1085 – 1091.

10. McAninly, J.; Williams, D. L. H.; Askew, S. C.; Butler, A. R.; Russell, C. Metal Ion Catalysis in Nitrosothiol (RSNO) Decomposition. *J. Chem. Soc., Chem. Commun.* **1993**, 1758 – 1759.
11. Oh, B. K.; Meyerhoff, M. E. Spontaneous Catalytic Generation of Nitric Oxide from S-Nitrosothiols at the Surface of Polymer Films Doped with Lipophilic Copper(II) Complex. *J. Am. Chem. Soc.* **2003**, *125*, 9552 – 9553.
12. Puiu, S. C.; Zhou, Z.; White, C. C.; Neubauer, L. J.; Zhang, Z.; Lange, L. E.; Mansfield, J. A.; Meyerhoff, M. E.; Reynolds, M. M. Metal Ion-mediated Nitric Oxide Generation from Polyurethanes via Covalently Linked Copper(II)-Cyclen Moieties. *J. Biomed. Mater. Res., Part B* **2009**, *91*, 203 – 212.
13. Neufeld, M. J.; Harding, J. L.; Reynolds, M. M. Immobilization of Metal-Organic Framework Copper(II) Benzene-1,3,5-tricarboxylate (CuBTC) onto Cotton Fabric as a Nitric Oxide Release Catalyst. *ACS Appl. Mater. Interfaces* **2015**, *7*, 26742 – 26750.
14. Harding, J. L.; Metz, J. M.; Reynolds, M. M. A Tunable, Stable, and Bioactive MOF Catalyst for Generating a Localized Therapeutic from Endogenous Sources. *Adv. Funct. Mater.* **2014**, *24*, 7503 – 7509.
15. Neufeld, M. J.; Ware, B. R.; Lutzke, A.; Khetani, S. R.; Reynolds, M. M. Water-Stable Metal–Organic Framework/Polymer Composites Compatible with Human Hepatocytes. *ACS Appl. Mater. Interfaces* **2016**, *8*, 19343 – 19352.
16. Kumar, M. N. V. R. A Review of Chitin and Chitosan Applications. *React. Funct. Polym.* **2000**, *46*, 1 – 27.
17. Rinaudo, M. Chitin and Chitosan: Properties and Applications. *Prog. Polym. Sci.* **2006**, *31*, 603 – 632.

18. Croisier, F.; Jérôme, C. Chitosan-based Biomaterials for Tissue Engineering. *Eur. Polym. J.* **2013**, *49*, 780 – 792.
19. Dai, T.; Tanaka, M.; Huang, Y.-Y.; Hamblin, M. R. Chitosan Preparations for Wounds and Burns: Antimicrobial and Wound-Healing Effects. *Expert Rev. Anti. Infect. Ther.* **2011**, *9*, 857 – 879.
20. Azad, A. K.; Sermsintham, N.; Chandkrachang, S.; Stevens, W. F. Chitosan Membrane as a Wound-Healing Dressing: Characterization and Clinical Application. *J. Biomed. Mater. Res., Part B* **2004**, *69*, 216 – 222.
21. Lu, Y.; Slomberg, D. L.; Schoenfisch, M. H. Nitric Oxide-releasing Chitosan Oligosaccharides as Antibacterial Agents. *Biomaterials* **2014**, *35*, 1716 – 1724.
22. Lu, Y.; Shah, A.; Hunter, R. A.; Soto, R. J.; Schoenfisch, M. H. S-Nitrosothiol-modified Nitric Oxide-releasing Chitosan Oligosaccharides as Antibacterial Agents. *Acta Biomater.* **2015**, *12*, 62 – 69.
23. Lutzke, A.; Pegalajar-Jurado, A.; Neufeld, B. H.; Reynolds, M. M. Nitric Oxide-releasing S-Nitrosated Derivatives of Chitin and Chitosan for Biomedical Applications. *J. Mater. Chem. B* **2014**, *2*, 7449 – 7458.
24. Keefer, K. L. Fifty Years of Diazeniumdiolate Research. From Laboratory Curiosity to Broad-Spectrum Biomedical Advances. *ACS Chem. Bio.* **2011**, *11*, 1147 – 1155.
25. Giustarini, D.; Milzani, A.; Colombo, R.; Dalle-Donne, I.; Rossi, R. Nitric Oxide and S-Nitrosothiols in Human Blood. *Clinica Chimica Acta.* **2003**, *330*, 85 – 98.
26. Stamler, J.S.; Jaraki, O.; Osborne, J.; Simon, D.I.; Keaney, J.; Vita, J.; Singel, D.; Valeri, C. R.; Loscalzo, J. Nitric Oxide Circulates in Mammalian Plasma Primarily as an

- S-Nitroso Adduct of Serum Albumin. *Proc. Natl. Acad. Sci. U.S.A.* **1992**, *89*, 7674 – 7677.
27. Singh, R. J.; Hogg, N.; Joseph, J.; Kalyanaraman, B., Mechanism of Nitric Oxide Release from S-Nitrosothiols. *J. Biol. Chem.* **1996**, *271*, 18596 – 18603.
28. Demessence, A.; D'Alessandro, D. M.; Foo, M. L.; Long, J. R., Strong CO<sub>2</sub> Binding in a Water-Stable, Triazolate-Bridged Metal-Organic Framework Functionalized with Ethylenediamine. *J. Am. Chem. Soc.* **2009**, *131*, 8784 – 8786.
29. Hart, T. W. Some Observations Concerning the S-Nitroso and S-Phenylsulphonyl Derivatives of L-Cysteine and Glutathione. *Tetrahedron Lett.* **1985**, *26*, 2013 – 2016.
30. Liu, M.; Zheng, H.; Chen, J.; Li, S.; Huang, J.; Zhou, C. Chitosan-chitin Nanocrystal Composite Scaffolds for Tissue Engineering. *Carbohydr. Polym.* **2016**, *152*, 832 – 840.
31. Takara, E. A.; Marchese, J.; Ochoa, N.A. NaOH Treatment of Chitosan Films: Impact on Macromolecular Structure and Film Properties. *Carbohydr. Polym.* **2015**, *132*, 25 – 30.
32. Zhang, Y.; Feng, X.; Yuan, S.; Zhou, J.; Wang, B. Challenges and Recent Advances in MOF-polymer Composite Membranes for Gas Separation. *Inorg. Chem. Front.* **2016**, *3*, 896 – 909.
33. Vanin, A. F.; Malenkova, I. V.; Serezhenkov, V. A. Iron Catalyzes both Decomposition and Synthesis of S-Nitrosothiols: Optical and Electron Paramagnetic Resonance Studies. *Nitric Oxide* **1997**, *1*, 191 – 203.
34. McAninly, J.; Williams D. L. H.; Askew, S. C.; Butler, A. R.; Russell, C. Metal Ion Catalysis in Nitrosothiol (RSNO) Decomposition. *J. Chem. Soc., Chem. Commun.* **1993**, 1758 – 1759.

35. Harding, J. L.; Reynolds, M. M. Composite Materials with Embedded Metal Organic Framework Catalysts for Nitric Oxide Release from Bioavailable S-Nitrosothiols. *J. Mater. Chem. B* **2014**, *2*, 2530 – 2536.
36. Pethrick, R. A., Eds. Physical Properties, Synthesis and Applications of Thermoplastic Polymers. *Polymer Yearbook*, *5*; Harwood Academic Publishers GmbH: 1989; 6.
37. Chan, A. D. C.; Li, X.; Harrison, D. J. Evidence for Water-Rich Surface Region in Poly(vinylchloride)-Based Ion-Selective Electrode Membranes. *Anal. Chem.* **1992**, *64*, 2512 – 2517.
38. Brisbois, E. J., Bayliss, J.; Wu, J.; Major, T. C.; Xi, C.; Wang, S. C.; Bartlett, R. H.; Handa, H.; Meyerhoff, M. E. Optimized Polymeric Film-based Nitric Oxide Delivery Inhibits Bacterial Growth in a Mouse Burn Wound Model. *Acta Biomater.* **2014**, *10*, 4132 – 4142.
39. Noble, D. R.; Swift, H. R.; Williams, D. L. H. Nitric Oxide Release from S-Nitrosoglutathione. *Chem. Commun.* **1999**, 2317 – 2318.
40. Oh, B. K.; Meyerhoff, M. E., Catalytic Generation of Nitric Oxide from Nitrite at the Interface of Polymeric Films Doped with Lipophilic Cu(II)-complex: A Potential Route to the Preparation of Thromboresistant Coatings. *Biomaterials* **2004**, *25*, 283 – 293.
41. Major, T. C.; Brant, D. O.; Burney, C. P.; Amoako, K. A.; Annich, G. A.; Meyerhoff, M. E.; Handa, H.; Bartlett, R. H. The Hemocompatibility of a Nitric Oxide Generating Polymer that Catalyzes S-Nitrosothiol Decomposition in an Extracorporeal Circulation Model. *Biomaterials* **2011**, *32*, 5957 – 5969.

42. Hwang, S.; Meyerhoff, M. E. Polyurethane with Tethered Copper (II)-Cyclen Complex: Preparation, Characterization and Catalytic Generation of Nitric Oxide from S-Nitrosothiols. *Biomaterials* **2008**, *29*, 2443-2452.
43. Luza, S. C.; Speisky, H. C. Liver Copper Storage and Transport During Development: Implications for Cytotoxicity. *Am. J. Clin. Nutr.* **1996**, *63*, 812 – 820.
44. Dicks, A. P.; Swift, H. R.; Williams, D. L. H.; Butler, A. R.; Al-Sa'doni, H. H.; Cox, B. G. Identification of Cu<sup>+</sup> as the Effective Reagent in Nitric Oxide Formation from S-Nitrosothiols. *J. Chem. Soc., Perkin Trans. 2* **1996**, 481 – 487.
45. Baciu, C.; Cho, K. B.; Gauld, J. W., Influence of Cu<sup>+</sup> on the RS-NO Bond Dissociation Energy of S-Nitrosothiols. *J. Phys. Chem. B* **2005**, *109*, 1334 – 1336.
46. Li, T.; Taylor-Edinbyrd, K.; Kumar, R. A Computation Study of the Effect of the Metal Organic Framework Environment on the Release of Chemically Stored Nitric Oxide. *Phys. Chem. Chem. Phys.* **2015**, *17*, 23403 – 23412.

## CHAPTER 5

# NITRIC OXIDE GENERATION FROM ENDOGENOUS SUBSTRATES USING COPPER(II) BENZENE-1,3,5-TRIS(1*H*-1,2,3-TRIAZOL-5-YL): INCLUSION WITHIN POLY (VINYL ALCOHOL) MEMBRANES TO INVESTIGATE REACTIVITY AND THERAPEUTIC POTENTIAL.<sup>4</sup>

### 5.1 Introduction

Over the past two decades, there has been considerable growth in the proposed use of metal–organic frameworks (MOFs) for a variety of wide-ranging applications. These unique materials are characterized by ordered networks formed from metal nodes and organic linkers, and may display one, two, or three-dimensional architectures. The remarkable degree of porosity exhibited by many MOFs confers correspondingly large surface areas and pore volumes that have led to their implementation in gas storage and separation.<sup>1</sup> Furthermore, the density of potential active sites and the ability to controllably alter the physical and chemical properties within the framework through variation or modification of the metal ion or organic constituents have facilitated their use in heterogeneous catalysis.<sup>1</sup> More recently, the utility of MOFs in biomedicine has been recognized, including use in drug delivery and antibacterial applications.<sup>2,3</sup> This biomedical potential has been united with the well-characterized gas storage properties of MOFs in the form of nitric oxide (NO)-releasing frameworks.<sup>4</sup> These efforts were prompted by the broad therapeutic action of NO, which is produced endogenously as a crucial signaling molecule and exhibits potent

---

<sup>4</sup> This chapter was reproduced in part with permission from:

Neufeld, M. J.; Lutzke, A.; Jones, W. M.; Reynolds, M. M. Nitric Oxide Generation from Endogenous Substrates Using Metal–Organic Frameworks: Inclusion within Poly(vinyl alcohol) Membranes to Investigate Reactivity and Therapeutic Potential. *ACS Appl. Mater. Interfaces* **2017**, *9*, 35628-35641. Copyright 2017 American Chemical Society. <http://pubs.acs.org/doi/full/10.1021/acsami.7b11846>

antithrombotic, antimicrobial, and wound-healing effects.<sup>5</sup> As examples, the adsorption and subsequent release of NO have been demonstrated with iron-based MIL-88 and copper-based CuBTC (HKUST-1).<sup>6,7</sup> This function has been expanded with the postsynthetic modification of CuBTC to include NO-forming *N*-diazeniumdiolate functional groups.<sup>8</sup> An alternative approach has utilized copper-based MOFs such as copper benzene-1,3,5-tricarboxylate (CuBTC, or HKUST-1) to promote the release of NO from *S*-nitrosothiols (RSNOs), compounds that naturally occur in blood as a component of mammalian biochemistry.<sup>9,10</sup> Because RSNOs decompose to form NO and disulfide ( $2 \text{ RSNO} \rightarrow 2 \text{ NO} + \text{RSSR}$ ) upon exposure to environmental triggers such as heat, light, and certain transition metal ions (e.g., copper), the controlled recruitment of these natural compounds for therapeutic applications has been the target of substantial prior research.<sup>11</sup> The established ability of particular copper-based MOFs to initiate NO-formation from RSNOs permits the development of polymeric biomaterials that also exhibit this property.

However, biological application of this phenomenon requires the immobilization of copper-based MOFs within polymer matrices while retaining the NO-generating therapeutic activity. As an example, it has been demonstrated that the water-stable, triazolate-bridged MOF CuBTTri ( $\text{H}_3\text{BTTri} = 1,3,5\text{-tris}[1H\text{-}1,2,3\text{-triazol-}5\text{-yl]benzene$ ) (**Figure 5.1a**) can be dispersed within polymers such as plasticized poly(vinyl chloride) (PVC) and chitosan (a polysaccharide primarily consisting of glucosamine repeating units) to produce processable formulations that retain the NO-generating properties of the MOF in the presence of RSNOs.<sup>12,13</sup>

Predictably, it was observed that the physical properties of the polymer exert a considerable influence on the ability of the MOF to interact with aqueous-phase RSNOs *in vitro*. Limited diffusion of the dissolved RSNO into hydrophobic polymer formulations resulted in an *8-fold reduction* in NO generation relative to an aqueous suspension of CuBTTri powder (i.e., not

blended within a polymer).<sup>14</sup> In comparison, a 10 wt. % CuBTTri/chitosan formulation induced a 65-fold increase in NO generation over the baseline thermal decomposition of *S*-nitrosoglutathione (GSNO) (**Figure 5.1b**), the most abundant small molecule RSNO present in blood.<sup>13</sup> In this earlier

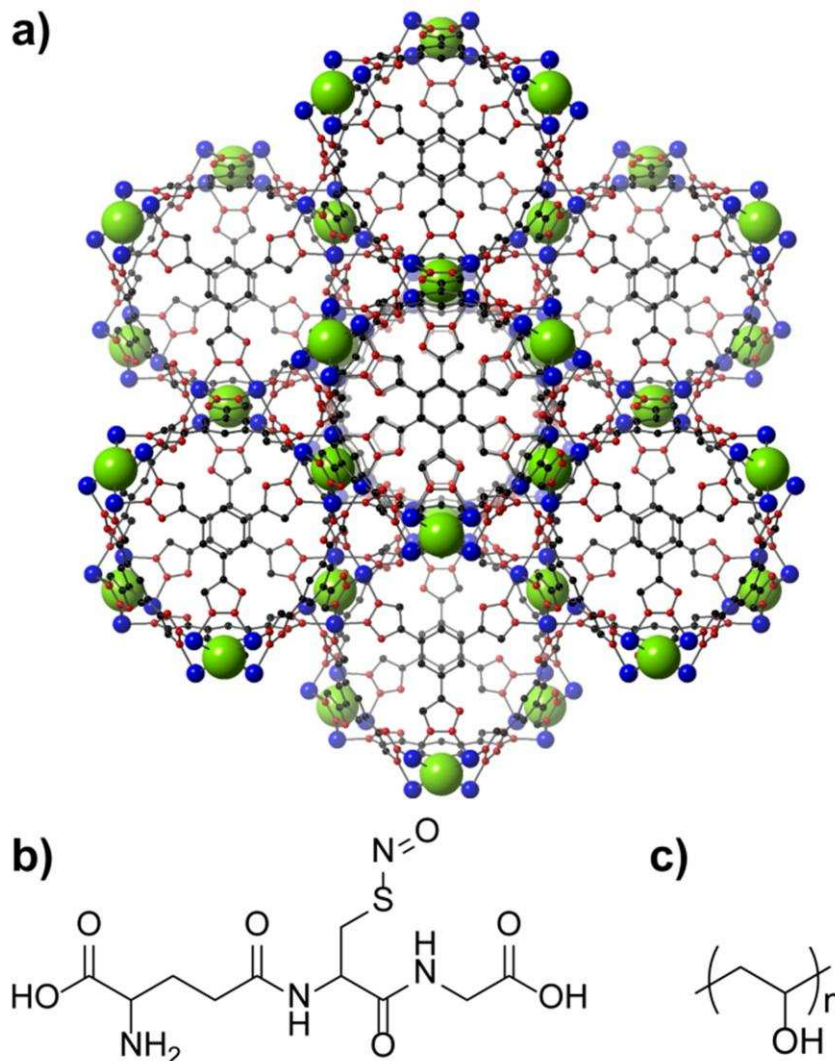


**Figure 5.1** (a) The structure of CuBTTri. Carbon (black), nitrogen (red), chlorine (green), and copper (blue) atoms are depicted with hydrogen atoms omitted for clarity. (b) The structure of *S*-nitrosoglutathione (GSNO). (c) The repeating unit of poly(vinyl alcohol) (PVA). Reproduced by permission of the American Chemical Society.

example, no statistically significant difference in CuBTTri performance was observed following incorporation within the polymer. From these prior results, it is clear that polymers exhibiting substantial water uptake facilitate the interaction of aqueous-phase RSNOs with blended MOFs.

For this reason, the use of copper-based MOFs to promote NO release from RSNOs may be best achieved through selection of hydrophilic polymer systems that permit optimization of this process for blood-contacting, therapeutic applications. In this respect, poly(vinyl alcohol) (PVA) (**Figure 5.1c**) represents a uniquely suitable candidate due to its hydrophilicity, hemocompatibility, and broad use in biomedicine. This polymer is a linear, water-soluble derivative of poly(vinyl acetate) produced through hydrolysis of ester groups. Cross-linking of PVA through various physical or chemical means produces insoluble materials that have been investigated for a wide range of medical applications, including drug delivery and tissue engineering.<sup>15</sup> Moreover, various NO-releasing, PVA-based materials have been used to fabricate wound dressings as well as promote vasodilation for treatment of cutaneous endothelial dysfunction associated with cardiovascular disease.<sup>16-18</sup>

Herein, we report the synthesis and characterization of hybrid materials prepared from water-stable CuBTri and PVA for the generation of NO from GSNO. The MOF was blended into aqueous solutions of PVA at 1, 5, and 10 wt. % relative to the polymer, and the PVA host material was subsequently cross-linked by exposure to glutaraldehyde (GA) under mildly acidic conditions. The water-swollen membranes prepared through this procedure were examined for their ability to promote NO release from GSNO under varying conditions and compared to the performance of aqueous suspensions of CuBTri powder. While PVA has been frequently used as a biomaterial, previous efforts involving the combination of PVA with MOFs or zeolites have generally targeted nonmedical applications such as chemical separation or water treatment.<sup>19,20</sup> This work describes the first material combining a water-stable MOF with PVA for potential therapeutic applications, and demonstrates that physiologically relevant levels of NO release can be induced from GSNO. Furthermore, the unique properties of CuBTri/PVA membranes permit the controlled study of

the NO-forming interaction between GSNO and CuBTTri in a manner that has not been previously possible. As a highly hydrophilic material, cross-linked PVA allows the comparatively rapid transport of GSNO to active sites within the polymer matrix. Unlike chitosan, PVA does not exhibit an independent ability to induce the decomposition of GSNO, thereby constraining observed effects to the influence of CuBTTri alone. Taken together, the attributes of CuBTTri/PVA membranes indicated the possibility for therapeutic use and provided the opportunity to evaluate critical performance parameters needed to facilitate the adaptation of copper-based MOFs to medical applications.

## **5.2 Materials and Methods**

### **5.2.1 Materials**

Copper(I) iodide (98%), diethylamine (99+%), *N*-ethylmaleimide (NEM, 99+%), glutaraldehyde (25% aqueous solution), high molecular weight poly(vinyl alcohol) (PVA, 98-99% hydrolyzed), 1,3,5-tribromobenzene (98%), and trimethylsilyl azide (94%) were purchased from Alfa Aesar (Ward Hill, MA, USA). Reduced glutathione (GSH, 98%) was purchased from AMRESCO (Solon, OH, USA). Trimethylsilylacetylene (99+%) was purchased from Chem-Impex International, Inc. (Wood Dale, IL, USA). Phosphate buffered saline (PBS) tablets and sodium nitrite were obtained from EMD Chemicals (Gibbstown, NJ, USA). Chelex 100 resin (200-400 mesh, sodium form) was procured from Bio-Rad (Hercules, CA, USA). Bis(triphenylphosphine)palladium(II) dichloride was purchased from Sigma-Aldrich (St. Louis, MO, USA). For NO analysis, ultra high purity (UHP) N<sub>2</sub> and O<sub>2</sub> gases were obtained from Airgas (Denver, CO, USA). Nitric oxide (NO; 43.6 ppm NO, balance N<sub>2</sub>) calibration gas was purchased from Air Liquide (Houston, TX, USA). Deionized water (18.2 MΩ·cm) was supplied by a Millipore Direct-Q water purification system (EMD Millipore, Billerica, MA, USA) and used in

all experiments. N<sub>2</sub> (UHP) was passed through activated charcoal and potassium permanganate filters prior to use as an NO carrier gas. Diethylamine was distilled prior to use. All other chemicals were used as received without any further purification.

### **5.2.2 Synthesis of copper(II) benzene -1,3,5-tris(1*H*-1,2,3-triazole-5-yl)**

The ligand 1,3,5-tris(1*H*-1,2,3-triazol-5-yl)benzene (H<sub>3</sub>BTTri) and MOF H<sub>3</sub>[(Cu<sub>4</sub>Cl)<sub>3</sub>(BTTri)<sub>8</sub>] (CuBTTri) were prepared following the general protocols given by Demessence et al.<sup>1</sup> The MOF was used in the hydrated form with the theoretical formula H<sub>3</sub>[(Cu<sub>4</sub>Cl)<sub>3</sub>(BTTri)<sub>8</sub>·(H<sub>2</sub>O)<sub>12</sub>]·72H<sub>2</sub>O.

### **5.2.3 Synthesis of cross-linked copper(II) benzene-1,3,5-tris(1*H*-1,2,3-triazole-5-yl) /poly(vinyl alcohol) membranes.**

Poly(vinyl alcohol) was dissolved by heating a 10 wt. % suspension of PVA in Millipore water at 90 °C for 4 h. To prepare 1, 5, and 10 wt. % CuBTTri/PVA membranes, an appropriate quantity of MOF (4, 21, or 44 mg) was suspended in 0.75 mL of Millipore water and placed in an ultrasound bath for 2 min to uniformly disperse the crystalline powder. This mixture was added to 4 mL of 10 wt. % aqueous PVA, and an additional 0.25 mL Millipore water rinse was used to ensure the quantitative transfer of MOF into the polymer solution. The final PVA concentration was 80 mg·mL<sup>-1</sup>, and this viscous solution was combined with 0.364 mL of 25 wt. % aqueous glutaraldehyde and 52 μL of glacial acetic acid. The mixture was agitated by vortex mixer until uniform then cast into a 5 cm circular polytetrafluoroethylene (PTFE) mold, and the solvent was allowed to evaporate for 2 days. The dry membrane was heated at 80 °C for 2 h, then immersed in 200 mL of Millipore water for 30 min. Following this initial immersion, the membrane was washed with 5 × 100 mL of Millipore water, then immersed for 1 day in 200 mL of Millipore water. The washing procedure was repeated with Millipore water, and the membrane was placed in 200 mL

of 0.1 % w/v Chelex 100 resin (adjusted to pH 7-8) for an additional day. After a further repetition of the washing procedure, the membrane was immersed in 200 mL of Millipore water for 2 days (with replacement of the medium after 1 day), then punched into smaller 15 mm diameter circular membranes that were air-dried and used in subsequent experiments. Control membranes were prepared without the addition of CuBTTri following an otherwise identical procedure.

#### **5.2.4 Synthesis of Tecoflex SG-80A Polyurethane Films.**

Tecoflex SG-80A (400 mg) was dissolved in 6 mL of freshly distilled THF. Separately, 44 mg of CuBTTri was suspended in 2 mL of THF and placed in an ultrasound bath for 2 min to form a uniform dispersion. This mixture was added to the polymer solution and vortexed until uniform, producing a final Tecoflex concentration of 50 mg·mL<sup>-1</sup>. The mixture was cast into a 5 cm circular PTFE mold, and the solvent was allowed to evaporate. Circular films (15 mm diameter) were punched for use in subsequent experiments.

#### **5.2.5 Synthesis of *S*-nitrosoglutathione.**

*S*-Nitrosoglutathione (GSNO) was synthesized following an adaptation of the method reported by Hart.<sup>2</sup> Glutathione (GSH; 1.54 g, 5.0 mmol) was suspended in 8 mL of Millipore water and dissolved by the addition of 2.5 mL of 2 M hydrochloric acid. This solution was cooled to 0 °C using an ice bath, and 0.345 g (5.0 mmol) of sodium nitrite was added in a single portion. After stirring for 40 min in the dark, the mixture was filtered to isolate a red precipitate that was subsequently washed with 5 × 5 mL of ice-cold Millipore water, 3 × 5 mL of acetone, and 3 × 5 mL of diethyl ether. The product was placed under vacuum (1 Torr) for 1 h to remove residual solvent, and afforded 0.865 ± 0.076 g (51 ± 5%) of GSNO. <sup>1</sup>H NMR (400 MHz, D<sub>2</sub>O): 4.70-4.61 (m, 1H), 4.20-3.90 (m, 2H), 3.93 (s, 2H), 3.78 (t, 1H, *J* = 6.4 Hz), 2.42 (t, 2H, *J* = 7.6 Hz), 2.18-2.01 (m, 2H). UV-vis (H<sub>2</sub>O): 335 (π → π\*), 545 (n<sub>N</sub> → π\*).

### **5.2.6 General characterization.**

Proton nuclear magnetic resonance ( $^1\text{H}$  NMR) spectra were acquired with an Agilent (Varian) Inova 400 MHz FT-NMR spectrometer (Agilent Technologies, Inc., Santa Clara, CA). Ultraviolet-visible (UV-vis) spectra were obtained in quartz cuvettes using a Nicolet Evolution 300 spectrophotometer (Thermo Electron Corp., Madison, WI). Attenuated total reflectance Fourier transform infrared (ATR-FTIR) spectra were obtained with a Nicolet 6700 FTIR spectrometer (Thermo Electron Corp.) equipped with a Smart iTR ATR sampling accessory fitted with a ZnSe crystal plate. Powder X-ray diffraction (pXRD) was carried out using a Bruker D-8 Discover DaVinci X-ray diffractometer (Cu-K $\alpha$  X-ray source, line focus) (Bruker, Billerica, MA, USA). Scanning electron microscopy (SEM) images of materials were acquired using a JEOL JSM-6500F scanning electron microscope (JEOL USA Inc., MA, USA) at a working distance of 10 mm and an accelerating voltage of 5.0 kV. Samples were sputter coated with 15 nm of gold prior to imaging.

### **5.2.7 Thermogravimetric analysis.**

Dynamic rate thermogravimetric analyses (TGA) were performed on TA Instruments TGA Q500 instrumentation (New Castle, DE, USA). Samples (~ 5-10 mg) were contained in ceramic holders using platinum sample pans. N $_2$  was used as the furnace purge gas at a flow rate of 60 mL·min $^{-1}$ . Samples were heated at a rate of 10 °C·min $^{-1}$  with Hi-Res<sup>TM</sup> settings of resolution number 5.0 and sensitivity value 3.0.

### **5.2.8 Differential scanning calorimetry.**

Differential scanning calorimetry (DSC) was performed using TA Instruments DSC2500 instrumentation with a RCS 90 cooling system. Samples (~5-10 mg) were contained in hermetically sealed aluminum sample pans. N $_2$  was used as the cell purge gas at a flow rate of 50

mL·min<sup>-1</sup>. Samples were cycled at a rate of 10 °C·min<sup>-1</sup>. The 1<sup>st</sup> cycle (-50 °C to 185 °C) ensured full desolvation and removal of each membrane's thermal history prior to studies. The 2<sup>nd</sup> and 3<sup>rd</sup> cycles (-50 °C to 220 °C) were used to assess thermal transitions and reversibility of each film.

### 5.2.9 Water uptake studies.

For all CuBTTri/polymer materials, the degree of water uptake was determined as follows: dry initial weights ( $W_i$ ) were obtained for samples of each material ( $n = 3$ ) using an Ohaus Discovery DV215CD analytical balance (0.01 mg readability). Samples were subsequently immersed in 5 mL of Millipore water for 24 h, then re-weighed to determine a final wet mass ( $W_f$ ) after blotting to remove excess water. The degree of swelling was calculated according to the following equation:

$$\% \text{ swelling} = \frac{W_f - W_i}{W_i} \times 100$$

### 5.2.10 Nitric oxide release measurements.

Nitric oxide (NO) release was quantified by chemiluminescence using Sievers nitric oxide analyzers (NOA 280i, GE Analytical, Boulder, CO, USA). Instruments were calibrated with UHP N<sub>2</sub> (0 ppm NO) and an NO standard (43.6 ppm NO, balance N<sub>2</sub>). Using custom glass analysis vessels, samples (either 15 mm diameter membranes/films or CuBTTri powder) were immersed/suspended in 10 mL of deoxygenated 10 mM PBS (at varying pH and temperature) with continuous UHP N<sub>2</sub> sparging and headspace flow. Aliquots of an aqueous GSNO solution were then injected into analysis vessels to produce a final GSNO concentration of 10 μM. The NO generated by decomposition of GSNO was swept into the instrument and quantified as gas-phase NO concentration (ppb), which was subsequently converted to NO release (mol) using an instrument-specific calibration constant previously obtained from reduction of sodium nitrite.

### 5.2.11 Statistical analysis

Analytical results are reported as the mean  $\pm$  standard deviation of a minimum of triplicate measurements. Where appropriate, statistical significance was determined by Student's t-test or one-way analysis of variance (ANOVA) at the 95% confidence level. Post hoc analysis consisted of Tukey's range test or the Tukey-Kramer method, as dictated by sample size.

### 5.3 Synthesis and characterization of copper(II) benzene-1,3,5-tris(1*H*-1,2,3-triazole-5-yl) /poly(vinyl alcohol) membranes

*S*-Nitrosothiols occur naturally in human blood at concentrations that have been reported to range from nanomolar to micromolar, depending on analytical methodology, natural variation, and donor morbidity.<sup>21</sup> This fact has prompted the development of therapeutic materials that are intended to induce the NO-forming decomposition of biological RSNOs when placed in contact with flowing blood. These materials have included polymer-immobilized organoselenium and tellurium catalysts as well as various systems based on immobilized copper complexes, nanoparticles, and MOFs.<sup>12-14,22-25</sup> The use of MOFs to induce the generation of NO from endogenous substrates could permit sustained production without adsorption of finite quantities of gaseous NO or incorporation of NO-forming functional groups. This concept was initially limited by the susceptibility of Cu-BTC to water-induced degradation, which does not permit extended exposure to physiological media such as blood.<sup>26</sup> It was later discovered that the water-stable, triazolate-bridged framework CuBTTri (originally proposed by Demessence et al. for CO<sub>2</sub> capture) similarly promotes NO release from RSNO substrates.<sup>14,27</sup> The MOF was found to remain crystalline after exposure to both boiling water and dilute hydrochloric acid, and retained its ability to induce NO release from RSNOs following immersion in whole blood. Moreover, CuBTTri does not exhibit the significant level of copper ion leaching observed from certain copper complexes

used to catalyze NO release from RSNOs.<sup>12-14, 26,28</sup> This retention of MOF function permits the development of polymer-based materials with the ability to produce therapeutic levels of NO directly from blood. For example, CuBTTri has been blended with biomedically-relevant polymers such as plasticized PVC, where it demonstrated the ability to promote NO release from RSNOs such as *S*-nitrosocysteine and *S*-nitroso-*N*-acetylpenicillamine (SNAP).<sup>12,14</sup> However, the ability of aqueous-phase, biological RSNOs to interact with blended CuBTTri (or other copper-based agents) is limited by the poor water uptake of hydrophobic polymers like PVC. In comparison, the promotion of NO release from an RSNO exposed to blended CuBTTri occurred more rapidly when the MOF was incorporated within chitosan, a hydrophilic polysaccharide.<sup>13</sup> Despite this improved performance, the potential blood-contacting applications for this material were constrained by the inherent hemostatic attributes of chitosan.<sup>29</sup> As additional complications, the basic glucosamine repeating units of chitosan are capable of reacting with acidic functional groups that occur as part of the structure of physiological RSNOs, and may also strongly bind transition metal ions that are independently capable of initiating RSNO decomposition.<sup>30,31</sup> As such, it is clear that MOF-based materials combining the water permeability of chitosan with the structural simplicity of PVC may permit NO generation from RSNOs and examination of the parameters influencing this behavior without interference from the polymer matrix.

### **5.3.1 Membrane preparation.**

Poly(vinyl alcohol) is a highly hydrophilic linear polymer derived from hydrolysis of poly(vinyl acetate). The CuBTTri blends prepared from hydrophilic PVA represent promising alternatives to previous systems due to the existing use of PVA in numerous blood-contacting applications, its lack of hemolytic properties, and the potential for considerable water permeability and transport of GSNO.<sup>32</sup> Moreover, the absence of acidic or basic functional groups (e.g., the

primary amine groups of chitosan) and the general structural simplicity of PVA allows it to function as a comparatively inert host for the MOF. Implementation of this concept is particularly beneficial in the case of studies intended to elucidate the NO-forming behavior of CuBTTri under varying conditions. For example, incorporation within a polymer matrix permits straightforward isolation and re-characterization of the immobilized MOF following experiments without requiring the separation of fine MOF particle suspensions. Because PVA has been frequently examined as a nontoxic biomaterial, there has been notable prior interest in the utilization of PVA or PVA-based materials as NO delivery platforms. For example, Masters et al. modified PVA hydrogels with *N*-diazoniumdiolate NO donor groups to prepare wound dressings, while the vasodilatory effect of NO was exploited by Marcelli and de Oliveira in the development of NO-releasing PVA films for the treatment of microvascular skin disorders.<sup>16,17,33,34</sup> In addition to these examples of NO-releasing derivatives, physically cross-linked PVA films were used to uptake and subsequently release GSNO itself as a therapeutic. Since PVA exhibits solubility in water, physical or chemical cross-linking techniques are frequently used to produce stable materials for use in biomedicine.<sup>15</sup> Cross-linking by reaction with dialdehydes such as GA occurs through the formation of acetal linkages between GA and the 1,3-diol units of independent PVA chains.<sup>35</sup> This type of cross-linking process permits the synthesis of water-insoluble membranes that encapsulate crystalline CuBTTri. The MOF was synthesized following the original protocol published by Demessence et al., and was characterized by powder X-ray diffraction (pXRD) and attenuated total reflectance Fourier transform infrared spectroscopy (ATR-FTIR) prior to use (**Figure 5.2a and 5.2b**).<sup>27</sup> The MOF was then blended into aqueous solutions of PVA in the presence of GA and acetic acid at 1, 5, and 10 wt. % loading relative to the polymer. It was observed that the direct addition of CuBTTri powder to aqueous PVA resulted in substantial MOF particle agglomeration

that reduced the visual uniformity of the mixture, potentially resulting from physical incompatibility between the MOF and polymer solution. This phenomenon was limited by adding CuBTTri as an aqueous suspension, which was gradually mixed with the polymer phase to promote a more uniform dispersion. Similar effects in organic solvents have been noted by multiple prior authors and may be attributable to the formation of a polymer coating on the MOF that inhibits

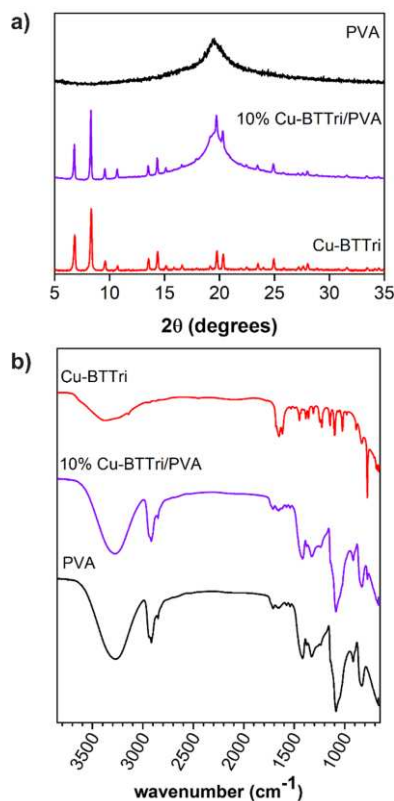


**Figure 5.2** (a) Powder X-ray diffraction patterns of CuBTTri, cross-linked PVA control membrane, and 10 wt. % CuBTTri/PVA membrane. The diffraction pattern of CuBTTri/PVA membrane displays peaks attributable to both PVA and CuBTTri, demonstrating retention of the MOF structure following incorporation within the polymer. (b) The ATR-FTIR spectra of CuBTTri, cross-linked PVA control membrane, and 10 wt. % CuBTTri/PVA membrane. Infrared absorption bands associated with CuBTTri are present at 1616 (C=C stretching) and 775 cm<sup>-1</sup> (C-H out-of-plane bending). Reproduced by permission of the American Chemical Society.

agglomeration.<sup>36,37</sup> While strong acid catalysts (e.g., sulfuric or hydrochloric acid) are commonly used to produce highly cross-linked PVA, the sensitivity of CuBTTri to harshly acidic conditions prompted the use of acetic acid as a milder alternative. After 2 days of curing at ambient

temperature, followed by 2 h at 80 °C, membranes were immersed in Millipore water for 1 day to remove residual acetic acid and GA. This immersion was followed by treatment with a 0.1 % w/v aqueous suspension of Chelex 100 resin to capture trace metal ions (chiefly iron or copper) that may diffuse from membranes into the surrounding aqueous medium. The membranes were immersed in Millipore water for an additional 2 days, punched into 15 mm diameter circles (water-swollen), then air-dried prior to characterization.

### 5.3.2 Membrane characterization.

Characterization of the 10 wt. % CuBTtri/PVA membranes by pXRD revealed the expected diffraction pattern of CuBTtri overlapping with a broad feature originating from semicrystalline PVA, supporting retention of the crystalline structure of the MOF following incorporation within the polymer matrix (**Figure 5.2a**).<sup>27</sup> At lower loading of 1 and 5 wt. % CuBTtri, key diffraction

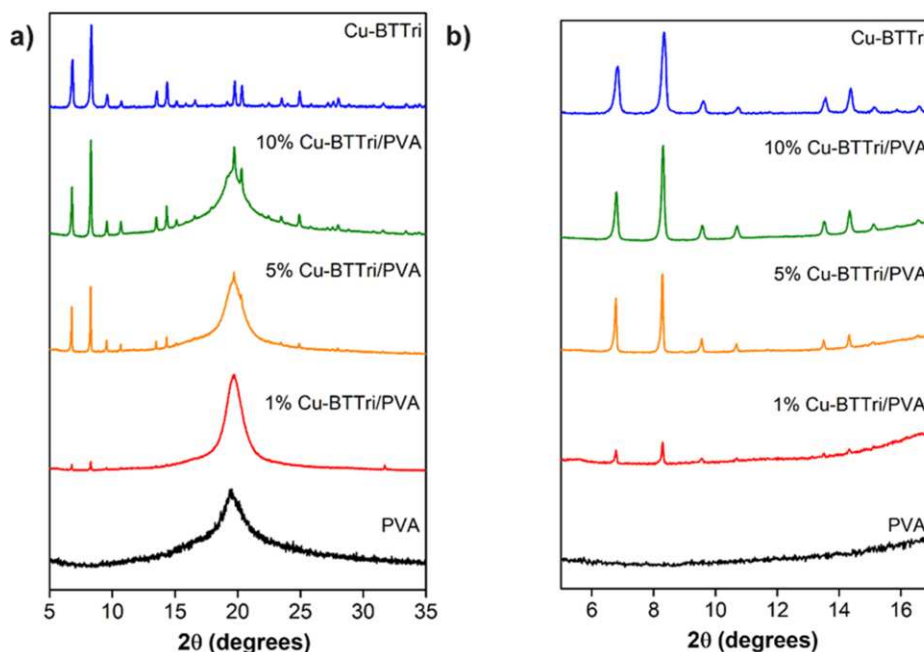


**Figure 5.3** pXRD patterns of (a) PVA, CuBTtri and 1, 5 and 10 wt. % CuBTtri/PVA membranes. (b) pXRD of the region between 4 and 16 degrees to better show the diffraction peaks associated with CuBTtri in the lower weight percent membranes. Patterns demonstrate the retention of major diffraction peaks associated with CuBTtri, indicating successful incorporation of CuBTtri into the PVA matrix. Reproduced by permission of the American Chemical Society.

peaks remain defined (**Figure 5.3**). Control membranes prepared from PVA alone exhibit characteristic IR absorption bands at 3600-3000 (O-H stretching), 2937, 2916, 2850 (CH stretching), 1709 (acetate C=O stretching), 1655 (H<sub>2</sub>O), 1418 (CH<sub>2</sub> bending), 1377 (CH<sub>2</sub> rocking), 1327, 1238 (CH rocking), 1086 (CO stretching), 916, and 830 cm<sup>-1</sup>.<sup>38</sup> The incorporation of 10 wt. % CuBTtri is accompanied by the appearance of bands at 1616 (C=C stretching) and 775 cm<sup>-1</sup> (C-H out-of-plane bending) associated with the triazolate-bridged MOF (**Figure 5.2b**). At 5 wt. % CuBTtri, these absorption bands are less pronounced but remain present (**Figure 5.4**). At a

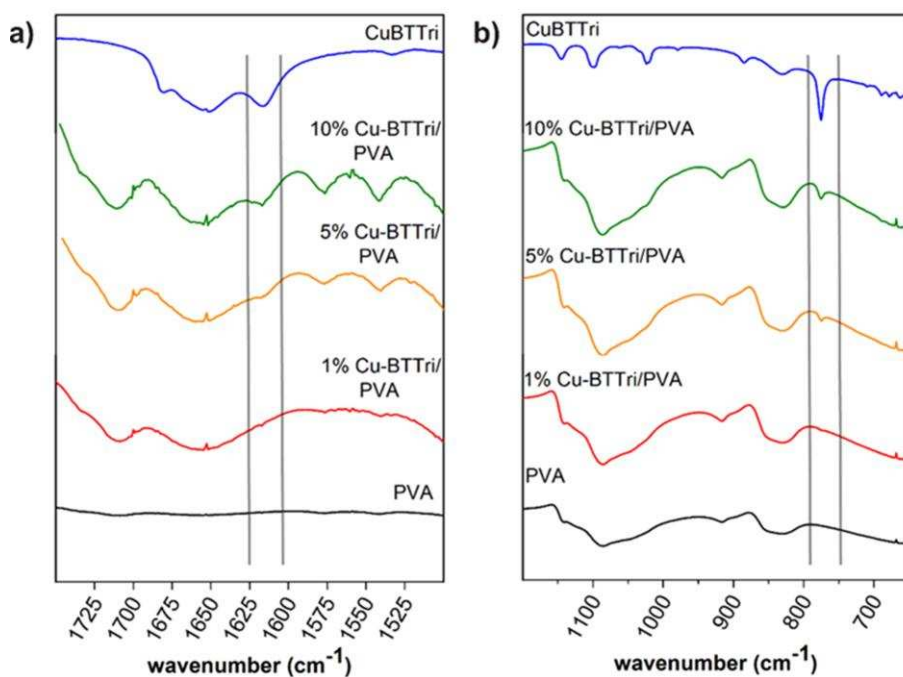


**Figure 5.4** ATR-FTIR spectra of CuBTtri, cross-linked PVA control membrane, and 10 wt. % CuBTtri/PVA membrane. The IR bands associated with CuBTtri are present at 1616 (C=C stretching) and 775 cm<sup>-1</sup> (C-H out-of-plane bending). At 5 wt. % CuBTtri these absorptions remain present but less pronounced, whereas at 1 wt. % CuBTtri, the major peaks associated with CuBTtri are no longer clearly resolved. Reproduced by permission of the American Chemical Society.

lower concentration of 1 wt. % CuBTtri, the absorption bands of the MOF are no longer clearly resolved (**Figure 5.4**). In all cases, no peaks directly assignable to GA are detectable. This outcome was predictable due to the comparatively mild cross-linking conditions, which are unlikely to result in extensive acetal formation and incorporation of GA within the PVA matrix.

However, the presence of cross-linking was qualitatively demonstrated by heating samples of GA cross-linked CuBTTri/PVA, cross-linked PVA, and non-crosslinked PVA in Millipore water. The PVA membrane prepared without exposure to GA readily redissolves in water, while cross-linked CuBTTri/PVA and PVA do not exhibit solubility at temperatures as high as 90 °C. Cross-linking under mild conditions is not an unexpected outcome since it has been previously observed that a degree of GA-mediated cross-linking occurs in the total absence of catalytic acid.<sup>39</sup> While PVA is capable of chelating copper ions through a variety of proposed binding mechanisms (particularly under strongly alkaline conditions), there is no spectroscopic evidence supporting the possibility that similar interactions occur between CuBTTri and PVA.<sup>40,41</sup> In general, both pXRD patterns and IR spectra of CuBTTri/PVA membranes are additive with respect to the spectra of individual constituents and do not indicate a detectable change in crystallinity or chemical structure of CuBTTri or PVA as a consequence of membrane preparation.

The thermal properties of 10 wt. % CuBTTri/PVA membranes were examined by thermogravimetric analysis (TGA) and differential scanning calorimetry (DSC). For TGA, studies were performed on the PVA control membranes and CuBTTri powder as well as the 10 wt. % CuBTTri/PVA membranes taken both before and after the materials were studied in NO release experiments. Samples were analyzed as prepared with the respective thermograms shown in **Figure 5.5a**. The thermal transitions observed for both the PVA and CuBTTri starting materials were consistent with the literature. Dehydration of the PVA control began at ~65 °C with membrane decomposition (colorless to light brown color change) beginning at ~225 °C.<sup>42,43</sup> The MOF showed significant dehydration at room temperature followed by desolvation beginning at ~145 °C with onset of decomposition observed at ~295 °C.<sup>27</sup> For 10% CuBTTri/PVA membranes, incorporation of the MOF as a polymeric dopant did not significantly alter the thermal stability of

the synthesized membranes. For the initial membrane, dehydration was observed at the same temperature as the PVA control with an onset of membrane decomposition (purple to tan/light brown color change) observed at  $\sim 245$  °C. After the membrane was subjected to NO release studies, the thermal behavior of the membrane showed no differences compared to the initial

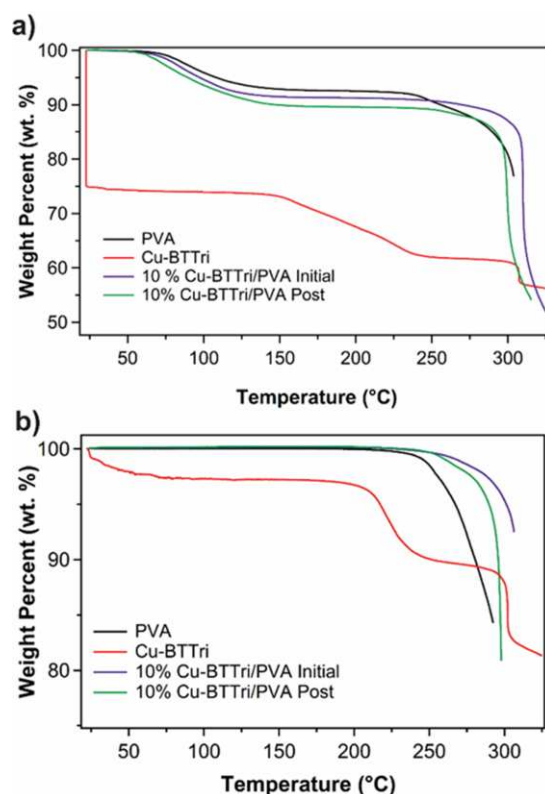


**Figure 5.5** (a) TGA of cross-linked PVA, CuBTtri, and 10 wt. % CuBTtri membranes before and after NO release experiments and exposure to GSNO. (b) TGA of dehydrated cross-linked PVA, CuBTtri, and 10 wt. % CuBTtri membranes before and after NO release experiments and exposure to GSNO. Both the as-prepared (a) and dehydrated (b) PVA membranes showed no decrease in thermal stability upon incorporation of CuBTtri into the PVA matrix. Reproduced by permission of the American Chemical Society.

membrane (with the exception of a slightly lowered onset of dehydration). Further studies examining the starting materials and membranes after dehydration at 90-95 °C for 24 h (**Figure 5.5b**) showed no significant differences in the thermal behavior of the materials (with only CuBTtri starting material showing less desolvation shifted to higher temperatures, beginning around 205 °C).

For DSC, PVA control membranes were assessed as well as the synthesized 10 wt. % CuBTTri/PVA membrane both before and after the membranes were subjected to NO release experiments. Samples were placed under vacuum at 65 °C for 3 h prior to DSC analysis. For the PVA control membrane, two reversible thermal transitions were observed: an endothermic glassy transition ( $T_g$ ) recovered at 56.5 °C and an endothermic melting transition ( $T_m$ ) recovered at 201.5 °C with an enthalpy of 42.86 J·g<sup>-1</sup> (**Figure 5.6**). Thermal transitions for PVA are well known to shift in temperature with respect to differences in molecular weight.<sup>42,44</sup> Thermal transitions of the 10 wt. % CuBTTri/PVA membrane matched strongly with the PVA control: an endothermic  $T_g$

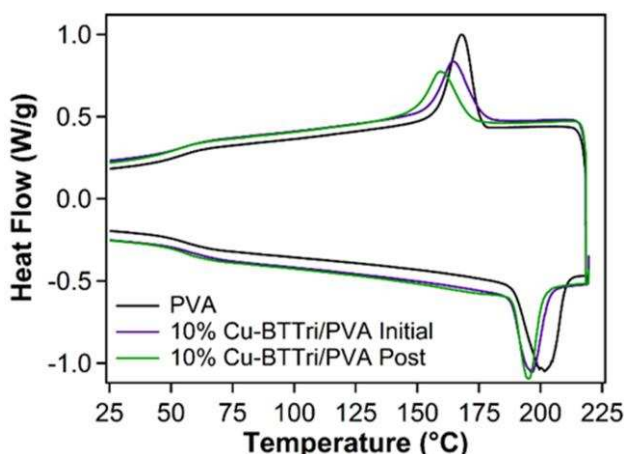


**Figure 5.6.** DSC of cross-linked PVA and 10 wt. % CuBTTri membranes before and after NO release experiments and exposure to GSNO. Both the initial and post NO release membranes showed no significant differences in thermal cycling as compared to the neat PVA membranes. Reproduced by permission of the American Chemical Society.

recovered at 56.8 °C and an endothermic  $T_m$  recovered at 196.1 °C with an enthalpy of 27.55 J·g<sup>-1</sup>. The slight depression in the  $T_m$  of the MOF-doped membrane is attributed to an eutectic effect as the MOF particles represent solid impurities as compared to the neat PVA membrane. Thus, the additional disorder and microstates within the doped polymer matrix allow melting to occur at slightly lower temperatures. Following NO release experiments, the 10 wt. % CuBTTri/PVA membrane showed no significant differences in the observed thermal transitions seen for the initial membrane.

Incorporation of CuBTri within the PVA matrix was demonstrated by scanning electron microscopy (SEM) imaging, which revealed the anticipated octahedral morphology of individual MOF crystallites (**Figure 5.7a-f**). Because the membranes were cured in poly(tetrafluoroethylene) (PTFE) molds, the sides of the membranes were expected to exhibit a degree of non-equivalence resulting from physical differences between the air and PTFE interfaces and gradual settling of the

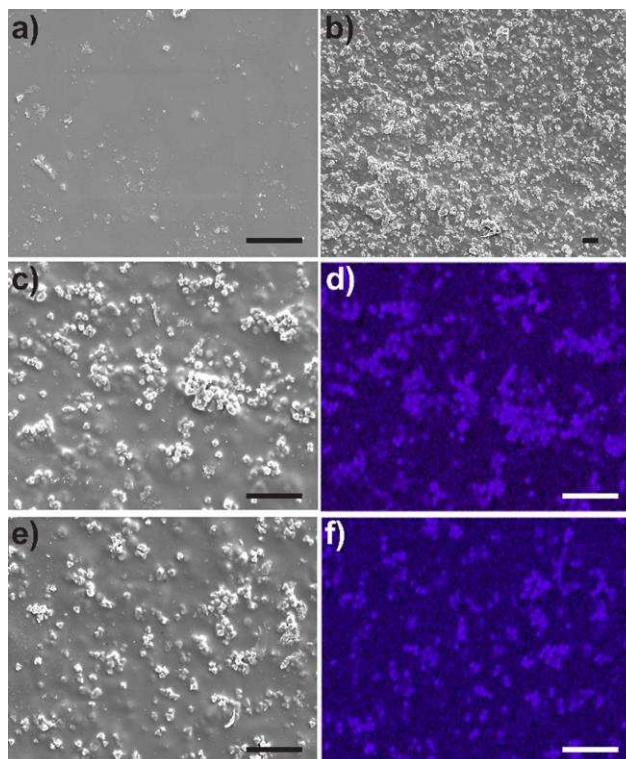


**Figure 5.7** Scanning electron microscopy images of (a) PVA control at 2,000× magnification and (b) 10 wt. % CuBTri membrane (air side) at 500× magnification. (c) The 10 wt. % CuBTri membrane (air side) at 2,000× magnification with (d) EDX copper overlay. (e) The 10 wt. % CuBTri membrane (PTFE side) at 2,000× magnification with (f) EDX copper overlay. Scale bars (lower right corner) correspond to 10  $\mu\text{m}$ . Reproduced by permission of the American Chemical Society.

MOF suspension. As compared in **Figure 5.7c and 5.7e**, the apparent surface distribution of CuBTri crystallites is relatively consistent between the air and PTFE interfaces of 10 wt. % CuBTri/PVA membrane. However, images acquired of 1 and 5 wt. % CuBTri/PVA membranes depict more pronounced differences in CuBTri surface distribution as the overall concentration

of the MOF decreases (**Figure 5.8**). This outcome is most directly attributable to settling of CuBTTri crystallites/agglomerates prior to evaporation of water. To further characterize the materials following incorporation of the copper-based MOF CuBTTri, the overall surface distribution of copper was imaged by energy-dispersive X-ray spectroscopy (EDX). **Figures 5.7d and 5.7f** show concentration of copper in regions of the 10 wt. % CuBTTri/PVA membrane that contain CuBTTri particles for both the air and PTFE interfaces. This analysis was also performed for 1 and 5 wt. % CuBTTri/PVA membranes, which display a similar concentration of copper at the location of MOF crystallites (**Figure 5.8**). Additionally, cross-sectional SEM imaging of the 10 wt. % CuBTTri/PVA membrane indicated a dry thickness of approximately 56  $\mu\text{m}$  with EDX confirming dispersion of copper throughout the interior of the membrane (**Figure 5.8**). Taken together, these results demonstrated successful incorporation of CuBTTri with improved uniformity between the air and PTFE interfaces at higher MOF loading. Although MOF particle agglomeration was observed in all images, the typical size of individual crystallites was relatively uniform at approximately 1  $\mu\text{m}$  in diameter. The outcome of blending CuBTTri into the PVA solution as an aqueous suspension was evident in the qualitatively improved uniformity of the MOF dispersion compared to prior work.

#### **5.4 Nitric oxide generation from *S*-nitrosoglutathione**

Nitric oxide exhibits antithrombotic properties that are crucial in the maintenance of the healthy vascular endothelium, and is also produced by the immune system as an antimicrobial agent.<sup>5,45</sup> As a diatomic radical that readily reacts with  $\text{O}_2$  and biomolecules such as hemoglobin, NO exhibits a physiological half-life ranging from seconds to milliseconds, permitting localized action in a biological environment.<sup>46</sup> In biomolecules, the *S*-nitrosation of thiol groups (such as those present in cysteine residues) produces natural RSNOs.<sup>47</sup> In principle, the use of copper-based

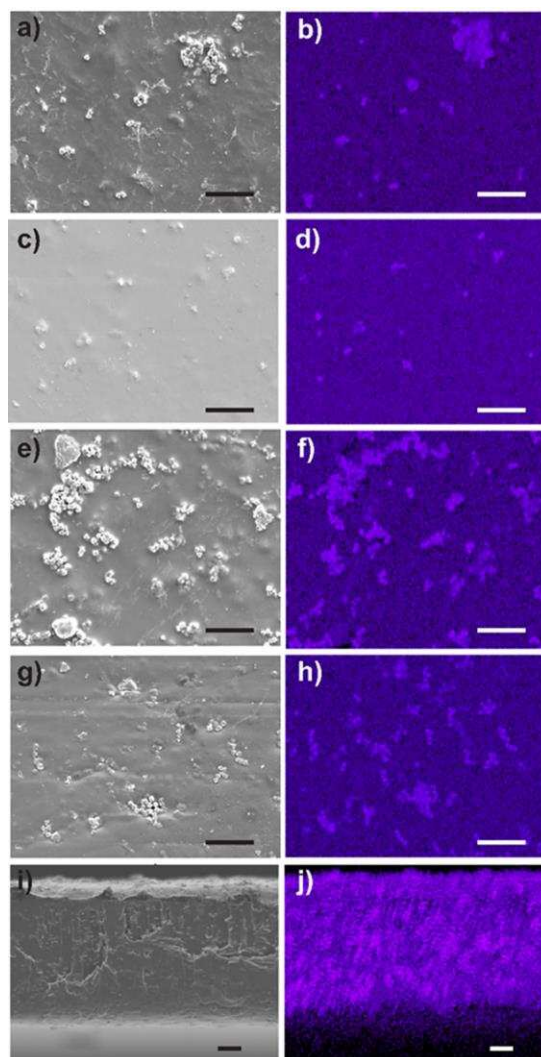


**Figure 5.8** SEM images of (a) 1 wt. % CuBTri membrane (air side) at 2,000× magnification, (b) EDX copper overlay, (c) 1 wt. % CuBTri membrane (PTFE side) at 2,000× magnification, (d) EDX copper overlay, (e) 5 wt. % CuBTri membrane (air side) at 2,000× magnification, (f) EDX copper overlay, (h) 5 wt. % CuBTri membrane (PTFE side) at 2,000× magnification, (g) EDX copper overlay, (i) cross-section of 10 wt. % CuBTri membrane at 1,000× magnification, and (j) EDX copper overlay. Scale bars (lower right corner) correspond to 10  $\mu\text{m}$ . Reproduced by permission of the American Chemical Society.

MOFs such as CuBTri permits the continuous generation of NO directly from RSNO substrates in blood, obviating the use of exogenous NO sources that are often limited by finite storage capacity. The possibility of generating NO from endogenous RSNOs is particularly attractive in the case of blood-contacting medical devices, such as extracorporeal circuits, venous catheters,

and hemodialysis membranes, where the natural antithrombotic function of NO may inhibit the formation of thrombi that are associated with artificial polymeric surfaces.<sup>5,11</sup> Similarly, the ability to produce NO in this fashion may facilitate the development of wound dressings that accelerate the healing process in the presence of perfusing blood. While it has been determined that RSNOs are present in blood at concentrations as high as the  $\mu\text{M}$  range, these compounds commonly occur in the form of macromolecules such as *S*-nitrosoalbumin (approximately 67 kDa) that are unlikely to rapidly interact with blended CuBTTri.<sup>48</sup> In contrast, GSNO (336 Da) is widely reported to be the most abundant low molecular weight RSNO available in blood.<sup>47</sup> For this reason, GSNO was utilized in NO release experiments as the most relevant endogenous RSNO. Although there has been controversy concerning the actual physiological level of RSNOs in blood, a concentration of 10  $\mu\text{M}$  GSNO was selected due to the use of similar  $\mu\text{M}$ -range concentrations in prior work.<sup>13,24,28,49</sup> Measurement of NO release was carried out using Sievers chemiluminescence-based NO analyzers, which rely on the gas phase reaction of NO with ozone to form excited state nitrogen dioxide ( $\text{NO} + \text{O}_3 \rightarrow \text{NO}_2^* + \text{O}_2$ ). The return of excited state  $\text{NO}_2$  to the ground state is accompanied by the emission of light, which is transduced and used to continuously measure the production of NO as a function of time. Chemiluminescence-based analysis is highly selective and permits detection of NO from solutions containing as little as 1 pmol of RSNO.<sup>50</sup> Using this technique, the ability of CuBTTri/PVA membranes to promote NO release under varying conditions was examined.

#### **5.4.1 Performance at physiological pH and temperature.**

To assess the ability of 10 wt. % CuBTTri/PVA membranes to generate NO from GSNO at physiological pH and temperature, membranes were submerged in pH 7.4 phosphate buffered saline (PBS) at 37 °C, and this mixture was deoxygenated by sparging with  $\text{N}_2$ . Prior to use, PBS

was treated with Chelex 100 resin to remove trace metal ions and was subsequently filtered and adjusted to the appropriate pH with dilute hydrochloric acid. Following deoxygenation, an aqueous solution of GSNO was injected to produce an initial GSNO concentration of 10  $\mu$ M. The reaction was then shielded from ambient light and allowed to progress until NO release returned to baseline levels (<1 ppb). During this period, N<sub>2</sub> was continuously bubbled through the solution to remove NO as it formed, and a flow of N<sub>2</sub> was used to transport NO from the headspace of the analysis vessel into the NO analyzer. The NO yield was calculated using the quantity of recovered NO determined by chemiluminescence and the theoretical amount of NO based on the quantity of added GSNO. After an average of 3.5  $\pm$  0.4 h (mean  $\pm$  SD), 97  $\pm$  6% of theoretical NO was released and quantified by chemiluminescence. The complete consumption of the initial quantity of GSNO produces the dramatic decline in NO release observed in the representative NO release profile plotted in **Figure 5.9a**. In comparison, control experiments using cross-linked PVA membrane (without CuBTTri) resulted in an NO yield of 2.5  $\pm$  0.1% over the same duration, a result that was representative of the baseline decomposition rate of GSNO under prevailing experimental conditions. This finding was confirmed by evaluating the decomposition of GSNO alone (without added membrane), which resulted in an NO recovery of 2.7  $\pm$  0.3%. These results indicate that the presence of 10 wt. % CuBTTri/PVA membrane induces a 36-fold increase in the rate of NO generation from GSNO. Furthermore, the absence of any statistically significant elevation in NO release in the presence of PVA controls indicates that the performance of the 10 wt. % CuBTTri/PVA membranes is wholly attributable to inclusion of the MOF. The essentially quantitative recovery of NO and the previous observation that oxidized glutathione is formed during the reaction indicate that the products likely correspond to those produced by thermal, light-induced, or copper ion-catalyzed decomposition ( $2 \text{ RSNO} \rightarrow 2 \text{ NO} + \text{RSSR}$ ).<sup>13</sup>

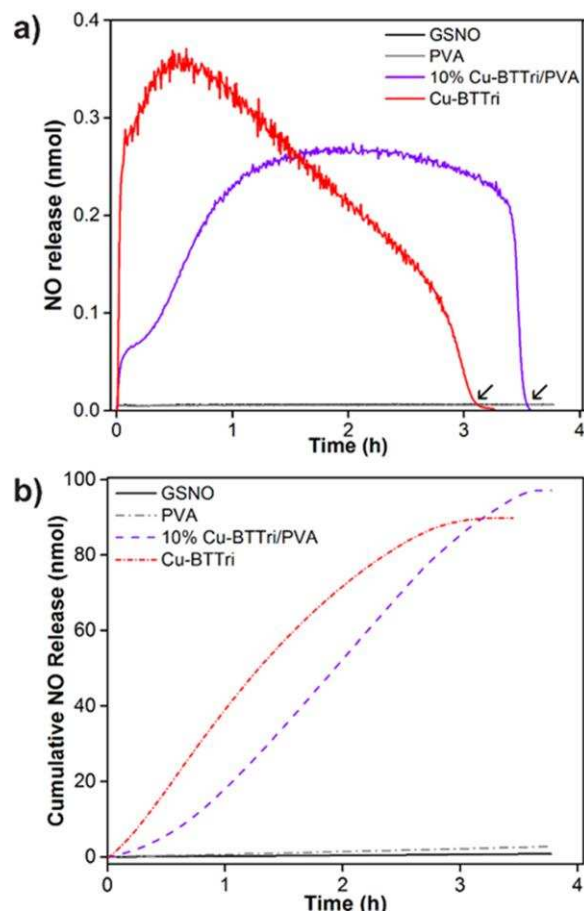


**Figure 5.9** (a) Representative NO release profiles depicting enhanced NO generation in the presence of CuBTtri and 10 wt. % CuBTtri/PVA membrane, compared with PVA control membrane and the thermal decomposition of GSNO. Consumption of available GSNO is accompanied by a rapid decrease in detected NO release, as shown by arrows. (b) Cumulative NO release plots for thermal GSNO decomposition, GSNO in the presence of PVA control membranes, and GSNO in the presence of 10% CuBTtri/PVA membranes. Experimental conditions: pH 7.4 PBS at 37 °C, with a 10  $\mu$ M initial GSNO concentration ( $n \geq 3$ ). Reproduced by permission of the American Chemical Society.

The pXRD patterns of the 10 wt. % CuBTtri/PVA membrane and CuBTtri powder after NO release experiments showed retention of the characteristic peaks associated with CuBTtri, providing qualitative support for the lack of MOF degradation (**Figure 5.10 and 5.11**). Following each experiment, inductively coupled plasma atomic emission spectroscopy (ICP-AES) was used to determine the amount of trace copper in the buffer solution, which was limited to  $0.34 \pm 0.08\%$  of the theoretical quantity present in 10 wt. % CuBTtri membrane. Because copper may produce

toxicological concerns at sufficient levels, this lack of appreciable copper leaching supports, at minimum, the use of CuBTTri/PVA membranes in short-term blood-contacting applications. To evaluate the potential for copper leaching under harsher conditions, samples of 10 wt. % CuBTTri/PVA were immersed in pH 7.4 PBS at 37 °C for 24 h at a thousand-fold higher, non-physiological GSNO concentration of 10 mM. At the end of this exposure period, ICP-AES was

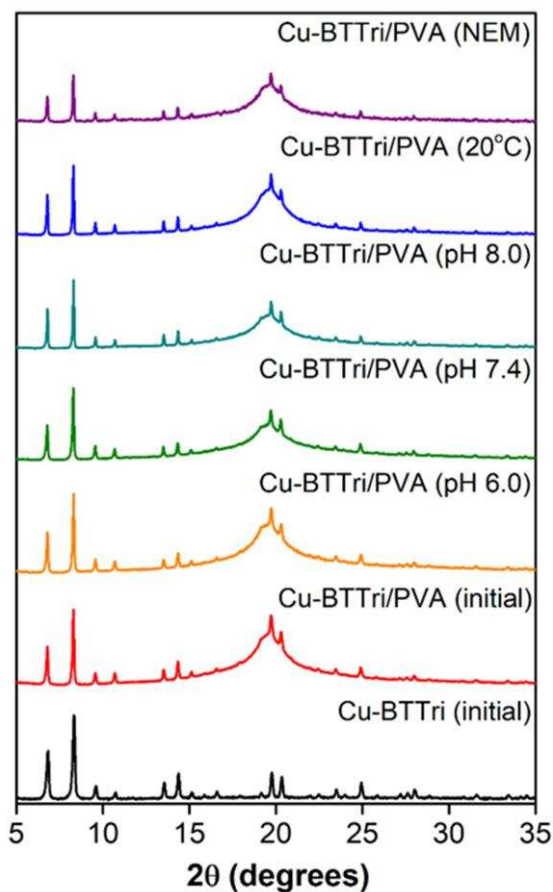


**Figure 5.10** pXRD of 10 % wt. CuBTTri/PVA membranes following NOA experiments under varying reaction conditions. Diffraction patterns show the retention of key peaks associated with CuBTTri, providing qualitative evidence that CuBTTri remains intact following promotion of NO from GSNO under varying conditions. Reproduced by permission of the American Chemical Society.

used to determine a quantity of copper in the buffer solution equivalent to  $2.5 \pm 0.2\%$  of the theoretical amount present in the membrane. In contrast, no leaching was observed in PBS alone under otherwise identical conditions. This result indicates that the MOF exhibits a remarkable degree of stability even at a GSNO concentration that vastly exceeds potential physiological levels.

Furthermore, this resistance to leaching compares favorably to previously reported polyurethane-bound copper(II)-cyclen complexes that were similarly used to promote NO release from GSNO.<sup>49</sup> In that example, 25% of available copper was removed after 24 h of immersion in PBS at a GSNO concentration of only 10  $\mu\text{M}$ .<sup>49</sup>

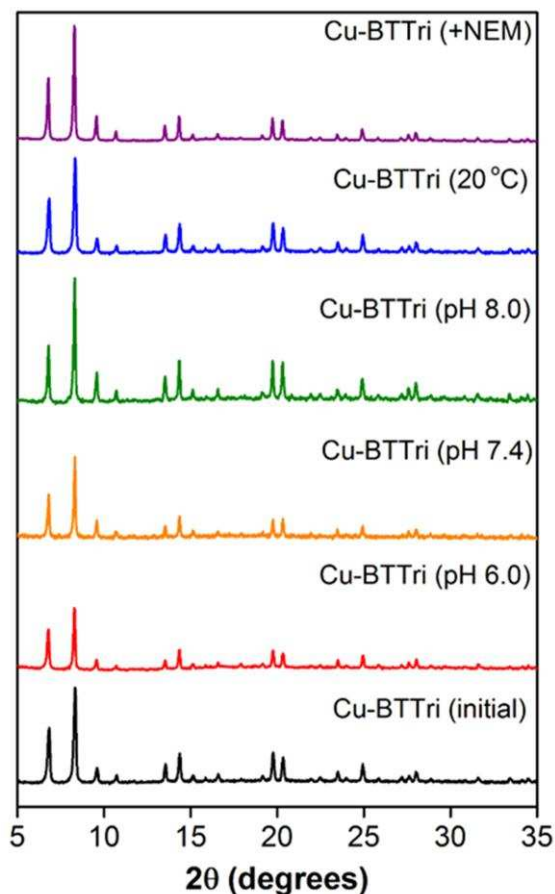


**Figure 5.11** pXRD diffraction patterns for CuBTtri particles upon completion of NO release experiments. Diffraction patterns show the retention of key peaks associated with CuBTtri, providing qualitative evidence that CuBTtri remains intact following promotion of NO from GSNO under varying conditions. Reproduced by permission of the American Chemical Society.

The MOF CuBTtri has previously been blended within chitosan membranes at 10 wt. % loading, where a similar ability to rapidly induce the decomposition of GSNO was observed.<sup>13</sup> However, control membranes prepared from chitosan alone independently produced a 7-fold increase in NO production relative to the baseline rate of GSNO decomposition. Because the

primary amine groups of chitosan facilitate chelation, this phenomenon was attributed to the presence of trace metal ions bound to the polymer. The absence of this behavior in PVA suggests

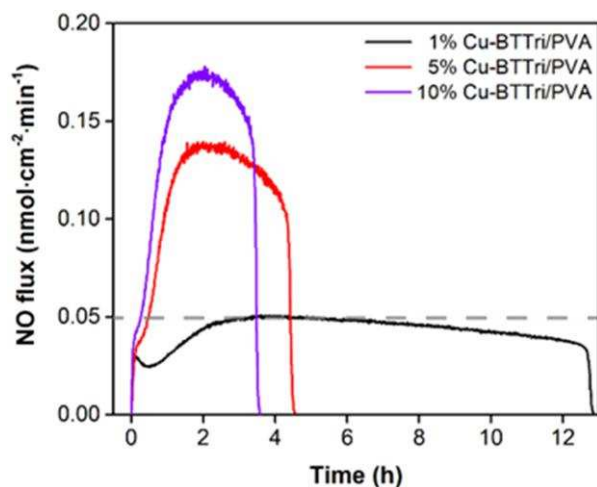


**Figure 5.12** NO flux ( $\text{nmol}\cdot\text{cm}^{-2}\cdot\text{min}^{-1}$ ) produced by 1, 5, and 10 wt. % CuBTTri/PVA membranes. Dashed line corresponds to an NO flux of  $0.05 \text{ nmol}\cdot\text{cm}^{-2}\cdot\text{min}^{-1}$ , a value that is frequently invoked as the lower limit of physiological endothelial flux.<sup>3</sup> Experimental conditions: pH 7.4 PBS at  $37 \text{ }^\circ\text{C}$ , with a  $10 \mu\text{M}$  initial GSNO concentration ( $n \geq 3$ ). Reproduced by permission of the American Chemical Society.

that the polymer matrix functions as an encapsulating support for CuBTTri without exerting a chemical influence on the reaction itself. The maximum NO flux observed from 10 wt. % CuBTTri/PVA was  $0.20 \pm 0.02 \text{ nmol}\cdot\text{cm}^{-2}\cdot\text{min}^{-1}$ , falling within the  $0.05$  to  $0.41 \text{ nmol}\cdot\text{cm}^{-2}\cdot\text{min}^{-1}$  range often associated with natural endothelial NO production (**Figure 5.12**).<sup>45,51,52</sup> This range has frequently been used as a benchmark to indicate antithrombotic therapeutic potential.<sup>51</sup> As an additional point of comparison, a quantity of CuBTTri powder equivalent to the mass contained in 10 wt. % CuBTTri/PVA membranes was exposed to  $10 \mu\text{M}$  GSNO under identical conditions (**Figure 5.9**). The use of this suspension of CuBTTri powder did not result in statistically significant differences in total NO yield ( $90 \pm 1\%$ ) or completion time ( $3.3 \pm 0.2 \text{ h}$ ) relative to 10 wt. % CuBTTri/PVA membrane (**Figure 5.13**). However, comparison of the NO release profiles of 10 wt. % CuBTTri/PVA and an equivalent mass of CuBTTri powder shows significantly slower initial release kinetics in the case where the MOF is incorporated within PVA. As a consequence,

50% of available NO is recovered in only  $1.3 \pm 0.1$  h in the case of CuBTtri powder, while the required time for 50% recovery is  $2.0 \pm 0.3$  h for 10 wt. % CuBTtri/PVA. This difference in kinetics likely arises from diffusion of GSNO into the membrane prior to interaction with

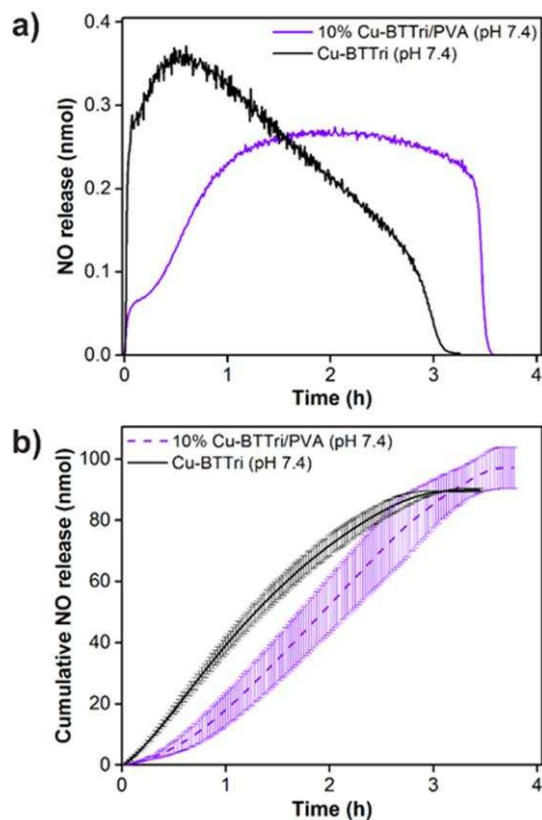


**Figure 5.13** (a) Representative NO release profiles and (b) cumulative NO release profiles for CuBTtri particles and 10 wt. % CuBTtri/PVA membranes, depicting their comparative performance. Experimental conditions: pH 7.4 PBS at 37 °C, with a 10  $\mu$ M initial GSNO concentration ( $n \geq 3$ ). Cumulative NO release plot depicts both the mean and standard deviation. Reproduced by permission of the American Chemical Society.

CuBTtri. Following these initial experiments, the 10 wt. % CuBTtri/PVA membranes were immersed in Millipore water for 3 days and reused in a second set of identical NO release experiments. The reused membranes resulted in an NO yield of  $103 \pm 8\%$ , with a 34% increase in the duration of the reaction to  $4.7 \pm 0.4$  h (**Figure 5.14**).

Notably, the ability of 10 wt. % CuBTtri/PVA membrane to promote the decomposition of GSNO in pH 7.4 PBS at 37 °C was maintained when the buffer solution was sparged with O<sub>2</sub> in place of N<sub>2</sub>. This result was determined by conducting the reaction for 3.5 h (the average completion time

under typical measurement conditions) with constant O<sub>2</sub> sparging. Any remaining GSNO was subsequently decomposed by injection of an aqueous solution of copper(II) chloride, and the resulting NO release was quantified under standard analytical conditions. This test resulted in the recovery of only 53 ± 12% of theoretical NO, and provides the first experimental confirmation that

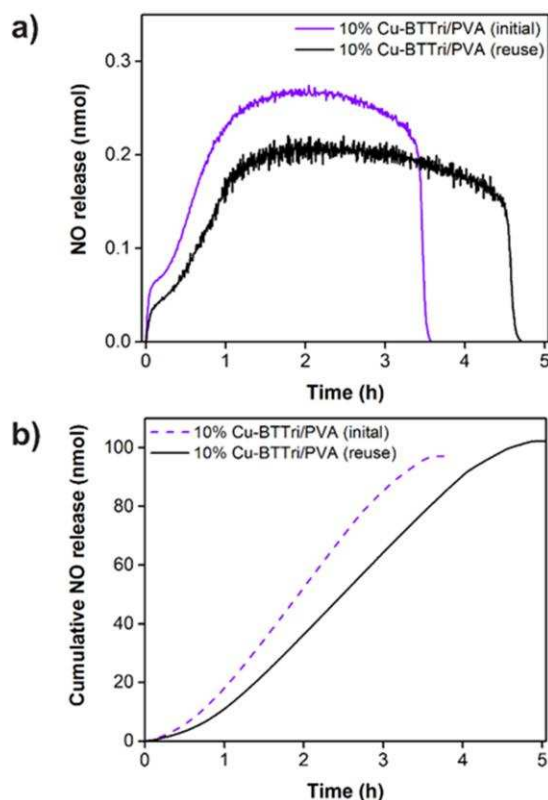


**Figure 5.14** (a) Representative NO release profiles and (b) cumulative NO release profiles for the initial use of 10 wt. % CuBTtri/PVA membranes and subsequent reuse after immersion in Millipore water for 72 h. Experimental conditions: pH 7.4 PBS at 37 °C, with a 10 μM initial GSNO concentration (n ≥ 3). Reproduced by permission of the American Chemical Society.

the reaction proceeds under aerobic conditions, albeit at a lower yield. A similar outcome for the *thermal* decomposition of RSNOs was observed by Grossi et al., where bubbling with O<sub>2</sub> was found to noticeably decrease the rate of decomposition.<sup>53</sup> Since the combination of NO and O<sub>2</sub> is known to form products such as nitrous acid (HNO<sub>2</sub>) under aqueous conditions, it may be the case that the change in chemical environment is solely responsible for the increased reaction time.<sup>54</sup>

Alternatively, O<sub>2</sub> may oxidize a putative copper(I) active site to an inactive copper(II) form, a process that has previously been observed in multiple copper-based MOFs.<sup>55</sup> The potential involvement of copper(I) sites has been invoked in computational studies that specifically investigated the interaction of RSNOs with copper-based MOFs, where reduction of framework copper(II) to copper(I) was included as a crucial step in the mechanistic process.<sup>56,57</sup> However, it remains unclear if this type of mechanism is operative in the case of CuBTtri and whether framework copper actively participates in the observed NO-forming activity of the MOF.

#### 5.4.2 Effect of varying copper(II) benzene-1,3,5-tris(1*H*-1,2,3-triazole-5-yl) concentration.

The influence of CuBTtri concentration on the performance of the CuBTtri/PVA membrane was determined by evaluating the ability of 1 and 5 wt. % CuBTtri/PVA membranes

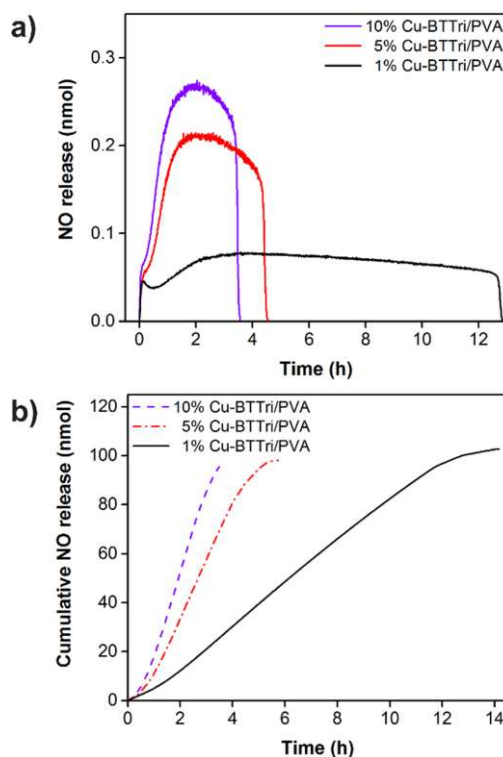


**Figure 5.15** (a) Representative NO release profiles depicting enhanced NO generation in the presence of the CuBTtri/PVA membranes at concentrations of 1, 5, and 10 wt. % CuBTtri. (b) Cumulative NO release plots for 1, 5 and 10 wt. % CuBTtri/PVA membranes. Experimental conditions: pH 7.4 PBS at 37 °C, with a 10  $\mu$ M initial GSNO concentration ( $n \geq 3$ ). Reproduced by permission of the American Chemical Society.

to induce NO release from GSNO in pH 7.4 PBS at 37 °C. At 5 wt. % CuBTTri, the total NO recovery of  $97 \pm 6\%$  was obtained after  $5.0 \pm 0.7$  h, representing a statistically significant 43% increase in reaction time compared to the 10 wt. % CuBTTri/PVA membranes (**Figure 5.15**). At 1 wt. % CuBTTri, total NO recovery ( $102 \pm 3\%$ ) required  $13 \pm 1$  h, corresponding to a 270% increase in completion time (**Figure 5.15**). The maximum NO fluxes observed for 5 and 1 wt. % CuBTTri membranes were  $0.16 \pm 0.06$  and  $0.051 \pm 0.008$  nmol·cm<sup>-2</sup>·min<sup>-1</sup>, respectively (**Figure 5.12**). These results indicate that lowering the concentration of CuBTTri from 10 to 1 wt. % predictably results in a significant lengthening of the reaction time but does not affect overall NO recovery. The observed reduction in maximum NO flux and extension in overall reaction time that accompanies the decrease in CuBTTri concentration may permit application-specific tuning of CuBTTri/polymer blends based on the amount of incorporated MOF. This behavior is directly attributable to the reduced availability of active species at lower MOF concentration as a similar relationship was observed by Major et al. in the case of copper nanoparticles blended into a hydrophilic polyurethane at various concentrations.<sup>25</sup>

#### **5.4.3 Effect of polymer water permeability.**

The water permeability and uptake of CuBTTri/polymer blends influences the rate at which dissolved RSNOs interact with the MOF. To investigate the water uptake properties of 10 wt. % CuBTTri/PVA membrane, dry samples were weighed and subsequently immersed in water for 24 h. The 10 wt. % CuBTTri/PVA membrane exhibited a swelling ratio of  $203 \pm 3\%$  (**Table 5.1**). For comparison, additional 10 wt. % CuBTTri films were prepared using Tecoflex SG-80A, a comparatively hydrophobic polyurethane often used for medical device fabrication. The swelling ratio of 10 wt. % CuBTTri/Tecoflex SG-80A films was determined gravimetrically to be  $2.0 \pm 0.3\%$ , indicating an approximate 100-fold difference in water uptake relative to hydrophilic PVA-

based membranes. The NO release profiles for GSNO in the presence of 10 wt. % CuBTTri/Tecoflex SG-80A films were subsequently acquired in pH 7.4 PBS at 37 °C over a

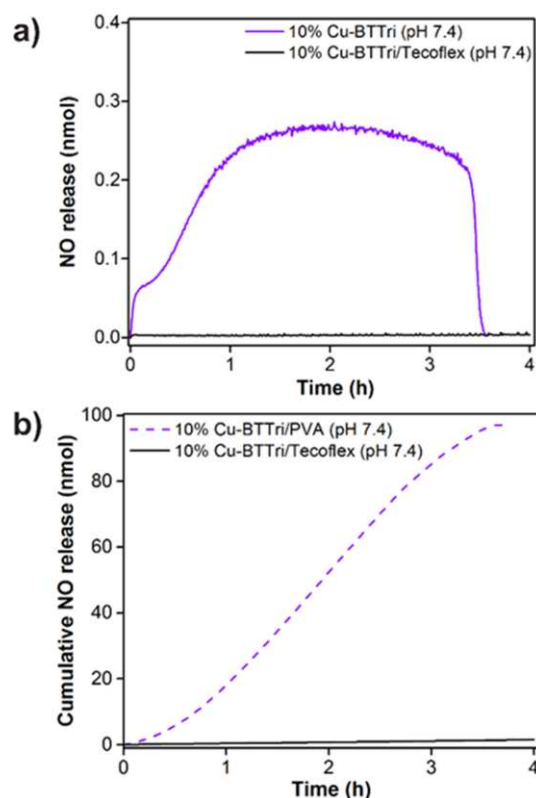


**Figure 5.16** (a) Representative NO release profiles depicting enhanced NO generation in the presence of 10 wt. % CuBTTri/PVA and the absence of this effect in the case of 10 wt. % CuBTTri/Tecoflex SG-80A. This outcome is primarily attributable to differences in water uptake between hydrophilic PVA and hydrophobic Tecoflex SG-80A. (b) Cumulative NO release plots for 10 wt. % CuBTTri/PVA membrane and 10 wt. % CuBTTri/Tecoflex SG-80A films. Experimental conditions: pH 7.4 PBS at 37 °C, with a 10  $\mu$ M initial GSNO concentration ( $n \geq 3$ ). Reproduced by permission of the American Chemical Society.

**Table 5.1** Tabulated water uptake data

| Sample                           | Water Uptake (%) |
|----------------------------------|------------------|
| 10 wt. % CuBTTri/PVA             | 203 $\pm$ 3      |
| 10 wt. % CuBTTri/Tecoflex SG-80A | 2.0 $\pm$ 0.3    |

duration corresponding to the completion time of experiments performed using 10 wt. % CuBTTri/PVA membranes. Over this period, only 1.5  $\pm$  0.4% of theoretical NO was recovered, compared to 97  $\pm$  6% for the 10% CuBTTri/PVA membranes (**Figure 5.16**). These results support prior observations that hydrophobic polymers with decreased water permeability/uptake inhibit

the NO-forming interaction of RSNOs with CuBTTri. In general, it is clear that only hydrophilic polymers such as PVA permit sufficiently rapid transport of GSNO to exploit the NO-forming capability of the MOF. The broader implication of this outcome is that medical devices fabricated from or coated with CuBTTri/polymer formulations are likely obligated to use hydrophilic polymers that facilitate diffusion of water and endogenous RSNOs into the polymer matrix. This observation is in agreement with a literature example using copper nanoparticles blended into polyurethane to produce NO from RSNOs.<sup>25</sup> In this case, contact between RSNOs and the active copper species was dependent upon the hydrophilicity of the polymer since the reaction was hypothesized to occur within the polymer itself and must therefore be preceded by RSNO transport into the material.

#### **5.4.4 Effect of lower temperature.**

Additionally, the impact of lower temperature on the ability of 10 wt. % CuBTTri/PVA membranes to promote NO release from GSNO was evaluated in pH 7.4 PBS. This assessment is of particular importance for topical blood-contacting applications (e.g., wound dressings) since skin temperature can be anticipated to range from near ambient temperature to a normal physiological value of approximately 37 °C.<sup>58</sup> For 10 wt. % CuBTTri/PVA membranes, lowering the temperature of the reaction from 37 °C to 20 °C resulted in an 84% decrease in NO recovery over 3.5 h (the duration of the reaction at 37 °C) from  $97 \pm 6\%$  (essentially quantitative) to  $16 \pm 1\%$  (**Figure 5.17[a, b], Figure 5.18**). When a suspension of CuBTTri powder was used, a similar, statistically significant decrease of 77% was observed ( $90 \pm 1$  to  $21 \pm 1\%$  NO recovery) (**Figure 5.17[c, d]**). These results indicate that the reaction of GSNO with CuBTTri is accelerated at physiological temperature, as expected. To further elucidate the role of temperature on the interaction of GSNO with CuBTTri, a 10 wt. % CuBTTri/PVA membrane was used to promote

NO release from GSNO at 37 °C then subsequently reused at 20 °C in an otherwise identical experiment. The rate of NO release remained largely consistent with previous experiments conducted at 20 °C, suggesting that elevation to 37 °C in the presence of GSNO does not activate

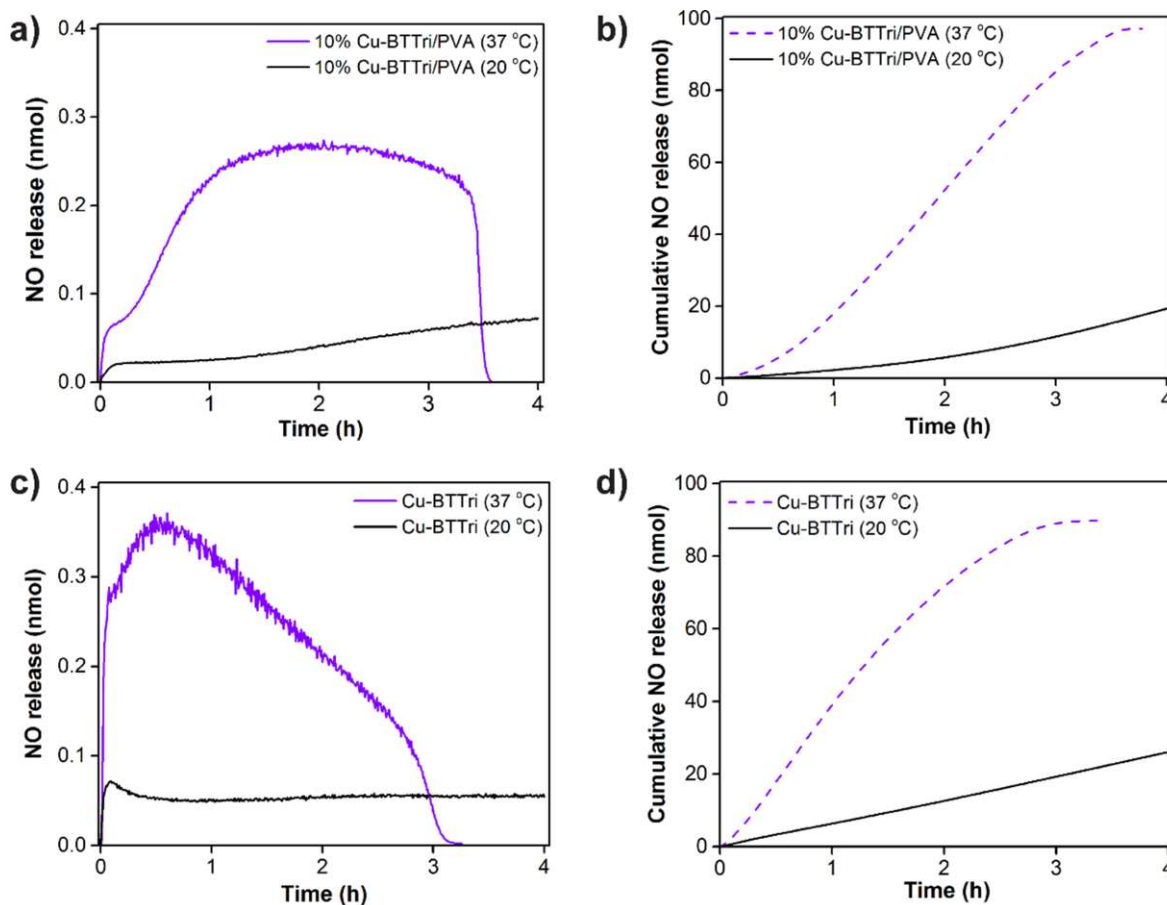


**Figure 5.17** (a) Representative NO release profiles and (b) cumulative NO release of 10 wt. % CuBTTri/PVA membranes at 37 °C and 20 °C. (c) Representative NO release profiles and (d) cumulative NO release plots for suspended CuBTTri powder at 37 °C and 20 °C. Experimental conditions: pH 7.4 PBS, with a 10  $\mu$ M initial GSNO concentration ( $n \geq 3$ ). Reproduced by permission of the American Chemical Society.

the MOF in an irreversible manner.

#### 5.4.5 Effect of varying pH conditions.

It has been previously observed that the stability of the *S*-nitrosothiol functional group is influenced by pH.<sup>59</sup> However, the influence of pH on the homogeneous copper-catalyzed decomposition of RSNOs or the ability of copper-based MOFs such as CuBTTri to promote NO

release from RSNOs has not been clearly established. For this reason, the ability of 10 wt. % CuBTTri/PVA membranes to decompose GSNO was evaluated in pH 6.0 and 8.0 PBS at 37 °C,

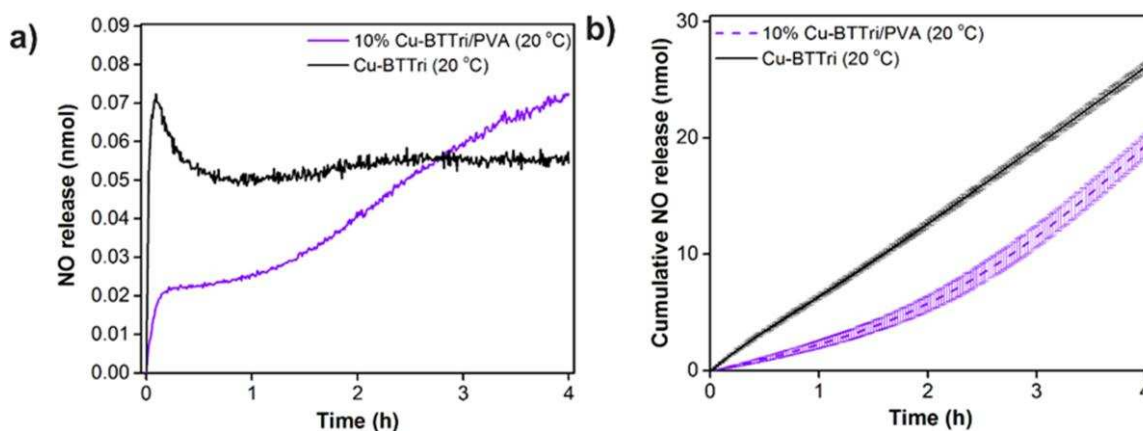


**Figure 5.18** (a) Representative NO release profiles and (b) cumulative NO release profiles for CuBTTri particles and 10 wt. % CuBTTri/PVA membranes, depicting their comparative performance at reduced temperature. Experimental conditions: pH 7.4 PBS at 20 °C, with a 10  $\mu$ M initial GSNO concentration ( $n \geq 3$ ). Cumulative NO release plot depicts both the mean and standard deviation. Reproduced by permission of the American Chemical Society.

supplementing existing data collected at pH 7.4. To avoid the possibility that alternative buffer systems might independently influence the behavior of the reaction, the pH 7.4 PBS used for other experiments was adjusted to the appropriate pH. At pH values of 6.0 and 8.0, the respective NO yields were  $96 \pm 1\%$  and  $103 \pm 4\%$  (**Figure 5.19**). Compared to the mean reaction time of  $3.5 \pm 0.4$  h for 10 wt. % CuBTTri/PVA at pH 7.4, depression to pH 6.0 resulted in a statistically significant 22% decrease to  $2.7 \pm 0.2$  h (**Figure 5.19**). Elevation of the pH to 8.0 increased the required reaction time by 17% to  $4.1 \pm 0.2$  h (**Figure 5.19[a, b]**). To explore the influence of pH specifically on CuBTTri, GSNO was exposed to an aqueous suspension of MOF powder in pH 6.0 and 8.0 PBS at 37 °C (**Figure 5.19[c, d]**). At pH 6.0, the total NO recovery was  $92 \pm 1\%$  after  $2.1 \pm 0.1$  h, corresponding to a statistically significant 36% decrease in reaction time (**Figure 5.19[c, d]**). At pH 8.0, a total of  $91 \pm 3\%$  of theoretical NO was recovered after  $3.2 \pm 0.3$  h at pH 8.0 (**Figure 5.19[c, d]**). Lower pH appears to consistently promote acceleration of the NO-forming

reaction with CuBTtri, regardless of whether CuBTtri is evaluated as a suspension or incorporated within a PVA matrix. In contrast, slight elevation in pH from 7.4 to 8.0 increases the duration of the reaction with 10 wt. % CuBTtri/PVA membrane but has no significant impact on the performance of the suspended MOF powder (**Figure 5.19[c, d]**, **Figure 5.20**). In the case of

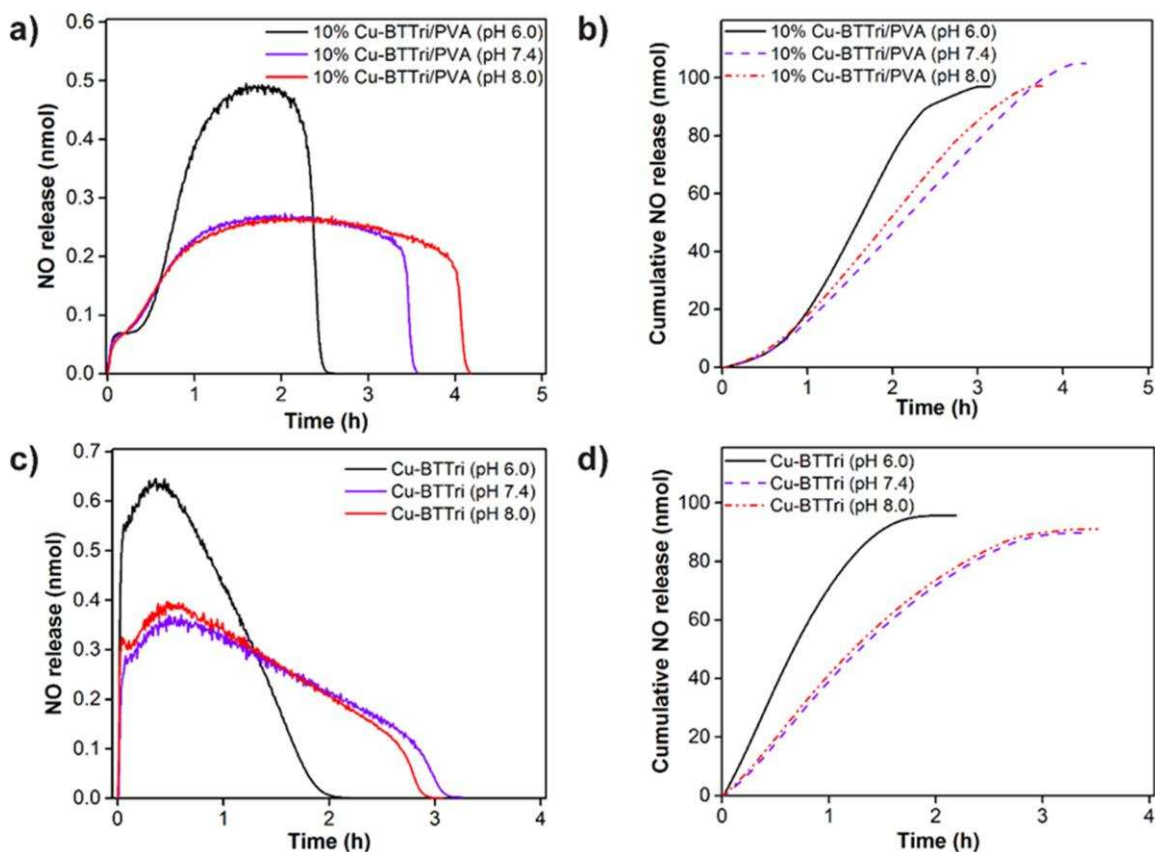


**Figure 5.19** (a) Representative NO release profiles and (b) cumulative NO release for 10 wt. % CuBTtri/PVA membranes at pH 6.0, 7.4 and 8.0. (c) Representative NO release profiles and (d) Cumulative NO release profiles for suspended CuBTtri powder at pH 6.0, 7.4 and 8.0. Experimental conditions: PBS at 37 °C, with a 10  $\mu$ M initial GSNO concentration ( $n \geq 3$ ). Reproduced by permission of the American Chemical Society.

10 wt. % CuBTtri/PVA membranes, the 17% increase in reaction time at pH 8.0 may be attributable to impaired GSNO diffusion through the PVA matrix. This hypothesis is supported by the observation that no difference in the overall reaction time between pH 7.4 and 8.0 is observed for suspended CuBTtri powder. At elevated pH, it may be predicted from the  $pK_a$  values of glutathione that an increasing fraction of acidic groups may exist in the negatively-charged

carboxylate form. This phenomenon may reduce the propensity of GSNO to diffuse through the PVA matrix. At pH 6.0, both the 10 wt. % CuBTTri/PVA membranes and the suspension of CuBTTri powder exhibit accelerated reactions with GSNO (**Figure 5.21**). The magnitude of this acceleration is slightly greater in the case of the CuBTTri powder suspension, which may indicate a diffusion-related delay as shown in **Figure 8**.

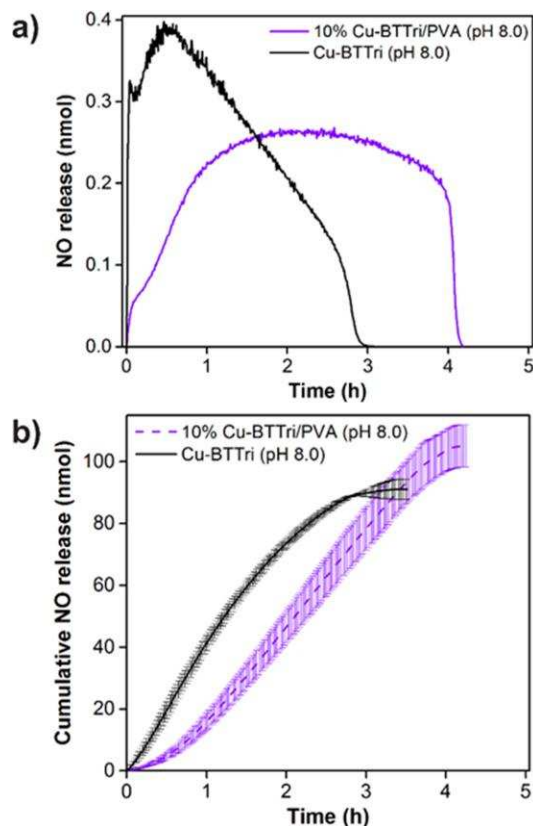


**Figure 5.20** (a) Representative NO release profiles and (b) cumulative NO release profiles for CuBTTri particles and 10 wt. % CuBTTri/PVA membranes, depicting their comparative performance at increased pH. Experimental conditions: pH 8.0 PBS at 37 °C, with a 10  $\mu$ M initial GSNO concentration ( $n \geq 3$ ). Cumulative NO release plot depicts both the mean and standard deviation. Reproduced by permission of the American Chemical Society.

As a comparative study, aqueous copper(II) chloride was used to decompose 10  $\mu$ M GSNO in PBS at 37 °C. As anticipated from the use of a homogeneous catalyst, the reaction between solution-phase copper ions and GSNO was significantly faster (<30 min completion time) than the rates observed for CuBTTri. In addition, the behavior of the reaction as the pH was reduced from 7.4 to 6.0 was reversed. Unlike the acceleration observed in the case of CuBTTri (whether in the

form of a suspended powder or blended PVA membrane), the time required for copper(II) chloride to decompose GSNO in PBS at 37 °C was significantly *lengthened* by 74% as the pH was decreased from 7.4 to 6.0. No statistically significant difference manifested at a slight pH elevation to 8.0 in accordance with the performance of suspended CuBTtri. These observations with

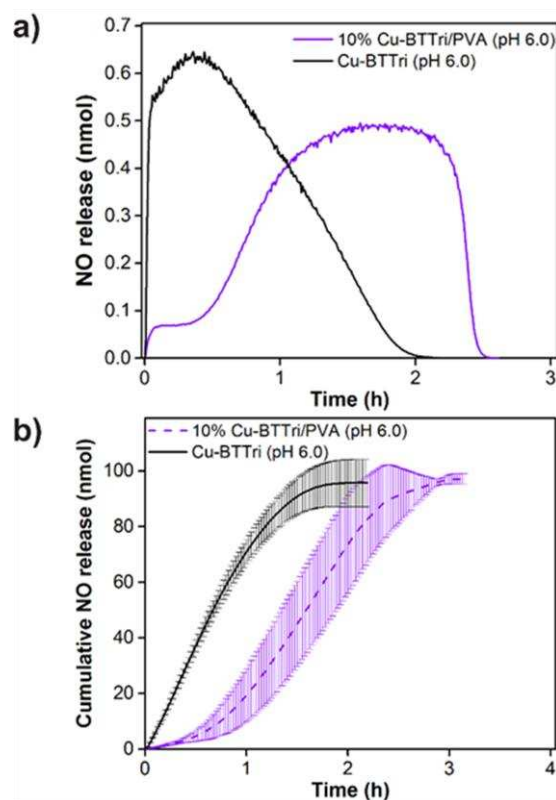


**Figure 5.21** (a) Representative NO release profiles and (b) cumulative NO release profiles for CuBTtri particles and 10 wt. % CuBTtri/PVA membranes, depicting their comparative performance at decreased pH. Experimental conditions: pH 6.0 PBS at 37 °C, with a 10  $\mu$ M initial GSNO concentration ( $n \geq 3$ ). Cumulative NO release plot depicts both the mean and standard deviation. Reproduced by permission of the American Chemical Society.

copper(II) chloride and GSNO may support the prevailing understanding of both RSNO stability and the mechanism for homogeneous copper-catalyzed decomposition of RSNOs. The rapid and complete NO-forming decomposition of RSNOs is typically effected by the addition of catalytic quantities of copper(II) salts.<sup>31,60,61</sup> Although copper(II) itself was initially implicated as the active species in this reaction, McAninly et al. proposed a mechanism based on the reduction of copper(II) to copper(I) by thiolate anions.<sup>61</sup> The crucial role of copper(I) in the catalytic

decomposition of RSNOs was later supported by the ability of neocuproine (a copper(I)-specific chelator) to arrest the reaction.<sup>62</sup>

The rate-determining, thiol-mediated reduction of copper(II) may result from trace thiol remaining in RSNO samples or the regeneration of thiol from RSNOs in aqueous media.<sup>63</sup> It may therefore be reasoned, a priori, that a decrease in pH (and corresponding decrease in the ratio of thiolate to thiol) could potentially impair the rate at which the active copper(I) species is generated, increasing the completion time of the NO-forming reaction. This hypothesis aligns with the NO-generating performance of copper(II) chloride as a function of pH. For example, it has been theorized that the decomposition of dissolved RSNOs is arrested under acidic conditions due to reduced thiolate concentration, which inhibits reduction of copper(II) to copper(I).<sup>64</sup> In contrast, the significant *acceleration* of the reaction between CuBTTri and GSNO as pH is decreased may imply that an alternative process is operative, which is sufficiently distinct in mechanism to produce an inversion of pH sensitivity. While the distinction in behavior between CuBTTri and solution-phase copper ions may arise from the comparative role of thiol in each reaction, it must be noted that the ability of copper ions to form sparingly soluble copper phosphate species may influence the kinetics of the latter reaction in PBS. Following the reactions with 10 wt. % CuBTTri/PVA membrane, the copper concentrations of the pH 6.0 and pH 7.4 buffer solutions were found to correspond to  $0.31 \pm 0.03$  and  $0.34 \pm 0.08\%$  of theoretical copper in the membranes, respectively. In the case of suspended CuBTTri powder, these values were  $0.32 \pm 0.01$  (pH 6.0) and  $0.20 \pm 0.03\%$  (pH 7.4). The absence of a statistically significant difference between the apparent level of copper leaching as a function of the pH decline from 7.4 to 6.0 indicates that pH-related decomposition of the MOF (and potential copper ion leaching) is not a clear factor in the acceleration of the reaction.

#### 5.4.6 Effect of thiol blocking with *N*-ethylmaleimide.

The ability of thiol to affect the structural characteristics of copper-based MOFs has been previously described. In the specific case of the carboxylate-derived MOF Cu-BTC, exposure to high concentrations of thiophenol or 1,3-propanedithiol in acetonitrile at 70 °C results in the decomposition of the MOF to copper(0) nanoparticles.<sup>65</sup> Ke et al. showed that Cu-BTC could be post-synthetically modified by exposure to dithioglycol (1,2-ethanedithiol), which resulted in grafting of the thiol to coordinatively unsaturated copper centers.<sup>66</sup> As previously discussed, it has also been suggested that the NO-forming behavior of Cu-BTC proceeds through the reduction of copper centers, a process that may be induced by thiol.<sup>56,57</sup> To explore the potential role of thiol/thiolate in the CuBTTri-promoted decomposition of GSNO, NO release experiments were performed using GSNO that had been incubated with a 10-fold excess of *N*-ethylmaleimide (NEM). This maleimide-based alkylating reagent reacts with thiol groups to form an effectively irreversible thioether linkage, and it is commonly used to modify cysteine residues in proteins.<sup>67</sup> In the case of 10 wt. % CuBTTri/PVA membranes, an 84% decrease in NO yield (over 3.5 h) was observed using GSNO that had been treated with NEM (from  $97 \pm 6\%$  to  $16 \pm 1\%$ ) (**Figure 5.22[a, b], Figure 5.23**). A smaller 39% decrease ( $90 \pm 1\%$  to  $55 \pm 2\%$ ) was observed when a suspension of CuBTTri powder was evaluated under identical conditions (**Figure 5.22[c, d], Figure 5.23**). While it was previously hypothesized that the function of CuBTTri may have little dependency on reduction by *thiolate* (as supported by acceleration of the reaction under acidic conditions), the reduction in NO production observed after GSNO was treated with NEM may indicate that residual thiol does have an influence on the activity of the MOF.

However, the fact that this effect is most pronounced when diffusion into the PVA matrix must occur prior to the reaction may support alternative hypotheses. The presence of a 10-fold

excess of NEM may simply inhibit the ability of GSNO to reach active sites within the MOF, whether through modification of the primary amine to form a bulkier derivative or through competitive interactions with the MOF itself.<sup>68</sup> The direct exposure of CuBTri powder to neat ethanethiol results in regeneration of the triazole ligand and loss of the diffraction pattern

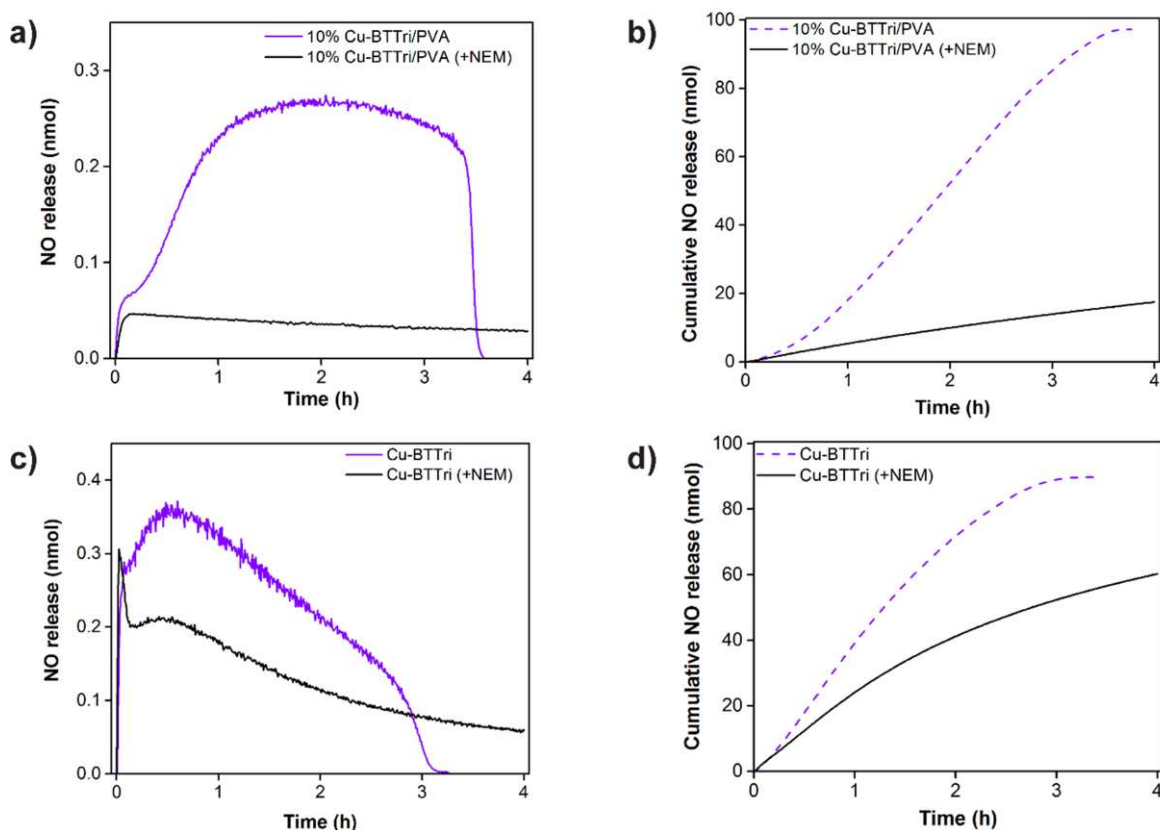


**Figure 5.22** (a) Representative NO release profiles and (b) cumulative NO release of 10 wt. % CuBTri/PVA membranes with and without NEM (c) Representative NO release profiles and (d) cumulative NO release profiles for CuBTri particles with and without NEM. Experimental conditions: pH 7.4 PBS at 37 °C, with a 10  $\mu$ M initial GSNO and 100  $\mu$ M NEM concentration ( $n \geq 3$ ). Reproduced by permission of the American Chemical Society.

associated with the MOF. Exposure to 3 mM glutathione (the thiol precursor to GSNO) in pH 7.4 PBS for 24 h at ambient temperature resulted in the release of  $16 \pm 1\%$  of theoretical copper into solution. These findings suggest that *high* concentrations of thiol are capable of degrading CuBTri. However, previous observations that physiological (10  $\mu$ M) and elevated (10 mM) concentrations of RSNO do not produce substantial copper leaching or loss of MOF structure

suggest that this type of degradation is unlikely to contribute to the NO-forming activity of CuBTTri. As further support for this hypothesis, the addition of NEM does not significantly reduce

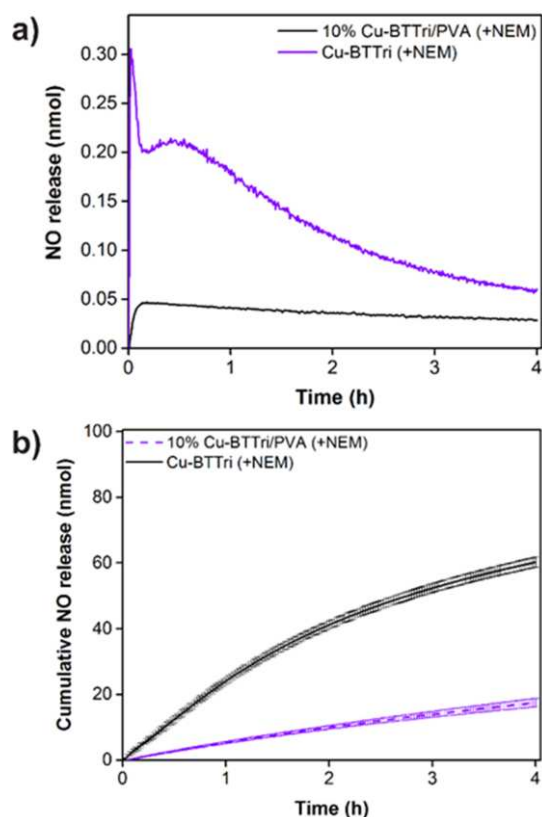


**Figure 5.23** (a) Representative NO release profiles and (b) cumulative NO release profiles for CuBTTri particles and 10 wt. % CuBTTri/PVA membranes in the presence of GSNO, with and without a 10-fold excess of NEM to illustrate the effect of adding a thiol-blocking agent. Experimental conditions: pH 7.4 PBS at 37 °C, with a 10  $\mu$ M initial GSNO concentration and a 100  $\mu$ M NEM concentration ( $n \geq 3$ ). Cumulative NO release plot depicts both the mean and standard deviation. Reproduced by permission of the American Chemical Society.

the trace amount of copper recovered subsequent to the reaction, with  $0.28 \pm 0.03\%$  of theoretical copper determined in the buffer solution by ICP-AES. This outcome suggests that, at physiological RSNO concentrations, the role of thiol/thiolate (if any) is unlikely to include the formation of labile copper species that are subsequently released into solution.

## 5.5 Summary and conclusions

Membranes were prepared from hydrophilic PVA and the triazolate-bridged MOF CuBTTri and subsequently evaluated for their ability to induce NO release from GSNO, a biomolecule

identified in blood. All results are summarized below (**Table 5.2**). In pH 7.4 PBS at 37 °C, it was demonstrated that 1, 5, and 10 wt. % CuBTTri/PVA membranes were able to effectively induce NO production from GSNO at levels that may be associated with antithrombotic effects. In the case of 10 wt. % CuBTTri/PVA membrane, a 36-fold increase in the rate of NO production was observed relative to the thermal decomposition of GSNO over an identical duration. While incorporation of 10 wt. % CuBTTri within PVA results in delayed NO production kinetics relative to a suspension of MOF particles, the overall completion time of the reaction was statistically unchanged. The maximum NO flux ranged from  $0.051 \pm 0.008$  (1 wt. % CuBTTri) to  $0.20 \pm 0.02$   $\text{nmol}\cdot\text{cm}^{-2}\cdot\text{min}^{-1}$  (10 wt. % CuBTTri) compared to an estimated endothelial flux of 0.05 to 0.4  $\text{nmol}\cdot\text{cm}^{-2}\cdot\text{min}^{-1}$ . This performance suggests that CuBTTri/PVA membranes may be suitable for the production of a physiologically-relevant NO flux from endogenous sources. The level of NO production and the time required to consume available GSNO are directly related to the weight percentage of CuBTTri blended into the membrane, which indicates the potential for controllable NO generation. This NO-generating activity is apparently unaccompanied by detectable degradation of the MOF itself (pXRD), and only trace quantities of copper (<1% of theoretical) are present in the buffer following the reaction. The ability of CuBTTri/PVA materials to initiate NO release from GSNO relies upon the substantial water uptake of the PVA membrane and hypothesized transport of GSNO to the active MOF species. Without this level of water uptake, as in the case of 10 wt. % CuBTTri films prepared from hydrophobic Tecoflex SG-80A, no short-term increase in NO production is observed. The NO-forming reaction between GSNO and CuBTTri exhibits temperature dependence and dramatically decreases in rate at 20 °C, with an NO yield of only  $16 \pm 1\%$  over 3.5 h, compared to  $97 \pm 6\%$  at 37 °C. This finding leads to the conclusion that therapeutically useful activity is most probable at or near physiological

temperature, as in the case of flowing blood. This result may also suggest that a significant thermodynamic barrier exists for the rate-determining step of the reaction, in contrast to the rapid and complete reaction of GSNO with homogeneous copper ion catalysts at ambient temperature. The reaction is also pH-dependent, with a substantial increase in the rate of NO production observed as pH declines from 7.4 to 6.0, contrasting with the opposite behavior in aqueous copper(II) chloride. This effect is present regardless of whether the MOF is incorporated within a PVA matrix, and is not accompanied by an increase in the quantity of trace copper in the buffer solution. The lack of soluble copper ion formation indicates that pH-related decomposition of either the MOF itself or secondary active species is not a clear factor in the acceleration of the reaction under mildly acidic conditions. When a 10-fold excess of the thiol-blocking reagent NEM is present during the reaction (pH 7.4 PBS, 37 °C), NO generation is reduced by 84% in the case of 10 wt. % CuBTTri/PVA membrane. A significantly less dramatic 39% decrease in the rate of the reaction is observed for a suspension of CuBTTri powder when exposed to NEM-treated GSNO. These findings reveal that trace thiol may influence the reaction, potentially through the reduction of copper sites as described elsewhere for Cu-BTC. The observed properties of CuBTTri/PVA blends indicate that the materials are capable of generating NO from the endogenous compound GSNO, and that therapeutically useful levels can be produced at physiological temperature and pH. These findings support the notion that CuBTTri/PVA has the potential to produce NO directly from blood, a phenomenon that would be advantageous given the large number of blood-contacting applications for PVA. Taken together, these studies have identified the characteristics (e.g., hydrophilicity) that CuBTTri/polymer blends must exhibit for optimized therapeutic use, and also provide a greater understanding of factors that influence CuBTTri reactivity in an effort to further investigate the role of the MOF in NO generation.

**Table 5.2** Tabulated nitric oxide release data

| Reaction Conditions                                     | NO Yield (%) <sup>b</sup> | Completion Time (h) <sup>c</sup> |
|---|---------------------------|----------------------------------|
| GSNO (pH 7.4, 37 °C) <sup>a</sup>                       | 2.7 ± 0.3                 | n/a                              |
| GSNO + PVA (pH 7.4, 37 °C) <sup>a</sup>                 | 2.5 ± 0.1                 | n/a                              |
| GSNO + 10 wt. % CuBTTri/Tecoflex SG-80A (pH 7.4, 37 °C) | 1.5 ± 0.4                 | n/a                              |
| GSNO + 10 wt. % CuBTTri/PVA (pH 7.4, 37 °C)             | 97 ± 6                    | 3.5 ± 0.4                        |
| GSNO + 10 wt. % CuBTTri/PVA (pH 6.0, 37 °C)             | 96 ± 1                    | 2.7 ± 0.2                        |
| GSNO + 10 wt. % CuBTTri/PVA (pH 8.0, 37 °C)             | 103 ± 4                   | 4.1 ± 0.2                        |
| GSNO + 10 wt. % CuBTTri/PVA (pH 7.4, 20 °C)             | 16 ± 1                    | n/a                              |
| GSNO + 1 wt. % CuBTTri/PVA (pH 7.4, 37 °C)              | 102 ± 3                   | 13 ± 1                           |
| GSNO + 5 wt. % CuBTTri/PVA (pH 7.4, 37 °C)              | 97 ± 6                    | 5.0 ± 0.7                        |
| GSNO + 10 wt. % CuBTTri/PVA (reuse, pH 7.4, 37 °C)      | 103 ± 8                   | 4.7 ± 0.4                        |
| GSNO + NEM + 10 wt. % CuBTTri/PVA (pH 7.4, 37 °C)       | 16 ± 1                    | n/a                              |
| GSNO + CuBTTri (pH 7.4, 37 °C) <sup>a</sup>             | 90 ± 1                    | 3.3 ± 0.2                        |
| GSNO + CuBTTri (pH 6.0, 37 °C) <sup>a</sup>             | 92 ± 1                    | 2.1 ± 0.1                        |
| GSNO + CuBTTri (pH 8.0, 37 °C) <sup>a</sup>             | 91 ± 3                    | 3.2 ± 0.3                        |
| GSNO + CuBTTri (pH 7.4, 20 °C) <sup>a</sup>             | 21 ± 1                    | n/a                              |
| GSNO + NEM + CuBTTri (pH 7.4, 37 °C) <sup>a</sup>       | 55 ± 2                    | n/a                              |

<sup>a</sup>Reactions consist of the NO-forming decomposition of 10 μM *S*-nitrosoglutathione (GSNO) at varying temperature, concentration, and pH, or in the presence of *N*-ethylmaleimide (NEM). <sup>b</sup>CuBTTri powder added in a quantity corresponding to the amount present in experiments conducted with 10 wt. % CuBTTri/PVA. <sup>c</sup>NO yield refers to measured NO/theoretical GSNO × 100. <sup>c</sup>Completion time refers to the mean time required for NO measurements to reach baseline levels, which is inferred to represent depletion of available GSNO. Experiments with incomplete NO recovery were performed for fixed intervals corresponding to the mean duration of the parent experiment. All values reported as mean ± standard deviation.

## REFERENCES

1. Furukawa, H.; Cordova, K. E.; O’Keeffe, M.; Yaghi, O. M. The Chemistry and Applications of Metal-Organic Frameworks. *Science* **2013**, *341*, 974–986.
2. McKinlay, A. C.; Morris, R. E.; Horcajada, P.; Férey, G.; Gref, R.; Couvreur, P.; Serre, C. BioMOFs: Metal-Organic Frameworks for Biological and Medical Applications. *Angew. Chem., Int. Ed.* **2010**, *49*, 6260–6266.
3. Wyszogrodzka, G.; Marszałek, B.; Gil, B.; Dorożyński, P. Metal-Organic Frameworks: Mechanisms of Antibacterial Action and Potential Applications. *Drug Discov. Today* **2016**, *21*, 1009–1018.
4. Hinks, N. J.; McKinlay, A. C.; Xiao, B.; Wheatley, P. S.; Morris, R. E. Metal Organic Frameworks as NO Delivery Materials for Biological Applications. *Microporous Mesoporous Mater.* **2010**, *129*, 330–334.
5. Carpenter, A. W.; Schoenfish, M. H. Nitric Oxide Release: Part II. Therapeutic Applications. *Chem. Soc. Rev.* **2012**, *41*, 3742–3752.
6. McKinlay, A. C.; Eubank, J. F.; Wuttke, S.; Xiao, B.; Wheatley, P. S.; Bazin, P.; Lavalley, J.-C.; Daturi, M.; Vimont, A.; De Weireld, G.; Horcajada, P.; Serre, C.; Morris, R. E. Nitric Oxide Adsorption and Delivery in Flexible MIL-88(Fe) Metal–Organic Frameworks. *Chem. Mater.* **2013**, *25*, 1592–1599.
7. Xiao, B.; Wheatley, P. S.; Zhao, X.; Fletcher, A. J.; Fox, S.; Rossi, A. G.; Megson, I. L.; Bordiga, S.; Regli, L.; Mark Thomas, K.; Morris, R. E. High-Capacity Hydrogen and Nitric Oxide Adsorption and Storage in a Metal–Organic Framework. *J. Am. Chem. Soc.* **2007**, *129*, 1203–1209.

8. Ingleson, M. J.; Heck, R.; Gould, J. A.; Rosseinsky, M. J. Nitric Oxide Chemisorption in a Postsynthetically Modified Metal–Organic Framework. *Inorg. Chem.* **2009**, *48*, 9986–9988.
9. Harding, J. L.; Reynolds, M. M. Metal Organic Frameworks as Nitric Oxide Catalysts. *J. Am. Chem. Soc.* **2012**, *134*, 3330–3333.
10. Neufeld, M. J.; Harding, J. L.; Reynolds, M. M. Immobilization of Metal-Organic Framework Copper(II) Benzene-1,3,5-tricarboxylate (CuBTC) onto Cotton Fabric as a Nitric Oxide Release Catalyst. *ACS Appl. Mater. Interfaces* **2015**, *7*, 26742–26750.
11. Wo, Y.; Brisbois, E. J.; Bartlett, R. H.; Meyerhoff, M. E. Recent Advances in Thromboresistant and Antimicrobial Polymers for Biomedical Applications: Just Say Yes to Nitric Oxide (NO). *Biomater. Sci.* **2016**, *4*, 1161–1183.
12. Neufeld, M. J.; Ware, B. R.; Lutzke, A.; Khetani, S. R.; Reynolds, M. M. Water-Stable Metal–Organic Framework/Polymer Composites Compatible with Human Hepatocytes. *ACS Appl. Mater. Interfaces* **2016**, *8*, 19343–19352.
13. Neufeld, M. J.; Lutzke, A.; Tapia, J. B.; Reynolds, M. M. Metal–Organic Framework/Chitosan Hybrid Materials Promote Nitric Oxide Release from S-Nitrosoglutathione in Aqueous Solution. *ACS Appl. Mater. Interfaces* **2017**, *9*, 5139–5148.
14. Harding, J. H.; Metz, J. M.; Reynolds, M. M. A Tunable, Stable and Bioactive MOF for Generating a Localized Therapeutic from Endogenous Sources. *Adv. Func. Mater.* **2014**, *24*, 7503–7509.
15. Muppalaneni, S.; Omidian, H. Polyvinyl Alcohol in Medicine and Pharmacy: A Perspective. *J. Develop. Drugs* **2013**, *2*, 1–5.

16. Marcilli, R. H.; de Oliveira, M. G. Nitric Oxide-releasing Poly(vinyl alcohol) Film for Increasing Dermal Vasodilation. *Colloids Surf. B Biointerfaces* **2014**, *116*, 643–651.
17. Masters, K. S.; Leibovich, S. J.; Belem, P.; West, J. L.; Poole-Warren, L. A. Effects of Nitric Oxide Releasing Poly(vinyl alcohol) Hydrogel Dressings on Dermal Wound Healing in Diabetic Mice. *Wound Repair Regen.* **2002**, *10*, 286–294.
18. Schanuel, F. S.; Raggio Santos, K. S.; Monte-Alto-Costa, A.; de Oliveira, M. G. Combined Nitric Oxide-releasing Poly(vinyl alcohol) Film/F127 Hydrogel for Accelerating Wound Healing. *Colloids Surf. B. Biointerfaces* **2015**, *130*, 182–191.
19. Zhang, Y.; Wang, N.; Ji, S.; Zhang, R.; Zhao, C.; Li, J.-R. Metal-Organic Framework/Poly(vinyl alcohol) Nanohybrid Membrane for the Pervaporation of Toluene/*n*-Heptane Mixtures. *J. Membr. Sci.* **2015**, *489*, 144–152.
20. Novel Super Adsorbents (PVA and PVA/Cu-MOF Nanofibres) as Effective Lead Ions Remover in Aqueous Solution. *Dig. J. Nanomater. Biostruct.* **2016**, *11*, 425–434.
21. Giustarini, D.; Milzani, A.; Dalle-Donne, I.; Rossi, R. Detection of S-Nitrosothiols in Biological Fluids: A Comparison Among the Most Widely Applied Methodologies. *J. Chromatogr. B* **2007**, *851*, 124–139.
22. Cha, W.; Meyerhoff, M. E. Catalytic Generation of Nitric Oxide from S-Nitrosothiols Using Immobilized Organoselenium Species. *Biomaterials* **2007**, *28*, 19–27.
23. Hwang, S.; Meyerhoff, M. E. Organoditelluride-mediated Catalytic S-Nitrosothiol Decomposition. *J. Mater. Chem.* **2007**, *17*, 1462–1465.
24. Oh, B. K.; Meyerhoff, M. E. Spontaneous Catalytic Generation of Nitric Oxide from S-Nitrosothiols at the Surface of Polymer Films Doped with Lipophilic Copper(II) Complex. *J. Am. Chem. Soc.* **2003**, *125*, 9552–9553.

25. Major, T. C.; Brant, D. O.; Burney, C. P.; Amoako, K. A.; Annich, G. M.; Meyerhoff, M. E.; Handa, H.; Bartlett, R. H. The Hemocompatibility of a Nitric Oxide Generating Polymer that Catalyzes *S*-Nitrosothiol Decomposition in an Extracorporeal Circulation Model. *Biomaterials* **2011**, *32*, 5957–5969.
26. Singh, M. P.; Dhumal, N. R.; Kim, H. J.; Kiefer, J.; Anderson, J. A. Influence of Water on the Chemistry and Structure of the Metal–Organic Framework Cu<sub>3</sub>(btc)<sub>2</sub>. *J. Phys. Chem. C* **2016**, *120*, 17323–17333.
27. Demessence, A.; D’Alessandro, D. M.; Foo, M. L.; Long, J. R. Strong CO<sub>2</sub> Binding in a Water-Stable, Triazolate-Bridged Metal–Organic Framework Functionalized with Ethylenediamine. *J. Am. Chem. Soc.* **2009**, *131*, 8784–8786.
28. Liu, K.; Meyerhoff, M. E. Preparation and Characterization of an Improved Cu<sup>2+</sup>-Cyclen Polyurethane Material that Catalyzes Generation of Nitric Oxide from *S*-Nitrosothiols. *J. Mater. Chem.* **2012**, *22*, 18784–18787.
29. Dash, M.; Chiellini, F.; Ottenbrite, R. M.; Chiellini, E. Chitosan—A Versatile Semi-Synthetic Polymer in Biomedical Applications. *Prog. Polym. Sci.* **2011**, *36*, 981–1014.
30. Qin, Y. The Chelating Properties of Chitosan Fibers. *J. Appl. Polym. Sci.* **2003**, *49*, 727–731.
31. Williams, D. L. H. The Mechanism of Nitric Oxide Formation from *S*-Nitrosothiols (Thionitrites). *Chem. Commun.* **1996**, 1085–1091.
32. Alexandre, N.; Ribeiro, J.; Gärtner, A.; Pereira, T.; Amorim, I.; Fragoso, J.; Lopes, A.; Fernandes, J.; Costa, E.; Santos-Silva, A.; Rodrigues, M.; Santos, J. D.; Maurício, A. C.; Luís, A. L. Biocompatibility and Hemocompatibility of Polyvinyl Alcohol Hydrogel

- Used for Vascular Grafting — *In Vitro* and *In Vivo* Studies. *J. Biomed. Mater. Res., Part A* **2014**, *102*, 4262–4275.
33. Seabra, A. B.; Da Rocha, L. L.; Eberlin, M. N. de Oliveria, M. G. Solid Films of Blended Poly (Vinyl Alcohol)/Poly (Vinyl Pyrrolidone) for Topical *S*-Nitrosoglutathione and Nitric Oxide Release. *J. Pharm. Sci.* **2005**, *94*, 994–1003.
  34. De Souza Godoy Simões, M. M.; de Oliveria, M. G. Poly(vinyl alcohol) Films for Topical Delivery of *S*-Nitrosoglutathione: Effect of Freezing-Thawing on the Diffusion Properties. *J. Biomed. Mater. Res., Part B* **2010**, *93*, 416–424.
  35. Bolto, B.; Tran, T.; Hoang, M.; Xie, Z. Crosslinked Poly(vinyl alcohol) Membranes. *Prog. Polym. Sci.* **2009**, *34*, 969–981.
  36. Zhang, Y.; Feng, X.; Yuan, S.; Zhou, J.; Wang, B. Challenges and Recent Advances in MOF-polymer Composite Membranes for Gas Separation. *Inorg. Chem. Front.* **2016**, *3*, 896–909.
  37. Denny Jr, M. S.; Cohen, S. M. In Situ Modification of Metal-Organic Frameworks in Mixed Matrix Membranes. *Angew. Chem. Int. Ed.* **2015**, *54*, 9029–9032.
  38. Krimm, S.; Liang, C. Y.; Sutherland, G. B. B. M. Infrared Spectra of High Polymers. V. Polyvinyl Alcohol. *J. Polym. Sci.* **1956**, *22*, 227–247.
  39. Figueiredo, K. C. S.; Alves, T. L. M.; Borges, C. P. Poly(vinyl alcohol) Films Crosslinked by Glutaraldehyde Under Mild Conditions. *J. Appl. Polym. Sci.* **2009**, *111*, 3074–3080.
  40. Hojo, N.; Shirai, H.; Hayashi, S. Complex Formation Between Poly(vinyl alcohol) and Metallic Ions in Aqueous Solution. *J. Polym. Sci., Polym. Symp.* **1974**, *47*, 299–307.

41. Hajipour, A. R.; Mohammadsaleh, F.; Sabzalian, M. R. Copper-containing Poly(vinyl alcohol) Composite Systems: Preparation, Characterization and Biological Activity. *J. Phys. Chem. Solids* **2015**, *83*, 96–103.
42. El-Zaher, N. A.; Osiris, W. G. Thermal and Structural Properties of Poly(vinyl alcohol) Doped with Hydroxypropyl Cellulose. *J. Appl. Polym. Sci.* **2005**, *96*, 1914–1923.
43. Dong, W. F.; Wang, Y.; Huang, C. G.; Xiang, S. F.; Ma, P. M.; Ni, Z. B.; Chen, M. Q. Enhanced Thermal Stability of Poly(vinyl alcohol) in Presence of Melanin. *J. Therm. Anal. Calorim.* **2014**, *115*, 1661–1668.
44. Guirguis, O. W.; Moselhey, M. T. H. Thermal and Structural Studies of Poly(vinyl alcohol) and Hydroxypropyl Cellulose Blends. *Natural Science* **2012**, *4*, 57–67.
45. Radomski, M. W.; Palmer, R. M. J.; Moncada, S. The Role of Nitric-Oxide and cGMP in Platelet-Adhesion to Vascular Endothelium. *Biochem. Biophys. Res. Commun.* **1987**, *148*, 1482–1489
46. Thomas, D. D.; Liu, X.; Kantrow, S. P.; Lancaster, J. R., Jr. The Biological Lifetime of Nitric Oxide: Implications for the Perivascular Dynamics of NO and O<sub>2</sub>. *Proc. Natl. Acad. Sci. U. S. A.* **2001**, *98*, 355–360.
47. Stamler, J.S.; Jaraki, O.; Osborne, J.; Simon, D.I.; Keaney, J.; Vita, J.; Singel, D.; Valeri, C. R.; Loscalzo, J. Nitric Oxide Circulates in Mammalian Plasma Primarily as an S-Nitroso Adduct of Serum Albumin. *Proc. Natl. Acad. Sci. U. S. A.* **1992**, *89*, 7674–7677.
48. Giustarini, D.; Milzani, A.; Colombo, R.; Dalle-Donne, I.; Rossi, R. Nitric Oxide and S-Nitrosothiols in Human Blood. *Clin. Chim. Acta* **2003**, *330*, 85–98.

49. Hwang, S.; Meyerhoff, M. E. Polyurethane with Tethered Copper (II)-Cyclen Complex: Preparation, Characterization and Catalytic Generation of Nitric Oxide from S-Nitrosothiols. *Biomaterials* **2008**, *29*, 2443–2452.
50. Diers, A. R.; Keszler, A.; Hogg, N. Detection of S-Nitrosothiols. *Biochim. Biophys. Acta* **2014**, *1840*, 892–900.
51. Skrzypchak, A. M.; Lafayette, N. G.; Bartlett, R. H.; Zhou, Z.; Frost, M. C.; Meyerhoff, M. E.; Reynolds, M. M.; Annich, G. M. Effect of Varying Nitric Oxide Release to Prevent Platelet Consumption and Preserve Platelet Function in an In Vivo Model of Extracorporeal Circulation. *Perfusion* **2007**, *22*, 193–200.
52. Vaughn, M. W.; Kuo, L.; Liao, J. C. Estimation of Nitric Oxide Production and Reaction Rates in Tissue by use of a Mathematical Model. *Am. J. Physiol.: Heart Circ. Physiol.* **1998**, *274*, H2163–H2176.
53. Grossi, L.; Montecvecchi, P. C.; Strazzari, S. Decomposition of S-Nitrosothiols: Unimolecular versus Autocatalytic Mechanism. *J. Am. Chem. Soc.* **2001**, *123*, 4853–4854.
54. Aga, R. G.; Hughes, M. N. Chapter Three – The Preparation and Purification of NO Gas and the Use of NO Releasers: The Application of NO Donors and Other Agents of Nitrosative Stress in Biological Systems. *Methods Enzymol.* **2008**, *436*, 35–48.
55. Duke, A. S.; Dolgoplova, E. A.; Galhenage, R. P.; Ammal, S. C.; Heyden, A.; Smith, M. D.; Chen, D. A.; Shustova, N. B. Active Sites in Copper-Based Metal-Organic Frameworks: Understanding Substrate Dynamics, Redox Processes, and Valence-Band Structures. *J. Phys. Chem. C* **2015**, *119*, 27457–27466.

56. Li, T.; Taylor-Edinbyrd, K.; Kumar, R. A Computational Study of the Effect of the Metal Organic Framework Environment on the Release of Chemically Stored Nitric Oxide. *Phys. Chem. Chem. Phys.* **2015**, *17*, 23403–23412.
57. Taylor-Edinbyrd, K.; Li, T.; Kumar, R. Effect of Chemical Structure of *S*-Nitrosothiols on Nitric Oxide Release Mediated by the Copper Sites of a Metal Organic Framework Based Environment. *Phys. Chem. Chem. Phys.* **2017**, *19*, 11947–11959.
58. Redisch, W.; Sheckman, E.; Stelle, J. M. Skin Temperature Response of Normal Human Subjects to Various Conditions. *Circulation* **1952**, *6*, 862–867.
59. Hornyák, I.; Marosi, K.; Kiss, L.; Gróf, P.; Lacza, Z. Increased Stability of *S*-Nitrosothiol Solutions via pH Modulations. *Free Radic. Res.* **2012**, *46*, 214–225.
60. Singh, R. J.; Hogg, N.; Joseph, J.; Kalyanaraman, B. Mechanism of Nitric Oxide Release from *S*-Nitrosothiols. *J. Biol. Chem.* **1996**, *271*, 18596–18603.
61. McAninly, J.; Williams, D. L. H.; Askew, S. C.; Butler, A. R.; Russell, C. Metal Ion Catalysis in Nitrosothiol (RSNO) Decomposition. *J. Chem. Soc., Chem. Commun.* **1993**, 1758–1759.
62. Dicks, A. P.; Swift, H. R.; Williams, D. L. H.; Butler, A. R.; Al-Sa'doni, H. H.; Cox, B. G. Identification of Cu<sup>+</sup> as the Effective Reagent in Nitric Oxide Formation from *S*-Nitrosothiols (RSNO). *J. Chem. Soc., Perkin Trans. 2* **1996**, 481–487.
63. Dicks, A. P.; Beloso, P. H.; Williams, D. L. H. Decomposition of *S*-Nitrosothiols: The Effects of Added Thiols. *J. Chem. Soc., Perkin Trans. 2* **1997**, 1429–1434.
64. Williams, D. L. H. The Chemistry of *S*-Nitrosothiols. *Acc. Chem. Res.* **1999**, *32*, 869–876.

65. Dhakshinamoorthy, A.; Alvaro, M.; Concepcion, P.; Garcia, H. Chemical Instability of  $\text{Cu}_3(\text{BTC})_2$  by Reaction With Thiols. *Catal. Commun.* **2011**, *12*, 1018–1021.
66. Ke, F.; Qiu, L.-G.; Yuan, Y.-P.; Peng, F.-M.; Jiang, X.; Xie, A.-J.; Shen, Y.-H.; Zhu, J.-F. Thiol-functionalization of Metal-Organic Framework by a Facile Coordination-Based Postsynthetic Strategy and Enhanced Removal of  $\text{Hg}^{2+}$  from Water. *J. Hazard. Mater.* **2011**, *196*, 36–43.
67. Gorin, G.; Martic, P. A.; Doughty, G. Kinetics of the Reaction of N-Ethylmaleimide with Cysteine and Some Congeners. *Arch. Biochem. Biophys.* **1966**, *115*, 593–597.
68. Sharpless, N. E.; Flavin, M. The Reactions of Amines and Amino Acids with Maleimides. Structure of the Reaction Products Deduced from Infrared and Nuclear Magnetic Resonance Spectroscopy. *Biochemistry* **1966**, *5*, 2963–2971.

## CHAPTER 6

### CONCLUDING REMARKS AND FUTURE DIRECTIONS

#### 6.1 Project Summary

While the principle of generating NO from endogenous substrates has been the subject of research for over a decade, the conscription of MOFs for this purpose is a relatively recent development. In the original 2012 report from Harding *et al.*, the commercial carboxylate-based MOF CuBTC was used to produce NO from *S*-nitrosocysteine in reagent alcohol. This seminal work demonstrated the feasibility of utilizing a copper-based MOF to catalyze the release of NO from RSNOs, albeit under conditions that were far from physiological relevance. *S*-nitrosocysteine is not known to occur endogenously except in the form of residues in macromolecular peptides, while the use of reagent alcohol was necessitated by the instability of CuBTC in water. Moreover, cysteine was added in a stoichiometric quantity relative to theoretical MOF copper sites to promote the reduction of  $\text{Cu}^{2+}$  to  $\text{Cu}^+$ , a process that may lead to the formation of structural defects and secondary catalysts. Additionally, measurement of NO generation was performed under anaerobic conditions, thus the ability of the MOF to generate NO under truly physiological conditions (aerobic) had not been demonstrated. In 2014, a subsequent publication established the concept of embedding CuBTC particles within a polymer matrix to model the fabrication of implantable devices. It was observed that the reaction rate may be influenced by the need for the RSNO substrate to diffuse through the polymer matrix before interacting with the MOF. This principle contributed to the notion of *localizing* the MOF to the surface of a polymeric substrate to minimize the influence of this type of diffusion.

Because the effective translation of copper-based MOFs to commercial blood-contacting applications requires their immobilization within a polymeric support, the work presented in this dissertation focused on identifying and optimizing the parameters needed to produce MOF-based materials that retain the therapeutic activity of the MOF itself. In Chapter 2, the concept of localizing the MOF to the surface of a polymer substrate was explored through the direct growth of CuBTC on carboxymethylated cotton fabric using a layer-by-layer (LBL) methodology. This LBL methodology was modified from a previous report by Pinto *et al.* who observed that the order of reagent addition impacted the degree of CuBTC deposition.<sup>1</sup> The CuBTC-coated fabric produced from this modified method exhibited significantly enhanced surface coverage, demonstrating how CuBTC deposition could be further optimized. Evaluation of the coated fabric indicated that the material was able to induce NO formation from *S*-nitrosocysteamine at rates comparable to unsupported CuBTC particles. Overall, this work demonstrated deposition of CuBTC onto a flexible polymeric material with excellent coverage, as well as promotion of NO release from *S*-nitrosocysteamine at therapeutically-relevant levels. However, this model system remained confined to alcohol and a non-physiological RSNO substrate, preventing its use in blood-contacting applications. The 2014 observation that water-stable CuBTTri could promote NO release from RSNOs in a manner analogous to the reactivity of CuBTC permitted progress toward MOF-based materials for practical biomedical use. Chapter 3 described the incorporation of CuBTTri within films made from PVC, a polymer used to fabricate the tubing used to transport blood in extracorporeal circuits (ECCs). This work was the first to assess the toxicological impact of CuBTTri-based materials, and used 3T3-J2 murine embryonic fibroblasts and primary human hepatocytes (PHHs) to model liver function. No significant toxicity was observed over 16 days of exposure, providing key support for the potential implementation of CuBTTri in medical

applications. Additionally, the ability of CuBTTri to enhance the rate of NO generation from RSNOs was retained following incorporation within PVC. Following exposure to SNAP at ambient temperature and physiological pH, it was observed that CuBTTri/PVC films were able to generate NO at a level frequently associated with antithrombogenic surfaces. However, SNAP does not occur endogenously, and the concentration of the compound used in NO release experiments was above the physiological values that are generally reported for RSNOs in blood. The absence of definitive evidence that either CuBTC or CuBTTri could initiate the decomposition of the physiological RSNO reservoir (which is largely composed of *S*-nitrosoalbumin and GSNO) remained a significant obstacle to further development. While the ability of CuBTTri/PVC to produce NO from GSNO was assessed in unpublished experiments, no enhancement in the rate of NO release was detected. In contrast, preliminary experiments had suggested that it was indeed possible for unbound CuBTTri particles to generate NO from GSNO, indicating that the hydrophobic polymer may inhibit diffusion of the substrate.

Based on these results, polymer formulations with increased hydrophilic character were evaluated in Chapters 4 and 5. Chapter 4 discussed the inclusion of CuBTTri within the naturally-derived polysaccharide chitosan to form membranes that were evaluated for their ability to enhance NO generation from GSNO. This was the first report which evaluated MOF-induced NO release from GSNO, the most abundant small-molecule RSNO in the blood. As previously mentioned, the RSNO concentrations used in prior accounts were non-physiological. In Chapter 4, a lower, near physiological concentration of GSNO is used (20  $\mu\text{M}$ ). Furthermore, incorporation of CuBTTri within hydrophilic chitosan did not impair the activity of the MOF, unlike earlier efforts using PVC. In an effort to provide insight into the mechanism of action, the major organic product of CuBTTri-promoted GSNO decomposition was identified as oxidized glutathione *via* mass

spectrometry. This result confirmed the hypothesis that the RSNOs are decomposed by the MOF to generate NO and the corresponding disulfide, similar to the decomposition products formed in the presence of copper ions. However, the mechanism of RSNO decomposition in the presence of CuBTTri remains unknown. While this project expanded the activity of CuBTTri to include a physiological RSNO substrate, chitosan exhibits pronounced hemostatic effects (properties which are used to stem blood loss from hemorrhagic injuries) that render it less than ideal for blood-contacting applications aimed at preventing thrombus formation.

The subsequent work from Chapter 5 resulted in the incorporation of CuBTTri within hydrophilic membranes prepared from PVA, a polymer that has been examined for numerous biomedical applications. These CuBTTri/PVA membranes promoted NO release from GSNO at physiological temperature and pH. It is particularly noteworthy that this NO release occurred at a surface flux within the range associated with the natural endothelium and was achieved from a GSNO concentration of 10  $\mu\text{M}$ , a concentration that is within the upper end of the reported physiological RSNO concentrations. Furthermore, a technique was developed in order to demonstrate for the first time that CuBTTri is capable of inducing NO production from GSNO under aerobic conditions. Moreover, in an effort to permit optimization for potential medical applications, a more comprehensive analysis of the parameters that could influence CuBTTri efficacy were investigated, including pH, temperature, and polymer material. These findings suggest that CuBTTri/PVA membrane holds promise for therapeutic utility through its ability to generate NO from endogenous substrates.

As mentioned in the introduction, these MOF-based materials must demonstrate several basic characteristics to be feasible for translation to clinical use. In general, the MOF must retain its structure and function upon incorporation into the polymeric material and at physiological

temperature and pH with minimal to no leaching of the organic ligand or copper. Additionally, interaction of the MOF with endogenously available RSNOs should result in the generation of NO flux ranges associated with the nonthrombogenic endothelium (**Figure 6.1**).

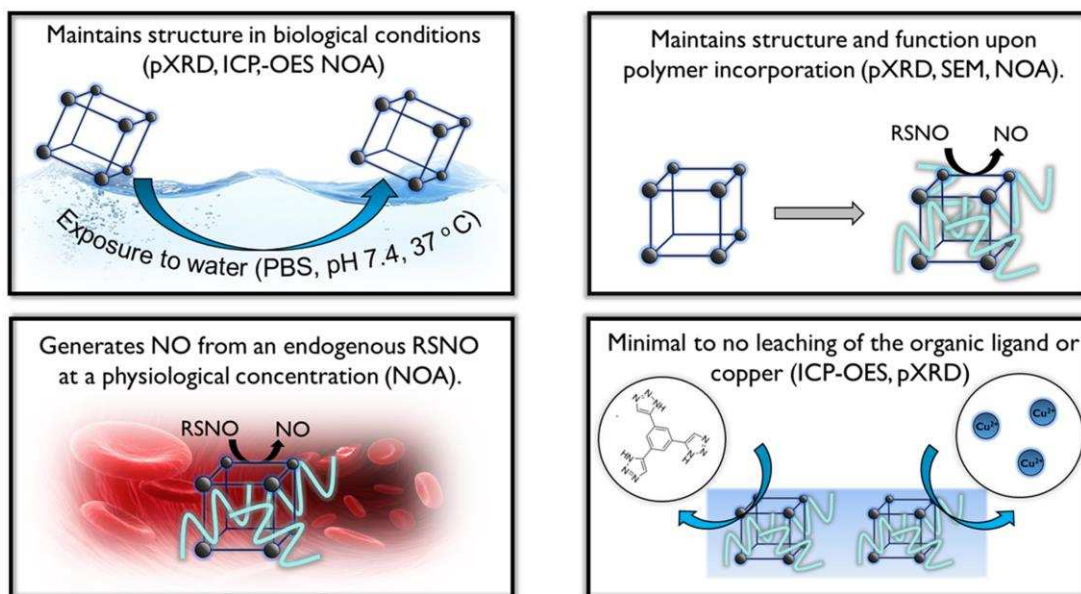


**Figure 6.1** Minimum characteristics MOF-based materials should demonstrate for clinical application. All requirements have been met.

Prior to this research, there was no direct evidence that MOF-polymer materials were capable of enhancing NO generation from RSNOs under truly physiologically relevant conditions. This dissertation demonstrated that materials based on CuBTri have met these requirements, advancing their translation to clinical use. Moving forward, there are several concepts that must be taken into consideration when further developing NO-producing MOF-based materials.

## 6.2 Device fabrication

The therapeutic potential of CuBTri is supported by clear evidence that the MOF retains its ability to induce the NO-forming decomposition of RSNOs after inclusion within several different polymer matrices. However, translation of this technology to clinical use requires the fabrication of devices that exploit the unique chemistry of copper-based MOFs. High similarity to

existing medical devices facilitates the clinical implementation of this chemistry, therefore the direct blending of CuBTTri within common medical polymers is desirable as a fabrication technique. While materials of this type remain in a developmental stage, a significant body of preliminary work has been carried out to examine the practicality of creating CuBTTri-based devices. Towards this end, MOF/polymer coatings have been applied to catheters, ECCs, and thromboelastography (TEG) cups. As depicted in both SEM and optical microscope images, CuBTTri is clearly dispersed throughout the entire surface of both Tygon and polyurethane blood flow loops (**Figure 6.2**). Additionally, cross-sectional analysis with EDS overlay shows the presence of CuBTTri within 20  $\mu\text{m}$  of the polymer layer deposited on the parent device. As

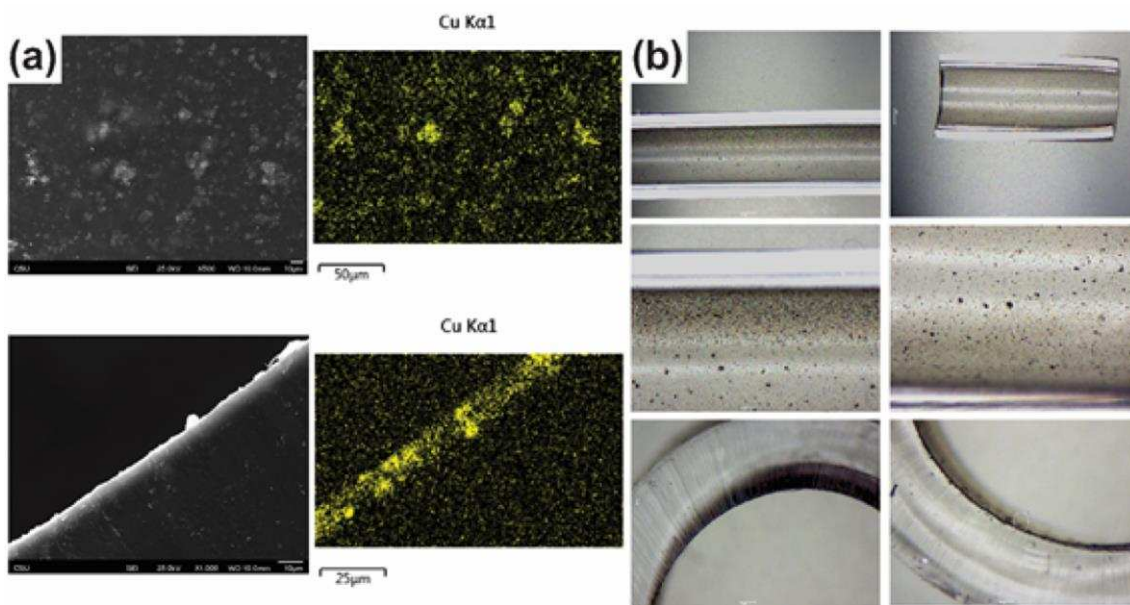


**Figure 6.2.** Fabrication of Cu-BTTri/polymer coated catheters (a) SEM imaging with EDS overlay showing the inside surface of the coated catheters and a cross section showing the thickness of the Cu-BTTri/polymer coating on the catheter. (b) Microscope imaging of the surface of the inner lumen of the Cu-BTTri/polymer coating.

characterized by EDS, copper (derived from the MOF) is dispersed over the entire inner surface of the device, with the greatest concentration occurring at sites where the presence of crystalline MOF is apparent.

However, this dispersion is far from uniform, with certain regions of the tubing displaying little to no coverage and areas with a higher degree of particle agglomeration. Indeed, this lack of uniformity represents one of the chief complications when fabricating MOF/polymer composite materials. The MOF and the polymer host material exhibit distinct physical and chemical properties that can induce the agglomeration of MOF particles. This complication has been observed elsewhere and can be partially addressed by priming of the MOF particles. This priming technique involves the suspension of the MOF particles in the selected solvent, followed by the addition of a small amount of the dissolved polymer solution. The MOF particles are then coated in a small amount of the polymer before being dispersed into the main polymer solution, thus decreasing the affinity of the particles for each other and creating a more homogenous dispersion.<sup>2</sup> While use of this approach has decreased the degree of particle agglomeration in coatings prepared using CuBTTri, the aggregation of MOF remains a substantial concern. For this reason, the utilization of extrusion would be advantageous to the development of MOF/polymer composites. During the process of extrusion, the raw materials (MOF and polymer) are mixed and melted, then the molten polymer mixture is forced through a die which shapes the material as it is cooled. This processing technique allows for the formation of a highly homogeneous material. The feasibility of this approach was demonstrated in 2014 by Harding *et al.* who blended CuBTC into a polyurethane using industrial extrusion processing methods to form both pellets and segments of tubing (**Figure 6.3**).<sup>3</sup>

Another important factor to consider when developing these MOF/polymer composite materials is the nature of the polymer (i.e., hydrophobic or hydrophilic) and its potential impact on the ability of the RSNOs to interact with the MOF. As demonstrated in Chapter 5, the use of a hydrophobic polyurethane compared to a hydrophilic crosslinked PVA significantly hindered NO

generation. In the case of the CuBTTri/Tecoflex SG-80A films, only  $1.5 \pm 0.4\%$  of theoretical NO was released, whereas  $97 \pm 6\%$  was recovered in the presence of the CuBTTri/PVA membranes. These materials had respective water uptake values of  $2.0 \pm 0.3$  and  $203 \pm 3\%$ , demonstrating the importance of the hydrophilic character of the polymer in facilitating NO generation. This

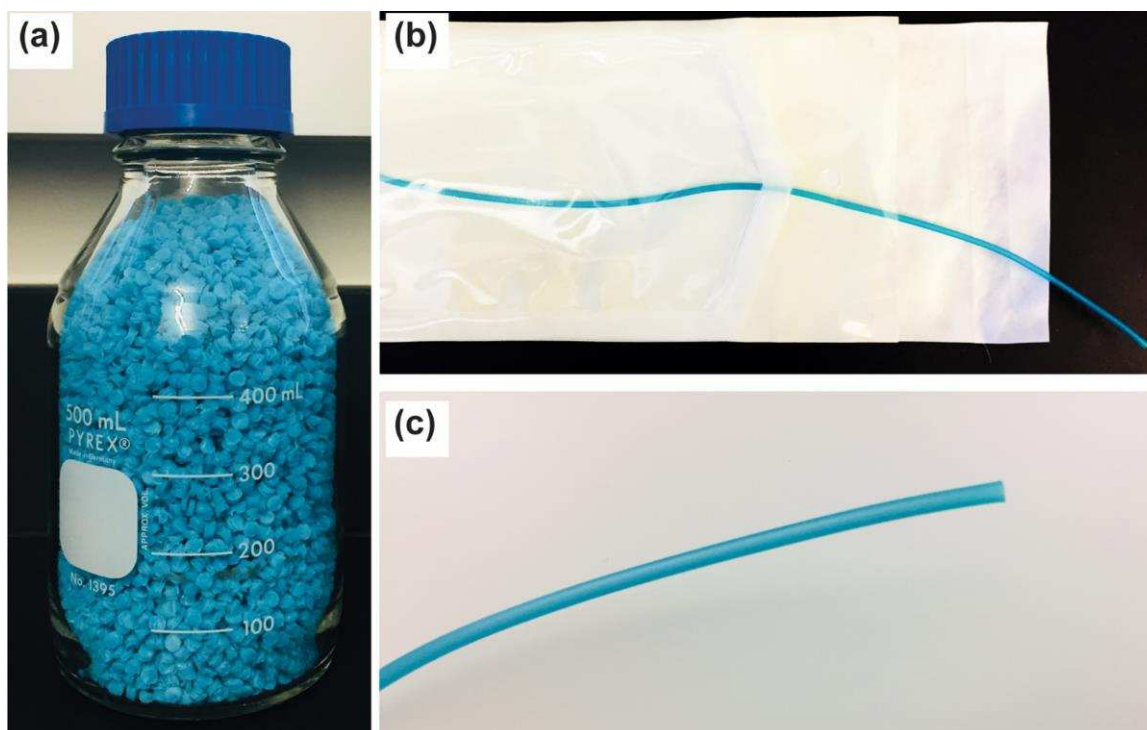


**Figure 6.3** Images of the CuBTC/polymer materials produced through industrial extrusion processes. (a) CuBTC/polymer pellets (b) CuBTC/polymer tubing.

phenomenon affects the clinical utility of the material, since its potential antithrombotic properties are dependent upon the NO-forming interaction of the MOF with endogenous RSNOs. However, the transport of GSNO through polymer matrices remains a poorly understood process. It is therefore obvious that the study of GSNO diffusion through polymers would provide valuable insight into the interaction of polymer-bound CuBTTri with RSNOs. In general, the nature of a polymeric material has been found to significantly influence the transport behavior for a given molecule. Factors such as degree of crosslinking, polarity, molecular weight, and extent of

unsaturation will all affect molecular transport.<sup>a</sup> In addition, the size and shape of the molecule will influence transport within a polymeric matrix.

As the nature of the polymeric material seems of vital importance in facilitating the interaction of CuBTTri with GSNO, a further understanding of these transport properties is necessary for their development. Once understood, these properties can aid in device fabrication aimed at optimizing NO generation from the endogenous RSNOs. An understanding of the polymer transport properties in combination with a reliable methodology for improving MOF dispersion throughout the polymer will ultimately aid in designing these MOF/polymer composite materials for biomedical applications.

### **6.3 Assessment of blood compatibility**

Biomaterials that include CuBTTri possess significant clinical potential due to the ability of the MOF to modulate biological processes such as clotting, infection, and wound healing. However, these materials are presently confined to the laboratory as a result of an unclear understanding of their behavior in a biological environment. Nevertheless, preliminary studies have revealed that CuBTTri may produce detectable effects in the presence of blood. For example, a collaboration with the *U.S. Army Institute of Surgical Research* assessed the impact of CuBTTri on real-time clot formation in human blood using TEG analysis.<sup>4</sup> TEG is an instrumental technique which uses viscoelastic methods to provide real-time kinetics of clot initiation, formation, strength, and breakdown. Typically, this technique has been used in clinical settings to assess a patient's bleeding and thrombotic risks. However, TEG is now utilized as an experimental technique to assess the influence of various biomaterials on blood at the blood-material interface under *ex vivo* conditions.<sup>5-6</sup> In this technique, whole blood is placed into a plastic cup which is capped with a lid containing a pin that is submerged in the blood. The pin is slowly oscillated at an angle of 4°45'.

As clot formation occurs, the impeded rotation of the pin and the corresponding change in torque is detected by the pin. The measurement is graphically represented as a trace profile over time which can be used to extrapolate the clotting time, clot formation, maximum clot strength, and fibrinolysis.<sup>7</sup>

In the collaborative manuscript currently under consideration by the *Journal of Trauma and Acute Care Surgery*, TEG was used to examine the efficacy of CuBTri in preventing thrombus formation by detecting changes in the stages of clot formation in real-time. These experiments were performed by dispersing the MOF powder in a small amount of PBS followed by addition to a sample of whole blood. When compared to the control (whole blood + PBS), the MOF powder produced a notable reduction in clot strength (MOF=53.67 ± 1.35 mm, C= 56.22 ± 1.42 mm) and an accelerated rate of clot lysis after 30 (MOF = 3.22 ± 0.99%, C = 0.82 ± 0.26%) and 60 min

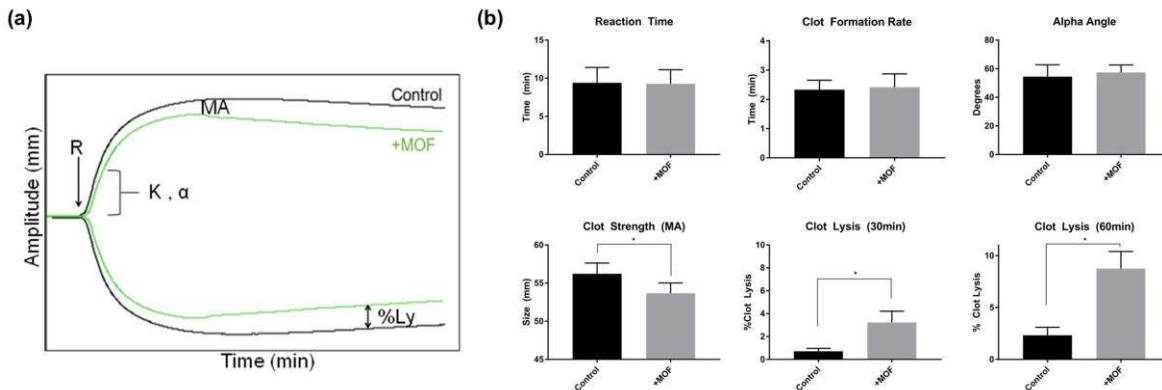


**Figure 6.4** (a) TEG trace of the MOF powder in blood (green) compared to the control (blood + PBS) (black). (b) Graphical representation of the mean ± standard error for reaction time, clot formation time, alpha angle, clot strength, clot lysis at 30 minutes, and clot lysis at 60 minutes as determined by TEG of human blood. (n=10)

(MOF = 8.75 ± 1.64%, C = 2.33 ± 0.77 %) (**Figure 6.4**). This observation of reduced clot strength and accelerated clot lysis was hypothesized to result from NO through inhibition of platelet aggregation and promotion of clot dissolution. However, it should be noted that no experiments were performed to further confirm this hypothesis. These initial experiments suggest that CuBTri holds potential in the inhibition of thrombus formation. However, the successful translation of

these MOFs in biomedical applications is dependent on their performance following inclusion in polymeric devices, as the character of the polymeric material can influence the MOFs ability to facilitate NO generation. Notably, when the same experiments were performed on samples in which the inside cup and peg had been coated with a hydrophobic MOF/polymer layer, no change in clotting kinetics was observed compared to the control (polymer coating).

Because it is critical that these materials generate NO in blood-contacting applications, a crucial area of refinement involves the continued investigation of polymer formulations that permit interaction of RSNOs with the encapsulated MOF. Based on existing evidence, it is reasonable to hypothesize that hydrophilic polymers which allow for increased water uptake may display a greater level of NO generation. Commercial hydrophilic polymer formulations that are potential candidates include Hydrothane™, Hydromed™ (D-7), and Tecophilic™ (SP-80A-150, SP-60D-60). HydroThane™ is a hydrophilic polyurethane exhibiting water absorption of up to 25% (by weight) and HydroMed™ is a hydrophilic polyurethane specifically designed for use as a coating on devices including catheters and heart valves with water absorption up to 30%. Notably, HydroMed™ has been used as a coating to decrease the adsorption of proteins and cellular material to devices. Tecophilic™ formulations are hydrophilic polyurethanes with water uptake of 60 and 150%. With the exception of HydroMed™, these polymer formulations can all be processed by extrusion. In addition to these hydrophilic formulations, hydrophobic materials such as Tygon and Tecoflex™ should be evaluated for the degree of platelet adhesion and activation on the surface as a point of comparison.

Despite the demonstrated ability of CuBTTri/polymer materials to generate NO from a biologically-available RSNO (Chapter 4 and 5) within the range of the endothelial flux, no *in vitro* or *in vivo* biological studies have been performed to investigate their performance. Because this

type of evaluation is a necessary step toward clinical use, it is sensible to pursue *in vitro* blood studies to assess the effect of the CuBTri/polymer materials on key blood clotting components such as platelets. This type of evaluation would provide insight into the impact of the polymer on the degree of platelet adhesion. If accompanied by parallel NO generation measurements, it may be possible to establish a relationship between the observed NO flux and the degree of platelet adhesion on the material. In principle, this would permit identification of optimal MOF/polymer formulations for the fabrication of blood-contacting materials that produce predictable levels of NO from blood. However, the design of such experiments requires acknowledgement of one of the most challenging aspects of NO generation from endogenous substrates: the unknown, and potentially highly variable RSNO content of human blood.

As the therapeutic properties of the MOF are based on its ability to generate NO by harvesting LMW RSNOs in the blood, the basal RSNO blood concentration must be sufficient to produce an NO flux capable of preventing thrombus formation. The concentration of RSNO in blood is a highly debated topic with existing reports ranging from sub-nM to  $\mu\text{M}$ . Additionally, questions arise related to the variability in available RSNO from person to person. To date, none of these questions have been satisfactorily addressed, and reports that utilize copper species (complexes or MOFs) rely on exogenous RSNO to demonstrate their function. A large majority of the publications that utilize copper complexes test their NO-forming properties using SNAP due to its high stability, yet this compound is not produced physiologically. Variability in blood RSNO concentration and its impact on the efficacy of the MOF should be assessed in part by performing blood studies on blood taken from multiple donors.

In reality, the potential lack of sufficient blood RSNO to produce antithrombotic effects is a significant limiting factor in the translation of MOF-based materials to clinical use. For this reason,

*in vitro* blood studies should be performed which assess the MOF/polymer both with and *without* the addition of exogenous GSNO. If the formulation is unable to prevent platelet adhesion without exogenous GSNO, it is likely that the materials will be unsuitable for internal blood-contacting applications. Nevertheless, such materials could potentially be utilized for external blood-contacting devices (e.g., ECC tubing) if the addition of exogenous RSNO results in an antithrombotic flux, since such compounds can be supplied in a relatively straightforward manner.

It should be noted that these CuBTTri/polymer composites are not isolated to blood-contacting applications. It was recently reported by Neufeld *et al.* that CuBTTri/chitosan films demonstrated a 75-79% reduction in the bacterial attachment of *Pseudomonas aeruginosa* compared to a chitosan control.<sup>8</sup> The observed decrease in attachment was related to the presence of CuBTTri in the films. Because no exogenous source of NO was present in the system, this may suggest that CuBTTri can independently function as an antibacterial agent. Extensive control experiments were performed in order to ensure that the observed antibacterial activity was not an artifact from the presence of copper ions. While the mechanism of action of CuBTTri against bacteria is currently unknown, these initial findings demonstrate the material's versatility in medical applications.

#### **6.4 Final Thoughts**

Since the basic observation that the suspension of blood in a solution of paraffin oil prolonged blood clotting in the early 19<sup>th</sup> century, research related to blood-material interactions has grown exponentially. The research discussed in this dissertation represents one aspect of an interdisciplinary approach needed for enhancing the integration between the human body and medical devices. The successful design of blood-contacting materials involves not only the materials and their surfaces, but also an understanding of human biology and the adequate

assessment of blood-material interactions. Each of these parameters plays a vital role in the development of enhanced blood-material interfaces. A promising approach involves mimicking biological mechanisms for internal regulation of the cardiovascular system. The use of MOFs for therapeutic NO generation from endogenous molecules offers a unique approach for enhancing blood-material interactions. Currently, the development of MOFs for biomedical applications remains in an adolescent stage, with no current use in patient care. For instance, an understanding of the biodegradability, stability, and toxicity of MOFs is an undeveloped field with information regarding these critical factors limited to only a handful of publications. In regards to the use of MOFs for biomedical applications, the majority of reports have focused their attention specifically on MOF particles. However, potential applications will remain limited unless the materials are incorporated within a polymeric support. When developing materials specifically for blood-contacting applications, NO release function is a well-established, promising approach to preventing thrombus formation. As polymeric encapsulation can significantly influence NO generation using MOFs, part of the challenge involves identification of polymers that optimize the productive, NO-forming interaction between aqueous-phase RSNOs and CuBTTri. Taken together, this work has expanded on the initial reports and has identified ideal characteristics that MOF/polymer composites should exhibit in order to optimize them for therapeutic use. This work serves as a starting point for developing MOF-based materials to their fullest capability for their intended use. The future investigation and assessment of their *in vivo* activity will aid in the refinement and advancement of these promising systems for medical applications.

## REFERENCES

1. da Silva Pinto, M.; Augusto Sierra-Avila, C.; Hinstroza, J. P. In situ Synthesis of a CuBTC Metal-Organic Framework (MOF 199) onto Cellulosic Fibrous Substrates: Cotton. *Cellulose* **2012**, *19*, 1771-1779.
2. Zhang, Y.; Feng, X.; Yuan, S.; Zhou, J.; Wang, B. Challenges and Recent Advances in MOF-polymer Composite Membranes for Gas Separation. *Inorg. Chem. Front.* **2016**, *3*, 896-909.
3. Harding, J. L.; Reynolds, M. M. Composite Materials with Embedded Metal Organic Framework Catalysts for Nitric Oxide Release from Bioavailable S-nitrosothiols. *J. Mater. Chem. B* **2014**, *2*, 2530-2536.
1. George, S. C.; Thomas, S. Transport Phenomena through Polymeric Systems. *Prog. Polym. Sci.* **2001**, *26*, 985-1017.
4. Roberts, T. R.; Neufeld, M. J.; Meledeo, M. A.; Cap, A. P.; Cancio, L. C.; Reynolds, M. M.; Batchinsky, A. I. Antithrombogenic Potential of a Metal Organic Framework Nitric Oxide Catalysts in *ex vivo* Blood. *Journal of Trauma and Acute Care Surgery* (under review)
5. Peng, H. T. Thromboelastographic Study of Biomaterials. *Journal of Biomedical Materials Research Part B Applied Biomaterials.* **2010**, *94*, 469-485.
6. Shankarraman, V.; Davis-Gorman, G.; Copeland, J. G.; Caplan, M. R.; McDonagh, P. F. Standardized Methods to Quantify Thrombogenicity of Blood-Contacting Materials via Thromboelastography. *Journal of Biomedical Materials Research Part B Applied Biomaterials* **2012**, *100*, 230-238.

7. Luddington, R. J. Thromboelastography/Thromboelastometry. *Clin. Lab. Haem.* **2005**, 27, 81-90.
8. Neufeld, B. H.; Neufeld, M. J.; Lutzke, A.; Schweickart, S. M.; Reynolds, M. M  
Antibacterial Surfaces: Metal–Organic Framework Material Inhibits Biofilm Formation  
of *Pseudomonas aeruginosa*. *Adv. Funct. Mater.* **2017**, 34, 1702255.